William Naundrup Bodé

Polymer-based acoustofluidics: bridging simulation and experiment
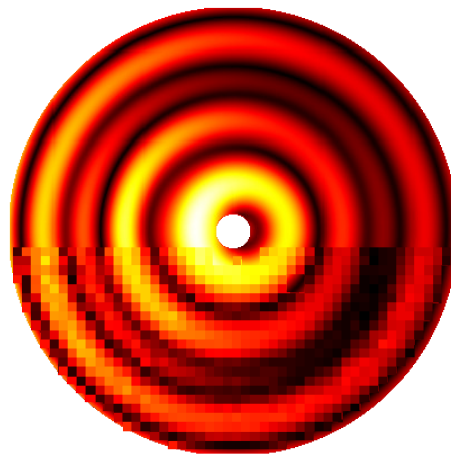
PhD thesis
Kongens Lyngby, 19 October 2022

Advised by Professor Henrik Bruus

Cover illustration: Measured (pixelated) and simulated (smooth) nanometer-sized mechanical displacement amplitude of a polymer glued onto a piezoelectric transducer vibrating 164,000 times per second. This comparison provided confidence in our model and convinced us that the simulated results were accurate and precise. The results would not have been achieved without the development of the UEIS method for ultrasound material characterization.

Polymer-based acoustofluidics: bridging simulation and experiment

Department of Physics
Technical University of Denmark
DTU Physics Building 309, DK-2800 Kongens Lyngby, Denmark
https://www.fysik.dtu.dk/microfluidics

Abstract

Acoustofluidics is an interdisciplinary field involving acoustics and microfluidics. Acousto-fluidic applications utilize the acoustic radiation force for label-free and gentle manipulation of particles. The label-free and gentle manipulation make the acoustofluidic technology suitable for biomedical applications. As acoustofluidic technology has matured throughout the last three decades, commercial interest has grown.

Typically, an acoustofluidic device is fabricated in silicon and glass using clean-room techniques, but as companies try to commercialize the technology, alternative and cost-efficient fabrication methods are desired, e.g., injection molded or 3D printed polymer devices. However, designing polymer-based acoustofluidic devices is not a straightforward procedure. Due to the low acoustic contrast between polymers and fluids, the design principles from clean-room fabricated silicon and glass-based devices are no longer applicable. Furthermore, the acoustic response in a polymer-based device is weakened due to the leakage and attenuation of acoustic waves. Therefore, polymer-based acoustofluidic devices require optimization to be competitive. Computer-aided device engineering can be used to efficiently test and optimize device designs; doing so requires accurate modeling.

In this thesis, our recently developed UEIS method will be used to determine complex-valued material parameters of different classes, including piezoceramics, a UV-curable adhesive, a polymer, and a 3D-print resin. The UEIS method provides a low-cost, easy-to-execute method that only requires simple equipment. The UEIS method is verified by ultrasound-through transmission and laser-Doppler velocimetry. The UEIS-determined material parameters enable precise and accurate modeling of polymer-based acoustofluidic devices allowing computer-aided device optimization and accurate 3D-print prototyping. Furthermore, we have developed a numerical model able to simulate acoustofluidic phenomena in multiphysics and complex systems, including the transducer, the coupling layer, and the fluid-filled microfluidic chip. The model capability is illustrated as we present simulations of polymer-based acoustofluidic devices, including the calculation of particle trajectories influenced by acoustic forces in continuous and stop-flow conditions. The particle trajectories are compared to experimental tracks providing a frequency-resolved one-to-one comparison between experiment and simulation without free parameters, i.e., an attempt to bridge simulation and experiment. I hope this thesis will provide insight into the challenges and possibilities within the field of polymer-based acoustofluidics.

Resumé

Akustofluidik er et tværfagligt felt, der kombinerer akustik og mikrofluidik. Akusto-fluidiske applikationer udnytter den akustiske strålingskraft til etiketfri og skånsom manipulation af partikler. Den etiketfri og skånsomme manipulation gør denne teknologi velegnet til biomedicinske applikationer. Efterhånden som teknologien er modnet gennem de sidste tre årtier, er den kommercielle interesse vokset.

Typisk fremstilles en akustofluidisk enhed i silicium og glas ved hjælp af renrums teknikker, men da virksomheder forsøger at kommercialisere teknologien, ønskes alternative og omkostningseffektive fremstillingsmetoder, f.eks. sprøjtestøbte eller 3D-printede polymerenheder. At designe polymerbaserede akustofluidiske enheder er ikke ligetil. På grund af den lave akustiske kontrast mellem polymerer og væsker er designprincipperne fra renrums fremstillede silicium- og glasbaserede enheder ikke længere anvendelige. Ydermere, er den akustiske respons i en polymerbaseret enhed svækket på grund af lækage og dæmpning af akustiske bølger. Polymerbaserede akustofluidiske enheder kræver optimering for at være konkurrencedygtige. Computerbaseret modellering kan bruges til effektivt at teste og optimere akustofluidisk enhedsdesign; det kræver dog nøjagtig modellering.

I denne afhandling vil vores nyligt udviklede UEIS-metode blive brugt til at bestemme materialeparametre med komplekse værdier af forskellige klasser af materialer, herunder to typer piezokeramik, et UV-hærdet lim, en polymer og en polymer brugt til 3D-print. UEIS-metoden er en billig og nem-at-udføre metode, der kun kræver simpelt udstyr. UEIS-metoden verificeres ved ultralyd-transmission og laser-Doppler hastighedsmålinger. De UEIS-bestemte materialeparametre muliggør præcis og nøjagtig modellering af polymerbaserede akustofluidiske enheder, hvilket også muliggør computerstøttet enhedsoptimering og nøjagtig 3D-print prototypefremstilling. Desuden har vi udviklet en numerisk model, der er i stand til at simulere akustofluidiske fænomener i multifysiske og komplekse systemer, som inkluderer transduceren, koblingslaget og den væskefyldte mikrofluidchip. Modellens ydeevne og potentiale er illustreret, da vi præsenterer simuleringer af polymerbaserede akustofluidiske enheder, herunder beregning af partikelbaner påvirket af akustiske kræfter under kontinuerlige og stop-flow forhold. Partikelbanerne sammenlignes med eksperimentelle målinger, der giver en frekvensopløst en-til-en sammenligning mellem eksperiment og simulering uden frie parametre, et forsøg på at forbinde simulering og eksperiment. Jeg håber, at denne afhandling vil give et indblik i udfordringer og muligheder inden for polymerbaseret akustofluidik.

Preface

This thesis is submitted in candidacy for the degree of Doctor of Philosophy from the Technical University of Denmark. The work was carried out at the Department of Physics in the Theoretical Microfluidics group headed by Professor Henrik Bruus. The project duration was three years, starting 1 September 2019. The project was supervised by Professor Henrik Bruus and co-supervised by Professor Thomas Laurell, head of the Department of Biomedical Engineering at Lund University. In addition, the project included a 3-months-stay at the Department of Biomedical Engineering at Lund University hosted by Associate Professor Per Augustsson.

Kongens Lyngby, 19 October 2022

William Naundrup Bodé

Acknowlegdement

I want to thank several people who directly or indirectly contributed to the outcome of this project. First, I want to thank current and previous colleagues at the TMF group: Gustav K. Modler, Søren A.S. Kuhberg, Bjørn G. Winckelmann, Fabian Lickert, Jonas H. Jørgensen, André Steckel, and Jacob S. Bach. I appreciate and admire our discussions of both fundamental and complex questions, but even more, everyday topics during the lunch break. I want to point out the collaboration with Fabian Lickert on our co-authored paper with shared first authorship, which I consider to be the main contribution and outcome of this project; I truly appreciate the work we did together.

Thanks to Erik Hansen from the DTU workshop for providing and fabricating microfluidic chip components. Thanks to Matthew Biviano and Magnus Paludan for introducing and helping with 3D printing. I also want to thank the people from Lund University, Per Augustsson for hosting my external stay at Lund University, Ola Jakobsson and Wei Qiu for helping out with the LDV measurements, Axel Tojo for providing the necessary equipment for the UTT measurements, and PhD student Lei Jiang for our collaboration on the PDMS-covered aluminum-based acoustofluidic device.

A special thanks to my supervisor Henrik Bruus. I first met Henrik during the quantum mechanics course as an undergraduate student. The way he communicated physics and science was amazing; at that point, I was already sold. I admire his ability to communicate science, his enthusiasm, and his dedication to physics. It is truly inspiring. I have worked with Henrik for almost four years during my BSc thesis, MSc thesis, and now this PhD project. It has been four years which I would never be without.

The outcome of this project would not be what it is if it was not for my colleagues at the TMF group, the people at DTU, and the people from Lund University. I also want to thank my friend Thor H. Snedker for his proofreading and the encouraging comments, and again thank you, Bjørn, for your theoretical assistance. Last but definitely not least, a wholehearted thanks to my coming wife Nikoline and my daughter Olivia. Having them at my side eased everything.

Contents

Publications in the PhD project

Peer-reviewed journal papers

I. <u>W. N. Bodé</u>, L. Jiang, T. Laurell, and H. Bruus, *Microparticle acoustophoresis in aluminum-based acoustofluidic devices with PDMS covers*,
Micromachines **11**(3), 1-15 (2020).
Enclosed in Section 6.1, Ref. [1].

II. <u>W. N. Bodé</u> and H. Bruus, *Numerical study of the coupling layer between transducer and chip in acoustofluidic devices*,
The Journal of the Acoustical Society of America **149**(5), 3096-3105 (2021).
Enclosed in Section 6.2, Ref. [2].

III. <u>W. N. Bodé</u>, F. Lickert, P. Augustsson, and H. Bruus, *Determination of the complex-valued elastic moduli of polymers by electrical impedance spectroscopy for ultrasound applications*,
Physical Review Applied (**resubmitted**), 1-11 (2022).
Enclosed in Section 6.3, Ref. [3].

Peer-reviewed conference contributions

1. <u>W. N. Bodé</u> and H. Bruus, *Modeling of acoustic streaming in Al-PDMS acoustofluidic chips*, The 9th Summer School of Complex Motion in Fluids, 18-24 August 2019, Gilleleje, Denmark, **poster presentation**.

2. <u>W. N. Bodé</u> and H. Bruus, *Modeling of acoustophoresis in hard microchannels with soft lids*, Acoustofluidics Conference, 25-28 August 2019, Enschede, Netherlands, **poster presentation**.

3. <u>W. N. Bodé</u> and H. Bruus, *A numerical study of the coupling layer between a piezoelectric bulk transducer and a glass device*, Acoustofluidics Conference, 26-27 August 2020, virtual conference, **oral presentation**.

4. <u>W. N. Bodé</u> and H. Bruus, *The elastic, dielectric, and piezoelectric constants of PZT transducers for acoustofluidics determined by electrical impedance spectroscopy*, Acoustofluidics Conference, 26-27 August 2021, virtual conference, **oral presentation**.

5. <u>W. N. Bodé</u>, F. Lickert, P. Augustsson, and H. Bruus, *Electrical impedance spectroscopy for acoustofluidic applications*, Acoustofluidics Conference, 19-21 October 2022, Glasgow, Scotland, **oral presentation**.

Other contributions

1. <u>W. N. Bodé</u> and H. Bruus, *3D modeling of polymer-based acoustofluidic devices*, The Swedish Center for Acoustofluidics and Cell Separation (SWECACS), 2 December 2019, Lund, Sweden, **oral presentation**.

2. <u>W. N. Bodé</u> and H. Bruus, *Simulation and characterization of polymer-based acoustofluidic devices*, The Swedish Center for Acoustofluidics and Cell Separation (SWECACS), 7 December 2021, Lund, Sweden, **oral presentation**.

List of figures

List of tables

Chapter 1

Introduction

The concept and working principles of acoustofluidics applications will be introduced with a focus on polymer-based devices. The introduction is followed by an overview of the research and the thesis. The research overview ties together, relate, and motivates the work published in the three papers listed in Chapter "Publications in the PhD project". The thesis overview provides a description of each chapter's content.

1.1 Introduction to polymer-based acoustofluidics

Acoustofluidics is an interdisciplinary research field involving acoustic waves and fluid dynamics in sub-millimeter-sized microfluidic systems, typically at megahertz frequencies in a laminar flow regime. For a laminar flow, particle trajectories are typically aligned with the streamlines providing a controlled and smooth transport of suspended particles without mixing. The particle trajectories can be manipulated by the acoustic radiation force $\boldsymbol{F}_{\mathrm{rad}}$ originating from the scattering of acoustic waves on a compressible particle. The acoustic waves are commonly generated by a piezoelectric transducer actuated at the desired frequency. Typically the acoustic radiation force is used to manipulate the particle motion perpendicular to the streamlines in a continuous flow, i.e., sorting and separating the particles facilitated by microchannel architectures. The movement of suspended particles through a fluid under the action of acoustic forces generated by acoustic actuation is referred to as acoustophoresis. The concept of acoustophoresis is illustrated in Fig. 1.1, in which the particles are focused toward the channel center and sorted in the middle channel outlet by a trichotomous branching flow. Usually, acoustofluidic devices are actuated at a resonance frequency where the acoustic response is at a maximum.

The manipulation of particles in acoustofluidic devices relies primarily on the acoustic radiation force; a compressible particle suspended in a fluid exposed to a sound field will be subject to a force originating from the stress induced by the scattering of acoustic waves.
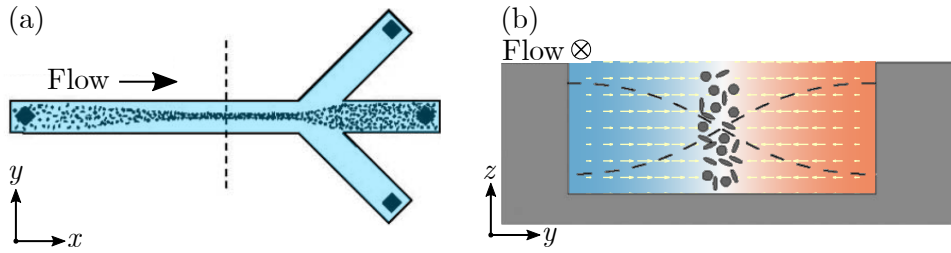
Figure 1.1: Conceptual sketch of acoustophoresis. (a) Top-view of a typical acoustofluidic design for particle (black dots) sorting with a flow in the x-direction. (b) Cross-sectional view of the channel in the yz-plane, in which a standing acoustic pressure half-wave is illustrated as a surface plot from negative (blue) to positive value (red) symmetric around zero (white). Due to the scattering of acoustic waves, particles will tend to move to the vertical pressure node (bright) facilitated by the acoustic radiation force $\boldsymbol{F}_{\mathrm{rad}}$ (yellow arrows). The cross-section plane is indicated as a dashed line in (a). The figure is adapted and modified from Ref. [4].

The acoustic radiation force depends on the particle and the fluid's acoustic properties, but also the acoustic pressure field, typically controlled by the channel geometry and actuation frequency. Particles are also affected by a drag induced by the acoustic streaming $\boldsymbol{v}_2$; a steady flow generated by the attenuation of acoustic waves. The two forces compete as the acoustic radiation force scales with the particle volume, whereas the drag induced by the acoustic streaming scales with the particle size.

Acoustofluidic devices are capable of manipulating particles in a wide range from tens of nanometer to tens of micrometer, primarily determined by the device design and the acoustic wavelength in the fluid, given by the actuation frequency typically between kilohertz and gigahertz. In this thesis, the range is narrowed down, focusing on the ultrasound megahertz regime, i.e., sub-millimeter-sized acoustic wavelengths. This range is suitable for manipulating ∼10-µm-sized particles, e.g., circulating tumor cells as well as red and white blood cells. An archetypical ultrasound acoustophoresis application is the separation of plasma from whole blood.

Acoustophoresis allows a gentle, label-free, and precise handling of particles. The particle size range covers most of the relevant biological particles in a typical liquid human biopsy, from proteins to blood cells [5]. Which makes the acoustofluidic technology suitable for a wide range of biomedical applications, including continuous-flow bioassay [6], trapping of bacteria [7], tumor cell enrichment [8], determination of hematocrit [9], bacteria detection [10], separation of living and dead cells [11], purification of lymphocytes [12] etc. The applications can be sub-categorized into continuous-flow systems and acoustic traps. In continuous-flow applications, particles are separated according to their acoustic properties relative to the fluid, whereas the acoustic traps retain particles against a flow. The acoustofluidic technology has recently gained popularity within tissue engineering, where acoustophoresis devices are used to manipulate and pattern cells typically submerged in a biodegradable hydrogel [13–16].

The acoustofluidic technology is now an established part of lab-on-a-chip systems and has proven efficient in separating, focusing, and analyzing biological samples. These systems are often fabricated in acoustically hard materials such as glass and silicon using clean-room techniques providing accurate and ideal resonators [6–11]. Acoustic hardness refers to the acoustic contrast between the fluid and the surrounding channel material. The acoustic contrast is defined as the ratio of acoustic impedance $\tilde{Z} = Z_{\mathrm{ac}}/Z_0$ between the surrounding material's acoustic impedance Z_{ac} and the fluid's acoustic impedance Z_0 defined as the product between the mass density and the sound speed. For glass and water, the acoustic contrast is $\tilde{Z} \sim 10$, so the glass is said to be acoustically hard, which signifies that the acoustic pressure field is confined to the channel. In acoustically hard materials, the resonance frequencies can be approximated by the channel geometry, and so the resonances are said to be hard-wall resonances. In this case, the model system can be approximated to the channel geometry by using idealized boundary conditions for the actuation as in Refs. [17–19].

For many biomedical applications, single-use is a requirement due to possible cross-contamination. In this case, clean-room fabrication in glass or silicon is an expensive procedure. Therefore, throughout the last decade, there has been a drive toward efficient, fast, and cheap fabrication techniques involving polymers for commercializing acoustofluidic platforms. However, polymers are acoustically soft materials $\tilde{Z} \sim 1$, which means that the acoustic pressure field is leaking and is no longer confined to the channel. Therefore, instead of the ideal hard-wall resonances, the entire whole-system dynamics now define the resonance frequencies. In Ref. [20], Moiseyenko and Bruus studied numerically how an acoustofluidic device is affected by changing the microfluidic chip material from glass/silicon to a polymer. By doing so, the acoustic contrast between the fluid and the chip is comparable yielding complex whole-system-ultrasound resonances (WSUR). Furthermore, the increased acoustic attenuation yields a weakened acoustic response. This work was the first attempt to study and understand how polymers influences and affect the acoustofluidic response; this was also the first step toward the start of this project.

To model polymer-based acoustofluidic devices, it is necessary to consider the entire system, including the transducer, the coupling layer, and the microfluidic chip, and not only the channel geometry. This also requires each component to be well-characterized for the model to be applicable and representative. The model accuracy is limited by the accuracy of the material parameters used as input to the model. These are sparsely reported, and when they are, they are often insufficient due to incomplete information. The scientific and technological motivation behind this thesis stem from this.

The first attempts of using polymer-based devices have been published, showing applications such as purification of lymphocytes [12], focusing of red blood cells, lipids, and polymer beads [21–25], as well as blood-bacteria separation [26]. Selected polymer-based devices from the literature are shown in Fig. 1.2 and represent the current state of polymer-based acoustofluidics. These devices can be sub-categorized as all-polymer or partly polymer-based, referring to the materials used for microfluidic chip fabrication. In Refs. [1, 27, 28] a polymer is used either as a cover or a spacer, typically fabricated in polydimethylsiloxane (PDMS) for fast and easy prototyping. In Refs. [29–31], the microfluidic chip is all-polymer based and fabricated in polystyrene (PS) or polymethyl-methacrylate (PMMA). All of which consist of a polymer-based microfluidic chip glued onto a transducer. This thesis investigates the physical consequences of introducing polymers in acoustofluidic systems using numerical models validated and supported by experiments. Apart from the studies by Moiseyenko and Bruus [20], the field of polymer-based acoustofluidics has been predominantly holistic. Here, we will try to analyze and treat each device component separately but also in combination to fully understand the dynamics and driving mechanisms when using polymers for acoustofluidic applications.
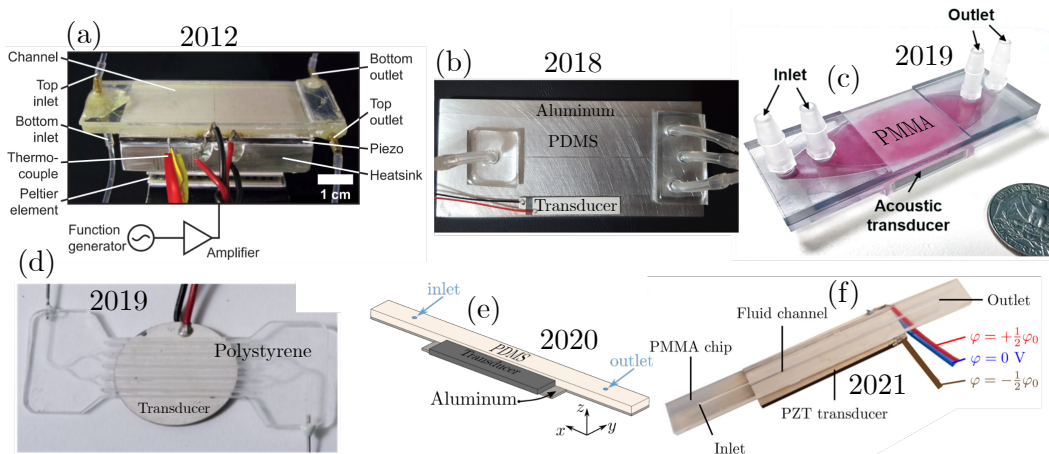
Figure 1.2: Selected pictures of polymer-based acoustofluidic devices from literature in chronological order from (a) to (f). (a) A microchannel acoustophoresis device fabricated using glass substrates and PMMA spacers for high-throughput separation of blood cells, adapted from Adams et al. [27]. (b) A micro-milled aluminum-based acoustophoresis device with a PDMS cover for fast and easy prototyping, adapted from Gautam et al. [28]. (c) A PMMA-based acoustophoresis device for high-throughput platelet separation, adapted from Gu et al. [29]. (d) An arrayed microchannel polystyrene-based acoustophoresis device, adapted from Dubay et al. [30]. (e) A micro-milled aluminum-based acoustophoresis device with a PDMS cover for microparticle streaming studies in soft-walled systems and split-electrode designs, adapted from Paper I [1]. (f) A PMMA-based acoustophoresis device with split-electrode design, adapted from Lickert et al. [31].

1.2   Overview of research related to this PhD project

The research related to this PhD project can be characterized as computer-assisted device engineering within the field of polymer-based acoustofluidics. The outcome of the research has been published in three peer-reviewed papers of different nature, but all related to polymer-based acoustofluidics. All three papers either support or tries to bridge simulation with experiment within the field of polymer-based acoustofluidics. The list below describes how my research progressed and attempts to link together the research related to this PhD project. Each item provides the motivation and story leading to each of the three papers. The papers are the results of our pursuit of precise modeling of polymer-based acoustofluidics with the ultimate goal of bridging simulation and experiment.

(1) **Modeling a polymer-based acoustofluidic device**
Already in Paper I [1], a numerical model was implemented, tested, and validated. The model includes the necessary components required to simulate acoustic phenomena in polymer-based acoustofluidic devices. The model is based on perturbation theory and effective boundary conditions to include viscous effects, enabling effective modeling of acoustic pressure and streaming. The components included in the model were the piezoelectric transducer, the fluid, and the PDMS-sealed aluminum-based microfluidic chip. The fields included in the model are the electric potential, the mechanical displacement, the acoustic pressure, and the acoustic streaming. The model enabled us to calculate the acoustic forces, including the acoustic radiation force and the acoustic streaming drag, in realistic conditions without idealized boundary conditions. The acoustic forces were then used to simulate the particle trajectories influenced by the acoustic radiation force and the acoustic streaming. In this paper, we studied the microparticle velocity fields in an aluminum-based microfluidic chip with a PDMS cover for various particle sizes. This study is an extension to the work by Gautam et al. [28], in which they studied a similar device for inexpensive prototyping of acoustofluidic devices. We extended the study by varying the particle sizes, and furthermore, we considered a new and similar device but with an anti-symmetric actuation for enhanced coupling. The anti-symmetric actuation was achieved by a split-electrode transducer design with an anti-symmetric bias.

Complex particle velocity patterns were observed experimentally and numerically, very different from classical acoustofluidic devices. The simulated results resembled the observed velocity patterns, but we saw a mismatch in magnitude and resonance frequencies. We quickly realized that our material parameters, used as input in the simulations, were not well-characterized even though provided by the manufacturer. After finishing the study, we realized that well-characterized material parameters are required to model polymer-based acoustofluidic devices accurately.

(2) **Numerical coupling-layer analysis in classical acoustofluidic systems**
It was evident that if we want to model complex polymer-based systems, we need to understand the structural influence of each device component. This led to our

studies in Paper II [2], where the coupling layer between the transducer and chip was studied numerically. For completeness, we considered two classical designs, the glass capillary with a localized actuation and the silicon-glass-based acoustophoretic chip with bulk actuation. Two coupling layers were considered for each device, a fluid (glycerol) and a solid (epoxy). The simulated results showed how the coupling layer works as a dissipative layer. However, as the coupling layer thickness becomes comparable to the wavelengths, the coupling layer also has a structural influence on the system resonances. In this paper, we realized that layered 3D models are well-approximated by 1D-layered models as studied in Refs.[32, 33].

(3) **Material parameter determination for ultrasound applications**
From here on out, we started looking into material characterization methods suitable for ultrasound acoustofluidic applications. Inspired by [34–38], I, together with my colleague Fabian Lickert, developed the ultrasound-electrical-impedance-spectroscopy (UEIS) method in Paper III [3], able to determine complex-valued material parameters otherwise sparsely reported in the literature and rarely provided by the manufacturer or supplier. The method is able to provide and determine material parameters of different classes, including piezoceramic materials, UV-curable adhesives, polymers, and 3D-print resins. With this method, we can now do table-top in-house material parameter determination. The method is versatile, cheap, easy to execute, and provides the missing tool for precise and accurate modeling of polymer-based acoustofluidic systems.

1.3   Thesis overview

The content of this thesis will to a large extent, be the application of the ultrasound-electrical-impedance-spectroscopy (UEIS) method for the determination of complex-valued elastic moduli, presented and developed in Paper III [3]. The method will be used to characterize acoustofluidic device components, including the piezoelectric transducer, the glue, and the microfluidic chip, enabling precise and accurate modeling of polymer-based acoustofluidic devices. The simulated results will be compared with experiments, including electrical impedance measurements, laser-Doppler velocimetry, and acoustophoresis particle tracking.

The thesis is written in such a way that it is self-contained and links together the main results contained in the associated papers. The papers are provided in Chapter 6 in agreement with the co-authors. The reader is encouraged to read them as they are referenced throughout this thesis. The following overview provides a short description of each chapter and suggestions for when to read the papers as the reader proceeds.

Chapter 1 Introduction — The concept of polymer-based acoustofluidics is introduced together with scientific and technological motivation.

Chapter 2: Theory of acoustofluidic devices — The equations required to model an acoustofluidic device are derived. The equations to be solved involve the Helmholtz equation for the acoustic pressure field, a Stokes flow equation for the acoustic streaming, Newton's second law for the mechanical displacement, and Gauss' law for the electric potential. The chapter will also present the acoustic energy density and the acoustic radiation force. The governing equations are followed by a section including the necessary boundary conditions to model an acoustofluidic device.

Chapter 3: Simulation of acoustofluidic devices — The basic concepts of the finite-element method (FEM) are introduced together with the weak formulation used to implement the governing equations and boundary conditions. The weak formulation for an axisymmetric system is formulated, in a Cartesian-like formulation, enabling two-dimensional modeling of an axisymmetric system. Furthermore, the theory of perfectly matched layers (PML) is described, which can be used to truncate the modeled geometry. Finally, the model is validated by numerical mesh convergence.

Chapter 4: Polymer-based acoustofluidics — The challenges of polymer-based acoustofluidics are illustrated with selected model examples. The main results of Paper I [1] are summarized, in which we studied the particle velocity patterns for a PDMS-sealed aluminum-based acoustofluidic device. In addition, I present an analytical solution to a soft-walled system providing new insight into soft-walled acoustofluidic systems explaining the velocity patterns and the shifted resonance frequency observed in Paper I [1]. It is appropriate to read Paper I [1] before reading Chapter 4.

Chapter 5: Characterization of acoustofluidic device components — Using the UEIS method presented in Paper III [3], each device component is characterized, including the piezoelectric transducer, the glue, and the microfluidic chip. The UEIS results are supported and supplemented by verification measurements, including laser-Doppler velocimetry (LDV) and particle tracking. The chapter is divided into three sections, one for each device component. The final section regarding the microfluidic chip includes a recent experimental and numerical study of the acoustic response, including particle trajectories influenced by the acoustic radiation force. It is appropriate to read Paper III [3] before Chapter 5, and Paper II [2] before Section 5.2.

Chapter 6: Published papers — In agreement with the co-authors, the papers published doing this project are included in their original form together with the supplemental material.

Chapter 7: A 3D-printed polymer-based acoustofluidic device — This chapter involves ongoing research, and we plan to publish the results in a fourth paper. The UEIS method is used to characterize a resin used for 3D printing, and the UEIS-determined elastic moduli are used to accurately design a 3D-printed polymer-based acoustofluidic device for fast and easy prototyping. Finally, we analyze the device in terms of acoustic response and acoustophoresis performance in steady flow conditions by numerical simulations.

Chapter 8: Conclusion and outlook — The thesis is concluded, and further outlooks and perspectives are discussed.

Chapter 2

Theory of acoustofluidic devices

The equations governing the acoustic fields in fluids, solids, and piezoelectric materials, are presented together with the boundary conditions used in implementing the numerical model. The content is a detailed presentation of the theory used in the three papers contained in Chapter 6 [1–3]. The presentation of the theory is inspired by the textbooks [39–42] and will to a large extent, be a summary of the theoretical and numerical results obtained in our group and published in Refs. [43–45]. Thermal effects are outside the scope of this thesis, and any process is assumed to be isentropic. The equation of state is used to relate pressure and density for a system in thermal equilibrium with constant entropy per unit mass. After introducing the physical fields and presenting the equations used in the numerical model, the boundary conditions will be presented in a dedicated section. The boundary conditions will be grouped into fluid-solid, electrode-transducer, and solid-air interfaces.

2.1 Acoustics in a fluid

The acoustic theory is derived using perturbation theory in the small parameter α, which turns out to be the Mach number. The fluid dynamics are represented by the mass density field $\tilde{\rho}(\boldsymbol{r}, t)$, the pressure field $\tilde{p}(\boldsymbol{r}, t)$, and the velocity field $\tilde{\boldsymbol{v}}(\boldsymbol{r}, t)$ all continuous functions of space $\boldsymbol{r}$ and time t. The equations governing the dynamics of a fluid in thermal equilibrium with dynamic viscosity η_0, bulk viscosity η_0^{b}, and viscous stress tensor $\boldsymbol{\tau}$, are the conservation of mass and momentum

$$\partial_t \tilde{\rho} = -\boldsymbol{\nabla} \cdot (\tilde{\rho}\tilde{\boldsymbol{v}}), \tag{2.1a}$$

$$\partial_t (\tilde{\rho}\tilde{\boldsymbol{v}}) = -\boldsymbol{\nabla}\tilde{p} + \boldsymbol{\nabla} \cdot \boldsymbol{\tau} - \boldsymbol{\nabla} \cdot (\tilde{\rho}\tilde{\boldsymbol{v}}\tilde{\boldsymbol{v}}) + \boldsymbol{f}, \tag{2.1b}$$

where $\boldsymbol{f}$ is a general body force. For a Newtonian fluid the viscous stress tensor $\boldsymbol{\tau}$ reads

$$\boldsymbol{\tau} = \eta_0 \left[\boldsymbol{\nabla}\tilde{\boldsymbol{v}} + (\boldsymbol{\nabla}\tilde{\boldsymbol{v}})^{\mathsf{T}} \right] + \left(\eta_0^{\mathrm{b}} - \frac{2}{3}\eta_0 \right) (\boldsymbol{\nabla} \cdot \tilde{\boldsymbol{v}})\boldsymbol{I}, \tag{2.2}$$

where the superscript T denotes the transpose of a tensor, and $\boldsymbol{I}$ is the unit tensor.

The equations describing acoustic waves and acoustic streaming in fluids are obtained by approximating the velocity, pressure, and density fields using a truncated perturbation expansion to second order. For a general field $\tilde{g}(\boldsymbol{r}, t)$ the truncated expansion in α reads

$$\tilde{g}(\boldsymbol{r}, t) = g_0(\boldsymbol{r}) + \alpha \tilde{g}_1(\boldsymbol{r}, t) + \alpha^2 \tilde{g}_2(\boldsymbol{r}, t), \tag{2.3}$$

where it is assumed that the unperturbed state $g_0(\boldsymbol{r})$ is time-independent and in thermal equilibrium. Acoustic waves can be considered as a small perturbation $\tilde{p}_1$ to the equilibrium pressure p_0 or equivalently in terms of the mass density, which defines the expansion parameter

$$\alpha = \frac{|\tilde{p}_1|}{p_0} = \frac{|\tilde{\rho}_1|}{\rho_0} \ll 1. \tag{2.4}$$

However, at resonance, having a quality factor Q, a stronger requirement is obtained since the expansion parameter α becomes $Q\alpha$ as shown in Ref. [19].

A closed set of equations can be obtained by the equation of state relating the pressure $\tilde{p}(\tilde{\rho}, S)$ to the mass density $\tilde{\rho}$ and the entropy per unit mass S. Consider the functional dependency $\tilde{p}(\tilde{\rho}, S)$ for a fluid in thermal equilibrium and with constant entropy per unit mass S. To first order, the Taylor expansion for the pressure $\tilde{p}$ about the equilibrium ρ_0 reads

$$\tilde{p} = p_0 + \left(\frac{\partial \tilde{p}(\rho_0)}{\partial \tilde{\rho}} \right)_S (\tilde{\rho} - \rho_0) = p_0 + \left(\frac{\partial \tilde{p}(\rho_0)}{\partial \tilde{\rho}} \right)_S \tilde{\rho}_1. \tag{2.5}$$

The partial derivative in Eq. (2.5) is identified as the isentropic sound speed squared $\left(\frac{\partial \tilde{p}(\rho_0)}{\partial \tilde{\rho}} \right)_S = c_0^2$. Collecting first-order terms in Eq. (2.5) gives the constitutive relation $\tilde{p}_1 = c_0^2 \tilde{\rho}_1$ between the first-order pressure field $\tilde{p}_1$ and the first-order density field $\tilde{\rho}_1$. The isentropic compressibility κ_0 can be identified as

$$\kappa_0 = \frac{1}{\rho_0} \left(\frac{\partial \tilde{\rho}(p_0)}{\partial \tilde{p}} \right)_S = \frac{1}{\rho_0 c_0^2}, \tag{2.6}$$

where the subscript S denotes a partial derivative at constant entropy per unit mass. The constitutive relation between pressure and density will be used in the proceeding section to provide a closed set of equations describing the acoustic fields in a fluid.

2.1.1   Acoustic pressure waves

Using the constitutive relation $\tilde{p}_1 = c_0^2 \tilde{\rho}_1$ for a quiescent fluid $\boldsymbol{v}_0 = \boldsymbol{0}$ without external forces, the collection of first-order terms in Eq. (2.1a) and Eq. (2.1b) gives a closed set of linear partial differential equations

$$\kappa_0 \partial_t \tilde{p}_1 = -\boldsymbol{\nabla} \cdot \tilde{\boldsymbol{v}}_1, \tag{2.7a}$$

$$\partial_t (\rho_0 \tilde{\boldsymbol{v}}_1) = -\boldsymbol{\nabla} \tilde{p}_1 + \eta_0 \nabla^2 \tilde{\boldsymbol{v}}_1 + \left(\frac{1}{3} \eta_0 + \eta_0^{\mathrm{b}} \right) \boldsymbol{\nabla} (\boldsymbol{\nabla} \cdot \tilde{\boldsymbol{v}}_1). \tag{2.7b}$$

In a linear system with a harmonic time response, given by the angular frequency $\omega = 2\pi f$ with excitation frequency f, the first-order terms can be written as $\tilde{g}_1(\boldsymbol{r}, t) = \mathrm{Re}\left[g_1(\boldsymbol{r})\mathrm{e}^{-\mathrm{i}\omega t}\right]$ in terms of the complex-valued amplitude $g_1(\boldsymbol{r})$. By these means, the time-derivative ∂_t can be substituted with $-\mathrm{i}\omega$ and the phase factor $\mathrm{e}^{-\mathrm{i}\omega t}$ can be factored out, leaving a set of time-independent equations for which only the complex-valued amplitudes $g_1(\boldsymbol{r})$ needs to be solved for. To obtain a single equation describing the first-order acoustic pressure field p_1, the velocity field is decomposed using a Helmholtz decomposition

$$\boldsymbol{v}_1 = \boldsymbol{v}_1^d + \boldsymbol{v}_1^\delta, \quad \text{where} \quad \boldsymbol{\nabla} \times \boldsymbol{v}_1^d = \boldsymbol{0} \quad \text{and} \quad \boldsymbol{\nabla} \cdot \boldsymbol{v}_1^\delta = 0, \tag{2.8}$$

and so Eq. (2.7a) becomes

$$\mathrm{i}\omega\kappa_0 p_1 = \boldsymbol{\nabla} \cdot \boldsymbol{v}_1^d. \tag{2.9}$$

By taking the divergence of Eq. (2.7b) and inserting Eq. (2.9), a single equation governing the acoustic pressure field p_1 is obtained

$$\nabla^2 p_1 = -k_c^2 p_1, \quad \text{with} \quad k_c^2 = \frac{1}{1 - \mathrm{i}\Gamma}k_0^2 \approx (1 + \mathrm{i}\Gamma)\,k_0^2, \tag{2.10a}$$

$$\Gamma = \left(\frac{\eta_0^{\mathrm{b}}}{\eta_0} + \frac{4}{3}\right)\eta_0\omega\kappa_0, \quad k_0 = \frac{\omega}{c_0} = \frac{2\pi}{\lambda}. \tag{2.10b}$$

The theory of acoustic pressure waves in a fluid is established, Eq. (2.10a) is a Helmholtz equation with a complex-valued wavenumber k_c, proportional to the acoustic wavenumber k_0 with acoustic wavelength λ, and with a damping coefficient Γ. The acoustic and fluid properties for ultra-pure water are provided in Table 2.1 for $f = 1\,\mathrm{MHz}$ at $25\,°\mathrm{C}$.

The irrotational part of Eq. (2.7b) combined with Eq. (2.9) gives the irrotational velocity in terms of the pressure gradient

$$\boldsymbol{v}_1^d = -\mathrm{i}\frac{1 - \mathrm{i}\Gamma}{\omega\rho_0}\boldsymbol{\nabla}p_1, \tag{2.11}$$

which also satisfies a Helmholtz equation with wavenumber k_c. By inserting Eq. (2.9) into Eq. (2.4) the perturbation expansion parameter α can be identified as the Mach number

Table 2.1: Acoustic and fluid properties for ultra-pure water at $f = 1$ MHz and $25\,°\mathrm{C}$ [18, 46–49]. The fluid properties include the fluid mass density ρ_0, the dynamic viscosity η_0, the bulk viscosity η_0^{b}, the isentropic sound speed c_0, the isentropic compressibility κ_0, and the acoustic impedance $Z_0 = \rho_0 c_0$. The acoustic properties are evaluated at $f = 1\,\mathrm{MHz}$ and include the acoustic wavelength λ, the damping coefficient Γ, the viscous boundary-layer thickness δ_{visc}, and the perturbation expansion parameter α.

ρ_0 (kg/m^3)	η_0 (mPa s)	η_0^{b} (mPa s)	c_0 (m/s)	κ_0 (1/TPa)	Z_0 (MPa s/m)	λ mm	$\Gamma \propto \omega$ -	$\delta_{\mathrm{visc}} \propto \omega^{-1/2}$ nm	α -
997.1	0.89	2.5	1496.7	448	1.5	1.5	1×10^{-5}	533	$\frac{|\boldsymbol{v}_1|}{c_0}\sim 10^{-6}$

$Ma = |\boldsymbol{v}_1|/c_0$. For typical acoustofluidic applications the velocity amplitude ranges between micrometer per second up to millimeter per second so $Ma \ll 1$ [1, 50–52].

Similarly, by considering the solenoidal part of Eq. (2.7b), the solenoidal velocity field $\boldsymbol{v}_1^\delta$ is found to be governed by a Helmholtz equation

$$\nabla^2 \boldsymbol{v}_1^\delta = -k_{\mathrm{s}}^2 \boldsymbol{v}_1^\delta, \quad \text{with} \quad k_{\mathrm{s}} = \frac{1+\mathrm{i}}{\delta_{\mathrm{visc}}}, \quad \text{and} \quad \delta_{\mathrm{visc}} = \sqrt{\frac{2\eta_0}{\omega\rho_0}}, \tag{2.12}$$

with a complex-valued wavenumber k_{s} and the characteristic boundary-layer thickness δ_{visc}. Notice how $\boldsymbol{v}_1^d$ and $\boldsymbol{v}_1^\delta$ are separated in length scales; at $f = 1\,\mathrm{MHz}$ the viscous boundary layer thickness is $\delta_{\mathrm{visc}} = 533\,\mathrm{nm}$ and the acoustic wavelength is $\lambda = 1.5\,\mathrm{mm}$, a three orders of magnitude difference. Solving the velocity field numerically on a discretized mesh requires both length scales to be resolved. However, Bach and Bruus [45] circumvented this problem as they developed a theory that includes the viscous effects analytically in the boundary conditions, leaving p_1 as the only required field when solving first-order acoustics. This is possible since $\mathrm{Re}(k_{\mathrm{s}}) = \mathrm{Im}(k_{\mathrm{s}})$ signifies a heavily damped solenoidal field that only exists in thin layers extending δ_{visc} from the fluid-solid interface. The fields $\boldsymbol{v}_1^d$ and $\boldsymbol{v}_1^\delta$ will be used as inputs to the boundary conditions presented in Section 2.4.1.

2.1.2 Acoustic streaming and radiation force

The linear theory presented in Section 2.1.1 provides the necessary equations to model acoustic pressure waves in a fluid. However, as mentioned in the introduction, there exists another essential second-order effect called acoustic streaming: a time-averaged flow sourced by the dissipation of energy contained in the acoustic waves. Acoustic streaming can be sub-categorized into bulk-driven and boundary driven. Due to the no-slip condition, the boundary-driven acoustic streaming arises from the large velocity gradients near rigid walls, causing time-averaged shear stress driving the acoustic streaming. The bulk-driven streaming arises from the dissipation of energy contained in traveling waves. The equations describing the acoustic streaming $\tilde{\boldsymbol{v}}_2$ are obtained by collecting the second-order terms in Eq. (2.1) and taking the time-average

$$0 = \rho_0 \boldsymbol{\nabla} \cdot \boldsymbol{v}_2 + \boldsymbol{\nabla} \cdot \langle \tilde{\rho}_1 \tilde{\boldsymbol{v}}_1 \rangle, \tag{2.13a}$$

$$\boldsymbol{0} = \boldsymbol{\nabla} \cdot \boldsymbol{\sigma}_2 - \rho_0 \boldsymbol{\nabla} \cdot \langle \tilde{\boldsymbol{v}}_1 \tilde{\boldsymbol{v}}_1 \rangle = -\boldsymbol{\nabla} p_2 + \boldsymbol{\nabla} \cdot \boldsymbol{\tau}_2 - \rho_0 \boldsymbol{\nabla} \cdot \langle \tilde{\boldsymbol{v}}_1 \tilde{\boldsymbol{v}}_1 \rangle, \tag{2.13b}$$

$$\boldsymbol{\tau}_2 = \eta_0 \left[\boldsymbol{\nabla} \boldsymbol{v}_2 + (\boldsymbol{\nabla} \boldsymbol{v}_2)^{\mathsf{T}} \right] + \left(\eta_0^{\mathrm{b}} - \frac{2}{3}\eta_0 \right) (\boldsymbol{\nabla} \cdot \boldsymbol{v}_2)\boldsymbol{I}, \tag{2.13c}$$

where the time-average operator $\langle \cdot \rangle$ is defined as

$$g_2(\boldsymbol{r}) = \langle \tilde{g}_2(\boldsymbol{r}, t) \rangle = \frac{\omega}{2\pi} \int_t^{t+2\pi/\omega} \tilde{g}_2(\boldsymbol{r}, t')\, \mathrm{d}t'. \tag{2.14}$$

When taking the time average of a product of two harmonic terms $\left\langle \tilde{g}_1 \tilde{h}_1 \right\rangle$, the following identity is useful

$$\left\langle \tilde{g}_1(\boldsymbol{r}, t) \tilde{h}_1(\boldsymbol{r}, t) \right\rangle = \frac{1}{2} \operatorname{Re}\left(g_1(\boldsymbol{r}) h_1(\boldsymbol{r})^*\right), \tag{2.15}$$

where the asterisk denotes complex conjugate.

As already mentioned, the boundary-driven acoustic streaming arises from the velocity field adapting to the no-slip condition over a very short length-scale $\delta_{\text{visc}} \sim 500\,\text{nm}$. Both the acoustic wavelength and the boundary layer must be resolved to model the acoustic streaming. Numerically this is challenging since the boundary layer is several orders of magnitude smaller than the acoustic wavelength. To overcome this challenge, Bach and Bruus [45] developed an effective theory enabling the modeling of acoustic streaming without resolving the boundary layer. In this theory, the viscous boundary layer effects are accounted for in an analytical slip-velocity boundary condition. The theory separates the acoustic streaming into a short-ranged velocity $\boldsymbol{v}_2^{\delta}$ decaying within the viscous boundary layer and a long-ranged $\boldsymbol{v}_2^{d}$ existing in the bulk domain. The long-ranged part of Eq. (2.13) can be approximated as an incompressible Stokes flow

$$0 = \boldsymbol{\nabla} \cdot \boldsymbol{v}_2^{d}, \tag{2.16a}$$

$$\boldsymbol{0} = -\boldsymbol{\nabla} p_2^{d} + \eta_0 \nabla^2 \boldsymbol{v}_2^{d} + \frac{\Gamma \omega}{c_0^2} \left\langle p_1 \boldsymbol{v}_1^{d} \right\rangle, \tag{2.16b}$$

where the short-ranged $\boldsymbol{v}_2^{\delta}$ is included in the boundary condition and evaluated in terms of the first-order acoustic fields. The Helmholtz Eq. (2.10a) and the incompressible Stokes flow Eq. (2.16) constitute the equations required for effective modeling of the first and second-order acoustic phenomena in a fluid, given by the acoustic pressure field p_1 and the acoustic streaming field $\boldsymbol{v}_2^{d}$.

Acoustic energy density

The energy density is the sum of kinetic and potential energy densities and is another time-averaged second-order quantity. For a quiescent fluid, the time-harmonic velocity disturbances $\tilde{\boldsymbol{v}}_1$ yields a time-averaged kinetic energy density $\frac{1}{2}\rho_0 \left\langle \tilde{\boldsymbol{v}}_1^2 \right\rangle$. The time-averaged potential energy density for a fluid compressed by an excess pressure $\tilde{p}_1$ is $\frac{1}{2}\kappa_0 \left\langle \tilde{p}_1^2 \right\rangle$. The acoustic energy density E_{ac} is defined as the spatial and time-averaged sum of kinetic and potential energy density

$$E_{\text{ac}} = \frac{1}{V} \int_{\Omega} \left(\frac{1}{2}\rho_0 \left\langle \tilde{\boldsymbol{v}}_1^2 \right\rangle + \frac{1}{2}\kappa_0 \left\langle \tilde{p}_1^2 \right\rangle \right) \mathrm{d}V = \frac{1}{V} \int_{\Omega} \left(\frac{1}{4}\rho_0 |\boldsymbol{v}_1|^2 + \frac{1}{4}\kappa_0 |p_1|^2 \right) \mathrm{d}V. \tag{2.17}$$

The acoustic energy density spectrum $E_{\text{ac}}(f)$ is used to locate resonance frequencies and as a measure of the acoustic response.

Acoustic radiation force

Another important second-order quantity is the acoustic radiation force $\boldsymbol{F}_{\mathrm{rad}}$, which forms the foundation for acoustofluidic applications and acoustophoresis. The acoustic radiation force arises from the scattering of acoustic waves on a compressible particle suspended in a fluid. In general, the acoustic radiation force is calculated by integrating the stress $\boldsymbol{\sigma}$ exerted by the fluid on the time-dependent particle surface $\partial\Omega(t)$ with normal vector $\boldsymbol{n}$ and taking the time-average

$$\boldsymbol{F}_{\mathrm{rad}} = \left\langle \oint_{\partial\Omega(t)} \boldsymbol{\sigma} \cdot \boldsymbol{n}\, \mathrm{d}A \right\rangle. \tag{2.18}$$

The conservation of momentum and Gauss' theorem can be used to re-formulate the integral in Eq. (2.18). For a time-harmonic response, the collection of second-order terms in the time-averaged rate-of-change of the momentum density $\langle \partial_t(\tilde{\rho}\tilde{\boldsymbol{v}}) \rangle$ is zero, as in Eq. (2.13b), so the volume integral must also be zero

$$\mathbf{0} = \int_{\Omega} \left(\boldsymbol{\nabla} \cdot \boldsymbol{\sigma}_2 - \rho_0 \boldsymbol{\nabla} \cdot \langle \tilde{\boldsymbol{v}}_1 \tilde{\boldsymbol{v}}_1 \rangle \right)\, \mathrm{d}V. \tag{2.19}$$

Consider a fluid domain Ω enclosing a solid particle, then by using Gauss' theorem, the volume integral in Eq. (2.19) can be re-written as a static surface integral $\partial\Omega_{\mathrm{out}}$ enclosing the particle plus the integral evaluated on the time-dependent particle surface $\partial\Omega(t)$ of opposite sign due to the normal vectors pointing in opposite directions

$$\mathbf{0} = \oint_{\partial\Omega_{\mathrm{out}}} \left(\boldsymbol{\sigma}_2 - \rho_0 \langle \tilde{\boldsymbol{v}}_1 \tilde{\boldsymbol{v}}_1 \rangle \right) \cdot \boldsymbol{n}\, \mathrm{d}A - \left\langle \oint_{\partial\Omega(t)} \boldsymbol{\sigma} \cdot \boldsymbol{n}\, \mathrm{d}A \right\rangle. \tag{2.20}$$

The complicated time-dependent surface integral in Eq. (2.18) can now be replaced by a steady surface integral enclosing the particle

$$\boldsymbol{F}_{\mathrm{rad}} = \oint_{\partial\Omega_{\mathrm{out}}} \left(\boldsymbol{\sigma}_2 - \rho_0 \langle \tilde{\boldsymbol{v}}_1 \tilde{\boldsymbol{v}}_1 \rangle \right) \cdot \boldsymbol{n}\, \mathrm{d}A, \tag{2.21}$$

which comes by the cost of the momentum-flux density $\rho_0 \langle \tilde{\boldsymbol{v}}_1 \tilde{\boldsymbol{v}}_1 \rangle$ entering the integral. In Ref. [43], Settnes and Bruus studied the acoustic radiation force on a particle exposed to a standing acoustic pressure wave in a viscous fluid, leading to the following expression for the acoustic radiation force on a particle of radius a, compressibility κ_{p}, and density ρ_{p}

$$\boldsymbol{F}_{\mathrm{rad}} = -\pi a^3 \left\{ \frac{2\kappa_0}{3} \mathrm{Re}\left(f_1 p_1^* \boldsymbol{\nabla} p_1 \right) - \rho_0 \mathrm{Re}\left[f_2^* \left(\boldsymbol{v}_1^d \right)^* \cdot \boldsymbol{\nabla} \boldsymbol{v}_1^d \right] \right\}, \tag{2.22}$$

where the monopole f_1 and dipole f_2 scattering coefficients are

$$f_1 = 1 - \frac{\kappa_{\mathrm{p}}}{\kappa_0}, \quad f_2 = \frac{2\left[1 - \gamma\right]\left(\tilde{\rho} - 1\right)}{2\tilde{\rho} + 1 - 3\gamma}, \tag{2.23a}$$

$$\gamma = -\frac{3}{2}\left[1 + \mathrm{i}\left(1 + \tilde{\delta}\right)\right]\tilde{\delta}, \quad \text{with} \quad \tilde{\rho} = \frac{\rho_{\mathrm{p}}}{\rho_0} \quad \text{and} \quad \tilde{\delta} = \frac{\delta_{\mathrm{visc}}}{a}. \tag{2.23b}$$

For an idealized standing acoustic pressure wave $p_1 = p_a \cos(k_0 z)$, the acoustic energy density becomes $E_{\mathrm{ac}} = \frac{1}{4}\kappa_0 p_a^2$ and the acoustic radiation force simplifies to

$$\boldsymbol{F}_{\mathrm{rad}} = 4\pi\Phi a^3 k_0 E_{\mathrm{ac}} \sin(2k_0 z), \tag{2.24}$$

where the acoustic contrast factor Φ is defined as

$$\Phi = \frac{1}{3}f_1 + \frac{1}{2}\mathrm{Re}(f_2^*), \tag{2.25}$$

which determines the sign and the amplitude of the acoustic radiation force, relative to the acoustic field strength.

2.2   Acoustics in an elastic solid

The acoustic fields in a fluid are driven by the no-slip velocity condition at the fluid-solid interface. To fully understand and study the acoustofluidic response, the dynamics in the surrounding elastic material must be included. The equation of motion governing the mechanical displacement field $\tilde{\boldsymbol{u}}$ in an elastic solid, undergoing small strain $|\boldsymbol{\nabla}\tilde{u}| \ll 1$, with mass density ρ_{sl} and stress tensor $\boldsymbol{\sigma}$, is governed by Newton's second law

$$\rho_{\mathrm{sl}}\partial_t^2\tilde{\boldsymbol{u}} = \boldsymbol{\nabla}\cdot\boldsymbol{\sigma}. \tag{2.26}$$

The gravitational body-force term has been neglected since it only leads to a tiny static deformation.

In a linear system subject to a time-harmonic response, the first-order perturbed displacement field can be written as $\tilde{u}_1(\boldsymbol{r},t) = \mathrm{Re}\left[u_1(\boldsymbol{r})\mathrm{e}^{-\mathrm{i}\omega t}\right]$ so Eq. (2.26) becomes

$$-\rho_{\mathrm{sl}}\omega^2\boldsymbol{u}_1 = \boldsymbol{\nabla}\cdot\boldsymbol{\sigma}. \tag{2.27}$$

The constitutive relation between the symmetric stress $\boldsymbol{\sigma}$ and strain $\boldsymbol{s} = \frac{1}{2}\left[\boldsymbol{\nabla}\tilde{\boldsymbol{u}}_1 + (\boldsymbol{\nabla}\tilde{\boldsymbol{u}}_1)^{\mathsf{T}}\right]$ for an elastic solid in thermal equilibrium, is given by the stiffness tensor $\boldsymbol{C}$

$$\boldsymbol{\sigma} = \boldsymbol{C}\boldsymbol{s}. \tag{2.28}$$

Using the Voigt notation, the symmetric stress and strain tensors can be reduced to six-dimensional vectors

$$\boldsymbol{\sigma}_{\mathrm{V}} = (\sigma_{xx}, \sigma_{yy}, \sigma_{zz}, \sigma_{yz}, \sigma_{xz}, \sigma_{xy}), \tag{2.29a}$$
$$\boldsymbol{s}_{\mathrm{V}} = (\partial_x u_{1,x}, \partial_y u_{1,y}, \partial_z u_{1,z}, \partial_y u_{1,z} + \partial_z u_{1,y}, \partial_x u_{1,z} + \partial_z u_{1,x}, \partial_x u_{1,y} + \partial_y u_{1,x}), \tag{2.29b}$$

and the constitutive relation in Eq. (2.28) can be compactly written as

$$\begin{pmatrix} \sigma_{xx} \\ \sigma_{yy} \\ \sigma_{zz} \\ \sigma_{yz} \\ \sigma_{xz} \\ \sigma_{xy} \end{pmatrix} = \begin{pmatrix} C_{11} & C_{12} & C_{13} & C_{14} & C_{15} & C_{16} \\ C_{12} & C_{22} & C_{23} & C_{24} & C_{25} & C_{26} \\ C_{13} & C_{23} & C_{33} & C_{34} & C_{35} & C_{36} \\ C_{14} & C_{14} & C_{34} & C_{44} & C_{45} & C_{46} \\ C_{15} & C_{25} & C_{35} & C_{45} & C_{55} & C_{56} \\ C_{16} & C_{26} & C_{36} & C_{46} & C_{56} & C_{66} \end{pmatrix} \begin{pmatrix} \partial_x u_{1,x} \\ \partial_y u_{1,y} \\ \partial_z u_{1,z} \\ \partial_y u_{1,z} + \partial_z u_{1,y} \\ \partial_x u_{1,z} + \partial_z u_{1,x} \\ \partial_x u_{1,y} + \partial_y u_{1,x} \end{pmatrix}. \tag{2.30}$$

The material's crystal symmetry gives the number of elements and the structure of the stiffness tensor. For an isotropic elastic solid, e.g., glass and polymers, the stiffness tensor structure is

$$
\boldsymbol{C}_{\mathrm{iso}} = \begin{pmatrix}
C_{11} & C_{12} & C_{12} & 0 & 0 & 0 \\
C_{12} & C_{11} & C_{12} & 0 & 0 & 0 \\
C_{12} & C_{12} & C_{11} & 0 & 0 & 0 \\
0 & 0 & 0 & C_{44} & 0 & 0 \\
0 & 0 & 0 & 0 & C_{44} & 0 \\
0 & 0 & 0 & 0 & 0 & C_{44}
\end{pmatrix}, \tag{2.31}
$$

where $C_{12} = C_{11} - 2C_{44}$ leaving two independent coefficients C_{11} and C_{44}. In general, the stiffness tensor is complex-valued $\boldsymbol{C} = \boldsymbol{C}' + \mathrm{i}\boldsymbol{C}''$ signifying mechanical losses, which means that a complete description of an isotropic elastic material requires five material parameters including the mass density ρ_{sl}.

2.3   Linear piezoelectricity

One way to generate ultrasound is to drive a piezoelectric material at megahertz frequencies using a function generator, exploiting the piezoelectric effect; by applying an electric voltage to a piezoelectric material, the piezoelectric coupling yields a mechanical deformation. To describe the dynamics of a piezoelectric material, the mechanical fields are supplemented by the electric potential $\tilde{\varphi}$, the electric field $\boldsymbol{E} = -\boldsymbol{\nabla}\tilde{\varphi}$, and the electric displacement field $\boldsymbol{D} = \boldsymbol{\epsilon}\boldsymbol{E}$. Assuming no free charges, the electric potential inside the piezoelectric material is governed by Gauss' law

$$
\boldsymbol{\nabla} \cdot \boldsymbol{D} = 0. \tag{2.32}
$$

The constitutive equations describing the piezoelectric effect in the stress-charge form are given in terms of the stiffness tensor $\boldsymbol{C}$, the dielectric tensor $\boldsymbol{\epsilon}$, and the piezoelectric coupling tensor $\boldsymbol{e}$

$$
\boldsymbol{\sigma} = \boldsymbol{C}\boldsymbol{s} - \boldsymbol{e}^{\mathsf{T}}\boldsymbol{E}, \tag{2.33a}
$$
$$
\boldsymbol{D} = \boldsymbol{e}\boldsymbol{s} + \boldsymbol{\epsilon}\boldsymbol{E}. \tag{2.33b}
$$

For a piezoelectric transducer belonging to the ∞mm symmetry class [53], which will be the case for the piezoceramic materials considered in this thesis, the stress-charge form is

compactly written using the Voigt notation

$$\boldsymbol{C} = \begin{pmatrix} C_{11} & C_{12} & C_{13} & 0 & 0 & 0 \\ C_{12} & C_{11} & C_{13} & 0 & 0 & 0 \\ C_{13} & C_{13} & C_{33} & 0 & 0 & 0 \\ 0 & 0 & 0 & C_{44} & 0 & 0 \\ 0 & 0 & 0 & 0 & C_{44} & 0 \\ 0 & 0 & 0 & 0 & 0 & C_{66} \end{pmatrix}, \tag{2.34a}$$

$$\boldsymbol{e} = \begin{pmatrix} 0 & 0 & 0 & 0 & e_{15} & 0 \\ 0 & 0 & 0 & e_{15} & 0 & 0 \\ e_{31} & e_{31} & e_{33} & 0 & 0 & 0 \end{pmatrix}, \tag{2.34b}$$

$$\boldsymbol{\epsilon} = \begin{pmatrix} \epsilon_{11} & 0 & 0 \\ 0 & \epsilon_{11} & 0 \\ 0 & 0 & \epsilon_{33} \end{pmatrix}, \tag{2.34c}$$

where $C_{66} = \frac{1}{2}(C_{11} - C_{12})$. As in Eq. (2.31), the parameters are complex-valued, leaving a total of 20 independent parameters to be determined for a complete description of a ∞mm piezoelectric material. The notation $\boldsymbol{M} = \boldsymbol{M}' + \mathrm{i}\boldsymbol{M}''$ is used to distinguish real and complex-valued parameters. The use and development of a method for the determination of both real and complex-valued parameters contained in Eqs. (2.31) and (2.34) will, to a large extent, be the main scope of this thesis.

2.4 Boundary conditions

This section presents the boundary conditions between the different interfaces, including the fluid-solid interface, the electrode-piezoceramic interface, and the solid-air interface. Together with the governing equations in the respective domains, this forms the theoretical foundation for the numerical implementation.

2.4.1 Fluid-solid interface

The coupling at the fluid-solid interface is what drives the acoustic fields inside the fluid. The fluid velocity has to satisfy the no-slip condition, and the stress has to be continuous at the fluid-solid interface $\partial\Omega_{\mathrm{int}}$, with normal vector $\boldsymbol{n}$ pointing into the fluid domain. Using the effective theory in Ref. [45], where the viscous boundary layer effects are included analytically in the boundary condition, the no-slip and continuous stress boundary conditions are

$$\boldsymbol{v}_1^d \cdot \boldsymbol{n} = -\mathrm{i}\omega\boldsymbol{u}_1 \cdot \boldsymbol{n} - \frac{\mathrm{i}}{k_{\mathrm{s}}}\boldsymbol{\nabla}_\parallel \cdot \left(\boldsymbol{v}_1^\delta\right)_\parallel, \quad \text{for} \quad \boldsymbol{r} \in \partial\Omega_{\mathrm{int}}, \tag{2.35a}$$

$$\boldsymbol{\sigma} \cdot \boldsymbol{n} = -p_1\boldsymbol{n} + \mathrm{i}k_{\mathrm{s}}\eta_0\boldsymbol{v}_1^\delta, \quad \text{for} \quad \boldsymbol{r} \in \partial\Omega_{\mathrm{int}}, \tag{2.35b}$$

where the subscript $\parallel$ denotes the parallel component with respect to the surface $\partial\Omega_{\mathrm{int}}$. Notice how the viscous effects are accounted for as a slip-like velocity in the no-slip condition Eq. (2.35a) and as shear stress in the continuous stress condition Eq. (2.35b).

To avoid explicit reference to $\boldsymbol{v}_1^\delta$, we use $\boldsymbol{v}_1^\delta = \left(-\mathrm{i}\omega\boldsymbol{u}_1 - \boldsymbol{v}_1^d\right)$, which is exactly the first-order no-slip condition. Instead of the long-ranged velocity field $\boldsymbol{v}_1^d$, Eq. (2.35a) can be written in terms of the pressure gradient

$$(\boldsymbol{n}\cdot\boldsymbol{\nabla})p_1 = \frac{\mathrm{i}\omega\rho_0}{1-\mathrm{i}\Gamma}\left(-\mathrm{i}\omega\boldsymbol{u}_1 - \frac{\omega}{k_\mathrm{s}}\boldsymbol{\nabla}\cdot\boldsymbol{u}_1\right) - \frac{\mathrm{i}}{k_\mathrm{s}}\left(k_\mathrm{c}^2 p_1 + \partial_n^2 p_1\right), \qquad (2.36)$$

where the operator ∂_n^2 is defined as $\partial_n^2 = (\boldsymbol{n}\cdot\boldsymbol{\nabla})(\boldsymbol{n}\cdot\boldsymbol{\nabla})$. Equations (2.35a) and (2.36) constitute the necessary boundary conditions to model acoustic pressure waves in a fluid, where the viscous boundary layer effects have been analytically taken into account in the boundary conditions.

When calculating the acoustic streaming, the no-slip condition has to be satisfied to second order, yielding a Stokes drift condition

$$\boldsymbol{v}_2 = -\left\langle\left(\boldsymbol{u}_1\cdot\boldsymbol{\nabla}\right)\boldsymbol{v}_1\right\rangle \quad \text{for} \quad \boldsymbol{r}\in\partial\Omega_\mathrm{int}. \qquad (2.37)$$

Again, the results obtained by Bach and Bruus [45] are used to implement the boundary conditions required to avoid explicit reference to fields existing in the boundary layer near the fluid-solid interface. To second-order, the analytical inclusion of viscous effects in the no-slip condition results in a slip condition sourced by the first-order terms

$$\boldsymbol{v}_2^d = (\boldsymbol{A}\cdot\boldsymbol{t}_1)\boldsymbol{t}_1 + (\boldsymbol{A}\cdot\boldsymbol{t}_2)\boldsymbol{t}_2 + (\boldsymbol{B}\cdot\boldsymbol{n})\boldsymbol{n}, \quad \text{for} \quad \boldsymbol{r}\in\partial\Omega_\mathrm{int}, \qquad (2.38a)$$

$$\begin{aligned}\boldsymbol{A} = &-\frac{1}{2\omega}\,\mathrm{Re}\left[\left(\boldsymbol{v}_1^\delta\right)^*\cdot\boldsymbol{\nabla}\left(\frac{1}{2}\boldsymbol{v}_1^\delta - \omega\boldsymbol{u}_1\right) + \omega\boldsymbol{u}_1^*\cdot\boldsymbol{\nabla}\boldsymbol{v}_1^d\right.\\ &\left. + \left(\frac{2-\mathrm{i}}{2}\boldsymbol{\nabla}\cdot\left(\boldsymbol{v}_1^\delta\right)^* + \mathrm{i}\left\{\mathrm{i}\omega\boldsymbol{\nabla}\cdot\boldsymbol{u}_1^* - \boldsymbol{n}\cdot\boldsymbol{\nabla}\left[\boldsymbol{n}\cdot\left(\boldsymbol{v}_1^d\right)^*\right]\right\}\right)\boldsymbol{v}_1^\delta\right],\end{aligned} \qquad (2.38b)$$

$$\boldsymbol{B} = \frac{1}{2\omega}\,\mathrm{Re}\left[\mathrm{i}\left(\boldsymbol{v}_1^d\right)^*\cdot\boldsymbol{\nabla}\boldsymbol{v}_1^d\right]. \qquad (2.38c)$$

The effective boundary conditions in Eq. (2.35) and Eq. (2.38) are valid for weakly curved boundaries and thin boundary layers $\delta_\mathrm{visc}/\min(\lambda, R) \ll 1$, where R is the curvature length-scale at the fluid-solid interface with unit tangent vectors $\boldsymbol{t}_1$ and $\boldsymbol{t}_2$.

2.4.2   Electrode-piezoceramic interface

The excitation voltage amplitudes give the boundary conditions between the electrodes and the transducer interface. Typically one of the electrodes is grounded ($\partial\Omega_\mathrm{elec,1}$) while the other ($\partial\Omega_\mathrm{elec,2}$) is driven at a sinusoidal signal with a constant voltage amplitude V_0,

$$\varphi_1 = V_1 = 0, \quad \text{for} \quad \boldsymbol{r}\in\partial\Omega_\mathrm{elec,1}, \qquad (2.39a)$$

$$\varphi_1 = V_2 = V_0, \quad \text{for} \quad \boldsymbol{r}\in\partial\Omega_\mathrm{elec,2}. \qquad (2.39b)$$

Experimentally, the electrical impedance Z is easily obtained using an impedance analyzer when applying the voltage to the piezoelectric element. Throughout this thesis, the electrical impedance will be used to characterize piezoelectric transducers and elastic materials.

By matching the measured electrical impedance spectrum to the simulated, the simulations can be used to decipher the signal providing insight into the dynamics. The electrical impedance is calculated by dividing the voltage difference, between the electrodes, by the current I

$$Z = \frac{V_2 - V_1}{I}. \tag{2.40}$$

The current is calculated by integrating the current density $\boldsymbol{J}_\varphi = \partial_t \left(\boldsymbol{D} - \epsilon_0 \boldsymbol{E} \right)$ over one of the electrodes

$$I = \int_{\partial\Omega_{\mathrm{elec},2}} \boldsymbol{J}_\varphi \cdot \boldsymbol{n} \, \mathrm{d}A = -\mathrm{i}\omega \int_{\partial\Omega_{\mathrm{elec},2}} \left(\boldsymbol{D} - \epsilon_0 \boldsymbol{E} \right) \cdot \boldsymbol{n} \, \mathrm{d}A, \tag{2.41}$$

where $\boldsymbol{n}$ is the normal vector to the electrode surface and ϵ_0 is the vacuum permittivity.

2.4.3   Solid-air interface

The zero-stress boundary conditions are imposed on exterior surfaces $\partial\Omega_{\mathrm{ext}}$ between solid and air

$$\boldsymbol{n} \cdot \boldsymbol{\sigma} = \boldsymbol{0} \quad \text{for} \quad \boldsymbol{r} \in \partial\Omega_{\mathrm{ext}}. \tag{2.42}$$

In reality, there is a stress due to viscous shear and ambient pressure from the surrounding air. Consider a solid vibrating at $f = 1\,\mathrm{MHz}$ with an amplitude of $|\boldsymbol{u}_1| = 1\,\mathrm{nm}$. The shear stress exerted on the solid by the fluid can be approximated by an oscillating boundary, where the velocity has to completely develop on a length-scale $\delta_{\mathrm{air}} = \sqrt{2\eta_{\mathrm{air}}/(\rho_{\mathrm{air}}\omega)} \sim 2\,\mu\mathrm{m}$, yielding a shear stress $\eta_{\mathrm{air}}\omega|\boldsymbol{u}_1|/\delta_{\mathrm{air}} \sim 50\,\mathrm{mPa}$. In a typical acoustofluidic device, the stress magnitude is in the order of MPa, so the zero-stress boundary condition is a good approximation. Furthermore, the compressibility of air is much smaller than typical elastic solids.

The zero-stress boundary condition is accompanied by a zero free-charge density condition at boundaries $\partial\Omega_{\mathrm{ext}}$ between the piezoelectric transducer electrodes and the air

$$\boldsymbol{n} \cdot \boldsymbol{D} = 0 \quad \text{for} \quad \boldsymbol{r} \in \partial\Omega_{\mathrm{ext}}. \tag{2.43}$$

Chapter 3

Simulation of acoustofluidic devices

The weak formulation will be derived, which forms the basis for solving differential equations using the finite-element method (FEM). The weak formulation will be re-formulated in the case of an axisymmetric system, enabling efficient modeling by reducing an axisymmetric three-dimensional geometry into a two-dimensional model domain. Furthermore, the technique of perfectly matched layers (PML) is presented. The PML technique is used to truncate numerical model domains in cases of non-reflecting outgoing waves. Finally, a model is validated by numerical mesh convergence and evaluated using different sets of polynomial test functions and mesh structures.

3.1   The finite-element method

The equations required for the numerical model implementation have been established in Chapter 2, and a method to solve and satisfy the differential equations and boundary conditions is needed. Here, we will use the finite-element method (FEM) to approximate the solution to the governing differential equations on a discretized mesh with an appropriate set of test functions. Here, the weak formulation is established, which will be the mathematical basis for constructing approximate solutions to the governing equations given the boundary conditions. When using the finite-element method, a physical domain Ω with boundary $\partial\Omega$ is discretized into a finite number of mesh vertices $n = 1, 2, \ldots, M$ connected by mesh elements, as illustrated in Fig. 3.1. The solution to a field $g(\boldsymbol{r})$ obtained by the finite-element method is approximated and represented by a superposition of test functions $\hat{g}(\boldsymbol{r})$ as

$$g(\boldsymbol{r}) \approx \sum_{n=1}^{M} c_n \hat{g}_n(\boldsymbol{r}), \tag{3.1}$$
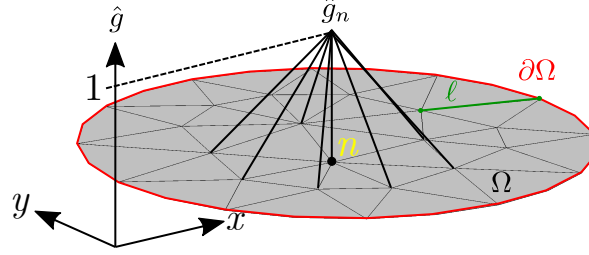
Figure 3.1: Sketch of a two-dimensional domain Ω (gray) with boundary $\partial\Omega$ (red line) represented by a triangular mesh with a maximum mesh-element size ℓ. Here, the test function $\hat{g}_n$ is chosen to be a first-order polynomial with value 1 at vertex n, located at $\boldsymbol{r}_n$, and 0 at adjacent vertices.

where the coefficients c_n are to be determined by numerical procedures. The test functions $\hat{g}_n(\boldsymbol{r})$ are continuous and holds the compact properties

$$\hat{g}_n(\boldsymbol{r}_m) = \begin{cases} 0, & m \neq n, \\ 1, & m = n. \end{cases} \tag{3.2}$$

The equations governing the fields included in our model can all be written in the generic form

$$\boldsymbol{\nabla} \cdot \boldsymbol{J}[g(\boldsymbol{r})] - F[g(\boldsymbol{r})] = 0, \tag{3.3}$$

known as the strong formulation in which $\boldsymbol{J}$ can be interpreted as a generalized flux density and F as a generalized force. The weak formulation is constructed by substituting the approximation Eq. (3.1) into Eq. (3.3), which leads to a defect $d(\boldsymbol{r})$ written as

$$\boldsymbol{\nabla} \cdot \boldsymbol{J}[g(\boldsymbol{r})] - F[g(\boldsymbol{r})] = d(\boldsymbol{r}). \tag{3.4}$$

The strong formulation is approximately satisfied if the projection of $d(\boldsymbol{r})$ onto any test function $\hat{g}_m(\boldsymbol{r})$ vanishes

$$\int_\Omega \hat{g}_m(\boldsymbol{r}) d(\boldsymbol{r}) \, \mathrm{d}V = \int_\Omega \hat{g}_m(\boldsymbol{r}) \left\{ \boldsymbol{\nabla} \cdot \boldsymbol{J}[g(\boldsymbol{r})] - F[g(\boldsymbol{r})] \right\} \mathrm{d}V = 0, \tag{3.5}$$

which is known as the weak formulation. For a linear mapping $\boldsymbol{J}[g(\boldsymbol{r})] = \sum_n c_n \boldsymbol{J}[\hat{g}_n(\boldsymbol{r})]$ and $F[g(\boldsymbol{r})] = \sum_n c_n F[\hat{g}_n(\boldsymbol{r})]$ the weak formulation Eq. (3.5) can be written as

$$\sum_{n=1}^M \left(\int_\Omega \hat{g}_m(\boldsymbol{r}) \left\{ \boldsymbol{\nabla} \cdot \boldsymbol{J}[\hat{g}_n(\boldsymbol{r})] - F[\hat{g}_n(\boldsymbol{r})] \right\} \mathrm{d}V \right) c_n = 0, \tag{3.6a}$$

compactly written as

$$\sum_{n=1}^M K_{mn} c_n = 0, \tag{3.7}$$

corresponding to M number of algebraic equations with unknowns c_n to solve for. The numerical task will be to calculate the integrals contained in K_{mn} and solve for the constants c_n to represent the approximate solution in Eq. (3.1). In the proceeding section, the boundary conditions will be considered and added to the weak formulation, resulting in a non-zero right-hand side of Eq. (3.7), which means that the unknown coefficients c_n can be obtained by matrix inversion procedures.

3.1.1   Boundary conditions implemented in the weak form

Here, two classes of boundary conditions are considered, one specifying the field value $g(\boldsymbol{r}) = h(\boldsymbol{r})$ at the boundary $\partial\Omega_D$ and another specifying the normal flux density $\boldsymbol{n}\cdot\boldsymbol{J} = q(\boldsymbol{r})$ at the boundary $\partial\Omega_N$. These are known as Dirichlet and Neumann boundary conditions, respectively. The boundary $\partial\Omega$ surrounding the domain Ω is the union between $\partial\Omega_D$ and $\partial\Omega_N$. The boundary conditions can be accessed by expanding Eq. (3.5) using integration by parts

$$\int_\Omega \left[(\boldsymbol{\nabla}\hat{g}_m)\cdot\boldsymbol{J} + \hat{g}_m F\right] \mathrm{d}V = \int_{\partial\Omega_D} \hat{g}_m \boldsymbol{n}\cdot\boldsymbol{J}\,\mathrm{d}A + \int_{\partial\Omega_N} \hat{g}_m \boldsymbol{n}\cdot\boldsymbol{J}\,\mathrm{d}A. \tag{3.8}$$

The Dirichlet condition specifying the field value $g(\boldsymbol{r}) = h(\boldsymbol{r})$ for $\boldsymbol{r} \in \partial\Omega_D$ implies that the test function $\hat{g}_m$ must vanish on the surface $\boldsymbol{r} \in \partial\Omega_D$, and together with the Neumann boundary condition $\boldsymbol{n}\cdot\boldsymbol{J} = q$ the weak formulation Eq. (3.8) becomes

$$\int_\Omega \left[(\boldsymbol{\nabla}\hat{g}_m)\cdot\boldsymbol{J} + \hat{g}_m F\right] \mathrm{d}V = \int_{\partial\Omega_N} \hat{g}_m q(\boldsymbol{r})\,\mathrm{d}A,$$
$$g(\boldsymbol{r}) = h(\boldsymbol{r}) \quad \text{for} \quad \boldsymbol{r} \in \partial\Omega_D, \tag{3.9}$$

reducing the number of equations to be solved by the number of vertices contained in $\partial\Omega_D$. The matrix inversion problem Eq. (3.7) can then be written as

$$K_{mn}c_n = b_m, \quad \text{for} \quad \boldsymbol{r}_m \in \Omega \cup \partial\Omega_N, \quad \text{and} \tag{3.10a}$$
$$b_m = h_m, \quad \text{for} \quad \boldsymbol{r}_m \in \partial\Omega_D. \tag{3.10b}$$

where

$$K_{mn} = \int_\Omega \left\{(\boldsymbol{\nabla}\hat{g}_m)\cdot\boldsymbol{J}[\hat{g}_n] + \hat{g}_m F[\hat{g}_n]\right\} \mathrm{d}V, \tag{3.11a}$$

$$b_m = \int_{\partial\Omega_N} \hat{g}_m q(\boldsymbol{r})\,\mathrm{d}A. \tag{3.11b}$$

The matrix inversion problem is generated in three steps: first, the coefficients contained in K_{mn} are assembled by calculating the integrals. Secondly, the Neumann boundary conditions are imposed to calculate b_m, and finally, the Dirichlet boundary conditions overwrite b_m for $\boldsymbol{r}_m \in \partial\Omega_D$.

Notice how the expanded version of the weak formulation in Eq. (3.8) is easier to solve compared to Eq. (3.6) since the complicated divergence $\boldsymbol{\nabla}\cdot\boldsymbol{J}$ is replaced by $\boldsymbol{\nabla}\hat{g}_m$, which is

Table 3.1: FEM details for implementation in Comsol Multiphysics, including the field name, the polynomial order (2D/3D), governing equation, the generalized flux density $\boldsymbol{J}$, the generalized force $\boldsymbol{F}$, the boundary condition, and the type of boundary condition.

Field	Pol. order (2D/3D)	Gov. eq.	$\boldsymbol{J}$	$\boldsymbol{F}$	Bound. cond.	Type
p_1	$4^{\text{th}}/3^{\text{rd}}$	Eq. (2.10a)	$\boldsymbol{\nabla} p_1$	$-k_{\text{c}}^2 p_1$	Eq. (2.36)	Neumann
$\boldsymbol{v}_2^d$	$3^{\text{rd}}/2^{\text{nd}}$	Eq. (2.16b)	$\eta_0 \boldsymbol{\nabla} \boldsymbol{v}_2^d - p_2^d \boldsymbol{I}$	$-\frac{\Gamma \omega}{c_0^2} \left\langle p_1 \boldsymbol{v}_1^d \right\rangle$	Eq. (2.38)	Dirichlet
p_2^d	$2^{\text{nd}}/1^{\text{st}}$	Eq. (2.16a)	$\boldsymbol{0}$	$\boldsymbol{\nabla} \cdot \boldsymbol{v}_2^d$	$\int_\Omega p_2^d \, \mathrm{d}V = 0$	Global constraint
$\boldsymbol{u}_1$	$4^{\text{th}}/3^{\text{rd}}$	Eq. (2.27)	$\boldsymbol{\sigma}$	$-\rho_{\text{sl}} \omega^2 \boldsymbol{u}_1$	Eq. (2.35b)	Neumann
φ_1	$4^{\text{th}}/3^{\text{rd}}$	Eq. (2.32)	$\boldsymbol{D}$	0	Eq. (2.39)	Dirichlet

known analytically given the set of polynomial test functions. The weak formulation is an integrated part in the Comsol Multiphysics software, and by using the *"weak form PDE module"*, the specific $\boldsymbol{J}$ and F are to be specified together with the appropriate class of boundary condition. For each field, the numerical details are given in Table 3.1, including the polynomial order of the test functions, the flux density $\boldsymbol{J}$, the force F, and the class of boundary condition. In the equations governing the acoustic streaming, Eq. (2.16), the second-order gradient pressure field $\boldsymbol{\nabla} p_2^d$ appear as a source term in Eq. (2.16b), the p_2^d level is then set by using a global constraint defined as $\int_\Omega p_2^d \, \mathrm{d}V = 0$.

3.2   Symmetries

When a system features certain symmetries, symmetry boundary conditions can reduce the model geometry. For example, consider a mirror plane with the surface normal $\boldsymbol{n}$; the model geometry can be reduced by one-half by imposing zero normal components and zero fluxes across the mirror plane. The boundary conditions on a mirror plane are given explicitly for each field in Table 3.2.

Another type of symmetry is axisymmetry, for which the geometry is rotationally invariant. For axisymmetric geometries, the model domain can potentially be reduced from a three-dimensional to two-dimensional model geometry. This reduction will not only halve the degrees of freedom but reduce it by a factor proportional to the mesh element

Table 3.2: List of symmetry conditions imposed on a mirror plane with normal vector $\boldsymbol{n}$ and tangent vectors $\boldsymbol{t}_i$. The symmetry conditions are tabulated for each field included in the model and classified as Dirichlet or Neumann, referring to the field value or the flux.

	p_1	$\boldsymbol{v}_2^d$	$\boldsymbol{u}_1$	φ_1	B. c. type
Normal component		$\boldsymbol{n} \cdot \boldsymbol{v}_2^d = 0$	$\boldsymbol{n} \cdot \boldsymbol{u}_1 = 0$		Dirichlet
Flux	$\boldsymbol{n} \cdot \boldsymbol{\nabla} p_1 = 0$	$\boldsymbol{t}_i \cdot \left(\eta_0 \boldsymbol{\nabla} \boldsymbol{v}_2^d - p_2^d \boldsymbol{I} \right) \cdot \boldsymbol{n} = 0$	$\boldsymbol{t}_i \cdot \boldsymbol{\sigma} \cdot \boldsymbol{n} = 0$	$\boldsymbol{n} \cdot \boldsymbol{D} = 0$	Neumann

size divided by the geometry length scale, typically in the order of 10^{-2} depending on the frequency and the geometry. A two-dimensional axisymmetric model is achieved by transforming Eq. (3.5) into cylindrical coordinates (r, ϕ, z) assuming ϕ-independent fields and re-writing it into a form identical to Eq. (3.5). By introducing the Cartesian-like gradient $\boldsymbol{\nabla}_{rz} = (\partial_r \boldsymbol{e}_r + \partial_z \boldsymbol{e}_z)$ the axisymmetric version of Eq. (3.5) becomes

$$\int_\Omega \hat{g}_m(\boldsymbol{r}) \left\{ \boldsymbol{\nabla}_{rz} \cdot \boldsymbol{J}_{rz} - F_{rz} \right\} \, \mathrm{d}r\mathrm{d}z = 0. \tag{3.12}$$

The task is now to find the transformed $\boldsymbol{J}_{rz}$ and F_{rz} which satisfy Eq. (3.12).

In Table 3.1, it is seen how $\boldsymbol{J}$ appears either as a vector or as a tensor, in the case of $\boldsymbol{J}$ being a vector, the transformed $\boldsymbol{J}_{rz}$ and F_{rz} becomes

$$\boldsymbol{J}_{rz} = 2\pi r \left(J_r \boldsymbol{e}_r + J_z \boldsymbol{e}_z \right), \quad \text{and} \quad F_{rz} = 2\pi r F, \tag{3.13}$$

where J_r and J_z are the flux density components in cylindrical coordinates. In cases where $\boldsymbol{J}$ appears as a tensor and $\boldsymbol{F}$ as a vector, the transformed $\boldsymbol{J}_{rz}$ and $\boldsymbol{F}_{rz}$ reads

$$\begin{aligned} \boldsymbol{J}_{rz} = 2\pi r \, \{ &J_{rr} \boldsymbol{e}_r \boldsymbol{e}_r + J_{rz} \boldsymbol{e}_r \boldsymbol{e}_z + J_{zr} \boldsymbol{e}_z \boldsymbol{e}_r \\ &+ J_{zz} \boldsymbol{e}_z \boldsymbol{e}_z + J_{r\phi} \boldsymbol{e}_r \boldsymbol{e}_\phi + J_{z\phi} \boldsymbol{e}_z \boldsymbol{e}_\phi \}, \end{aligned} \tag{3.14}$$

and

$$\boldsymbol{F}_{rz} = 2\pi r \tilde{\boldsymbol{F}} + 2\pi J_{\phi\phi} \boldsymbol{e}_r - 2\pi J_{\phi r} \boldsymbol{e}_\phi, \tag{3.15}$$

where $\tilde{\boldsymbol{F}}$ is the cylindrical transformation of $\boldsymbol{F}$. All fields are considered independent of ϕ and with zero ϕ components. Implementing the axisymmetric version of the weak formulation for a scalar field is straightforward and only acquires a factor $2\pi r$ as shown in Eq. (3.13). However, for a vector field, the implementation requires knowledge of the tensor components in $\boldsymbol{J}_{rz}$ and the extra terms appearing in $\boldsymbol{F}_{rz}$, for the acoustic streaming $\boldsymbol{v}_2^d$ the non-zero components are

$$\begin{aligned} J_{rr}^{\left(\boldsymbol{v}_2^d\right)} = \left(\eta_0 \partial_r v_{2,r}^d - p_2^d \right), \quad J_{rz}^{\left(\boldsymbol{v}_2^d\right)} = \eta_0 \partial_z v_{2,r}^d, \\ J_{zr}^{\left(\boldsymbol{v}_2^d\right)} = \eta_0 \partial_r v_{2,z}^d, \quad J_{zz}^{\left(\boldsymbol{v}_2^d\right)} = \left(\eta_0 \partial_z v_{2,z}^d - p_2^d \right), \end{aligned} \tag{3.16a}$$

$$J_{\phi\phi}^{\left(\boldsymbol{v}_2^d\right)} = \eta_0 \frac{v_{2,r}^d}{r} - p_2^d. \tag{3.16b}$$

Similarly, the transformed components for the mechanical displacement field in an isotropic solid are provided

$$\begin{aligned} J_{rr}^{(\boldsymbol{u}_1)} &= C_{11} \partial_r u_{1,r} + C_{12} \left(\frac{u_{1,r}}{r} + \partial_z u_{1,z} \right), \\ J_{rz}^{(\boldsymbol{u}_1)} &= J_{zr}^{(\boldsymbol{u}_1)} = C_{44} \left(\partial_r u_{1,z} + \partial_z u_{1,r} \right), \\ J_{zz}^{(\boldsymbol{u}_1)} &= C_{12} \frac{1}{r} \partial_r \left(r u_{1,r} \right) + C_{11} \partial_z u_{1,z}, \end{aligned} \tag{3.17a}$$

$$J_{\phi\phi}^{(\boldsymbol{u}_1)} = C_{12} \partial_r u_{1,r} + C_{11} \frac{u_{1,r}}{r} + C_{12} \partial_z u_{1,z}. \tag{3.17b}$$

For the constitutive relation in Eq. (2.33a), the mechanical displacement field is supplemented by the electric field given by the piezoelectric coupling tensor. For a ∞mm piezoelectric material, the axisymmetric transformation gives the following non-zero components

$$J_{rr}^{(\boldsymbol{u}_1 \leftrightarrow \varphi_1)} = C_{11}\partial_r u_{1,r} + C_{12}\frac{u_{1,r}}{r} + C_{13}\partial_z u_{1,z} + e_{31}\partial_z\varphi,$$

$$J_{rz}^{(\boldsymbol{u}_1 \leftrightarrow \varphi_1)} = J_{zr}^{(\boldsymbol{u}_1 \leftrightarrow \varphi_1)} = C_{44}\left(\partial_r u_{1,z} + \partial_z u_{1,r}\right) + e_{15}\partial_r\varphi, \qquad (3.18\text{a})$$

$$J_{zz}^{(\boldsymbol{u}_1 \leftrightarrow \varphi_1)} = C_{13}\frac{1}{r}\partial_r\left(r u_{1,r}\right) + C_{33}\partial_z u_{1,z} + e_{33}\partial_z\varphi,$$

$$J_{\phi\phi}^{(\boldsymbol{u}_1 \leftrightarrow \varphi_1)} = C_{12}\partial_r u_{1,r} + C_{11}\frac{u_{1,r}}{r} + C_{13}\partial_z u_{1,z} + e_{31}\partial_z\varphi. \qquad (3.18\text{b})$$

Except for the first-order no-slip condition in Eq. (2.36) and the acoustic streaming slip-condition in Eq. (2.38), the boundary conditions are not altered by the axisymmetric implementation apart from $\boldsymbol{\nabla} \to \boldsymbol{\nabla}_{rz}$, $(x, y, z) \to (r, z)$, and the Neumann conditions acquiring a factor of $2\pi r$ due to the surface integral.

The axisymmetric formulation of the first-order no-slip condition in Eq. (2.36) is

$$(\boldsymbol{n} \cdot \boldsymbol{\nabla})p_1 = \frac{\mathrm{i}\omega\rho_0}{1 - \mathrm{i}\Gamma}\left[-\mathrm{i}\omega\boldsymbol{u}_1 - \frac{\omega}{k_s}\left(\boldsymbol{\nabla}_{rz} \cdot \boldsymbol{u}_1 + \frac{u_{1,r}}{r}\right)\right] - \frac{\mathrm{i}}{k_s}\left(k_c^2 p_1 + \partial_n^2 p_1\right), \qquad (3.19)$$

in this case, the boundary condition acquires an additional term $\frac{u_{1,r}}{r}$ due to the divergence. Similarly, for the acoustic slip condition Eq. (2.38), the divergence contributes with extra terms, and the boundary condition in axisymmetric coordinates is written as

$$\boldsymbol{A}_{rz} = \boldsymbol{A} + \left[\frac{2 - \mathrm{i}}{2}\frac{\left(v_{1,r}^\delta\right)^*}{r} + \omega\frac{u_{1,r}^*}{r}\right]\boldsymbol{v}_1^\delta, \qquad (3.20\text{a})$$

$$\boldsymbol{B}_{rz} = \boldsymbol{B}, \qquad (3.20\text{b})$$

where the three-component Cartesian vectors in $\boldsymbol{A}$ and $\boldsymbol{B}$ are replaced by the two-component cylindrical vectors with r and z components together with $\boldsymbol{\nabla} \to \boldsymbol{\nabla}_{rz}$. Furthermore, for any vector field, i.e., $\boldsymbol{u}_1$ and $\boldsymbol{v}_2^d$, the r-component has to be zero at the rotational axis at $r = 0$ since the fields have to be invariant of ϕ.

3.3 Perfectly matched layers

A perfectly matched layer (PML) is a numerical technique used to truncate computational domains in numerical simulations. The technique is typically used to simulate propagating waves in unbounded domains but can also be used in finite domains whenever an outgoing wave is completely attenuated and non-reflecting. The technique involves an artificial domain in continuation of the physical region of interest, which absorbs incoming waves. Mathematically this is achieved by a complex coordinate transformation: for a

wave traveling in the x-direction with angular frequency $\omega = 2\pi f$, the complex coordinate transformation inside the PML domain ($L_{\mathrm{phys}} \leq x < L_{\mathrm{phys}} + L_{\mathrm{pml}}$) is

$$x \rightarrow x + \frac{\mathrm{i}}{\omega} \int_{L_{\mathrm{phys}}}^{x} \mu(s)\,\mathrm{d}s, \quad \text{for} \quad x \in [L_{\mathrm{phys}}, L_{\mathrm{phys}} + L_{\mathrm{pml}}[, \tag{3.21}$$

and whenever the partial derivative ∂_x appears, it should be replaced by

$$\partial_x \rightarrow \frac{1}{1 + \frac{\mathrm{i}}{\omega}\mu(x)} \partial_x, \quad \text{for} \quad x \in [L_{\mathrm{phys}}, L_{\mathrm{phys}} + L_{\mathrm{pml}}[. \tag{3.22}$$

The task is now to appropriately define the absorbing function $\mu(x)$. In this thesis, we use an unbounded continuous absorbing function of the form

$$\mu(x) = \begin{cases} 0, & \text{for} \quad x \leq L_{\mathrm{phys}}, \\ \frac{2c}{L_{\mathrm{pml}} - (x - L_{\mathrm{phys}})} - \frac{2c}{L_{\mathrm{pml}}}, & \text{for} \quad x > L_{\mathrm{phys}}, \end{cases} \tag{3.23}$$

as in Ref. [54], which provides a PML layer without spurious reflections at $x = L_{\mathrm{phys}} + L_{\mathrm{pml}}$, even though the thickness of the PML layer L_{pml} is finite and comparable to the wavelength $\lambda = c/f$, where c is the sound speed in the physical domain. In cases where the PML contains two different materials, as in Paper II [2], the PML size L_{pml} should be comparable to the wavelength in the material with the largest sound speed. The solution should be independent of the PML domain size and properties, which is verified by a numerical convergence test as in Paper II [2].

3.4 Numerical mesh convergence analyses

The numerical models are verified by numerical mesh convergence as in Ref. [17]. The convergence measure $\mathcal{E}$ is defined as the L_2-norm of the difference between a field variable $g(\boldsymbol{r})$ and the best possible resolved field solution $g_{\mathrm{ref}}(\boldsymbol{r})$

$$\mathcal{E} = \sqrt{\frac{\int_\Omega |g - g_{\mathrm{ref}}|^2\,\mathrm{d}V}{\int_\Omega |g_{\mathrm{ref}}|^2\,\mathrm{d}V}}. \tag{3.24}$$

A model is converged when $\mathcal{E}$ reaches a pre-desired limit, in this case, 1% for the first-order fields and 10% for the second-order fields. In the elastic domains, the maximum mesh-element size $\ell = \lambda_{\mathrm{tr}}/\Delta$ is given by a fraction of the transverse wavelength λ_{tr} in terms of the mesh scale Δ. Similarly, the maximum mesh element size in the fluid domain is given as a fraction of half the acoustic wavelength $\ell = \lambda/(2\Delta)$. By sweeping the mesh scale Δ, the mesh is gradually refined, and the convergence measure $\mathcal{E}$ is calculated as g approaches g_{ref}.

The convergence measure $\mathcal{E}$ can be used to find the optimal set of polynomial test functions. Consider the sets of polynomial test functions in Table 3.3. For each set, a mesh

Table 3.3: Sets of polynomial test functions used to find the most efficient set. Each entry indicates the polynomial order used for the test functions for each field.

	$\boldsymbol{u}_1$	φ_1	p_1	$\boldsymbol{v}_2^d$	p_2^d
Set 1	2nd	2nd	2nd	2nd	1st
Set 2	3rd	3rd	3rd	2nd	1st
Set 3	4th	4th	4th	3rd	2nd

convergence is conducted by evaluating $\mathcal{E}$ as the mesh is gradually refined. The results are plotted in Fig. 3.2, showing the convergence measure as a function of degrees of freedom (DOF). Set 3 provides the most efficient convergence; the first-order fields have converged below 1% at 29,810 DOF and the second-order fields below 10% at 207,900 DOF. This mesh convergence was calculated for a model including all the field variables presented in Chapter 2. The model consists of a water-filled polymer cavity glued onto a piezoelectric transducer, similar to the model used in the studies presented in Section 5.3.1 and Chapter 7.
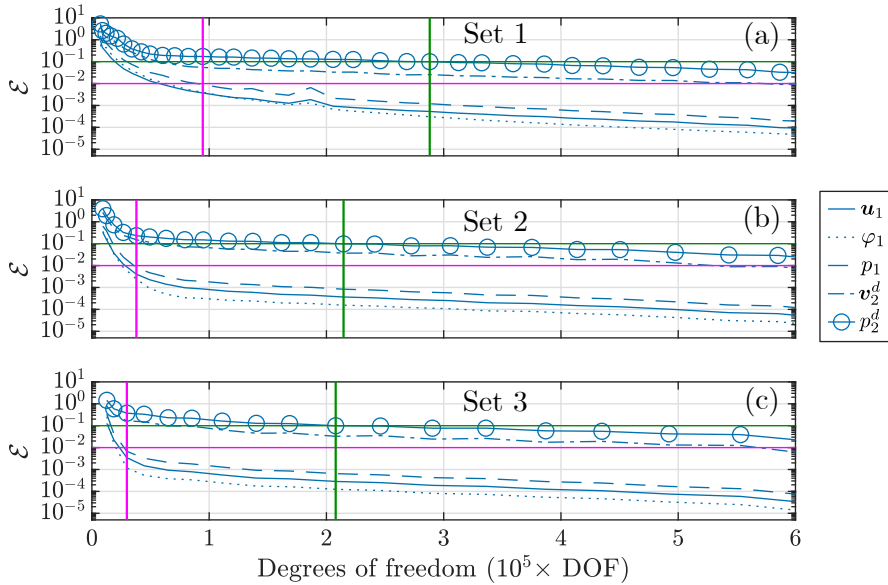
Figure 3.2: Mesh convergence for different sets of polynomial test functions. The corresponding set of polynomial test functions is provided in Table 3.3. The vertical magenta lines indicate the DOF at which the first-order fields have converged below 1%, whereas the green vertical lines indicate at which DOF the second-order fields have converged below 10%.

Furthermore, the convergence measure can be used to evaluate and find the most efficient mesh structure. In this case, the convergence measure $\mathcal{E}$ is calculated using the polynomials in "Set 3" in Table 3.3 for an unstructured free triangular mesh, a structured mapped mesh, and a mix of the two for various mesh scales Δ. In each case, the degrees of freedom are evaluated together with $\mathcal{E}$, and the results are plotted in Fig. 3.3. For this model, the unstructured triangular mesh has reached the desired limit of $\mathcal{E} = 1\%$ at $\Delta = 1.5$ with 29,810 DOF for the first-order fields. In comparison, the two other cases require $\Delta = 2$, yielding 40,000 degrees of freedom. The second-order fields require $\Delta = 5$ for the free triangular mesh and $\Delta = 5.5$ for the mapped and mixed mesh, all yielding $\sim 200,000$ DOF. This is an example of how a numerical mesh convergence is conducted and how the mesh can be optimized in terms of structure. In this case, the free triangular mesh provided the most efficient mesh structure. Another example of a mesh convergence is given in Paper III [3] in Fig. S1.
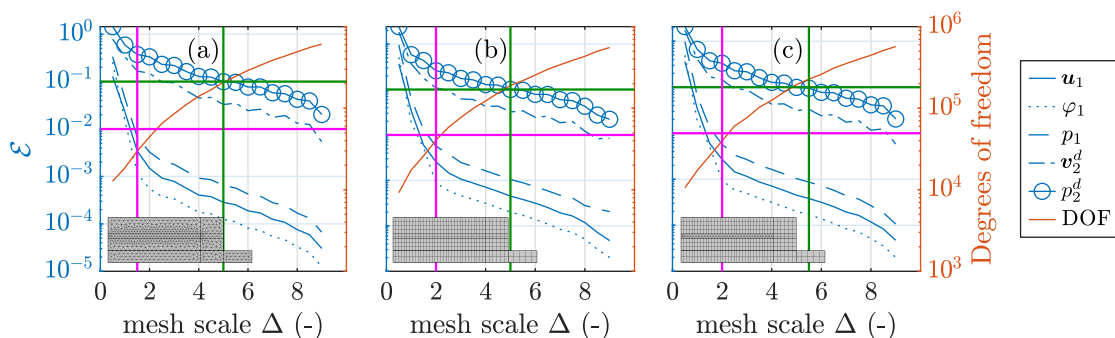
Figure 3.3: Convergence measure $\mathcal{E}$ as a function of maximum mesh-element size $\ell = \lambda_{\mathrm{tr}}/\Delta$ given by the mesh scale Δ for three different mesh structures: (a) An unstructured triangular mesh, (b) a structured mapped mesh, and (c) a triangular mesh in the fluid domain and a structured mesh in the solid domains. Each mesh is shown for $f = 1\,\mathrm{MHz}$. The vertical magenta lines indicate the mesh scale at which the first-order fields have converged below 1%, whereas the green vertical lines indicate at which mesh scale the second-order fields have converged below 10%.

Chapter 4

Polymer-based acoustofluidics

The concepts and challenges of working with polymer-based acoustofluidics are illustrated and discussed. Different model examples demonstrate the challenges arising from an all-polymer-based acoustofluidic device, including idealized actuation modeling and microfluidic chip-material variations. In Paper I [1], we studied the particle velocity fields in PDMS-sealed aluminum-based acoustofluidic devices. This study was our first attempt to bridge simulation and experiment for a polymer-based acoustofluidic device. The results will be summarized in a dedicated section, and as a bonus, an analytical solution to an idealized 2D system resembling the PDMS-sealed aluminum-based device will be presented. The original paper is included in Chapter 6 with permission from the co-authors.

4.1 Whole-system ultrasound resonances in polymer-based acoustofluidics

Generally speaking, acoustofluidic devices can be grouped into two groups referring to the propagation of waves: one type which is driven by an interdigital transducer (IDT) array, providing what is called surface acoustic waves (SAW), and another type of device driven by bulk acoustic transducers, where the propagation of waves are referred to as bulk acoustic waves (BAW). Surface acoustic waves are, as the name indicates, waves that propagate on the surface of a substrate, whereas bulk acoustic waves propagate throughout the entire bulk. Only BAW devices will be considered in this thesis.

Commercializing the acoustofluidic technology for biomedical applications implies certain restrictions for the fabrication processes. Especially for single-use applications, the production cost has to be minimized. Transitioning to polymer-based devices is one way to accommodate this. Consider, for example, the *AcouPlast* project: aiming to tap into a 900-million-euro-per-year market by developing a polymer-based acoustofluidic chip to separate plasma from whole blood, enabling point-of-care diagnostics with single-use cartridges. The project has the title *"Acoustofluidic blood plasma separation polymer chip for Point-of-Care diagnostics"*. It is a collaboration between the companies AcouSort AB and Ortofon A/S, and the Technical University of Denmark and Lund University.

The project is funded by the *Eurostars 2* program, supporting innovative research and product development for commercialization. [55]

For the last ten years, polymer-based acoustofluidics have gained interest, and the field is still maturing. The term polymer-based acoustofluidics refers to the inclusion of a polymer in the microfluidic chip design, examples are: spacers for microfluidic channels [27, 56], cover films [1, 28], and all-polymer-based microfluidic devices [12, 29–31]. Typical polymers used for acoustofluidic device fabrication are polystyrene (PS), polydimethylsiloxane (PDMS/silicone), and polymethylmethacrylate (PMMA/acrylic). Acoustic properties for selected polymers, glass, and silicon are provided in Table 4.1.

In a classical acoustophoresis device fabricated in either glass or silicon, the acoustic resonance frequency can be approximated by the so-called hard-wall resonance frequency given by the channel dimensions, the fluid sound speed c_0, and the desired mode. Consider, for example, the hard-wall half-wave resonance frequency $f_{\lambda/2} = \frac{c_0}{2W_{\mathrm{ch}}}$ achieved by tuning the frequency near to where the channel width W_{ch} matches half the wavelength. In a hard-wall system, the acoustic waves are confined to the fluid due to the large acoustic contrast between the fluid and the microfluidic chip material, which provides ideal resonators with large quality factors. Furthermore, a hard-walled system provides the necessary conditions to approximate the no-slip condition by the zero-velocity boundary condition $\boldsymbol{n}\cdot\boldsymbol{\nabla}p_1 = 0$, which in turn provides ideal acoustic eigenmodes decoupled from the surrounding solid. This approximation holds in systems where the material surrounding the fluid has a much larger acoustic impedance compared to the contained fluid. However, by introducing polymers, the acoustic impedance is comparable to water, and the acoustic waves begin to leak out since the surrounding material yields to the fluid motion. As a result, the surrounding material can no longer completely sustain the acoustic pressure waves. The extreme case is that of a free liquid where $p_1 = 0$ on the interface, for polymers we find ourselves in the regime between the hard-wall $\boldsymbol{n} \cdot \boldsymbol{\nabla}p_1 = 0$ and the zero stress condition $p_1 = 0$, and the boundary conditions can no longer be approximated be either of the two.

Table 4.1: Acoustic properties of selected solids at $25\,^{\circ}\mathrm{C}$ and $f = 1\,\mathrm{MHz}$, including the mass density ρ_{sl}, the longitudinal sound speed c_{lo}, the longitudinal wavelength λ_{lo}, the acoustic impedance $Z_{\mathrm{ac}} = \rho_{\mathrm{sl}}c_{\mathrm{lo}}$, and the acoustic contrast Z_{ac}/Z_0 between solid/water and $Z_{\mathrm{ac}}/Z_{\mathrm{air}}$ for solid/air, where $Z_{\mathrm{air}} = 410\,\mathrm{Pa\,s/m}$.

	Density	Sound speed	Wavelength	Acoustic impedance	Acoustic contrast		Source
	ρ_{sl}	c_{lo}	λ_{lo}	Z_{ac}	$\frac{Z_{\mathrm{ac}}}{Z_0}$	$\frac{Z_{\mathrm{ac}}}{Z_{\mathrm{air}}}$	
	$(\mathrm{kg/m}^3)$	$(\mathrm{m/s})$	(mm)	$(\mathrm{MPa\,s/m})$	-	-	
Silicon	2329	8435	8.4	19.6	13.2	48×10^3	[57]
Glass	2520	5824	5.8	14.7	9.8	36×10^3	[34]
PMMA	1162	2486	2.5	2.9	1.9	7×10^3	Paper III [3]
Polystyrene	1050	2350	2.5	2.89	1.7	6×10^3	[58]
PDMS	1031	1030	1.0	1.1	0.7	3×10^3	[59]

In Ref. [20], Moiseyenko and Bruus studied how a classical acoustophoresis device is affected by changing the microfluidic chip material from glass/silicon into PDMS/PMMA. Instead of the classical hard-wall resonances observed in glass and silicon-based devices, the resonances are now classified as whole-system-ultrasound resonances (WSUR), relying on the acoustic contrast between the chip and the surrounding air. As a result, the design principles relying on hard-wall resonance are no longer applicable. Instead, the acoustic resonances in the fluid are strongly coupled to the motion in the surrounding material.

Modeling a polymer-based acoustofluidic device is a challenge. The concept of WSUR requires each device component to be well-characterized to represent the whole-system dynamics accurately. Otherwise, the model results can be misleading. In Ref. [20], Moiseyenko and Bruus studied numerically the consequences of introducing polymers comprising the microfluidic chip material in a classical acoustophoresis design sketched in Fig. 4.1(a.1). Their model consisted of a 2D-cross section comprising the channel architecture. The system was driven by an idealized actuation, approximating the actual actuation given by the transducer. This section extends the study by including a piezoelectric transducer to show the effect of having an idealized actuation versus the actual actuation given by the piezoelectric transducer. The study is further extended by considering a glass-based capillary device illustrated in Fig. 4.1(b).

The two devices sketched in Fig. 4.1 are probably two of the most studied acoustofluidic designs. The microfluidic chip design shown in Fig. 4.1(a) is a classical acoustophoresis device studied in Refs. [20, 50, 52] for the separation of plasma from whole blood. In
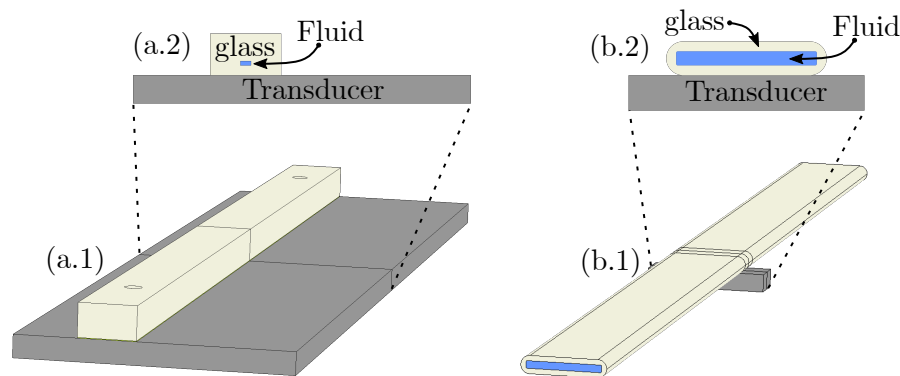
Figure 4.1: (a.1) Sketch of the classical acoustophoresis device experimentally studied in Refs. [20, 50, 52] comprising a glass-based microfluidic chip glued onto a bulk transducer for separation of particles in a continuous flow. (b.1) Sketch of the glass-based capillary-tube device studied in Refs. [2, 7, 60–63] comprising a glass-based capillary tube glued onto a small transducer for acoustic particle trapping. The cross-sections, corresponding to the 2D model geometries, are shown in (a.2) and (b.2) for each device, respectively, together with component labels.

this device, a horizontal half-wave pressure resonance is generated by a bulk ultrasound transducer to migrate large and heavy particles into the vertical pressure node facilitated by the acoustic radiation force. In this context, particles are large when the particle size is much larger than the viscous boundary layer thickness $\delta_{\mathrm{visc}} \sim 500\,\mathrm{nm}$ and heavy when the particle compressibility κ_{p} is smaller than the fluid compressibility κ_0, i.e. when the acoustic contrast factor Eq. (2.25) is positive.

In this type of device, the fluid motion is perpendicular to the thickness mode in the piezoelectric transducer driving the resonance, so the device is said to be a transversal resonator. The model geometry and dimensions are similar to that in Ref. [20]: a channel of width $W_{\mathrm{ch}} = 377\,\mu\mathrm{m}$ and height $H_{\mathrm{ch}} = 157\,\mu\mathrm{m}$ embedded in a glass chip of width $W_{\mathrm{chip}} = 2.52\,\mathrm{mm}$ and height $H_{\mathrm{chip}} = 1.5\,\mathrm{mm}$. The model is now extended by including a piezoelectric transducer of width $12\,\mathrm{mm}$ and thickness $1\,\mathrm{mm}$, off-centered by $2\,\mathrm{mm}$. The device is illustrated in Fig. 4.1(b.1) and the model is limited to the 2D cross-section illustrated in Fig. 4.1(b.2).

The glass-based capillary tube device sketched in Fig. 4.1(b) is also a classical and thoroughly studied device, see for example Refs. [2, 7, 60–63]. This device utilizes a pressure node parallel to the transducer thickness mode to focus particles into the horizontal plane. Furthermore, the localized actuation yields an in-plane acoustic radiation trapping force, able to trap and retain particles against a flow. In this case, the fluid motion is parallel to the transducer thickness mode driving the resonance, so this device is said to be a layered resonator. The model geometry and dimensions are similar to that in Paper II [2]: a channel of width $2\,\mathrm{mm}$ and height $200\,\mu\mathrm{m}$ embedded in a glass capillary with wall thicknesses of $140\,\mu\mathrm{m}$ glued onto a transducer of width $3.4\,\mathrm{mm}$ and thickness $0.5\,\mathrm{mm}$. Both models consist of a glass-based microfluidic chip glued onto a lead-zirconate-titanate (PZT) piezoelectric transducer. The parameters used to model the piezoelectric transducer are that of a Pz27 piezoceramic with parameters from Paper III [3], and the glass parameters are that of SLS float glass taken from Ref. [34].

4.1.1   Idealized actuation versus transducer actuation

To illustrate the effect of having an idealized actuation versus the actual actuation, the acoustic energy density spectrum $E_{\mathrm{ac}}(f)$ is simulated for the two cases. The idealized actuation is implemented as a displacement boundary condition $\boldsymbol{u}_{\mathrm{act}} = u_{\mathrm{act}}(y)\boldsymbol{e}_z$ between the transducer and the microfluidic chip interface. For the acoustophoresis device, the idealized actuation is antisymmetric around the channel centered at $y = 0$ with the shape

$$u_{\mathrm{act}}(y) = d_0 \left(\frac{y}{W_{\mathrm{chip}}} + \frac{3}{2} \right), \tag{4.1}$$

and

$$u_{\mathrm{act}}(y) = d_0, \tag{4.2}$$

for the glass-based capillary tube device. Both with an actuation amplitude of $d_0 = 0.2\,\mathrm{nm}$. The results are shown in Fig. 4.2 for both devices. The $E_{\mathrm{ac}}(f)$ spectra show how the

idealized actuation causes a mismatch between both devices' resonance frequencies and acoustic response. With the idealized actuation, there is no chance to bridge simulation with experiment without the use of free parameters, and the results can be misleading. However, the idealized actuation can be used to study general trends and fundamental acoustic phenomena in the fluid at single-frequency actuation and hard-wall systems, as in Refs. [17–20]. For a complete description, the idealized actuation is insufficient. The transducer must be included in the model, especially for polymer-based acoustofluidics, where the complex whole-system ultrasound dynamics give the acoustic response.

4.1.2 Microfluidic chip material transition

To illustrate how the acoustic response is affected by going from a glass-based to a polymer-based microfluidic chip, an artificial material with mass density $\rho^{(s)}$, and stiffness components $C_{11}^{(s)}$ and $C_{44}^{(s)}$, is defined as a linear interpolation between glass and PMMA

$$\rho^{(s)} = \rho^{(pmma)} + \left(\rho^{(glass)} - \rho^{(pmma)}\right) s, \tag{4.3a}$$

$$C_{11}^{(s)} = C_{11}^{(pmma)} + \left(C_{11}^{(glass)} - C_{11}^{(pmma)}\right) s, \tag{4.3b}$$

$$C_{44}^{(s)} = C_{44}^{(pmma)} + \left(C_{44}^{(glass)} - C_{44}^{(pmma)}\right) s, \tag{4.3c}$$

given by the parameter s. The PMMA parameters are taken from Paper III [3], and the glass parameters are taken from Ref. [34]. The effect of this material transitioning is illustrated with a model example, where the acoustic energy density spectrum $E_{ac}(f)$ is calculated while sweeping the parameter s, which defines the microfluidic chip material.
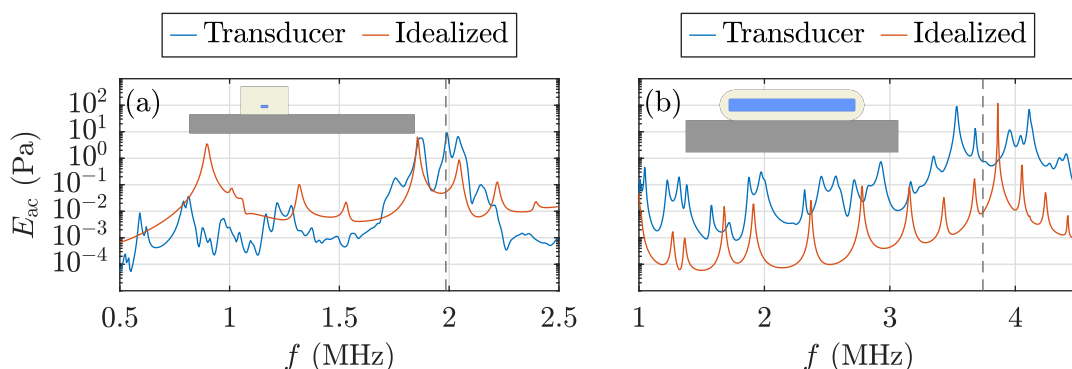
Figure 4.2: Idealized actuation versus transducer actuation for two classical acousto-fluidic devices. (a) Acoustic energy density spectrum $E_{ac}(f)$ for a glass-based acousto-fluidic device using an idealized actuation versus the coupled transducer actuation. (b) Similar to (a) but for a glass-based capillary trapping device. The ideal half-wave resonance frequencies are indicated as dashed vertical lines at $f_{\lambda/2} = 1.99$ MHz for the device shown in (a) and 3.74 MHz for the device shown in (b). The model geometries are shown as inserts in each figure.

This procedure is conducted for both the acoustophoresis device and the capillary trapping device. The results are illustrated in Fig. 4.3(a)-(b). In both cases, the plot shows how $E_{ac}(f)$ gradually degrades as the microfluidic chip material approaches the polymer PMMA. For the acoustophoresis device design, Fig. 4.3(a), there are three major resonances in the case of $s = 1$ (glass); these frequencies are shifted towards lower frequencies as $s \rightarrow 0$ (PMMA) and are almost completely degraded in terms of the acoustic energy density. In the case of the capillary-tube device, there are two major resonances, these are also completely degraded as $s \rightarrow 0$, but the resonance frequencies remain almost constant while varying the microfluidic chip material.

To evaluate the acoustofluidic performance, the figure of merit $\mathcal{F}(f)$ is also evaluated while sweeping s. The figure of merit $\mathcal{F}(f)$ is a measure of how efficient the particles are focused and was first introduced in Ref. [20] and slightly modified here

$$\mathcal{F}_y = \frac{\int \text{sgn}(-y) F_{\text{rad},y}\, dV}{\int |F_{\text{rad},z}|\, dV} E_{ac} \quad \text{and} \quad \mathcal{F}_z = \frac{\int \text{sgn}(-z) F_{\text{rad},z}\, dV}{\int |F_{\text{rad},y}|\, dV} E_{ac}, \tag{4.4a}$$

where $\text{sgn}(y)$ extracts the sign of y. The figure of merit $\mathcal{F}_y$ is suited for acoustophoresis applications in which particles are focused toward the vertical channel-center line at $y = 0$.
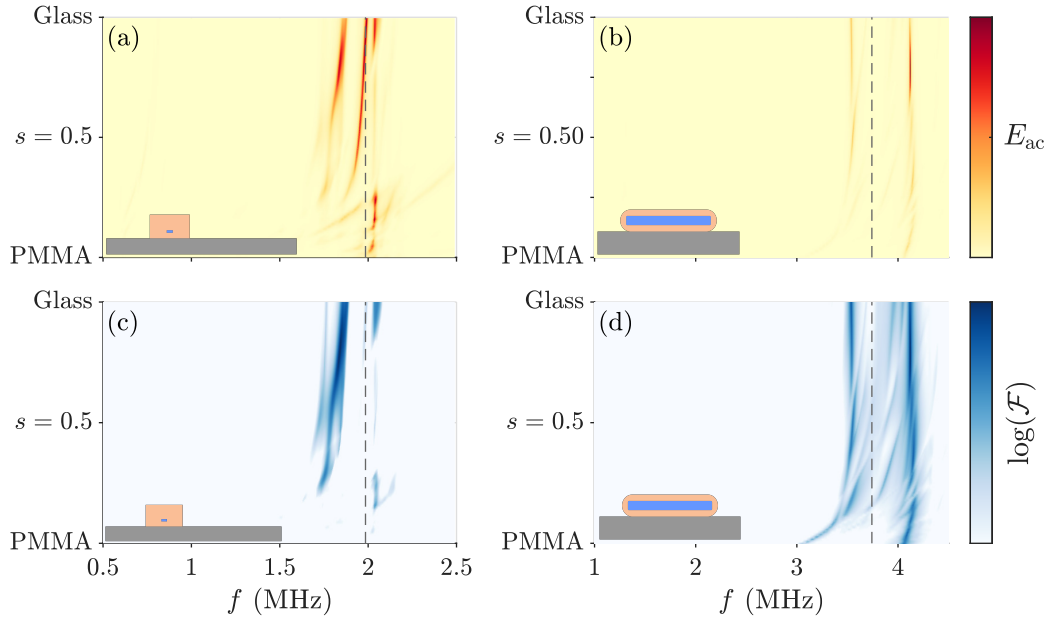
Figure 4.3: Surface plot of the simulated acoustic energy density spectrum $E_{ac}(f)$ as a function of microfluidic chip material varying linearly between PMMA ($s = 0$) and glass ($s = 1$) for two classical acoustofluidic devices: An acoustophoresis device in (a) and an acoustofluidic capillary trap in (b). (c) and (d) are similar to (a) and (b), but instead of $E_{ac}(f)$, the figure of merit spectrum $\mathcal{F}(f)$ is plotted on a logarithmic scale. The ideal hard-wall half-wave resonance frequencies $f_{\lambda/2} = 1.99$ MHz, and 3.74 MHz are indicated as vertical lines in each plot. The 2D model geometries are shown as inserts in each plot.

Similarly, for the capillary device, the merit $\mathcal{F}_z$ is large when the radiation force is uniform and points toward the horizontal pressure node at channel mid-height $z = 0$. These measures can be modified to suit the desired acoustic radiation force field.

In Fig. 4.3(c)-(d) the figure of merit spectrum $\mathcal{F}(f)$ is plotted as s is varied. This plot illustrates how the acoustofluidic performance is affected when transitioning into a polymer-based device. The picture is the same; the acoustophoresis performance is degrading as $s \to 0$. However, the performance in the capillary-based device seems robust to the material transition compared to the acoustophoresis device.

Section summary: It is evident that one cannot just replace a glass or silicon-based microfluidic chip with a polymer and expect it to work. For polymers, the hard-wall resonance condition is no longer a good approximation since the acoustic impedances are comparable, and the lower sound speed in polymers complicates the system resonances. As seen in Fig. 4.3, the effect is most pronounced in the acoustophoresis device; here, the resonance frequencies are shifted, and the acoustic response is completely degraded for $s = 0$ (PMMA). For the capillary device, the picture is different. In Fig. 4.3(b), the acoustic response is also degrading as $s \to 0$, but the resonance frequencies are almost constant as s is varied. From these results, we can conclude that acoustic resonances parallel to the primary thickness mode of the transducer (layered resonators) are more robust compared to the perpendicular case (transverse resonators).

To compete with classical glass/silicon-based devices, the polymer-based needs design optimization. In virtue of the WSUR concept, the system components must be well-characterized and considered in the model, including not only the transducer but also the glue and the microfluidic chip. If we want to understand and model polymer-based acoustofluidic devices, we simply need a complete and well-characterized model of the acoustofluidic device without idealized boundary conditions for the actuation. The characterization of each device component will follow in the next chapter.

4.2   Microparticle acoustophoresis in a polymer-based acoustofluidic device

This section provides a summary and discussion of Paper I [1] including the main results and the faced challenges doing this study. The paper is included in Chapter 6 in its original form, in agreement with the co-authors.

This study was our first attempt to model a polymer-based acoustofluidic device. The model included an aluminum-based microfluidic chip that was sealed with a PDMS cover and glued onto a piezoceramic Pz26 transducer. Two devices were studied. The first device consisted of an aluminum-based microfluidic chip fabricated using micro-milling. The channel was sealed using a PDMS cover, and the transducer was mounted on the side. The second device was similar, but instead of mounting the transducer on the side, a split-electrode transducer with anti-symmetric bias was mounted on the bottom for enhanced coupling of anti-symmetric modes. The two devices are sketched in Fig. 4.4. A similar device was studied by Gautam et al. [28] for simple and inexpensive acoustophoresis, achieved by simple fabrication techniques and low-cost materials. In Paper I [1], we used a similar approach to fabricate the devices. We extended the work by Gautam et al. [28] as we varied the particle diameters ranging between 1 and 4.8 µm, thereby probing the acoustic streaming. Furthermore, we studied a similar device having a split-electrode transducer for enhanced coupling. Numerical simulations supported the experiments to gain insight into the device dynamics.

The particle velocity field was analyzed in both devices by experimental and simulated particle tracking of polystyrene particles with diameters 1, 2, and 4.8 µm. The measured and simulated particle velocity fields are shown in Fig. 4.5 for the two devices at resonance. The resonance frequencies were located at $f = 2.048\,\mathrm{MHz}$ for the side-mounted transducer and $f = 2.095\,\mathrm{MHz}$ for the split-electrode transducer, both very different from the ideal half-wave resonance frequency $f_{\lambda/2} = 1.7\,\mathrm{MHz}$. For the smallest particles, the acoustic
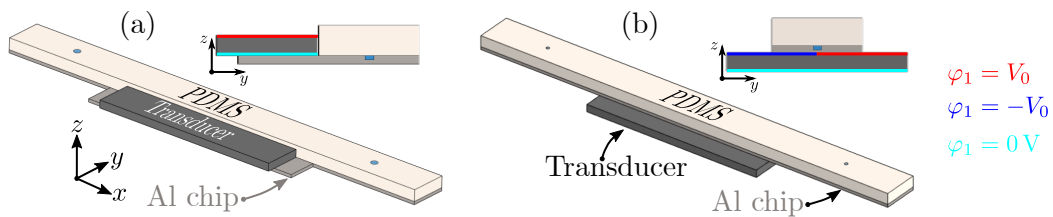
Figure 4.4: Sketch of the devices studied in Paper I [1]. (a) A PDMS-covered aluminum-based microfluidic chip with a Pz26 transducer mounted on the side. A 2D cross-sectional view is shown together with the electrode bias: grounded (cyan) and biased (red). (b) Similar to (a) but with a transducer mounted beneath the channel with a split-electrode design. The cross-sections comprising the model geometries are shown in both (a) and (b). The figures are modified and adapted from Paper I [1].
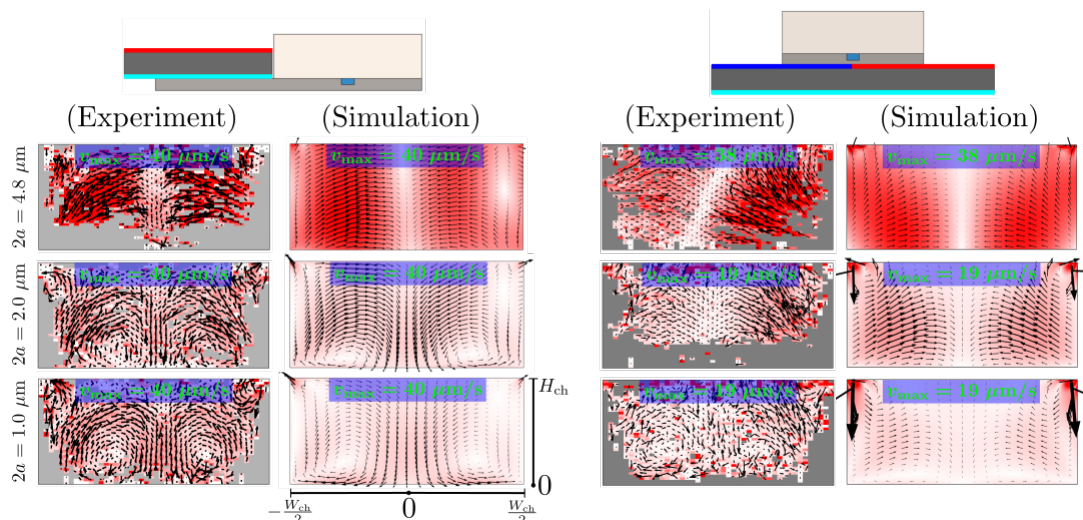
Figure 4.5: Left panel: Simulated and measured particle velocity fields for the side-actuated aluminum-based device with a PDMS cover. The simulated and measured particle velocity fields were evaluated for polystyrene particles with diameters 1, 2, and 4.8 µm. The particle velocity fields are illustrated as surface and vector plots where each row corresponds to a certain particle diameter in descending order. The transducers were actuated at 20 V peak-to-peak, and the particle velocity magnitude ranges from 0 µm/s (light) to v_{max} (red), ranging between 19 and 40 µm/s as indicated in each figure. The channel width and height are respectively $W_{\mathrm{ch}} = 440$ µm and $H_{\mathrm{ch}} = 200$ µm. The right panel is similar to the left panel but for the anti-symmetrically actuated device, achieved by a split-electrode transducer with anti-symmetric bias. The figures are modified and adapted from Paper I [1].

streaming dominated the particle velocity field resulting in two large rolls and two small rolls near the soft lid. For the largest particles, the acoustic radiation force dominated the velocity field, exhibiting focusing toward the center and the soft PDMS cover.

For soft walls where the stress exerted on the fluid is vanishing, the acoustic streaming boundary condition Eq. (2.38) reduces to a Stokes drift $\boldsymbol{v}_2^d = \left\langle (\boldsymbol{u}_1 \cdot \boldsymbol{\nabla}) \, \boldsymbol{v}_1^d \right\rangle$, since the zero stress implies $\boldsymbol{v}_1^\delta = \boldsymbol{0}$ on this interface. The generated streaming in devices with soft walls fundamentally differs from streaming induced by a standing pressure wave in fluids surrounded by hard walls, where the acoustic streaming is primarily dictated by the tangential velocity gradients. Since the bottom wall is hard and the top wall is soft, the acoustic streaming is a mix of the two mentioned situations. This led to a numerical study where the aluminum chip was sealed at both top and bottom with PDMS covers. The acoustic response was optimized numerically by manually tuning the top and bottom cover film thicknesses. The microfluidic chip was actuated by a split-electrode design for enhanced coupling of anti-symmetric resonances. The device and the simulated particle trajectories are shown in Fig. 4.6. With this soft-walled design, the acoustic streaming was suppressed,
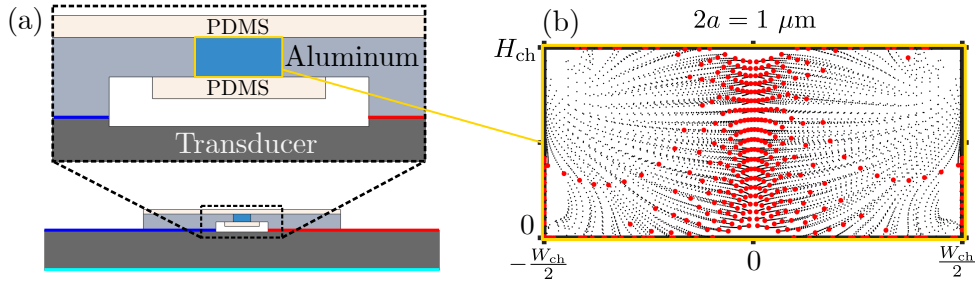
Figure 4.6: (a) Cross-sectional view of a double-sided PDMS-covered aluminum-based device design for sub-micron acoustophoresis. (b) Simulated 1-µm-diameter-polystyrene particle trajectories. The channel dimensions are $W_{ch} = 440\,\mu m$ and $H_{ch} = 200\,\mu m$, identical to the device in Fig. 4.5. The figures are modified and adapted from Paper I [1].

and the resulting simulated particle velocity field for 1-µm-diameter polystyrene particles mimicked the classical acoustophoresis focusing towards the vertical pressure node. However, due to the vanishing stress near the top and bottom, some particles migrated to the top and bottom interfaces.

Section summary: Even though our model included the piezoelectric transducer, the aluminum-based chip, and the PDMS sealing, the predicted numerical resonance frequencies were off by 2-12% and 30-50% for the particle velocity magnitudes. Retrospectively, the model was inaccurate and incomplete due to the poorly characterized and missing material parameters. The microfluidic chip was glued onto the transducer using superglue and neglected in the model due to insufficient and missing material parameters. The PDMS and the aluminum parameters were rather well-characterized. However, the piezoelectric parameters provided by the manufacturer were simply not well-characterized, causing inaccurate modeling, as will be discussed and investigated in the proceeding chapter. The uncertainties in the model parameters were too many, and from this point on, our pursuit of a complete model with well-characterized material parameters began. The following chapter will be dedicated to material parameter determination and component characterization for acoustofluidic application.

Analytical solution to the acoustic pressure field in a soft-wall system

As a bonus to Paper I [1], I present an analytical solution to the acoustic pressure field p_1 in an idealized 2D soft-wall system. The system resembles the PDMS-covered aluminum-based acoustofluidic channel cross-section, and the walls are represented by either soft or hard-wall boundary conditions. The solution provides insight into the particle velocity field and the shift in resonance frequency, both different from classical hard-walled acoustophoresis devices.

Consider a rectangular fluid channel of width W_{ch} and height H_{ch} centered at Origo in the yz plane. The channel is uniformly actuated on the side-walls at $y = \pm W_{\text{ch}}/2$ with a constant velocity magnitude $\text{Re}\left(v_0 e^{-i\omega t}\right) \boldsymbol{e}_y$ in the y direction. The bottom wall at $z = -H_{\text{ch}}/2$ is stationary, and the top wall at $z = H_{\text{ch}}/2$ is free. The corresponding idealized boundary conditions are

$$\frac{-i}{\omega \rho_0} \partial_y p_1 = v_0, \quad \text{for} \quad y = \pm \frac{W_{\text{ch}}}{2}, \tag{4.5a}$$

$$\partial_z p_1 = 0, \quad \text{for} \quad z = -\frac{H_{\text{ch}}}{2}, \tag{4.5b}$$

$$p_1 = 0, \quad \text{for} \quad z = \frac{H_{\text{ch}}}{2}. \tag{4.5c}$$

The solution to the Helmholtz Eq. (2.10a) with $k_{\text{c}} \approx k_0$ is solved by separation of variables with the acoustic wavenumber $k_0^2 = k_y^2 + k_z^2$. In virtue of Eq. (4.5a), the acoustic pressure solution is anti-symmetric around $y = 0$ and the solution is of the form $p_1 = [c_1 \cos(k_z z) + c_2 \sin(k_z z)] \sin(k_y y)$. The relation

$$c_1 = -c_2 \tan\left(k_z \frac{H_{\text{ch}}}{2}\right) \quad \text{and} \quad c_2 = -c_1 \tan\left(k_z \frac{H_{\text{ch}}}{2}\right), \tag{4.6a}$$

between the constants c_1 and c_2 is determined by Eqs. (4.5b) and (4.5c), which is satisfied for $k_z = k_z^{(n)} = \frac{\pi}{2H_{\text{ch}}}(2n+1)$ yielding

$$p_1 = \sum_n^{\infty} c_n \left[\cos\left(k_z^{(n)} z\right) - (-1)^n \sin\left(k_z^{(n)} z\right)\right] \sin(k_y y). \tag{4.7}$$

The constants c_n are determined by Eq. (4.5a)

$$k_y \sum_n^{\infty} c_n \left[\cos\left(k_z^{(n)} z\right) - (-1)^n \sin\left(k_z^{(n)} z\right)\right] \cos\left(k_y \frac{W_{\text{ch}}}{2}\right) = i\omega \rho_0 v_0. \tag{4.8}$$

Multiplying both sides of Eq. (4.8) with $\left[\cos\left(k_z^{(m)} z\right) - (-1)^m \sin\left(k_z^{(m)} z\right)\right]$ followed by an integration in z from $-H_{\text{ch}}/2$ to $H_{\text{ch}}/2$ gives

$$c_{\tilde{n}} = i \frac{4 \sin\left(\frac{\pi}{4}\tilde{n}\right)}{\pi \tilde{n}} \frac{\omega \rho_0 v_0}{k_y \cos\left(k_y \frac{W_{\text{ch}}}{2}\right)}, \tag{4.9}$$

arriving at a final expression for the acoustic pressure field

$$p_1(y, z) = \sum_{\tilde{n}}^{\infty} i \frac{4 \sin\left(\frac{\pi}{4}\tilde{n}\right)}{\pi \tilde{n}} \frac{\omega \rho_0 v_0}{k_y \cos\left(k_y \frac{W_{\text{ch}}}{2}\right)}$$
$$\times \left[\cos\left(k_z^{(\tilde{n})} z\right) - i^{\tilde{n}-1} \sin\left(k_z^{(\tilde{n})} z\right)\right] \sin(k_y y), \tag{4.10}$$

where $\tilde{n}$ is an odd integer. Theoretically, the resonance frequencies are identified as minima in the denominator i.e. when $k_y = \frac{\pi}{W_{\text{ch}}}\tilde{m}$, where $\tilde{m}$ is an odd integer. The acoustic wavenumber k_0 at resonance becomes

$$k_0(\tilde{m}, \tilde{n}) = \sqrt{k_y^2 + k_z^2} = \sqrt{\left(\frac{\tilde{m}\pi}{W_{\text{ch}}}\right)^2 + \left(\frac{\tilde{n}\pi}{2H_{\text{ch}}}\right)^2} = \frac{\omega}{c_0} = \frac{2\pi f}{c_0}. \qquad (4.11)$$

Consider the lowest resonance frequency

$$f_{\text{res},0} = \sqrt{f_{\lambda/2}^2 + \left(\frac{c_0}{4H_{\text{ch}}}\right)^2}, \quad \text{for} \quad \tilde{n} = \tilde{m} = 1. \qquad (4.12)$$

Notice how the classical half-wave resonance frequency $f_{\lambda/2} = c_0/(2W_{\text{ch}})$ is shifted due to the appearance of a soft lid. For the channel dimensions $W_{\text{ch}} = 440\,\mu\text{m}$ and $H_{\text{ch}} = 200\,\mu\text{m}$ studied in Paper I [1], the analytical obtained resonance frequency Eq. (4.12) becomes $f_{\text{res},0} = 2.51\,\text{MHz}$, very different from $f_{\lambda/2} = 1.7\,\text{MHz}$ due to the low channel aspect ratio. For the two devices studied in Paper I [1] and sketched in Fig. 4.4, the experimental resonance frequencies were observed at 2.048 and 2.095 MHz respectively, different from the analytically obtained but both larger than $f_{\lambda/2} = 1.7\,\text{MHz}$. The analytical solution for the acoustic pressure field is plotted in Fig. 4.7 at $f_{\text{res},0} = 2.51\,\text{MHz}$ for an arbitrary velocity magnitude, together with the resulting acoustic radiation force vector field. The resulting acoustic radiation force field is very similar to the observed particle trajectories in Fig. 4.5 for the largest particle diameters. In this case, the acoustic radiation force dominates the particle velocity field, demonstrating particle motion toward the channel center and the soft PDMS cover.
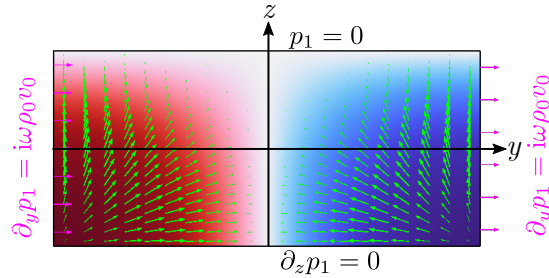
Figure 4.7: Analytical solution to the acoustic pressure field p_1 and the acoustic radiation force $\boldsymbol{F}_{\text{rad}}$ for a fluid-filled channel with oscillating side walls, a soft lid, and a fixed bottom wall. The channel dimensions are $W_{\text{ch}} = 440\,\mu\text{m}$ and $H_{\text{ch}} = 200\,\mu\text{m}$. The acoustic pressure field is plotted as a surface plot from minimum (blue) to maximum value (red) symmetric around zero (white) at $f_{\text{res},0} = 2.51\,\text{MHz}$. The acoustic radiation force $\boldsymbol{F}_{\text{rad}}$ is evaluated for 4.8-µm-diameter polystyrene particles. The $\boldsymbol{F}_{\text{rad}}$ is plotted as a vector plot (green arrows) with lengths proportional to the magnitude. The boundary conditions used in the analytical model are indicated on each boundary, and the side-wall actuation is indicated with magenta arrows.

Chapter 5

Characterization of acoustofluidic device components

In Section 4.1, the concept and challenges of polymer-based acoustofluidics were discussed and illustrated with model examples, motivating the need for well-characterized device components and well-determined material parameters for reliable modeling. This chapter presents an in-depth analysis and characterization of each device component for ultrasound acoustofluidic applications, including the piezoelectric transducer, the coupling layer, and the microfluidic chip, in combination, comprising an acoustofluidic device.

The content structure is similar to Paper III [3], in which the UEIS method was developed, providing an easy-to-execute method for determining complex-valued elastic moduli. The chapter will be divided into three sections: the first section is dedicated to the characterization of piezoelectric transducers involving electrical characterization and piezoceramic material determination. The material parameters are validated by laser-Doppler velocimetry, comparing simulated and measured displacement amplitudes at several frequencies.

The second section is dedicated to the transmission and coupling of acoustic waves through the coupling layer between the transducer and the microfluidic chip. This section includes a summary of the main results obtained in Paper II [2] and is followed by a material characterization of a UV-curable optical adhesive, in which the complex-valued elastic moduli are determined by the UEIS method.

In the third and final section, the UEIS method will be used to determine a polymer's complex-valued elastic moduli, which will be used to fabricate an all-polymer-based acoustofluidic device. The device consists of an all-polymer-based microfluidic chip coupled onto a disk-shaped transducer using the characterized adhesive. The acoustofluidic device will be characterized in terms of the acoustic response by measuring particle trajectories influenced by the acoustic forces. In this case, all the components are well-characterized in terms of material parameters enabling the construction of a complete

43

and well-characterized model of a polymer-based acoustofluidic device. The model is then used to simulate the acoustic response and particle trajectories, providing a one-to-one comparison between simulation and experiment.

5.1 Piezoceramic transducers for acoustofluidic applications

In BAW devices, sound waves are generated by an ultrasound transducer, typically a piezoceramic element with surface electrodes coupled to a function generator providing a sinusoidal electrical signal at MHz frequencies. In turn, the piezoelectric coupling yields a time-harmonic mechanical displacement field. Since the transducer is the driving mechanism in BAW acoustofluidic devices, any attempt to model a complete system accurately requires a well-characterized transducer, typically achieved by electrical characterization techniques.

A piezoceramic in itself is not piezoelectric, but the randomly oriented ceramic grain polarization can be permanently and uniformly oriented by applying a strong external electric field defining the polarization direction. The electric field is typically oriented in the thickness direction of the piezoceramic material, in this case, the z-direction. A commonly used transducer in BAW acoustofluidic applications is the piezoelectric Pz26 transducer [9, 27, 50, 52, 62, 64–67]. The Pz26 material is a lead-zirconate-titanate (PZT) based piezoceramic material offering high Curie temperature, high mechanical quality factor Q_m, low dielectric loss, and low aging rate, produced by the company Meggitt. In addition to the common Pz26, the less popular Pz27 piezoceramic will be considered, offering the same features as Pz26 except for a much lower mechanical quality factor. The piezoelectric performance can be evaluated in terms of different quantities, such as the mechanical quality factor Q_m, the dielectric loss factor $\tan(\delta_{33})$, the electromechanical coupling factors k_{pq}, the planar coupling factor k_p, and the thickness coupling factor k_t. The electromechanical coupling factor squared is the ratio between stored mechanical energy and electrical energy applied, where the subscript pq refers to the principle directions. The planar and thickness coupling factors refer to specific modes. These quantities are tabulated in Table 5.1 for a Pz26 and a Pz27 transducer. Even though the Pz26 has a much larger mechanical quality factor, the electromechanical coupling factors are comparable.

Often, the transducer thickness mode is matched to the hard-wall half-wave resonance frequency $f_{\lambda/2} = c_0/(2W_\mathrm{ch})$ for enhanced coupling and to achieve acoustofluidic devices with large quality factors, which makes the thickness coupling factor k_t the preferred measure when choosing between transducer materials. For the device geometries presented in Section 4.1, with primary channel dimensions $377\,\mu\mathrm{m}$ and $200\,\mu\mathrm{m}$, the corresponding $f_{\lambda/2}$ are approximately 2 and 4 MHz. The effective sound speed c_t in a piezoelectric material, given by

$$c_\mathrm{t} = \left(\frac{\epsilon'_{33}\rho_\mathrm{pzt}}{C'_{33}\epsilon'_{33} + (e'_{33})^2} \right)^{-1/2}, \tag{5.1}$$

can be used to match the transducer thickness $t = c_\mathrm{t}/(2f_{\lambda/2})$ for enhanced coupling.

Table 5.1: Piezoelectric properties of the Pz26 and the Pz27 piezoceramic. The listed properties include the mechanical quality factor Q_m, the dielectric loss factor $\tan(\delta_{33})$, the electromechanical coupling factors k_pq, and the effective sound speed c_t. The parameters are provided by Meggitt [68].

	Q_m (-)	$\tan\delta_{33}$ (-)	k_{31}^2 (-)	k_{33}^2 (-)	k_{15}^2 (-)	k_p^2 (-)	k_t^2 (-)	c_t (m/s)
Pz26	3333	0.003	0.107	0.467	0.306	0.325	0.221	4522
Pz27	74	0.017	0.107	0.488	0.371	0.348	0.221	4330

The effective sound speed c_t is obtained by considering a 1D model of a piezoceramic with $\boldsymbol{u}_1 = u_{1,z}(z)\boldsymbol{e}_z$, where the z-direction is oriented parallel to the polarization. The effective sound speed for the Pz26 and Pz27 materials are included in Table 5.1 and are almost equal in magnitude. The corresponding transducer thickness at 2 or 4 MHz is then ~ 1 and ~ 0.5 mm, respectively.

5.1.1 Electrical impedance characterization of piezoceramic transducers

The electrical impedance spectrum $Z(f)$ can be used to characterize and evaluate the piezoelectric transducer, for example, in terms of resonance frequencies, mechanical quality factors, and furthermore, to extract piezoceramic material parameters. Only disk-shaped transducers will be considered in this thesis since the geometry allows for axisymmetric modeling of the transducer reducing the degrees of freedom substantially. This reduction enables numerical sweeps, i.e., simulating electrical impedance spectra that would otherwise have been infeasible in the case of a three-dimensional model.

When measuring the electrical impedance spectrum $Z(f)$, the piezoelectric transducer was clamped between two spring-loaded pins, carrying the electrical signal, to minimize the contact force and meet the idealized axisymmetric modeling and boundary conditions of a free transducer. A photo of the experimental setup is shown in Fig. 5.1(a). The setup consists of a 3D-printed clamp in which the spring-loaded probes are fitted. Wires are soldered onto the pins and connected to an impedance analyzer, which is connected to a laptop through a USB connection—very simple and straightforward. The electrical impedance measurements were performed using a Vector Network Analyzer Bode 100 (OMICRON electronics GmbH, Klaus, Austria) in the frequency interval from 500 Hz to 5 MHz in steps of 0.5 kHz. The measurements were calibrated by open, short, and load impedance measurements. To investigate how the clamping affects the electrical impedance spectrum, the clamping position Δ, measured as the distance away from the rotational axis, was varied while measuring $|Z(f)|$ for a Pz27-TH0.5-OD10 transducer. The results are shown in Fig. 5.1(b), and it is seen how the electrical impedance spectrum is not affected by the clamping position. These results are used to verify the symmetry and zero-stress boundary condition of a free piezoelectric transducer used in the axisymmetric model.
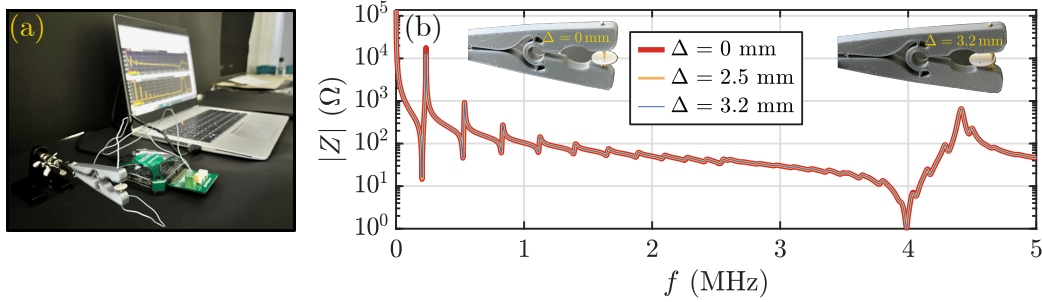
Figure 5.1: (a) Photo of the simple experimental setup for measuring the electrical impedance spectrum. The setup consists of a 3D-printed clamp in which spring-loaded probes are fitted and connected to an impedance analyzer. (b) Measured electrical impedance spectrum $|Z(f)|$ for a Pz27-TH0.5-OD10 transducer at various clamping positions Δ away from the rotational axis. Pictures of the measurements are shown for the two cases: the perfectly centered $\Delta = 0\,\text{mm}$ and the extreme off-centered $\Delta = 3.2\,\text{mm}$.

The electrical impedance spectrum is used to compare the Pz26 and Pz27 piezoceramic materials. The electrical impedance spectrum is measured for a disk-shaped Pz26 and a Pz27 transducer with nominal geometry. The nomenclature PzXY-TH0.5-OD10 will be used to distinguish transducers and as a shortened word for a disk-shaped PzXY transducer of thickness 0.5 mm and diameter 10 mm.

Due to the piezoelectric coupling, a local minimum in the electrical impedance magnitude spectrum $|Z(f)|$ corresponds to a mechanical resonance. Therefore, the representation of the complex-valued electrical impedance spectrum $Z(f)$ will solely be presented as the magnitude spectrum $|Z(f)|$ throughout this thesis. Furthermore, the magnitude $|Z(f)|$ will be plotted on a semi-logarithmic plot since $|Z(f)|$ can vary by six orders of magnitude when considering a broad frequency spectrum from 500 Hz to 5 MHz.

The measured spectrum for a Pz26-TH0.5-OD10 and a Pz27-TH0.5-OD10 transducer is plotted in Fig. 5.2, showing multiple local minima indicating several mechanical resonance frequencies. The first minimum corresponds to the first planar mode accompanied by planar harmonics, whereas the global minimum around 4 MHz corresponds to the primary thickness mode. For the Pz27-TH0.5-OD10 transducer, the planar harmonics are almost completely attenuated as the frequency is increased up to 3 MHz. In contrast, the Pz26-TH0.5-OD10 resonances are weakly attenuated and much more rippled around the thickness mode. Usually, the thickness resonance frequency is chosen to match the hard-wall resonance frequency in the fluid channel for enhanced coupling of modes. Due to the higher quality factor, the Pz26 transducer is much more peaked around its resonances, whereas the Pz27 spectrum is much smoother.
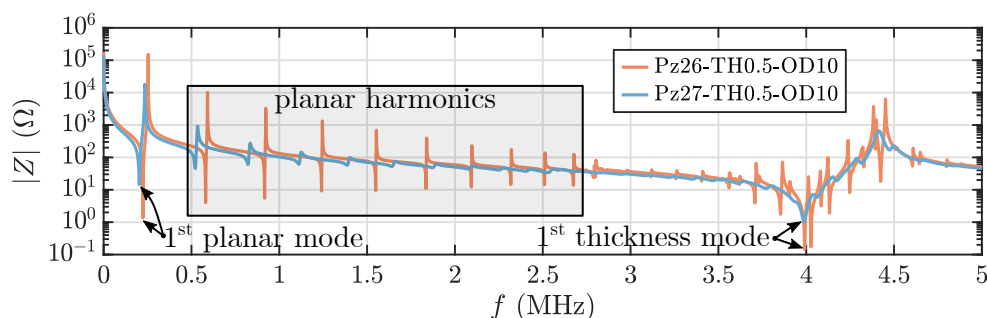
Figure 5.2: Measured electrical impedance spectra $|Z(f)|$ for a Pz26-TH0.5-OD10 and a Pz27-TH0.5-OD10 transducer, both disk-shaped and of nominal geometry. The planar modes are indicated together with the first thickness mode.

Reproducibility is a crucial feature for the commercialization and design optimization of acoustofluidic devices for biomedical platforms. Here the electrical impedance spectrum is used to evaluate the variations in transducer behavior with nominal dimensions. In Fig. 5.3(a) and (b), the impedance spectrum is plotted for three Pz26 transducers from the same batch and with nominal dimensions. Fig. 5.3(b) shows a zoom-in on the thickness resonance, and even though the Pz26 transducers are taken from the same batch, we see variations in features, magnitudes, and resonance frequencies. A similar plot is given in Fig. 5.3(c)-(d), but for the Pz27 material, this material shows much fewer in-batch variations; features, magnitudes, and resonance frequencies are almost identical, however slightly shifted presumably due to small variations in the thicknesses. So even though Meggitt promises low batch-to-batch variations, we see in-batch variations, especially for the Pz26 transducers around the primary thickness mode.
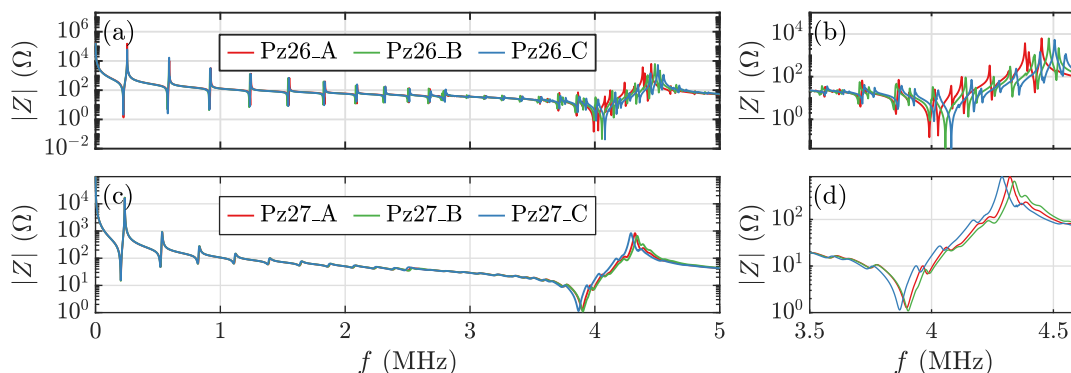
Figure 5.3: Measured electrical impedance spectra $|Z(f)|$ for six disk-shaped transducers of nominal dimensions but different materials. The three Pz26-TH0.5-OD10 spectra are plotted in (a), and a zoom-in near the thickness mode is given in (b). The transducers are taken from the same batch indicated with suffixes A, B, and C. Figure (c) and (d) is similar to (a) and (b) but for three Pz27-TH0.5-OD10 transducers.

5.1.2 UEIS-determined piezoelectric material parameters

Modeling a piezoceramic transducer belonging to the ∞mm symmetry class, which is the case for both Pz26 and Pz27, requires the knowledge of the ten complex-valued material parameters contained in Eq. (2.34). There exist standardized methods for the determination of piezoceramic parameters [69, 70]. The basic principle behind the methods is to decouple and identify fundamental modes and their resonance frequencies using specific transducer geometries with certain aspect ratios, including disks, bars, and cylinders. Again, the resonance frequencies are identified as minima in the electrical impedance spectrum. One example is the determination of the stiffness component C_{13}; according to the CENELEC standard [70], a disk-shaped transducer with an aspect ratio of at least ten is needed to decouple and separate the thickness mode from other modes. As shown in the textbook [71] (p. 128-137), this requirement is not good enough; for a complete separation of modes, the aspect ratio should be at least 50. Furthermore, determining certain parameters within the CENELEC method requires the knowledge and input of other parameters, which means that errors contained in those will propagate into other parameters, effectively providing an inaccurate set of parameters. So the standardized methods are flawed by insufficient geometry requirements and propagating errors. Here, an alternative method is used, namely the ultrasound-electrical-impedance-spectrum (UEIS) method, which only requires a single disk-shaped transducer. The method was developed in Paper III [3] and supplements dynamic techniques for material characterization, involving resonant ultrasound spectroscopy [72], transmission techniques [59, 73], impulse excitation [74], laser velocimetry, and triangulation [36, 75]. The UEIS method will be summarized in this and the following section. For further details, see Paper III [3] enclosed in Chapter 6.

The UEIS method uses the optimization algorithm `fminsearchbnd` to match the simulated electrical impedance spectrum $Z_{\mathrm{sim}}(f)$ with the measured $Z_{\mathrm{exp}}(f)$. The `fminsearchbnd` algorithm is a bounded version of the Nelder–Mead algorithm described in Chapter C. The matching is obtained by varying the piezoceramic material parameters $\mathcal{P}_i$ in the simulation, including the five complex-valued stiffness components $\boldsymbol{C} = \boldsymbol{C}' + \mathrm{i}\boldsymbol{C}''$, the three real-valued piezoelectric coupling components $\boldsymbol{e} = \boldsymbol{e}'$, and the two complex-valued dielectric components $\boldsymbol{\epsilon} = \boldsymbol{\epsilon}' + \mathrm{i}\boldsymbol{\epsilon}''$, in total 17 independent parameters plus the mass density.

The optimization algorithm requires three choices, (i) initial values $\mathcal{P}_i^0$ for the optimization parameters $\mathcal{P}_i$, (ii) upper and lower bounds for $\mathcal{P}_i$, and (iii) a cost function $\mathcal{C}$ to minimize by varying the parameters contained in $\mathcal{P}_i$. Even though the standardized methods can be flawed, the obtained set of parameters can be used as initial values to the UEIS method in combination with values in the literature. The bounds are chosen to be $\pm 30\%$ from the initial values, and the cost function $\mathcal{C}$ is given as

$$\mathcal{C} = \sqrt{\sum_i \left[\log_{10}\left(|Z_{\mathrm{exp}}(f_i)|\right) - \log_{10}\left(|Z_{\mathrm{sim}}(f_i)|\right)\right]^2}, \qquad (5.2)$$

corresponding to the L_2-norm of the logarithmic difference between measured $|Z_{\mathrm{exp}}(f_i)|$

and simulated $|Z_{\mathrm{sim}}(f_i)|$ spectra. The logarithmic difference is used since the electrical impedance magnitude is peaked and varies by several orders of magnitude. The subscript i indicates a discrete set corresponding to the sampled frequencies in the measurements.

Furthermore, for each evaluation of the cost function $\mathcal{C}$, it is required that the dissipation is positive to check if the complex-valued parameters suggested by the algorithm are feasible. This condition is fulfilled when

$$\boldsymbol{K} = \mathrm{Im} \begin{pmatrix} -\boldsymbol{C} & \boldsymbol{e}^{\mathsf{T}} \\ \boldsymbol{e} & \boldsymbol{\epsilon} \end{pmatrix}, \tag{5.3}$$

is positive definite, and if not we set $\mathcal{C} = \infty$. The derivation of this constraint is presented in Chapter A.

Choosing a disk-shaped transducer for effective axisymmetric modeling, i.e., numerical speed, comes by the cost of low sensitivity to certain parameters including ϵ'_{11}, C''_{12}, C''_{13}, C''_{44}, and ϵ''_{33}. Therefore, the fitting procedure used in the UEIS method is divided into three subroutines where the parameters are grouped according to the relative sensitivity measure

$$\mathcal{S}(\mathcal{P}_i) = \mathcal{P}_i \frac{\partial \mathcal{C}}{\partial \mathcal{P}_i} \approx \frac{\mathcal{C}(1.1\mathcal{P}_i) - \mathcal{C}(0.9\mathcal{P}_i)}{1.1 - 0.9}, \quad \mathcal{P}_j = \mathcal{P}_j^0 \quad \text{for} \quad j \neq i. \tag{5.4}$$

Parameters are highly sensitive if $\mathcal{S}(\mathcal{P}_i) > 1$, medium sensitive if $0.1 < \mathcal{S}(\mathcal{P}_i) < 1$, and minor sensitive if $\mathcal{S}(\mathcal{P}_i) < 0.1$. The complex part of the dielectric parameter ϵ''_{33} was not included in the fitting procedure since $\mathcal{S}(\epsilon''_{33}) \approx 0$, other transducer geometries might give another picture in terms of the sensitivity measure. The UEIS method requires the geometry and the density to be well-characterized; an error in either will propagate into the UEIS-determined material parameters.

After measuring the electrical impedance spectrum, the measurements are loaded into the UEIS script, and after running the fitting procedure for approximately ten hours, the parameters are provided. In Fig. 5.4, the measured and simulated spectrum for a Pz26-TH0.5-OD10 and a Pz27-TH0.5-OD10 transducer is plotted when using the parameters provided by the manufacturer Meggitt and the fitted parameters obtained by the UEIS method. The parameters are provided in Tables B.1 and B.2 as an average computed from several UEIS fitting procedures.

From Fig. 5.4, it is evident that the material parameters provided by Meggitt, for both the materials, are insufficient for accurate modeling of the piezoelectric transducers. Therefore, combined with the low in-batch variation and the achieved numerical accuracy, we have chosen to continue our studies favoring the Pz27 transducer.
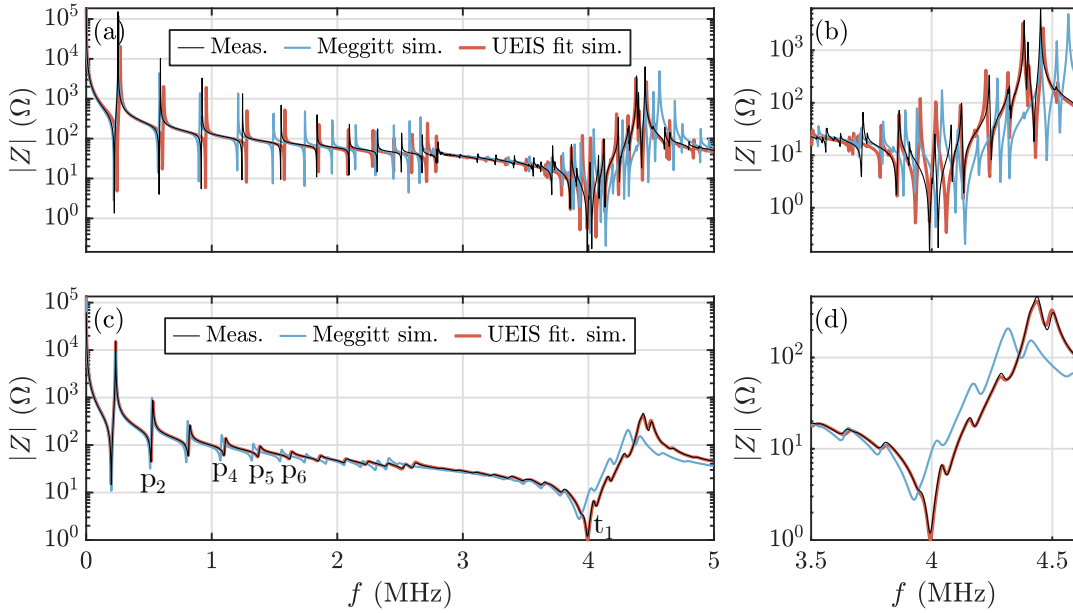
Figure 5.4: Comparison between measured and simulated electrical impedance spectrum $|Z(f)|$ given the parameters from the manufacturer Meggitt [68] (Meggitt sim.) and the UEIS-determined parameters (UEIS fit sim.), for a Pz26-TH0.5-OD10 transducer in panel (a) and (b) and a Pz27-TH0.5-OD10 transducer in panel (b) and (d). The modes used for the laser-Doppler velocimetry validation are indicated with a "p" or a "t" referring to planar or thickness and a subscript referring to the harmonic.

5.1.3   Validation by laser-Doppler velocimetry

The simulated impedance spectrum for the Pz27 transducer fits the measured, so the UEIS-fitted parameters provide an adequate estimate of the Pz27 material. To further support and validate the UEIS-determined Pz27 parameters, the simulated mechanical displacement field at resonance is compared to measurements obtained by a single-point laser-Doppler vibrometer system VibroFlex Connect (Polytec, Waldbronn, Germany), to which I had access to during my external research stay at the Department of Biomedical Engineering, Lund Univerity. The LDV technique utilizes the Doppler frequency shift caused by a wave reflected by a vibrating surface. The velocity of the vibrating surface can be inferred from the frequency shift at a known wavelength obtained by laser interferometers. The LDV technique can be used to measure surface vibrations down to picometer displacement amplitudes.

The single-point LDV system is used to measure point vibrations. However, by mounting the sample on a motorized stage, the mechanical displacement field can be spatially resolved. Furthermore, by probing the current, the phase can be extracted from the electrical signal providing temporal resolution.

The mechanical displacement field $\tilde{u}_{1,z}(x, y, t)$ normal to the electrode surface of a Pz27-TH0.5-OD10 transducer was measured at chosen frequencies. The chosen frequencies corresponded to certain resonances as indicated by "$p_{2,4,5,6}$" or "t_1" in Fig. 5.4 referring to the planar harmonic or the primary thickness mode, with an applied peak-to-peak voltage of $V_{pp} = 2\,\text{V}$. For each of those frequencies, the simulated and measured normal displacement amplitude $|u_{1,z}|$ is compared in Fig. 5.5. At each frequency, the measured and simulated displacement amplitude $|u_{1,z}|$ is plotted on the same scale, in which the simulated amplitudes deviate between 3% and 10% from the measured. With the UEIS-fitted Pz27 parameters, not only the features but also the magnitude is captured within 10% in the simulated modes. Furthermore, the time evolution for the fifth planar mode at $f_{p_5} = 1.370\,\text{MHz}$ is compared in Fig. 5.6, where the simulated and measured $\tilde{u}_{1,z}(x, y, t)$ is plotted, respectively. By opening this document using *Adobe Reader*, Fig. 5.6 can be watched as an animation, showing the time-harmonic vibration of the measured and simulated $\tilde{u}_{1,z}(x, y, t)$ undergoing a full cycle. This validation provided confidence in the UEIS method for piezoceramic material determination. It also paved the way and led to the extended UEIS procedure in which the electrical impedance spectrum of a loaded and already-characterized transducer is used to determine the elastic moduli of the loaded material.
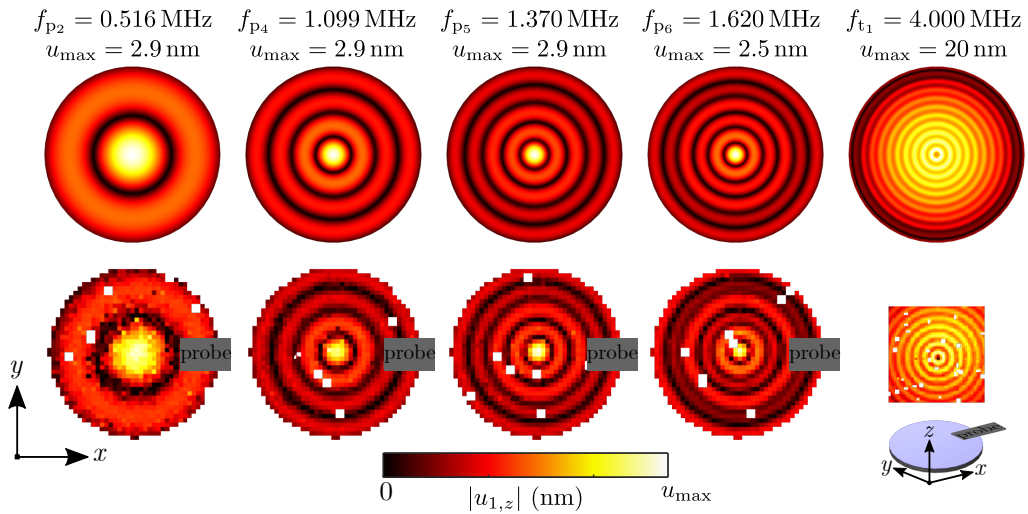
Figure 5.5: Simulated (top-row) and measured (bottom-row) normal displacement amplitude $|u_{1,z}(x, y)|$ for a Pz27-TH0.5-OD10 transducer actuated at different frequencies (columns) with an applied peak-to-peak voltage of $V_{pp} = 2\,\text{V}$. The displacement amplitude $|u_{1,z}|$ range from 0 to max u_{max} depending on the frequency and indicated for each column. The first four modes corresponds to the planar harmonics p_2, p_4, p_5, and p_6. The last column corresponds to the primary thickness mode t_1 as indicated in Fig. 5.4(c). The displacement amplitude was measured on the top electrode surface as indicated with a blue selection in the lower right corner. The electrode probe was shadowing the laser marked as a gray region.

(a) Simulated (b) Measured
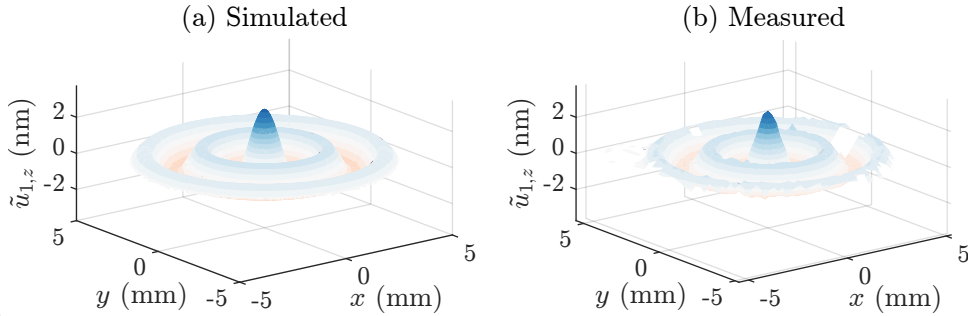
Figure 5.6: Simulated and measured normal displacement field $\tilde{u}_{1,z}(x,y,t)$ for a Pz27-TH0.5-OD10 piezoceramic transducer actuated with a peak-to-peak amplitude of $V_{\mathrm{pp}} = 2\,\mathrm{V}$ at $f_{\mathrm{p}_5} = 1.370\,\mathrm{MHz}$ corresponding to the fifth planar harmonic. The displacement field was measured on the electrode surface. The figure can be watched as an animation showing the time-harmonic displacement field undergoing a full cycle. This requires the document to be opened with *Adobe Reader*. The static figure shows $\tilde{u}_{1,z}(x,y,t)$ at the phase with maximum amplitude.

5.2 Characterization of coupling layers for acoustofluidic applications

This section is dedicated to the coupling layer between the transducer and the microfluidic chip for acoustofluidic applications. The section is divided into two parts; in the first section, the results obtained in Paper II [2] will be summarized, including a structural analysis of coupling layers between the transducer and microfluidic chip for acoustofluidic applications. This is followed by a section in which the UEIS method is used to determine the elastic moduli of a UV-curable optical adhesive.

5.2.1 Structural analysis of coupling layers

In Paper II [2], the structural influence of the coupling layer between the transducer and the microfluidic chip for acoustofluidic applications was studied by numerical modeling. The model includes a water-filled microfluidic chip coupled onto a piezoelectric transducer, including the coupling layer in-between. By numerical simulations, we studied how the coupling layer influences the acoustic response for two classical and widely used acoustofluidic device designs, similar to those considered in Section 4.1 and sketched in Fig. 4.1. Two coupling layer materials were considered for both devices; a solid epoxy glue and a viscous glycerol layer.

Coupling layers in layered resonators

The first device considered in Paper II [2] was the layered glass-based capillary tube coupled onto a small transducer as sketched in Fig. 4.1(b). This type of acoustofluidic device

was studied in Refs. [7, 60–62, 76] for local and in-plane acoustic trapping of particles. The model used to study the coupling layers for layered resonators was three-dimensional and included the transducer, the water-filled glass capillary, and the coupling layer resembling the entire acoustofluidic device shown in Fig. 4.1(b). The model extends the 1D modeling of layered acoustic resonators in Refs. [32, 33].

In the simplest case, a layered resonator consists of five layers, the transducer, the coupling layer, the matching layer, the fluid layer, and the reflector layer. In this case, the coupling layer directly influences the acoustic response since the combined layer dynamics is what gives the acoustic response. Therefore, in an ideal layered resonator, the thickness of each domain should be carefully chosen to match the desired motion inside the fluid layer. Take, for example, the case of the glass-based capillary-tube trap in which a resonating standing acoustic pressure half-wave, parallel to the transducer actuation, is utilized to focus particles toward the horizontal pressure node located at the channel mid-height. Ideally, the half-wave resonance in the fluid should be matched to the half-wave thickness mode in the piezoelectric transducer, which in turn gives the coupling, matching, and reflector layer thicknesses. According to this 1D-layer principle, the layer thicknesses should correspond to half a wavelength in the transducer and the fluid layer, a quarter wavelength in the reflector layer, and in combination, the coupling and the matching layer should correspond to a quarter wavelength, see for example Ref. [77].

When the layer thicknesses deviate from the ideal 1D principle, as is the case for the glass-based capillary-tube trapping device studied in Refs. [7, 60–62, 76], the required symmetry for the standing half-wave pressure resonance is broken. In this case, the acoustic pressure resonances are asymmetric, and instead of the ideal anti-symmetric half-wave resonance frequency, two asymmetric resonance frequencies appear as observed in Paper II [2] and also in Fig. 4.3(b). In this case, an increased coupling layer thickness will either result in a sustained or attenuated coupling according to the simple phase criterion

$$\text{sustained coupling if} \quad \Phi_{\text{crit}} > \pi, \tag{5.5a}$$

$$\text{attenuated coupling if} \quad \Phi_{\text{crit}} < \pi, \tag{5.5b}$$

where Φ_{crit} is given by the sum of phases in the layers below the fluid layer

$$\Phi_{\text{crit}} = \sum_i \frac{\omega}{c_{\text{lo}}^{(i)}} H_i, \quad \text{for} \quad i = \text{transducer, matching.} \tag{5.6}$$

The criterion is only valid for $\Phi_{\text{crit}} < \frac{3\pi}{2}$. In Paper II [2], the criterion in Eq. (5.5) was accompanied with the coupling-layer attenuation length scale

$$\Delta_0 = \frac{Z_{\text{cl,ml}} c_{\text{lo}}^{(\text{cl})}}{2\omega_{\text{res}}} \cot\left(\frac{\omega_{\text{res}} H_{\text{ml}}}{c_{\text{lo}}^{(\text{ml})}}\right), \quad \text{where} \quad Z_{\text{cl,ml}} = \frac{\rho^{(\text{cl})} c_{\text{lo}}^{(\text{cl})}}{\rho^{(\text{ml})} c_{\text{lo}}^{(\text{ml})}}, \tag{5.7}$$

at which the resonance is attenuated. The length scale Δ_0 is a function of the angular frequency at resonance ω_{res}, the matching layer thickness H_{ml}, the acoustic contrast between

coupling and matching layer $Z_{\mathrm{cl,ml}}$, and the longitudinal sound speeds in the coupling $c_{\mathrm{lo}}^{(\mathrm{cl})}$ and the matching layer $c_{\mathrm{lo}}^{(\mathrm{ml})}$. The expression in Eq. (5.7) was derived in the limit of thin coupling layers $H_{\mathrm{cl}} \ll \frac{c_{\mathrm{lo}}^{(\mathrm{cl})}}{\omega_{\mathrm{res}}}$. Furthermore, the matching and reflector layer is assumed to be of the same thickness and material.

Together with the criterion in Eq. (5.5), the expression in Eq. (5.7) can be used to design robust layered devices avoiding attenuation caused by the coupling layer thickness and choice of material. Notice how Δ_0 is directly proportional to the acoustic impedance in the coupling layer, signifying that acoustically hard coupling-layer materials are preferred for robust devices.

Coupling layers in transverse resonators

For the classical acoustophoresis device shown in Fig. 4.1(a), the resonance is generated perpendicular to the primary thickness-mode-actuation direction, and the device is said to be a transverse resonator. Opposite to the layered resonator, these devices rely on horizontal half-wave pressure resonances, ideal for fluid-particle separation in continuous flow and lab-on-chip integration. Typically, the transverse resonator is designed according to the hard-wall resonator principle, where the resonance frequency can be approximated by the channel dimensions. Similar design principles, as for the layered resonator, can be used to match the motion by specific chip and channel dimensions for enhanced coupling, again see Ref. [77]. However, 1D design principles are less useful in this case since two-dimensional modes predominantly generate and drive the transverse resonances.

Since the transverse resonator relies on an anti-symmetric half-wave pressure resonance, the symmetric thickness mode of the transducer driving the resonance must be broken. Usually achieved either by off-centering the transducer as in Ref. [50], but can also be achieved by skew channel dimensions or by a split-electrode design as in Ref. [1, 31]. For transverse resonators, the coupling layer serves as a transmission layer. In the first case, where the symmetry breaking is achieved by off-centering the transducer, the transmission of shear waves is wanted for enhanced driving of the half-wave resonance in the fluid. Again, two coupling layers were included in the simulation of the acoustophoresis device: a solid epoxy and a viscous glycerol layer. Since a fluid cannot sustain a shear wave, the glycerol coupling layer will cause an insufficient coupling for transverse resonators. In Paper II [2], the model results showed that in transverse resonators, the resonance was attenuated at a very thin coupling-layer thickness around 100 nm for a glycerol coupling layer. In contrast, the solid epoxy coupling layer provides a sustained coupling for coupling-layer thicknesses below 20 μm.

The coupling layer influences the resulting acoustic response for both layered and transverse resonators. The layered resonator can sustain a solid epoxy and a viscous glycerol coupling layer. However, as the coupling layer thickness increases, the resonance will either sustain or attenuate according to Eq. (5.5). This attenuation happens on a length scale

that depends on the resonance frequency, the matching layer thickness, and the coupling and matching layer material parameters. Transverse resonators are very sensitive to fluid coupling layers since the resonance requires the transmission of transverse waves for strong coupling, and in this case, solid coupling layers are preferred.

For both devices, the microfluidic chip material was either glass or silicon/glass. Turning to polymer-based acoustofluidics only complicates the system resonances due to the lower sound speeds compared to glass and silicon. The glue layer must be well-characterized and considered for a complete and accurate model. The following section will be dedicated to the material characterization of glues and polymers using the UEIS method, enabling accurate modeling of polymer-based acoustofluidic devices.

5.2.2 UEIS-determined elastic moduli of a UV-curable adhesive

In Section 5.1.2, the Pz26 and Pz27 piezoceramic material parameters were fitted by matching the simulated electrical impedance spectrum to the measured. This procedure was only the first out of two steps in the complete UEIS method developed in Paper III [3]. The first step involving piezoceramic material determination by numerical fitting procedures is, to a large extent, similar to the procedures in Refs. [35, 37, 38, 78]. In the second step, the characterized transducer is loaded by gluing on a ring-shaped material. Then, the resulting electrical impedance spectrum is matched to the simulated by varying the loaded material parameters while keeping the UEIS-fitted piezoelectric parameters fixed.

The two-step procedure, including the determination of the complex-valued elastic moduli of the loaded material, makes the UEIS method new and different from the procedures studied in Refs. [35, 37, 38, 78].

The second step starts by co-axially gluing an isotropic ring-shaped material onto the already-characterized disk-shaped transducer, as sketched in Fig. 5.7. The ring-shaped loading allows accessibility to the electrodes. Furthermore, the ring-shaped loading allows the model geometry to be reduced to a two-dimensional axisymmetric model domain for numerical efficiency and speed. Similar to the first step, the simulated electrical impedance spectrum is matched to the measured by varying the material parameters used in the simulation. The measured electrical impedance spectrum is obtained by clamping the transducer in-between two point contacts as shown in Fig. 5.7(c). The experimental setup is very simple and consists of a 3D-printed sample holder, in which the sample is clamped between two spring-loaded contacts. The contacts are connected to an impedance analyzer driven by a laptop. A photo of the setup is shown in Fig. 5.7(d).

In the second step, the UEIS-fitted piezoceramic material parameters are fixed in the simulation. The optimization algorithm only varies the loaded material parameters, including the two complex-valued stiffness components C_{11} and C_{44}. The fitting procedure is similar to the one used for the piezoceramic characterization; initial values are provided for C_{11} and C_{44} using an average of literature values or values provided by the supplier,
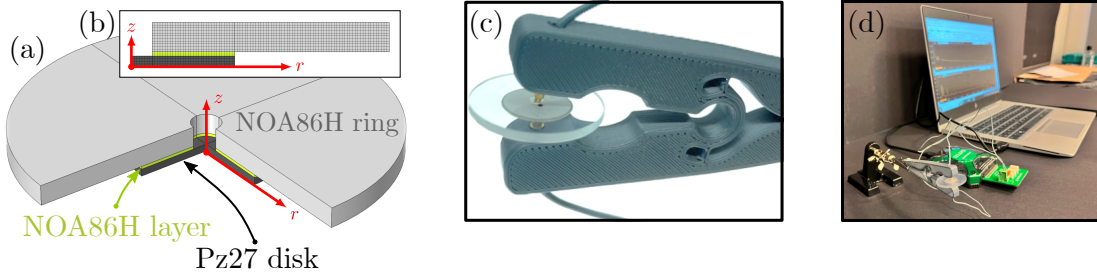
Figure 5.7: (a) System sketch showing the NOA86H ring glued onto a disk-shaped Pz27 transducer. A quarter of the geometry is left out to show the different layers. (b) Axisymmetric model geometry in the rz plane, including a structured mesh. (c) Experimental sample holder for electrical impedance measurements. (d) Photo of the experimental setup, including the 3D-printed sample holder and the impedance analyzer connected to a laptop. The figures are modified and adapted from Paper III [3].

the bounds are set to $\pm 40\%$ relative to the initial values, and the cost function $\mathcal{C}$ defined in Eq. (5.2) is minimized by the optimization algorithm. For each cost function evaluation, it is checked if

$$\boldsymbol{K}_{\mathrm{iso}} = \mathrm{Im}\left(-\boldsymbol{C}\right) = -\boldsymbol{C}'', \tag{5.8}$$

is positive definite. The check is similar to Eq. (5.3) and provides a condition to check if the imaginary parts are physically allowed for the dissipation not to be negative valued. This check is accompanied by the inequality $2C_{44}' \leq C_{11}'$ derived from Poisson's ratio ν being conditioned to $0 < \nu \leq 1/2$ for a linear isotropic material.

In this case, the UEIS method was used to determine the complex-valued elastic moduli of the UV-curable optical adhesive NOA86H provided by Norland Products Inc. This was achieved by casting the adhesive using a 3D-printed ring mold covered with a release agent followed by UV-curing. Afterward, the NOA86H ring was released from the mold and glued onto an already-characterized Pz27 transducer using the same NOA86H adhesive. While curing the NOA86H ring onto the Pz27 transducer, the ring was co-axially held in place using a 3D-printed mount. Then, before gluing together the components, the ring dimensions and density were carefully measured. The dimensions of the ring follow the same notation as for the PzXY nomenclature, so in this case, a ring-shaped transducer of outer diameter 19 mm, inner diameter 1.9 mm, and thickness 1.5 mm is written as NOA86H-TH1.5-OD19-ID1.9.

Before running the UEIS procedure, the stability of the NOA86H adhesive, after finalized curing, was evaluated by measuring the electrical impedance spectrum every hour for a period of 39 hours in ambient conditions. The results are shown in Fig. 5.8. It is seen how the impedance spectrum is constant during the 39 hours in ambient conditions, signifying that the NOA86H adhesive is fully cured and stable under ambient conditions.
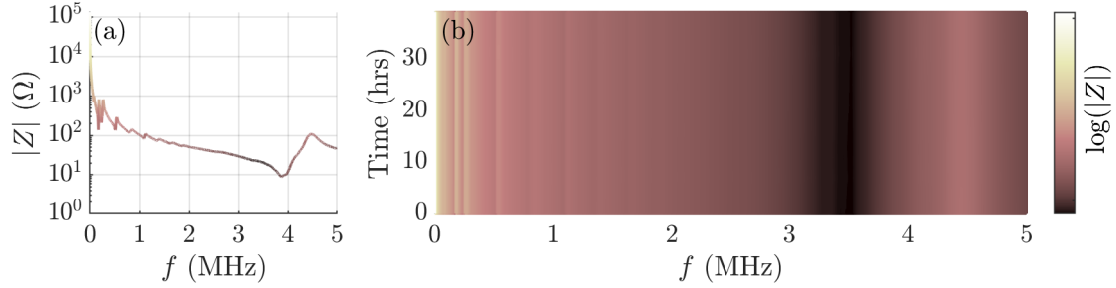
Figure 5.8: (a) Measured electrical impedance spectrum $|Z(f)|$ for a NOA86H-TH1.5-OD19-ID1.9 ring glued onto a Pz27-TH0.5-OD10 transducer. (b) Surface plot of NOA86H-loaded transducer spectrum as a function of time in ambient conditions after finalized assembling. The measurements were sampled every hour for a period of 39 hours. The color scheme follows a logarithmic scale, as indicated in (a).

The measured electrical impedance spectrum was then loaded into the UEIS fitting software, and after ten hours, the complex-valued elastic moduli of the NOA86H adhesive were provided. The NOA86H parameters obtained by the UEIS method are provided in Table B.3, and the fitted spectrum is plotted in Fig. 5.9 together with the loaded and unloaded measured electrical impedance spectrum. By looking at Fig. 5.9, it is seen how the loading of a transducer affects the impedance spectrum. Notice how the Pz27 resonances are damped (larger impedance values) by the NOA86H-ring loading, but also how new resonances appear at frequencies 75, 169, and 231 kHz for the NOA86H-loaded Pz27 system. The first appearing modes are primarily transverse and the resonance frequencies at which the first modes appear can be approximated by the ring diameter 19 mm and the transverse sound speed $c_{\mathrm{tr}}^{(\mathrm{noa86h})} = 984\,\mathrm{m/s}$, in this case, $f = 19\,\mathrm{mm}/984\,\mathrm{m\,s}^{-1} = 52\,\mathrm{kHz}$.
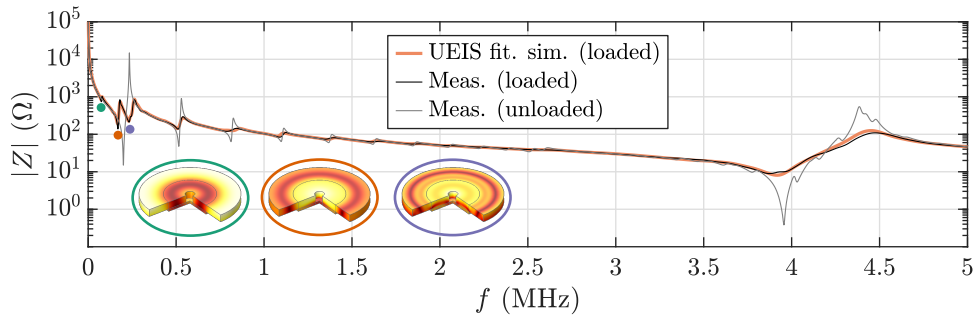
Figure 5.9: Measured and UEIS-fitted electrical impedance spectrum $|Z(f)|$ for a ring-shaped NOA86H-TH1.5-OD19-ID1.9 glued onto a UEIS-characterized Pz27-TH0.5-OD10 transducer, plotted together with the unloaded Pz27-TH0.5-OD10-transducer spectrum. The figure also includes selected modes at 75, 169, and 231 kHz. The modes are shown as inserts, and the color plot indicates the mechanical displacement amplitude $|\boldsymbol{u}_1|$ at $V_{\mathrm{pp}} = 2\,\mathrm{V}$ from min (dark) to max (light), where the maximum amplitudes are 9, 17, and 10 nm respectively.

Section summary: At this point, the UEIS method has been successfully used to characterize disk-shaped transducers together with an optical adhesive. In the proceeding section, the UEIS method will be used to determine the elastic moduli of a polymer. The polymer will be used to fabricate an all-polymer-based acoustofluidic device, in which all the components' material parameters are known and determined by the UEIS method, enabling a complete and accurate model of ultrasound acoustofluidic devices without free parameters.

5.3 Characterization of a polymer used for acoustofluidic device fabrication

In previous sections, the UEIS method was used to determine piezoceramic material parameters for disk-shaped Pz26 and Pz27 transducers. The UEIS-determined material parameters for the disk-shaped Pz27 transducer were used to determine the elastic moduli of a NOA86H optical adhesive by gluing a UV-cured NOA86H ring onto the Pz27 transducer and performing the UEIS fitting procedure. By using the NOA86H adhesive to glue on the already-cured NOA86H ring, the system only comprised two materials, the Pz27 piezoceramic, and the NOA86H adhesive.

A well-characterized glue enables loading and characterization of other materials, e.g., a polymer as in Paper III [3], where the loaded system consists of a PMMA ring glued onto a disk-shaped Pz27 transducer using the NOA86H adhesive. Now the system comprises three materials: a Pz27 piezoceramic, a NOA86H adhesive, and a polymer. In Paper III [3], two different PMMA-ring diameters (20 mm and 25 mm) with a thickness of 1.4 mm were considered together with two different Pz27-transducer-disk diameters (6.35 mm and 10 mm) with a thickness of 0.5 mm in combination a total of four different configurations. Conducting the UEIS fitting procedure for the four different configurations provided less than 1% relative errors for the real parts $C'_{11} = 7.18(4)\,\mathrm{GPa}$ and $C'_{44} = 1.553(8)\,\mathrm{GPa}$, and less than 6.5% for the imaginary parts $C''_{11} = -0.183(5)\,\mathrm{GPa}$ and $C''_{44} = -0.111(7)\,\mathrm{GPa}$. The UEIS-determined elastic moduli of the PMMA were validated by ultrasonic-through-transmission (UTT) measurements. The UTT technique is a time-of-flight-based method for measuring sound speeds. The principle is simple: a pulse is transmitted through a media with known sound speed c_0, e.g., water, afterward a sample is submerged in between the transmitter and the receiver, and the difference in arrival times is used to calculate the sample sound speed. The longitudinal sound speed c_{lo} is obtained at normal incidence and for incident angles above $\theta_{\mathrm{crit}} = \sin^{-1}(c_0/c_{\mathrm{lo}})$ only transverse waves are transmitted, for details see Refs. [3, 73, 79]. The difference between UEIS and UTT-determined parameters was less than 1.5% for the real parts and less than 12% for the imaginary.

Furthermore, the UEIS-determined elastic moduli of the PMMA were validated by laser-Doppler velocimetry (LDV): the measured displacement amplitudes were compared to simulated displacement amplitudes using the UEIS-determined material parameters as

input to the model. The validation was similar to Section 5.1.3, where the mechanical displacement $\tilde{u}_{1,z}$, normal to the transducer electrode, of an unloaded Pz27 transducer was measured at different frequencies. In this case, the $\tilde{u}_{1,z}$ for a PMMA-TH1.4-OD25-ID2.0 ring glued onto a Pz27-TH0.5-OD10 Pz27 disk was measured at frequencies 58 and 164 kHz with a peak-to-peak voltage of $V_{pp} = 2\,V$. The PMMA surface was sputtered with a thin layer of gold for increased intensity of the reflected laser signal. After gluing the PMMA onto the Pz27 transducer, a slight offset of 0.4 mm was observed, disrupting the axisymmetry. The breaking of symmetry was observed in the LDV measurements, and the offset was included in the simulation. The LDV measurements are shown in Fig. 5.10 together with the simulated values for the normal displacement amplitude $|u_{1,z}|$ at frequencies 58 and 164 kHz. Again, the features matches, and the maximum displacement amplitudes agree within 10% for both frequencies, even when the axisymmetry is broken by the off-centered gluing of the PMMA ring onto the Pz27 transducer. Finally, the characterized PMMA was used to fabricate a microfluidic chip for acoustofluidic application studied in the proceeding section.
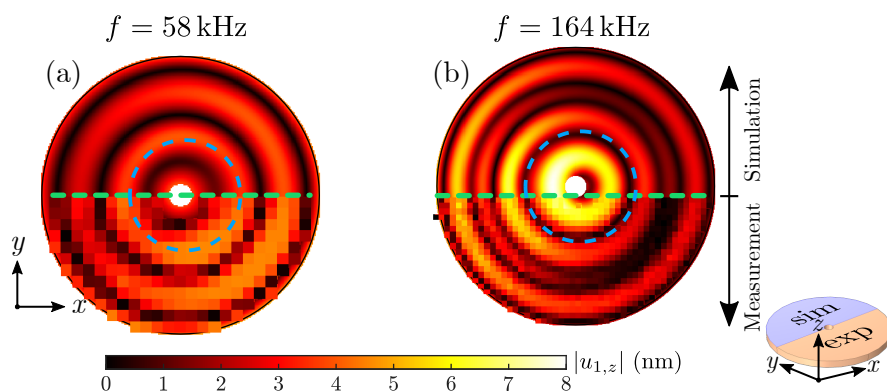
Figure 5.10: Measured and simulated normal displacement amplitude $|u_{1,z}|$ from 0 (dark) to 8 nm (light) for a PMMA-TH1.4-OD25-ID2.0 ring glued onto a Pz27-TH0.5-OD10 transducer. The displacement field was measured at two frequencies, $f = 58\,kHz$ in (a) and $f = 164\,kHz$ in (b) at a peak-to-peak voltage amplitude $V_{pp} = 2\,V$. The green dashed line separates the measured (pixelated) and simulated (smooth) data. The blue dashed line indicates the disk-shaped Pz27 perimeter. The normal displacement amplitude was measured on the PMMA-surface half-plane as indicated with a blue selection in the lower right corner.

5.3.1 Particle tracking in a polymer-based acoustofluidic device

In this section, a polymer-based acoustofluidic device will be analyzed in terms of measured and simulated particle trajectories influenced by the acoustic radiation force in stop-flow conditions. The polymer used to fabricate the device is the PMMA (Diakon TD525, Lucite International, Rotterdam, Netherlands) studied and characterized in Paper III [3] and summarized in the preceding section. The PMMA-based microfluidic chip was fabricated

by milling a 400-µm-deep cavity in a PMMA slide comprising the base, and afterward, the base and the cover were cut out using a lathe. The in- and outlet were drilled in the PMMA cover. The chip geometry was limited by the PMMA slide sample thicknesses of 1.4 mm, defining the cover and base thickness. The measured dimensions are given in Table 5.2, and the device is shown in Fig. 5.11. The glue layer thicknesses were obtained by subtracting the total layer thickness with the Pz26, base, and cover thickness.

This device is used as a proof-of-concept, showing that the UEIS method can be used to characterize material parameters enabling accurate and precise modeling of ultrasound acoustofluidic systems. Unfortunately, at this point, the Pz27 transducers were out-of-stock. Instead, we decided to move on with a Pz26 transducer compromising the model accuracy. All the materials were characterized using the UEIS method: including the Pz26-TH1.0-OD25 transducer, the UV-curable NOA86H adhesive, and the PMMA. The material parameters are provided in Chapter B.

The device assembling process consisted of a two-step procedure:

I. First, the PMMA base was glued onto the Pz26 transducer using the UV-curable NOA86H adhesive. The two parts were squeezed together to get as thin a glue layer as possible, and excess glue was wiped off before UV curing.

II. In the second step, the PMMA cover was carefully glued onto the PMMA base. A syringe was used to spread the glue evenly on a thin rim to avoid glue leaking inside the cavity,

afterward, the cavity was filled with milli-Q water using a syringe.
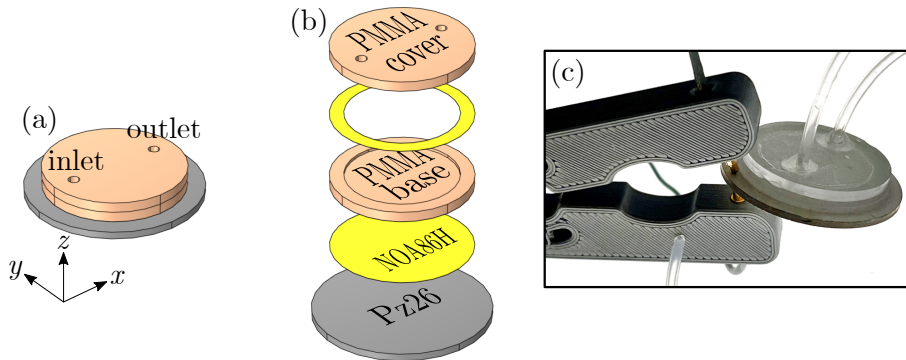
Figure 5.11: (a) Sketch of the PMMA-based acoustofluidic device comprising a PMMA-based cavity (beige) glued onto a disk-shaped Pz26 transducer (gray). (b) Exploded view of the device, showing each device component: a PMMA cover (beige) glued onto a PMMA base (beige) glued onto a Pz26 transducer (gray). The components were glued together using the NOA86H adhesive (yellow). (c) Picture of the experimental setup for measuring the electrical impedance spectrum.

Table 5.2: Measured dimensions for the PMMA-based acoustofluidic device components. The in- and outlet were positioned at ± 6.81 mm from the center axis with a diameter of 2 mm.

	Thickness (mm)	Outer diameter (mm)	Inner diameter (mm)	Cavity (µm)
Pz26	1.028	25.028	-	-
NOA86H	0.015	-	-	-
PMMA base	1.447	25.025	16.025	396
NOA86H rim	0.020	-	-	-
PMMA cover	1.429	25.025	-	-

Each step was assessed by the measured electrical impedance spectrum and compared to simulations as shown in Fig. 5.12. The features at kHz frequencies are well-captured by the simulated curves. However, at the primary thickness mode around 2 MHz, the measured and simulated curves deviate due to inaccurate modeling of the Pz26 transducer as was previously shown in Fig. 5.4.

In step II, the PMMA cover was glued onto the PMMA base, which was already glued onto the transducer, resulting in a system that is no longer axisymmetric due to the in- and outlet. However, a 2D axisymmetric model was used to simulate the impedance curves in Fig. 5.12(b)-(c). After step II, the cavity was filled with water, and by looking at Fig. 5.12(c), the measured and simulated curves match reasonably well, both having a global minimum at $f = 1.98$ MHz. Likewise, it is assumed that the acoustic response and dynamics match reasonably, so the simulated results can be used for insight into the acoustofluidic device dynamics.
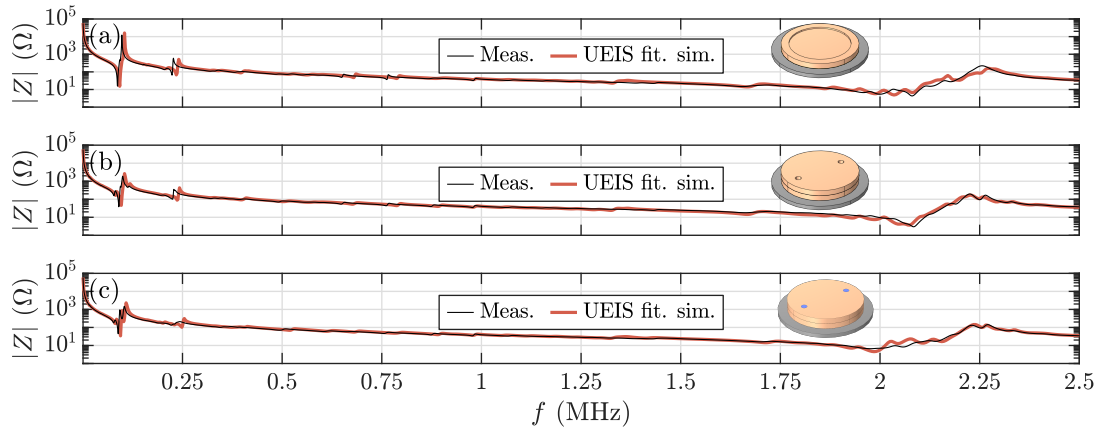
Figure 5.12: Measured and simulated impedance spectrum $|Z(f)|$ for each assembling step: (a) Step I: PMMA-base glued onto the Pz26 transducer. (b) Step II: PMMA cover glued onto the PMMA base, and (c) a water-filled cavity without tubings. The system configuration is shown as inserts for each step in the corresponding figure.

In Fig. 5.13(a), the energy density spectrum $E_{ac}(f)$ is compared between a 2D axisymmetric model and a 3D model, both resembling the PMMA-based acoustofluidic device. The simulated spectra are almost identical in magnitude and features: the main resonance frequencies deviate by 0.5% with a value of 1.98 MHz in the 2D axisymmetric model and 1.99 MHz in the 3D model. The acoustic energy density is 3% larger in the 2D axisymmetric case, most likely due to the inclusion of in- and outlet in the 3D model. The rubber-like tubings fitted in the in and outlet, as shown in Fig. 5.11(c), are modeled as perfectly matched layers, representing attenuated outgoing waves. The acoustic pressure field $\tilde{p}_1$ and the vertical displacement field $\tilde{u}_{1,z}$ at resonance frequency are plotted in Fig. 5.13(b)-(c) for the 2D axisymmetric and the 3D model, respectively. The simulated modes are very similar and almost invariant and uniform in the radial direction resembling a 1D layered resonator with a half-wave in the transducer, base, and channel, together with a full wave in the cover. At this frequency the longitudinal wavelength in the PMMA is $\lambda_{lo} = 1.25$ mm and the acoustic wavelength in the water is $\lambda_0 = 0.75$ mm. Even though the device is no longer axisymmetric, the 2D axisymmetric model seems a good approximation due to the system's nearly axisymmetric geometry with small asymmetries at in- and outlet.
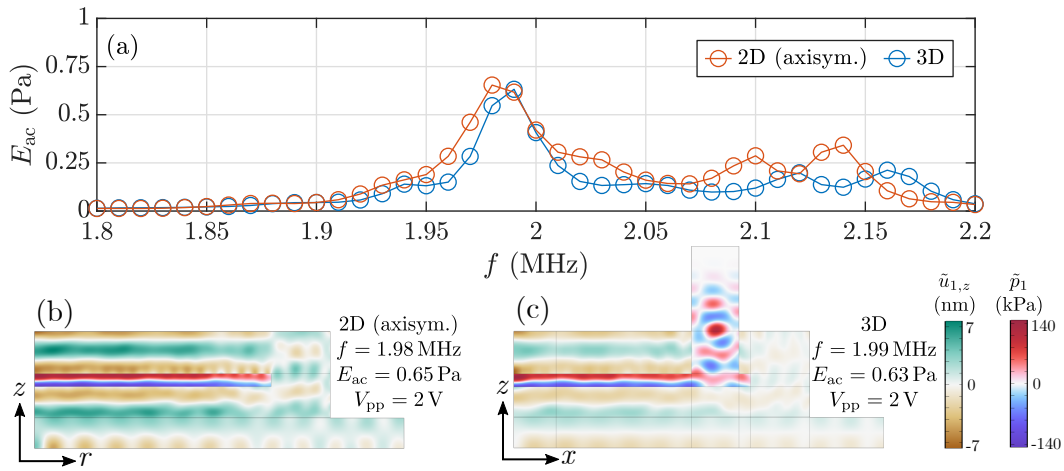
Figure 5.13: Simulated acoustic energy density spectrum $E_{ac}(f)$ for the PMMA-based cavity device and acoustic field plots. (a) A comparison between the acoustic energy density spectrum $E_{ac}(f)$ obtained for a 2D axisymmetric model and a full 3D model near the main resonance at 1.99 MHz. (b) Simulated acoustic pressure $\tilde{p}_1$ and vertical displacement $\tilde{u}_{1,z}$ at $f = 1.99$ MHz, for the 2D axisymmetric model. The fields are evaluated at a phase where the pressure amplitude is at a maximum. (c) Similar to (b), but for the full 3D model evaluated on the xz mirror plane.

The acoustofluidic response was further analyzed by tracking spherical 10-µm-diameter fluorescent polystyrene particles influenced by the acoustic forces in stop-flow conditions. The spherical 10-µm-diameter particles were submerged in an OptiPrep/water solution, a commonly used fluid/particle solution for acoustofluidic experiments to mimic red and white blood cells. OptiPrep was added to milli-Q water at a 20% $^{V}/_{V}$ ratio to match the density of the polystyrene particles, i.e., to obtain a neutrally buoyant solution avoiding sedimentation. To make the water/OptiPrep/particle solution, 300 µL of a *PS-Fluo-Red-Fi317* particle solution with a concentration of 45×10^3 particles per µL was added to 30 mL of the OptiPrep/water solution yielding a particle concentration of 450 particles per µL. The tubings were fitted in the in- and outlet and sealed with the UV-curable NOA86H adhesive. The open-source *DefocusTracker* software [80] was used to track and calculate the particle positions and velocities.

Experimental setup for particle tracking: The PMMA-based acoustofluidic cavity was mounted on a motorized stage using a 3D-printed holder. The Pz26 transducer was probed with a four-terminal sensor; two wires were used to apply the electrical signal. The two others measured the electric potential directly over the transducer. The electrical signal was generated by an *Analog Discovery 2* function generator. The fluorescent particles were illuminated with an LED through an objective, and the fluorescent signal was passed through a cylindrical lens and captured with a camera. A syringe pump was used for flow control. The experimental setup is shown in Fig. 5.14.
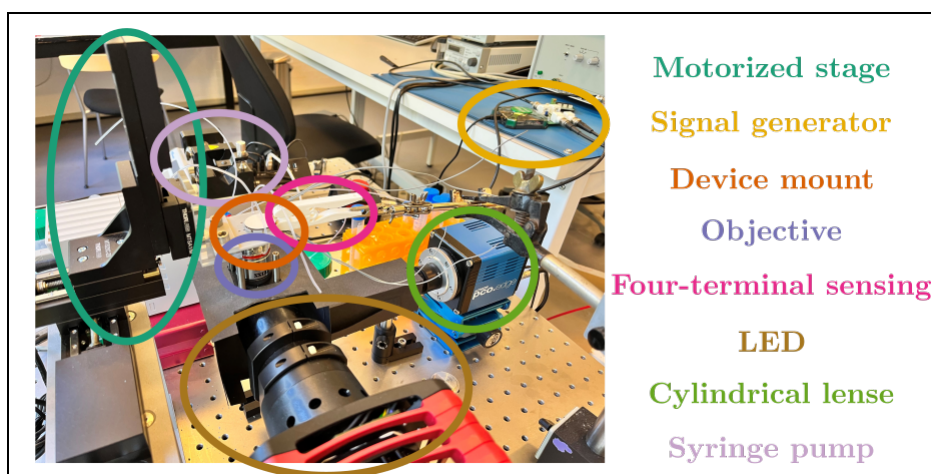
Figure 5.14: Picture of the experimental setup for fluorescent particle tracking. The setup consists of a motorized stage, a signal generator, a 3D-printed device mount, an objective, a four-terminal sensor, an LED, a cylindrical lens, and a syringe pump.

Experimental procedure for particle tracking: The OptiPrep/water/particle solution was injected with a syringe pump. The fluorescent particles were illuminated with an LED and observed through a cylindrical lens, and captured with a camera. The particle

trajectories were measured under stop-flow conditions. The electrical signal was provided at a constant voltage amplitude of $V_{\text{pp}} = 2\,\text{V}$ and was triggered by the camera's signal to match the time. The images used for the particle tracking were captured at 25 fps during 7 s. This procedure was conducted in a frequency interval from 1.8 to 2.2 MHz in steps of 10 kHz, near the predicted resonance at $f = 1.99\,\text{MHz}$ as shown in Fig. 5.13(a). The device was flushed between each frequency to bring in new particles.

The equation of motion for a particle in a fluid influenced by the acoustic forces is solved numerically to compare the measured and simulated particle velocities. The equation of motion for a spherical particle of radius a, mass $m_{\text{p}} = \frac{4}{3}\pi a^3 \rho_{\text{p}}$, and mass density ρ_{p} submerged in a quiescent and neutrally buoyant fluid influenced by the acoustic radiation force $\boldsymbol{F}_{\text{rad}}$ and a drag $\boldsymbol{F}_{\text{drag}} = 6\pi\eta_0 a(\boldsymbol{v}_2^d - \boldsymbol{v}_{\text{p}})$ is

$$m_{\text{p}}\frac{\text{d}\boldsymbol{v}_p}{\text{d}t} = \boldsymbol{F}_{\text{rad}} + \boldsymbol{F}_{\text{drag}} = \boldsymbol{F}_{\text{rad}} + 6\pi\eta_0 a(\boldsymbol{v}_2^d - \boldsymbol{v}_{\text{p}}) = \boldsymbol{F}_{\text{rad}} + \boldsymbol{F}_{\text{str}} - 6\pi\eta_0 a\boldsymbol{v}_{\text{p}}. \tag{5.9}$$

To obtain a characteristic velocity scale we assume a constant $\boldsymbol{F}_{\text{rad}}$ and $\boldsymbol{F}_{\text{str}}$, so Eq. (5.9) simplifies to an ordinary differential equation for $\boldsymbol{v}_p$ with a terminal velocity scale $v_{\text{t}} = \frac{|\boldsymbol{F}_{\text{rad}}| + |\boldsymbol{F}_{\text{str}}|}{6\pi\eta_0 a}$, and so the particle Reynolds number can be defined as $Re_{\text{p}} = \frac{2\rho_0 a v_{\text{t}}}{\eta_0}$.

For a standing pressure wave, the acoustic radiation force scale as $F_{\text{rad}} = 4\pi\Phi k_0 a^3 E_{\text{ac}}$ (see Eq. (2.24)) and the acoustic streaming scale as $|\boldsymbol{v}_2^d| = \frac{3}{2}\frac{E_{\text{ac}}}{\rho_0 c_0}$ see for example the acoustofluidic scaling laws presented in Ref. [81]. For the simulated response shown in Fig. 5.13 having $E_{\text{ac}} = 0.63\,\text{Pa}$ at $f = 1.99\,\text{MHz}$ and with the parameters provided in Table 2.1 and in Table 5.3 for a 10-µm-diameter polystyrene particle in an OptiPrep/water solution, the terminal velocity scale is $v_{\text{t}} = 15\,\text{µm/s}$ and the particle Reynolds number becomes $Re_{\text{p}} = 2 \times 10^{-4}$. Furthermore, the acoustic radiation force is dominating $|\boldsymbol{F}_{\text{str}}|/|\boldsymbol{F}_{\text{rad}}| = 0.04$, and by these means, the inertial term and the acoustic streaming drag in Eq. (5.9) can be neglected, so Eq. (5.9) is approximated as an ordinary first order differential equation

$$\frac{\text{d}\boldsymbol{r}_{\text{p}}}{\text{d}t} = \boldsymbol{v}_{\text{p}} = \frac{\boldsymbol{F}_{\text{rad}}}{6\pi\eta_0 a}, \tag{5.10}$$

in terms of the particle position $\boldsymbol{r}_{\text{p}}(t)$. By using the COMSOL module "Particle Tracing for Fluid Flow", the particle trajectories $\boldsymbol{r}_{\text{p}}(t)$ is solved by numerical integration $\boldsymbol{r}_{\text{p}}(t) = \int_0^t \boldsymbol{v}_{\text{p}}(\boldsymbol{r}(t'))\,\text{d}t'$.

The calculated particle trajectories was simulated in the same region as in the experiment, corresponding to the center-region $-1.25\,\text{mm} < x < 1.25\,\text{mm}$ and $-1.0\,\text{mm} < y < 1.0\,\text{mm}$ given by the cameras field-of-view. The number of particles in the simulation matched the number of successful tracks in the experiment, typically in the order of 300 tracks. As shown in Fig. 5.13(c), a vertical pressure node is formed near the center of the channel, so the particle velocities will be dominated by the forces in the vertical z-direction.

Table 5.3: Acoustic scattering properties for spherical 10-μm-diameter-polystyrene particles in a 20% V/v OptiPrep to water solution, including the mass density ρ_p, the compressibility κ_p, the monopole f_1 and dipole f_2 scattering coefficients, and the acoustic contrast factor Φ. [17]

ρ_p $(\mathrm{kg/m}^3)$	κ_p $(1/\mathrm{TPa})$	f_1 (-)	f_2 (-)	Φ (-)
1050	249	0.44	0	0.15

To compare the measured particle velocity profiles $v_{z,i}$ in the z-direction with the simulated, using a single measure, we define an averaged velocity measure

$$V_z(t) = \frac{1}{N} \sum_{i=1}^{N} |v_{z,i}(t)|, \tag{5.11}$$

where the subscript i refers to the particle track, and t is the time after the electrical signal was applied to the transducer at time $t = 0$ s. The absolute value accommodates particles moving in opposite directions due to the standing half-wave-like acoustic pressure field observed in Fig. 5.13(b)-(c). Each of the vertical particle-velocity profiles $v_{z,i}(t)$ are calculated by numerical differentiation of the corresponding measured vertical particle tracks $r_{z,i}$.

A relevant timescale is found by considering the particle velocity in an idealized standing pressure half-wave. The time t_{foc} it takes to migrate a particle from z_0 to z_f can be approximated by integrating $\frac{dz}{dt} = F_{\mathrm{rad}}(z)/(6\pi\eta_0 a)$. Using the expression for the radiation force Eq. (2.24) for a standing pressure wave, the result is

$$t_{\mathrm{foc}} = \frac{3}{4} \frac{\eta_0}{\Phi k_0^2 a^2 E_{\mathrm{ac}}} \left\{ \ln \left[\tan \left(k_0 z_f \right) \right] - \ln \left[\tan \left(k_0 z_0 \right) \right] \right\}. \tag{5.12}$$

For a standing acoustic pressure half-wave with acoustic wavenumber $k_0 = \frac{\pi}{H_{\mathrm{ch}}}$ in a channel of height H_{ch}, the time it takes for a particle to travel from $z_0 = \frac{H_{\mathrm{ch}}}{8}$ to $z_f = \frac{3H_{\mathrm{ch}}}{8}$ is

$$t_{\mathrm{foc}} \approx \frac{3}{2} \frac{\eta_0}{\Phi k_0^2 a^2 E_{\mathrm{ac}}}. \tag{5.13}$$

For the water and particle parameters provided in Table 2.1 and Table 5.3, respectively, the focusing time is $t_{\mathrm{foc}} = 8.2$ s for the simulated resonance shown in Fig. 5.15 having $E_{\mathrm{ac}} = 0.63$ Pa at $f = 1.99$ MHz.

The averaged particle velocity measure $V_z(t)$ was evaluated after $t = 1.3$ s corresponding to approximately one-sixth of the focusing timescale $t_{\mathrm{foc}} = 8.2$ s. In Fig. 5.15, the measured and simulated $V_z(t)$ are compared, providing a frequency-resolved one-to-one comparison between experiment and simulation, without free parameters.
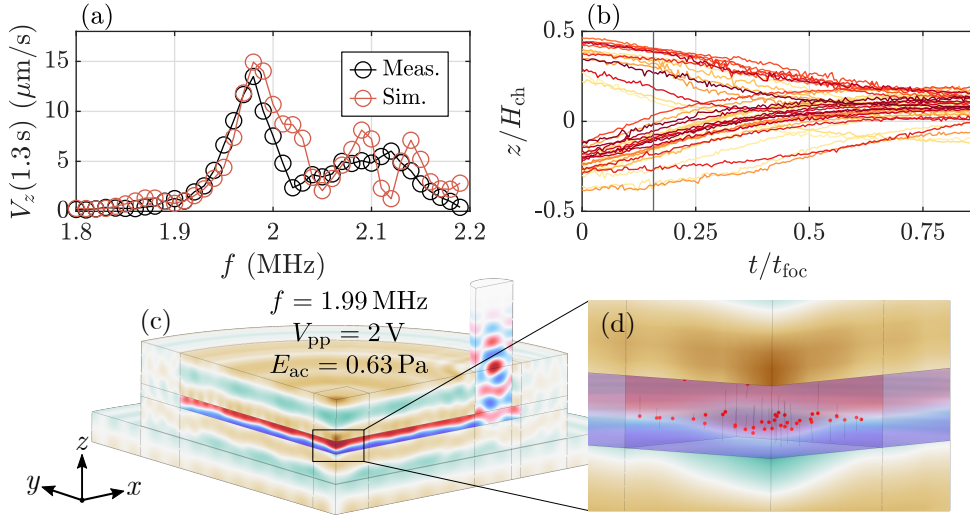
Figure 5.15: (a) Measured and simulated $V_z(f)$ spectrum evaluated after one-sixth of the focusing time $t_{foc}/6 \approx 1.3\,$s for the polymer-based acoustofluidic cavity actuated at a constant peak-to-peak voltage amplitude of $V_{pp} = 2\,$V. (b) Plot of the 40 vertical particle tracks, at $f = 1.98\,$MHz, with the largest net displacement in a channel of height $H_{ch} = 396\,\mu$m. The tracks are plotted as the z-position versus time in units of the focusing time $t_{foc} = 8.2\,$s. (c) 3D plot of the simulated $\tilde{u}_{1,z}$ and $\tilde{p}_1$ at $f = 1.98\,$MHz evaluated at the phase corresponding to the maximum pressure amplitude. (d) Simulated particle trajectories after $t_{foc} = 8.2\,$s, actuated at $f = 1.98\,$MHz with a peak-to-peak voltage of $V_{pp} = 2\,$V. The particles are confined to the camera's field-of-view region $(2 \times 2.5)\,$mm^2.

The measured V_z peak is located at 1.98 MHz with a value of $V_z(1.3\,\text{s}) = 13.5\,\mu$m/s, whereas the simulated is also at 1.98 MHz with a value of $15\,\mu$m/s. A perfect match in frequency and a mismatch of 11% in magnitude. However, in the simulated spectrum, two extra peaks appear at 2.09 and 2.14 MHz, and only a single peak at 2.12 MHz is visible in the measured spectrum, presumably because of the inaccurate modeling of the Pz26 transducer. The 40 vertical particle tracks, at $f = 1.98\,$MHz, with largest net displacement are plotted in Fig. 5.15(b). The banded pattern indicates a snaky vertical pressure node, as was also the case for the simulated response in Fig. 5.13(c).

Chapter summary: In this chapter, the UEIS method was used to characterize each component used to fabricate an acoustofluidic device, enabling precise and accurate modeling of a polymer-based acoustofluidic device. When the Pz27 transducer is available, we plan to carry out an identical experiment replacing the Pz26 transducer with a Pz27, for increased numerical accuracy, together with repeated experiments to obtain statistical measures. In the following chapter, the papers are presented in versions identical to the published versions in chronological order. The papers are followed by a chapter including preliminary results involving a 3D-printed polymer-based acoustofluidic device. In which the UEIS method will be used to determine the complex-valued elastic moduli of a 3D-print resin enabling fast, easy, and accurate prototyping.

Chapter 6

Published papers

6.1   Paper I: Micromachines 11(3), 1-15 (2020)

Microparticle acoustophoresis in aluminum-based acoustofluidic devices with PDMS covers

Authors: W. N. Bodé, L. Jiang, T. Laurell, and H. Bruus.

Microparticle Acoustophoresis in Aluminum-Based Acoustofluidic Devices with PDMS Covers

William Naundrup Bodé [1],*[iD]**, Lei Jiang** [2] **and Thomas Laurell** [2] **and Henrik Bruus** [1],*[iD]

[1] Department of Physics, Technical University of Denmark, DTU Physics Building 309,
    DK-2800 Kongens Lyngby, Denmark

[2] Department of Biomedical Engineering, Lund University, 221 00 Lund, Sweden; jiang.lei@bme.lth.se (L.J.);
    thomas.laurell@bme.lth.se (T.L.)

* Correspondence: winabo@dtu.dk (W.N.B.); bruus@dtu.dk (H.B.); Tel.: +45-4525-3307 (H.B.)

check for
updates

Abstract: We present a numerical model for the recently introduced simple and inexpensive micromachined aluminum devices with a polydimethylsiloxane (PDMS) cover for microparticle acoustophoresis. We validate the model experimentally for a basic design, where a microchannel is milled into the surface of an aluminum substrate, sealed with a PDMS cover, and driven at MHz frequencies by a piezoelectric lead-zirconate-titanate (PZT) transducer. Both experimentally and numerically we find that the soft PDMS cover suppresses the Rayleigh streaming rolls in the bulk. However, due to the low transverse speed of sound in PDMS, such devices are prone to exhibit acoustic streaming vortices in the corners with a relatively large velocity. We predict numerically that in devices, where the microchannel is milled all the way through the aluminum substrate and sealed with a PDMS cover on both the top and bottom, the Rayleigh streaming is suppressed in the bulk thus enabling focusing of sub-micrometer-sized particles.

Keywords: acoustofluidics; microparticle acoustophoresis; numerical modeling; aluminum microdevices; polydimethylsiloxane (PDMS) covers

1. Introduction

Acoustofluidic devices based on bulk acoustic waves for microparticle handling are traditionally made by microfabrication in acoustically hard materials, such as silicon or glass, yielding acoustic resonators with relatively high Q values [1]. Such devices can be fabricated controllable and with high accuracy, but may suffer from a high production cost. Several solutions have been proposed and successfully demonstrated to achieve simple and inexpensive acoustofluidic devices. Simple mass-produced glass capillary tubes have been used for trapping of microparticles [2–7] and even nanoparticles [8,9]. The first attempts of using polymer-based devices have been published showing applications such as focusing of polymer beads [10–13], lipids [10], and red blood cells [11,14], as well as blood-bacteria separation [15] and purification of lymphocytes [16]. Although a cheaper material, polymers are difficult to use in acoustofluidics due to their low acoustic contrast relative to water, but recently it was shown how to circumvent this problem by use of the whole-system-resonance principle [17]. According to this principle, the acoustic contrast between the ambient air and the whole device allows the excitation of specific whole-system vibrational resonance modes, which support strong acoustofluidic responses in a given embedded liquid-filled cavity, without the corresponding acoustic pressure being a localized cavity resonance as in conventional devices.

Another solution is to combine acoustically hard materials with the soft rubber polydimethylsiloxane (PDMS). In 2012, Adams et al., presented experiments and simulations of a high-throughput, temperature-

controlled microchannel acoustophoresis device made by rapid prototyping. The device was based on a PDMS-gasket defining the side-walls and shape of the acoustofluidic chamber, which then was sealed using standard microscope slides [18]. Also Xu et al., used such a glass-PDMS-glass structure in their recent device for isolation of cells from dilute samples using bead-assisted acoustic trapping [19]. Similarly in 2018, Gautam et al., designed, fabricated, and tested simple and inexpensive micromachined PDMS-covered aluminum-based microfluidic devices for acoustic focusing of particles and cells [20]. These devices appear to be versatile and truly simple to fabricate, as the desired microchannel system is micromilled into the surface of an aluminum base and bonded with a PDMS cover. Since neither theory nor simulation was presented by Gautam et al. [20], we develop in this work a numerical model for such devices and validate them experimentally: In Section 3 for a basic design similar to that in Ref. [20], where a microchannel is micromilled into the surface of an aluminum base and sealed with a PDMS cover as sketched in Figure 1 and with the dimensions given in Table 1; and in Section 4 for a geometrically symmetric, but anti-symmetrically ac-voltage-actuated device.

In the main part of our work, we use the validated numerical model to predict the answer to the following three questions: (1) Does the exceptionally low transverse speed of sound $\sim 100\,\mathrm{m/s}$ in the nearly incompressible PDMS imply a singular behavior of the acoustic streaming near the PDMS-aluminum corners of the device? (2) Does anti-symmetric excitation using a split-top-electrode configuration as in Ref. [17] lead to better acoustophoresis? And finally, (3) does the use of the acoustically soft PDMS cover lead to a suppression of the bulk-streaming rolls generated by the water-PDMS interface, and if so, would PDMS covers sealing both the top and bottom part of devices, where the microchannel is milled all the way through the aluminum base, lead to a suppression of all bulk-streaming rolls in the device? The answers to these questions turn out to be predominantly affirmative.
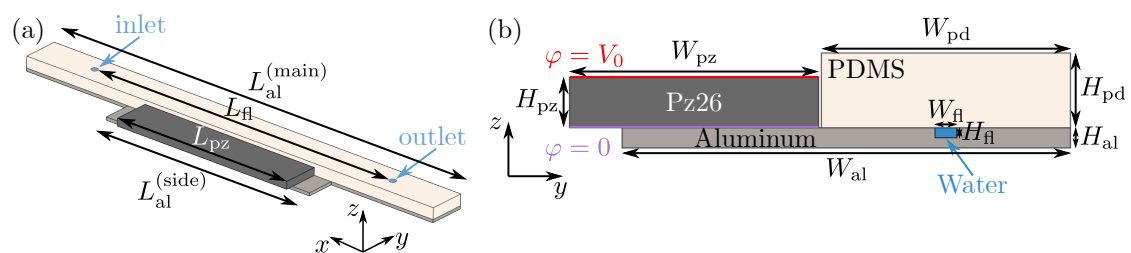
Figure 1. (**a**) 3D sketch drawn to scale of the single-PDMS-cover (beige) aluminum-based (light gray) device driven by a piezoelectric PZT-Pz26 transducer (dark gray, placed on a protrusion next to the PDMS) with silver electrodes (not shown). The inlet and outlet channels are marked by small circles. (**b**) Cross-sectional view of the device at the vertical center plane, used in the 2D model presented in Section 3, where the 9-µm-thick electrodes of the Pz26 transducer are connected to ground (purple) and to the driving ac-voltage (red). The gap between the Pz26 and the PDMS cover is $\frac{1}{8}W_{\mathrm{fl}}$.

Table 1. Dimensions of the two chip geometries shown in Sections 1 and 4.

Chip		Units	Pz26	Electrodes	Al (Main)	Al (Side)	PDMS	Channel
	Length	mm	25	25	60	30	60	44
Section 1	Width	mm	5	5	5	4	5	0.44
	Height	mm	1	0.009	0.4	0.4	1.5	0.2
	Length	mm	25	25	60	–	60	44
Section 4	Width	mm	10	10	5	–	5	0.44
	Height	mm	1	0.009	0.4	–	1.5	0.2

2. Theory: The Governing Equations and Boundary Conditions

We follow the work by Skov et al. [21] in our theoretical and numerical modeling of the acoustofluidic system sketched in Figure 1. The continuum fields of the model are the following: An electric potential scalar field $\tilde{\varphi}(\mathbf{r}, t)$ is present in the piezoelectric domain (Pz26), an elastic displacement vector field $\tilde{\mathbf{u}}(\mathbf{r}, t)$ is present in all four solid domains (Pz26, aluminum, silver

electrodes, and PDMS), and an acoustic pressure scalar field $\tilde{p}_1(\boldsymbol{r},t)$ as well as a steady acoustic streaming velocity vector field $\boldsymbol{v}_2(\boldsymbol{r})$ and pressure $p_2(\boldsymbol{r})$ are present in the water-filled microchannel. As in typical experiments, the system is driven by a time-harmonic ac-voltage $V_0\,\mathrm{e}^{-\mathrm{i}\omega t}$ of amplitude V_0 and angular frequency $\omega = 2\pi f$, where f is the ultrasound frequency, applied to the silver electrodes of the Pz26 transducer. Consequently, to first order in the applied voltage, all fields acquire a time-harmonic phase factor $\mathrm{e}^{-\mathrm{i}\omega t}$ and a complex-valued spatially varying amplitude,

$$\tilde{\varphi}(\boldsymbol{r},t) = \varphi(\boldsymbol{r})\mathrm{e}^{-\mathrm{i}\omega t}, \qquad \tilde{\boldsymbol{u}}(\boldsymbol{r},t) = \boldsymbol{u}(\boldsymbol{r})\mathrm{e}^{-\mathrm{i}\omega t}, \qquad \text{and} \qquad \tilde{p}_1(\boldsymbol{r},t) = p_1(\boldsymbol{r})\mathrm{e}^{-\mathrm{i}\omega t}. \tag{1}$$

In the following, the common phase factor $\mathrm{e}^{-\mathrm{i}\omega t}$ is left out of the linear equations. Only the space-dependent amplitudes are computed, but multiplying them by $\mathrm{e}^{-\mathrm{i}\omega t}$ recovers the time dependence.

2.1. The Piezoelectric Transducer

We model a standard lead-zirconate-titanate (PZT) transducer of type Pz26 polarized in the z direction. The mechanical stress tensor σ and the electric displacement field $\boldsymbol{D}$ are given in terms of the gradients of the elastic displacement field $\boldsymbol{u}$ and the electric potential φ by the electromechanical coupling matrix. Using the compact Voigt notation, this constitutive relation is given by

$$\begin{pmatrix} \sigma_{xx} \\ \sigma_{yy} \\ \sigma_{zz} \\ \sigma_{yz} \\ \sigma_{xz} \\ \sigma_{xy} \\ D_x \\ D_y \\ D_z \end{pmatrix} = \begin{pmatrix} C_{11} & C_{12} & C_{13} & 0 & 0 & 0 & 0 & 0 & -e_{31} \\ C_{12} & C_{11} & C_{13} & 0 & 0 & 0 & 0 & 0 & -e_{31} \\ C_{13} & C_{13} & C_{33} & 0 & 0 & 0 & 0 & 0 & -e_{33} \\ 0 & 0 & 0 & C_{44} & 0 & 0 & 0 & -e_{15} & 0 \\ 0 & 0 & 0 & 0 & C_{44} & 0 & -e_{15} & 0 & 0 \\ 0 & 0 & 0 & 0 & 0 & C_{66} & 0 & 0 & 0 \\ 0 & 0 & 0 & 0 & e_{15} & 0 & \varepsilon_{11} & 0 & 0 \\ 0 & 0 & 0 & e_{15} & 0 & 0 & 0 & \varepsilon_{11} & 0 \\ e_{31} & e_{31} & e_{33} & 0 & 0 & 0 & 0 & 0 & \varepsilon_{33} \end{pmatrix} \begin{pmatrix} \partial_x\,u_x \\ \partial_y\,u_y \\ \partial_z\,u_z \\ \partial_y u_z + \partial_z\,u_y \\ \partial_x u_z + \partial_z\,u_x \\ \partial_x u_y + \partial_y\,u_x \\ -\partial_x\varphi \\ -\partial_y\varphi \\ -\partial_z\varphi \end{pmatrix}. \tag{2}$$

Here, C_{ik} are the elastic coefficients, ε_{ik} are the electric permittivities, and e_{ik} are the piezoelectric coupling constants. The remaining components of σ are given by the symmetry relations $\sigma_{ik} = \sigma_{ki}$.

The governing equations in the piezoelectric Pz26 material of mass density ρ_{sl} are the Cauchy equation for the elastic displacement field $\boldsymbol{u}$ and, for frequencies less than 100 MHz in systems smaller than 1 m without free charges, the quasi-static Gauss law for the electric potential φ,

$$-\omega^2\rho_{\mathrm{sl}}\boldsymbol{u} = \boldsymbol{\nabla}\cdot\sigma, \qquad \boldsymbol{\nabla}\cdot\boldsymbol{D} = 0. \tag{3}$$

The boundary conditions for the Pz26 domain with surface normal vector $\boldsymbol{n}$ are continuity of φ, $\boldsymbol{u}$ and $\sigma\cdot\boldsymbol{n}$ across the elastic solid interfaces to the silver electrodes, and zero stress as well as zero electric charge on surfaces exposed to air,

$$\text{Pz26 domain} \leftarrow \text{charged electrode:} \qquad \varphi = V_0, \quad \sigma\cdot\boldsymbol{n} \text{ and } \boldsymbol{u} \text{ continuous,} \tag{4a}$$
$$\text{Pz26 domain} \leftarrow \text{grounded electrode:} \qquad \varphi = 0, \quad \sigma\cdot\boldsymbol{n} \text{ and } \boldsymbol{u} \text{ continuous,} \tag{4b}$$
$$\text{Pz26 domain} \leftarrow \text{air:} \qquad \boldsymbol{n}\cdot\boldsymbol{D} = 0 \quad \text{and} \quad \sigma\cdot\boldsymbol{n} = \boldsymbol{0}. \tag{4c}$$

Here, the notation $A \leftarrow B$ refers to the influence of B on domain A with outward surface normal $\boldsymbol{n}$.

2.2. The Elastic Aluminum Base, PDMS Cover, and Silver Electrodes

The aluminum base, the PDMS cover, and the silver electrodes on the Pz26 transducer can all be described as isotropic, linear elastic materials. Again using the compact Voigt notation, the corresponding constitutive equation relating the strain and the stress are given by

$$
\begin{pmatrix} \sigma_{xx} \\ \sigma_{yy} \\ \sigma_{zz} \\ \sigma_{yz} \\ \sigma_{xz} \\ \sigma_{xy} \end{pmatrix} = \begin{pmatrix} C_{11} & C_{12} & C_{12} & 0 & 0 & 0 \\ C_{12} & C_{11} & C_{12} & 0 & 0 & 0 \\ C_{12} & C_{12} & C_{11} & 0 & 0 & 0 \\ 0 & 0 & 0 & C_{44} & 0 & 0 \\ 0 & 0 & 0 & 0 & C_{44} & 0 \\ 0 & 0 & 0 & 0 & 0 & C_{44} \end{pmatrix} \begin{pmatrix} \partial_x u_x \\ \partial_y u_y \\ \partial_z u_z \\ \partial_y u_z + \partial_z u_y \\ \partial_x u_z + \partial_z u_x \\ \partial_x u_y + \partial_y u_x \end{pmatrix}. \tag{5}
$$

For isotropic materials only C_{11} and C_{44} are independent, since the constraint $C_{12} = C_{11} - 2C_{44}$ applies. The transverse and longitudinal speed of sound becomes $c_{\text{lo}} = \sqrt{C_{11}/\rho_{\text{sl}}}$ and $c_{\text{tr}} = \sqrt{C_{44}/\rho_{\text{sl}}}$, respectively. The governing equation for the displacement field u in an elastic solid with mass density ρ_{sl} is the Cauchy equation

$$
-\omega^2 \rho_{\text{sl}} u = \nabla \cdot \sigma. \tag{6}
$$

The boundary conditions for the elastic solid domains with surface normal vector n are continuity of u and $\sigma \cdot n$ across the elastic solid interfaces, and zero stress on surfaces exposed to air,

$$
\text{solid domain} \leftarrow \text{adjacent solid:} \quad \sigma \cdot n \text{ and } u \text{ continuous,} \tag{7a}
$$

$$
\text{solid domain} \leftarrow \text{air:} \quad \quad \quad \sigma \cdot n = \mathbf{0}. \tag{7b}
$$

The boundary conditions for the fluid-solid interfaces are given below.

2.3. Pressure Acoustics in the Water-Filled Microchannel

The governing equation for the acoustic pressure p_1 inside a fluid with mass density ρ_{fl}, speed of sound c_{fl}, dynamic viscosity η_{fl}, and bulk viscosity $\eta_{\text{fl}}^{\text{b}}$ is the Helmholtz equation

$$
\nabla^2 p_1 + \frac{\omega^2}{c_{\text{fl}}^2}\left(1 + i\frac{\Gamma_{\text{fl}}}{2}\right)p_1 = 0, \quad \text{where} \quad \Gamma_{\text{fl}} = \left(\frac{4}{3}\eta_{\text{fl}} + \eta_{\text{fl}}^{\text{b}}\right)\omega\kappa_{\text{fl}} \quad \text{and} \quad \kappa_{\text{fl}} = \frac{1}{\rho_{\text{fl}}c_{\text{fl}}^2}. \tag{8}
$$

The acoustic velocity v_1 in the bulk of the fluid is a potential flow given by the acoustic pressure p_1,

$$
v_1 = -i\frac{1 - i\Gamma_{\text{fl}}}{\omega\rho_{\text{fl}}}\nabla p_1. \tag{9}
$$

The boundary conditions for the fluid-solid interface are continuity of the stress and the velocity. In Ref. [21] the explicit form of these boundary conditions were derived taking into account the viscous boundary layer in the fluid. By introducing the shear wavenumber $k_{\text{s}} = (1 + i)/\delta$, where $\delta = \sqrt{2\eta_{\text{fl}}/(\omega\rho_{\text{fl}})}$ is the thickness of the viscous boundary layer, and expressing the displacement velocity as $v_{\text{sl}} = -i\omega u$, the fluid-solid boundary conditions become,

$$
\text{Solid domain} \leftarrow \text{fluid:} \quad \sigma \cdot n = -p_1 n + ik_{\text{s}}\eta_{\text{fl}}(v_{\text{sl}} - v_1), \tag{10a}
$$

$$
\text{Fluid domain} \leftarrow \text{solid:} \quad v_1 \cdot n = v_{\text{sl}} \cdot n + \frac{i}{k_{\text{s}}}\nabla_\parallel \cdot (v_{\text{sl}} - v_1)_\parallel. \tag{10b}
$$

Here, the viscous loss in the fluid is taken into account in the boundary conditions, and it appears through the slip velocity $v^\delta = (v_{\text{sl}} - v_1)$.

2.4. Acoustic Streaming in the Water-Filled Microchannel

Steady acoustic streaming arises in the fluid due to the inherent nonlinear fluid dynamics, here the time-average of products of time-harmonic fields. Following Bach and Bruus [22], the streaming velocity v_2 is governed by a real-valued incompressible Navier–Stokes equation with a body force due to the real part of the acoustic energy-flux density,

$$\boldsymbol{\nabla} \cdot \boldsymbol{v}_2 = 0 \quad \text{and} \quad \mathbf{0} = -\boldsymbol{\nabla} p_2 + \eta_{\text{fl}} \nabla^2 \boldsymbol{v}_2 + \frac{\Gamma_{\text{fl}} \omega}{2 c_{\text{fl}}^2} \text{Re}\{p_1^* \boldsymbol{v}_1\}. \tag{11}$$

The no-slip condition on the fluid-solid interface requires that $v_2 = -\langle (\boldsymbol{u} \cdot \boldsymbol{\nabla}) \boldsymbol{v}_1 \rangle$, which leads to the boundary condition for the acoustic streaming v_2 at the fluid-solid interface,

$$\boldsymbol{v}_2 = (\boldsymbol{A} \cdot \boldsymbol{e}_{\parallel}) \, \boldsymbol{e}_{\parallel} + (\boldsymbol{B} \cdot \boldsymbol{e}_{\perp}) \, \boldsymbol{e}_{\perp}, \tag{12a}$$

$$\boldsymbol{A} = -\frac{1}{2\omega} \text{Re}\left\{ v_1^{\delta 0*} \cdot \boldsymbol{\nabla} \left(\frac{1}{2} v_1^{\delta 0} - i v_{\text{sl}}^0 \right) - i v_{\text{sl}}^{0*} \cdot \boldsymbol{\nabla} v_1 \right.$$
$$\left. + \left[\frac{2-i}{2} \boldsymbol{\nabla} \cdot v_1^{\delta 0*} + i \left(\boldsymbol{\nabla} \cdot v_{\text{sl}}^{0*} - \partial_{\perp} (v_1 \cdot \boldsymbol{e}_{\perp})^* \right) \right] v_1^{\delta 0} \right\}, \tag{12b}$$

$$\boldsymbol{B} = \frac{1}{2\omega} \text{Re}\{i v_1^{0*} \cdot \boldsymbol{\nabla} v_1\}, \tag{12c}$$

where the superscript "0" indicates a field evaluated along the fluid-solid interface. The subscripts $\parallel$ and $\perp$ and the unit vectors $\boldsymbol{e}_{\parallel}$ and $\boldsymbol{e}_{\perp}$ refer to the parallel and normal direction to the solid wall respectively. The steady pressure p_2 accompanying v_2 is governed by the continuity for v_2, and since it only appears as a gradient in Equation (11), we must fix the level of p_2 by the constraint $\int_{\Omega_{\text{fl}}} p_2 \, \mathrm{d}y \mathrm{d}z = 0$.

2.5. The Acoustic Radiation and Drag Force on Suspended Microparticles

Suspended spherical particles of radius a and mass density ρ_{pa} will experience the radiation force $\boldsymbol{F}_{\text{rad}}$ due to acoustic scattering, which is given by the potential U_{rad} with monopole and dipole scattering coefficients f_0 and f_1, respectively [23],

$$\boldsymbol{F}_{\text{rad}} = -\boldsymbol{\nabla} U_{\text{rad}} \quad \text{where} \quad U_{\text{rad}} = \frac{4}{3} \pi a^3 \left(\frac{1}{4} f_0 \kappa_{\text{fl}} |p_1|^2 - \frac{3}{8} f_1 \rho_{\text{fl}} |v_1|^2 \right). \tag{13}$$

The velocity v_{pa} of a suspended particle at position $\boldsymbol{r}(t)$ in the water is determined by a balance between the Stokes drag force $\boldsymbol{F}_{\text{drag}} = 6\pi \eta_{\text{fl}} a (v_2 - v_{\text{pa}})$, the acoustic radiation force $\boldsymbol{F}_{\text{rad}}$, and the buoyancy force $\boldsymbol{F}_{\text{buoy}} = -\frac{4}{3}\pi a^3 (\rho_{\text{pa}} - \rho_{\text{fl}}) g \boldsymbol{e}_z$,

$$\boldsymbol{v}_{\text{pa}}(\boldsymbol{r}) = \boldsymbol{v}_2(\boldsymbol{r}) + \frac{\boldsymbol{F}_{\text{rad}}(\boldsymbol{r})}{6\pi \eta_{\text{fl}} a} - \frac{2}{9} \frac{a^2}{\eta_{\text{fl}}} (\rho_{\text{pa}} - \rho_{\text{fl}}) g \boldsymbol{e}_z. \tag{14}$$

The particle trajectory is then given by integration in time as $\boldsymbol{r}_{\text{pa}}(t) = \int_0^t v_{\text{pa}}(\boldsymbol{r}(t')) \, \mathrm{d}t'$. Inertia is neglected here, because the largest particle with radius $a = 2.4$ µm moves slower than $v_{\text{pa}} < 1$ cm/s yielding a small particle Reynolds number, $\text{Re}_{\text{pa}} = \frac{1}{\eta_{\text{fl}}} \rho_{\text{fl}} a v_{\text{pa}} \approx 0.03 \ll 1$.

We define the horizontal y axis such that the channel is centered around $y = 0$. To determine at which frequencies f acoustic resonance modes appear that leads to good particle focusing towards the vertical center plane located at $y = 0$, we introduce the focusing figure of merit $\mathcal{F}(f)$. This is a modified version of the figure of merit $\mathcal{R}$ defined in Ref. [17], as follows: $\mathcal{F}$ should be large, when at the same time the average acoustic energy density E_{ac} is large, and the acoustic radiation force

F_{rad} has the property that its average horizontal y component is large and points toward the center, whereas its average vertical z component has a small magnitude,

$$\mathcal{F}(f) = \frac{\int_{\Omega_{fl}} \mathrm{sgn}(-y)\, F_{rad,y}\, \mathrm{d}y\mathrm{d}z}{\int_{\Omega_{fl}} |F_{rad,z}|\, \mathrm{d}y\mathrm{d}z}\, E_{ac}, \quad \text{where} \quad E_{ac} = \frac{\int_{\Omega_{fl}} \left[\frac{1}{4}\kappa_{fl}\,|p_1|^2 + \frac{1}{4}\rho_{fl}\,|v_1|^2\right]\, \mathrm{d}y\mathrm{d}z}{\int_{\Omega_{fl}} 1\, \mathrm{d}y\mathrm{d}z}. \tag{15}$$

Here, $\mathrm{sgn}(-y)$ designates minus the sign of the y coordinate.

3. Numerical Implementation and Experimental Validation of the Single-PDMS-Cover Model

To illustrate the numerical implementation of the model, we choose the geometry as sketched in Figure 1, with the dimensions listed in Table 1, and the material parameters given in Appendix A. This device geometry is similar to the one in Ref. [20], namely an aluminum-based device with a straight channel and a single PDMS cover. Our general numerical modeling is then validated experimentally for this device and further supported by the results presented in Section 4, for the anti-symmetric actuated design.

3.1. Model Implementation in COMSOL Multiphysics

The model system of Figure 1 as well as its governing equations and boundary conditions given in Section 2, are implemented in the commercial finite-element method software COMSOL Multiphysics 5.4 [24] using the *weak form PDE* module, closely following the method presented in Ref. [21]. We use quartic Lagrange shape functions for p_1, cubic for u, φ, and v_2, and quadratic for p_2. For simplicity, we approximate the device by an infinitely long straight channel, and thus restrict the computation to the 2D cross section. The material parameters used in the model are given in Appendix A. The simulations were performed on a workstation with a 3.5-GHz Intel Xeon CPU E5-1650 v2 dual-core processor and with 128 GB RAM.

3.2. Manufacturing Method of the Chip for the Experimental Validation

A sketch of the device fabrication method is shown in Figure 2. A more detailed description of the process steps is given in the following.
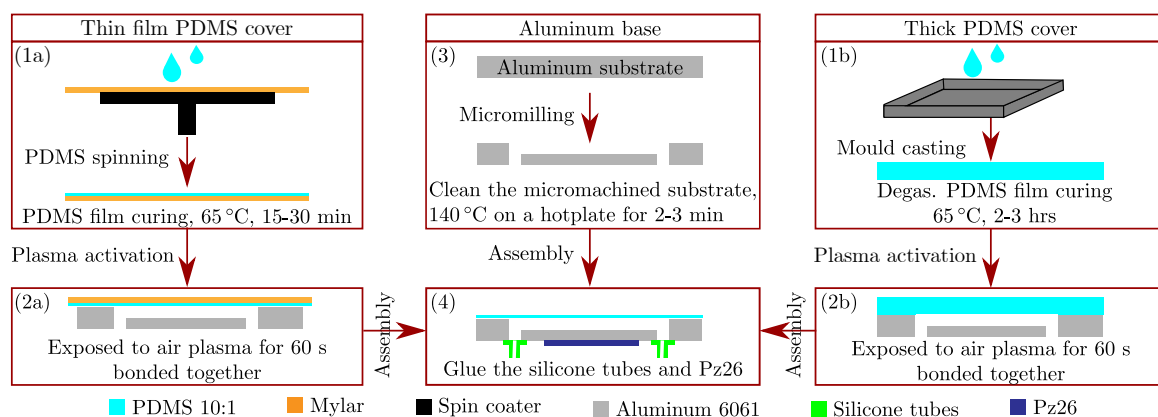
Figure 2. Schematic showing the sequence in the fabrication of the aluminum devices with PDMS covers. Production of a thin PDMS cover on a Mylar sheet by (**1a**) spinning and curing followed by (**2a**) bonding to the aluminum base by plasma activation and removal of the Mylar sheet. (**1b**) Production of a thick PDMS cover by mould casting followed by (**2b**) bonding to the aluminum base by plasma activation. (**3**) Fabrication of the channel in the aluminum base by micromilling. (**4**) Attachment of silicone tubes and the Pz26 transducer.

The aluminum base. A microchannel was milled in an aluminum substrate (alloy 6061, McMaster-Carr, Los Angeles, CA, USA) using a CNC milling machine (Solectro AB, Lomma, Sweden).

The micromachined substrate was cleaned with acetone, ethanol, and Milli-Q (Millipore Corporation, Burlington, MA, USA), and dried on a 140 °C hotplate for 2–3 min prior to bonding with the PDMS film covering the channel. This constitutes the base of the device.

The PDMS covers. Sylgard 184 silicone elastomer (Dow Corning, Ellsworth Adhesives, Germantown, WI, USA) was mixed with the curing agent at the commonly used weight ratio of 10:1 and degassed. Two types of covers were made: (a) Thin PDMS-film covers, by deposition of 1 mL of elastomer on a 100-μm-thick 100-mm-by-100-mm plastic transparency sheet (Mylar), followed by spin-coating and curing at 65 °C for 15–30 min, and (b) 1.5-mm-thick PDMS covers by conventional mould casting.

Device assembly. Afterwards, the cured PDMS film and cleaned aluminum substrates were treated with air plasma in a Zepto plasma cleaner (Diener electronic GmbH + Co. KG, Ebhausen, Germany) for 60 s. PDMS and aluminum were subsequently bonded together and cured at 80 °C for 4 min. After curing, the Mylar sheet was removed from the PDMS-aluminum assembly. For flow connections, silicone tubes with inner diameters that match 1/16″ Teflon tubings, were glued to the base of the device. A PZT ceramic transducer (Pz26, Meggitt A/S, Kvistgaard, Denmark) designed for 2 MHz actuation was superglued to the final device.

3.3. Experimental Validation of the Numerical Model

The electrodes of the Pz26 transducer were coupled to an ac-voltage generator operating at 20 V peak-to-peak ($V_0 = 10$ V) at frequencies ranging from 1.5 to 2.5 MHz. After stopping the particle-loading flow, the position and velocity v_{pa} of fluorescently-marked polystyrene particles (see Table A3 in Appendix A) was measured using the single-camera general defocusing particle tracking (GDPT) technique [25,26] with fluorescent polystyrene beads. We use a 10 μm × 5 μm grid size and a recorded image frame rate of 10 Hz, and the motion of $2a = 4.8$, 2.0, and 1.0 μm-diameter tracer particles is tracked for 30, 60, and 120 s, respectively. During the data processing, the outliers were filtered out by limiting the displacement deviation of all the particles, by limiting the velocity magnitude, and by restricting the particle count to 2 in each grid.

To validate our 2D model, we compare in Figure 3 simulated and measured particle behavior. The top row show top-view micrographs of the microchannel under flow-through condition, where 4.8-μm-diameter particles in bright-field are seen to focus in the center, Figure 3a. This resonance mode is called "S" for "side actuated" and was located at $f = 2.048$ MHz. This focusing is confirmed by the fluorescent image Figure 3b, which however also reveals particles accumulating near the corners of the device. In Figure 3c,d, we show measured and simulated particle velocities v_{pa} in the vertical cross section for different particle diameters. It is seen that the 2D model captures the following five main features in the measured particle velocity field, even though the 2D model geometry of Figure 1b assumes a translational invariant cross section along the x direction, which the experimental 3D geometry of Figure 1a clearly does not have. (1) The numerically predicted resonance is located at $f = 1.803$ MHz, only 12% below the experimental value. (2) As expected, for large particles $2a = 4.8$ μm the motion is dominated by the radiation force, which is partly focusing in the vertical nodal plane at $y = 0$ and partly pointing towards the soft PDMS cover and the top corners. As the particle size is reduced to $2a = 2.0$ μm and then further to $2a = 1.0$ μm, acoustic streaming becomes more dominant for the particle motion. This cross-over is clearly seen both in model and measurement of Figure 3c,d in the form of streaming flow rolls. (3) Near the hard aluminum bottom, the classical pair of counter-rotating Rayleigh streaming rolls appears. (4) Near the soft PDMS cover, the acoustic streaming rolls are confined to the top corners where it reaches its maximum value. This is a consequence of the low transverse speed of sound ~100 m/s in PDMS, or equivalently, the nearly incompressible nature of PDMS. Finally, (5) The magnitude $v_{pa} = 40$ μm/s of the simulated particle velocity matches that of the measured one for the 4.8-μm-diameter particles, whereas it is roughly 30–50% smaller for the 2.0- and 1.0-μm-diameter particles.
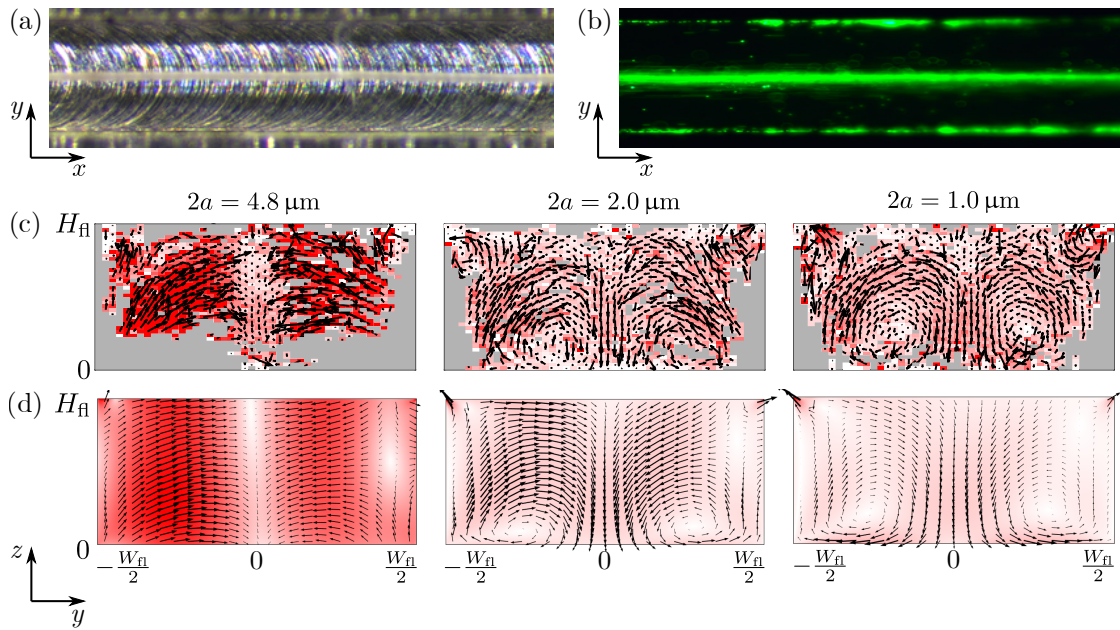
Figure 3. (**a**) Bright-field micrograph under flow-through condition showing acoustophoretic focusing of 4.8-μm-diameter polystyrene particles at the center (gray band). (**b**) Similarly for fluorescently-marked particles, but now also revealing that some particles are accumulating at the upper corners of the channel. (**c**) Vector plot (black arrows) and color plot ranging from 0 μm/s (white) up to 40 μm/s (red) of the particle velocities v_{pa} in the vertical cross section measured by GDPT at resonance mode "S", $f = 2.048$ MHz, for different particle diameter $2a = 4.8$ μm, 2.0 μm, and 1.0 μm. (**d**) Same vector and color plot as (c) but for the simulated results of v_{pa} in the 2D geometry shown in Figure 1b at the numerically determined resonance frequency $f = 1.803$ MHz (12% lower).

4. Modeling of Single-PDMS-Cover Devices with Anti-Symmetric Voltage Actuation

Following the results of Ref. [17], we investigate numerically, if better acoustophoresis, quantified by the focusing figure of merit $\mathcal{F}$ defined in Equation (15), is obtained by exciting the half-wave resonance mode (which is anti-symmetric around the nodal plane at $y = 0$). This is achieved by splitting the top electrode and applying an anti-symmetric ac voltage, as sketched in Figure 4 for a device with a split-gap of size 50 μm × 40 μm cut into the top surface of the Pz26 transducer. Here, the PDMS, the channel, and the aluminum base are translational invariant along the x direction.
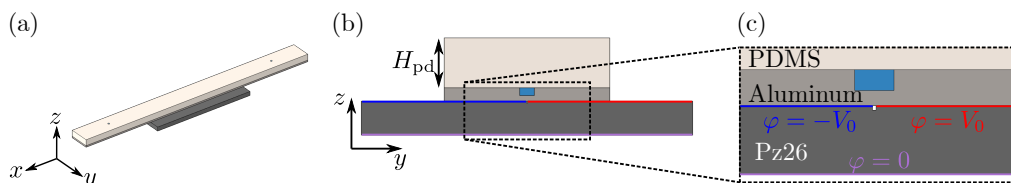
Figure 4. (**a**) 3D sketch drawn to scale of the proposed device driven by an anti-symmetric ac voltage. (**b**) The vertical cross section showing the thickness H_{pd} of the PDMS cover. (**c**) Zoom-in on the water-filled microchannel showing the PDMS cover, the aluminum base, the Pz26 transducer, and its 9-μm-thick silver electrodes, with ground on the bottom electrode (purple) and anti-symmetric ac voltage positive/negative (blue/red) applied to the split top electrode.

4.1. Numerical Optimization of the Thickness of the PDMS Cover

To illustrate how the thickness H_{pd} of the PDMS cover affects the resonances, we vary H_{pd}, and for each value, we sweep the frequency f from 1.5 MHz to 2.5 MHz in steps of 5 kHz to locate the resonances in terms of peaks in the focusing figure of merit $\mathcal{F}$ versus f. Such a spectrum is plotted in Figure 5a, where the area of each point is proportional to $\mathcal{F}$. For the same cover thickness $H_{pd} = 1.5$ mm

as in the side-actuated mode "S" of Figure 3 with $E_{ac} = 8.9$ J/m^3, we find a resonance mode "A'" at $f = 2.095$ MHz with $E_{ac} = 4.6$ J/m^3. An even better resonance mode can be found. In Figure 5a a strong resonance, which depends on the PDMS-cover thickness, is indicated by the blue curve. The optimal cover thickness along this curve is found to be $H_{pd} = 80$ µm at $f = 2.070$ MHz, identified as resonance mode "A", which yields an acoustic energy density of 96 J/m^3, twenty times larger than "A'".
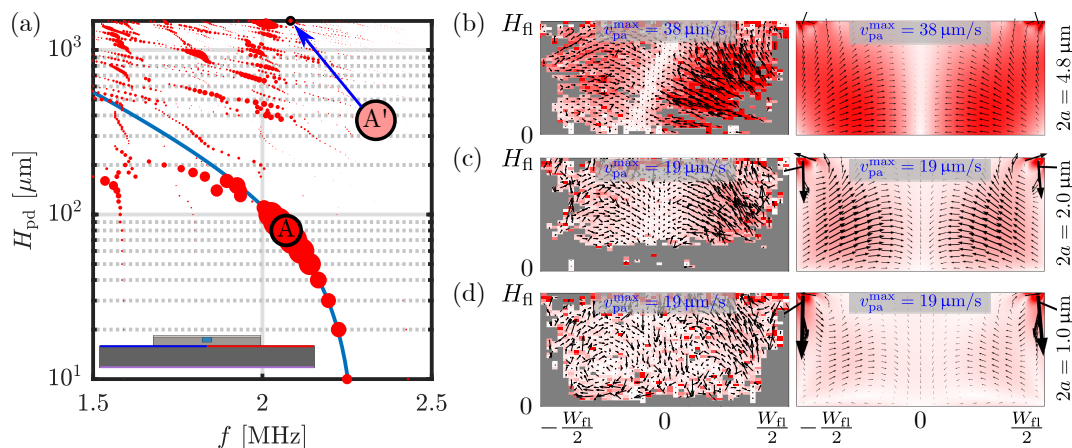
Figure 5. (**a**) Resonance peaks in the single-PDMS-cover aluminum-based device with anti-symmetric voltage actuation, Figure 4, as a function of the actuation frequency f and the thickness H_{pd} of the PDMS cover. The area of the points is proportional to the focusing figure of merit $\mathcal{F}$ defined in Equation (15). The "A'" marks the resonance mode for $H_{pd} = 1.5$ mm as in mode "S" of Figure 3. The "A" marks the resonance for the optimal cover thickness $H_{pd} = 80$ µm. The blue curve indicates resonances sensitive to H_{pd}. (**b**–**d**) Color and vector plot of the measured (left column) and simulated (right column) acoustophoretic particle velocity v_{pa} of mode "A'", for particle diameters 4.8, 2.0, and 1.0 µm, respectively. The measured resonance frequency was $f = 2.052$ MHz and the simulated was found at $f = 2.095$ MHz (2% higher). All color plots range from 0 µm/s (white) up to v_{pa}^{max} (red) with values 38 or 19 µm/s as indicated in each panel.

In Figure 5b–d are shown experimental and simulated acoustophoretic particle velocities v_{pa} for three different particle diameters $2a = 4.8$, 2.0 and 1.0 µm in mode "A'". The magnitude $v_{pa} = 38$ µm/s for $a = 2.4$ µm in Figure 5b is similar to that for mode "S", $v_{pa} = 40$ µm/s in Figure 3c. As for mode "S" in Figure 3, also Figure 5 shows the well-known cross-over from radiation-force-dominated focusing motion of the largest particles to the streaming-roll-dominated motion of the smallest particles. Particular to the single-PDMS-cover device is, firstly, that in Figures 3c and 5d there is only one pair of counter-rotating vortices near the bottom aluminum wall, the other pair near the top-PDMS-cover is suppressed as anticipated, and secondly, very strong localized vortices appear in the top corners of the channel where the PDMS-cover joins the aluminum base.

For both mode "S" in Figure 3 and the anti-symmetric mode "A'" in Figure 5b–d there is good qualitative agreement between particle velocities v_{pa} and resonance frequencies f measured in 3D and simulated in 2D assuming translational invariance. Quantitatively, the agreement in f is better for mode "A'" ($+2\%$) than for mode "S" (-12%), presumably because the translational invariance is more severely broken in the latter case. In both cases the velocity magnitudes agrees within 30–50%. The skew (white) zero-velocity band observed in Figure 5b (left) indicates that the experimental device was not completely symmetric as in the model Figure 5b (right). The agreement between measured and simulated particle velocities v_{pa} implies that our model can provide reliable estimates of the acoustic energy densities E_{ac} in the devices.

4.2. The Role of Variations in the PDMS Material Properties

We suspect that the strong top-corner vortices appearing in Figures 3 and 5 are due to the nearly incompressible nature of PDMS, or equivalently, the very low transverse speed of sound in PDMS. To investigate this hypothesis, we define an artificial polymer alloy of PDMS and Poly(Methyl MethAcrylate), $PDMS_x PMMA_{1-x}$ with mixing ratios x. In Figure 6 we study the four mixing ratios $x = 1.0, 0.99, 0.95$, and 0 in covers 80 μm thick. For each case, the resonance peak with the largest figure of merit $\mathcal{F}$ was found, and in close-up views of the channel are shown the corresponding particle velocity $\boldsymbol{v}_{pa}$ in the water and the displacement $\boldsymbol{u}$ in the surrounding solid.

In the case of a pure PDMS cover Figure 6a, a large displacement is narrowly confined to the top corners, this was also evident in Figures 3 and 5, where the maximum particle velocity was seen near the top corners. Already at 99% PDMS and 1% PMMA, Figure 6b, the transverse speed of sound in the polymer is two times greater than in pure PDMS, and the displacement field at the polymer-water interface is now more evenly distributed. This is even more pronounced for the case of 95% PDMS and 5% PMMA, Figure 6c, similarly for pure PMMA, Figure 6d. Note that in the latter case, the displacement in the cover is also resonating close to its transverse half-wave frequency. In conclusion, the low transverse speed of sound in PDMS seems to imply the appearance of strong streaming vortices localized near the PDMS-aluminum corners of the device.
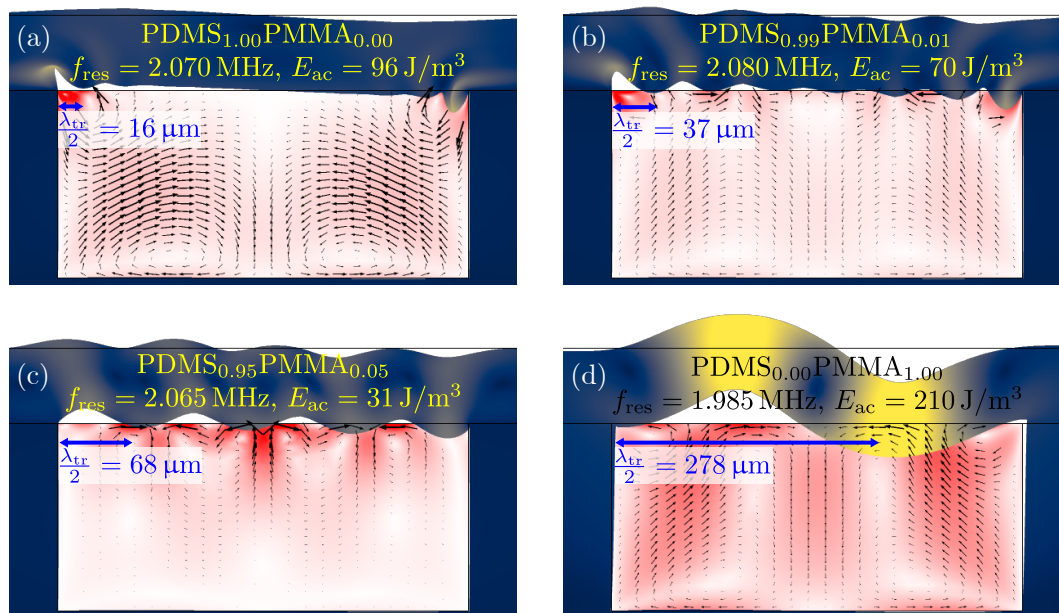
Figure 6. Zoom-in on the resonance modes for four different mixing ratios x of the artificial polymer alloy $PDMS_x PMMA_{1-x}$ with (**a**) $x = 1.00$, (**b**) $x = 0.99$, (**c**) $x = 0.95$, and (**d**) $x = 0.0$. For each case, the resonance frequency f_{res} is noted together with the average acoustic energy density E_{ac}, and the transverse wavelength λ_{tr} in the artificial PDMS-PMMA polymer cover. The color plots indicates the particle velocity magnitude $|\boldsymbol{v}_{pa}|$ in the water ranging from 0 (white) to the maximum value $v_{pa}^{max} = 258$ μm/s (red), and of the displacement $\boldsymbol{u}$ in surrounding solids ranging from 0 (dark blue) to 70 nm (yellow). The deformation is scaled 500 times to be visible.

5. Modeling Dual-PDMS-Cover Aluminum Devices with Anti-symmetric Voltage Actuation

In Figures 3c,d and 5d showing the acoustophoretic velocity fields for small microparticles suspended in the single-PDMS-cover device, we notice that whereas the usual Rayleigh flow rolls are present near the bottom aluminum wall, they seem to be suppressed near the PDMS cover. We therefore study the dual-PDMS-cover device sketched in Figure 7a to examine if both sets of Rayleigh flow rolls near the top and bottom wall can be suppressed. In Figure 7b we show one example of plotting the focusing figure of merit $\mathcal{F}$ of Equation (15) as a function of frequency f,

here for the specific case of $H_{top} = H_{bot} = 110$ μm. The strongest resonance is found at $f = 2.302$ MHz and is marked "B". A point with an area proportional to the computed value of $\mathcal{F}$ is then plotted at $(H_{top}, H_{bot}) = (110$ μm, 110 μm$)$ in the scatter plot of Figure 7c. Similarly, the strongest resonances are found and plotted in the scatter plot for three different parametric sweeps in the two cover thicknesses: (1) H_{bot} varies for fixed $H_{top} = 80$ μm (blue line), (2) H_{top} varies for fixed $H_{bot} = 110$ μm (yellow line), (3) the equal cover thicknesses $H_{top} = H_{bot}$ varies (cyan line). The strongest resonance or best value of the focusing figure of merit $\mathcal{F}$ is found at the peak "B" corresponding to the equal cover thicknesses $H_{top} = H_{bot} = 110$ μm driven at the frequency $f = 2.302$ MHz.
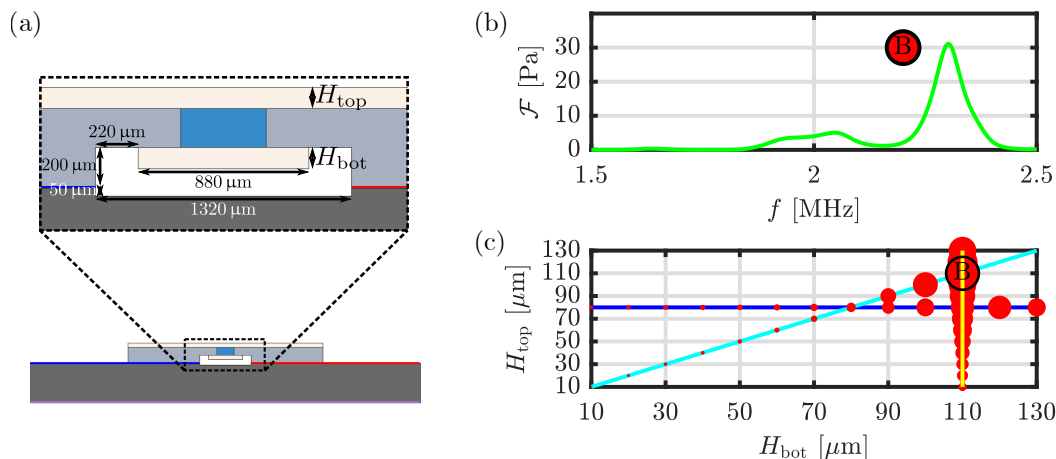
Figure 7. (**a**) Zoom-in on the channel in the dual-PDMS-cover setup, indicating the top cover thickness H_{top} and the bottom cover thickness H_{bot}. (**b**) Plot of the focusing figure of merit $\mathcal{F}$ versus frequency computed for the case $H_{top} = H_{bot} = 110$ μm leading to the identification of a strong resonance peak "B" at $f = 2.302$ MHz. (**c**) Scatter plot with area of the points proportional to the focusing figure of merit $\mathcal{F}$ for the strongest resonances identified in parametric sweeps of H_{bot} for fixed $H_{top} = 80$ μm (blue line), of H_{top} for fixed $H_{bot} = 110$ μm (yellow line), and for equal cover thicknesses $H_{top} = H_{bot}$ (cyan line). The configuration with the highest focusing quality is indicated with an encircled B.

In Figure 8, we study if indeed the streaming flow rolls are suppressed in the dual-PDMS-cover device compared to the single-PDMS-cover device. We compute the position of 400 1-μm-diameter polystyrene particles at discrete time steps (black dots) starting at a uniform distribution at time $t = 0$, where the acoustic field is turned on, and ending at time $t_{focus} = \frac{3}{2\Phi} \frac{c_{fl}^2}{\omega^2 a^2} \frac{\eta_{fl}}{E_{ac}}$ (red dots), the so-called focusing time determined by the acoustic contrast factor Φ given in Table A3 in Appendix A. Inertial effects can be ignored since the Reynolds number $\mathrm{Re}_{pa} = \frac{\rho_{fl} a v_{pa}}{\eta_{fl}} < 0.03$ for the given particles and acoustic fields.

Comparing the particle trajectories of mode "A" in the single-PDMS-cover device Figure 8a to those of mode "B" in the dual-PDMS-cover device Figure 8b, we clearly see that in the latter case the streaming flow rolls are suppressed. The dual-PDMS-cover device is therefore predicted to be a good candidate system for controlled focusing of sub-micrometer-sized particles. For this to work, it is of course essential that the focusing time is sufficiently short. For the given device actuated at $V_0 = 10$ V, the focusing time of the 1-μm-diameter particles is prohibitively long, namely $t_{focus} = 23.6$ s. Raising the driving voltage by a factor $\sqrt{20} \approx 4.5$ to $V_0 = 45$ V would lower the focusing time to $t_{focus} \approx 1$ s, because $t_{focus} \propto V_0^2$.
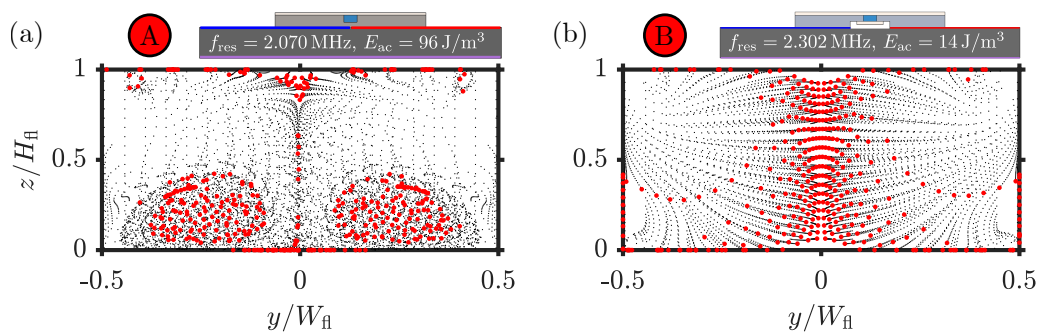
Figure 8. The positions (black dots) of suspended 1-µm-diameter polystyrene particles at discrete time steps from initial time $t = 0$ to final time $t = t_{\text{focus}}$ in anti-symmetrically actuated devices at selected resonance modes. The final positions at time $t = t_{\text{focus}}$ are marked by red dots. (**a**) Resonance mode "A" of Figure 5 with $E_{\text{ac}} = 96$ J/m^3 and $t_{\text{focus}} = 4.3$ s with two large vortices extending from the hard bottom aluminum-water interface, two small ones near the PDMS-aluminum corners and poor focusing. (**b**) Resonance mode "B" of Figure 7 with $E_{\text{ac}} = 14$ J/m^3 and $t_{\text{focus}} = 23.6$ s exhibiting four small vortices near the corners and good focusing.

6. Conclusions

We have developed a model for analyzing the single-PDMS-cover aluminum-base device with side actuation, recently introduced by Gautam et al. [20]. The model, currently restricted to the case of a constant 2D cross section in a translational invariant device, is validated experimentally with fair qualitative and quantitative agreement by fabricating and characterizing two types of single-PDMS-cover aluminum-base devices: One which is actuated with a symmetric ac-voltage on a Pz26 transducer placed at the side of the channel, and another with an anti-symmetric ac-voltage on a transducer placed right under the channel. Both numerical simulations and experiments support our hypothesis that using a soft PDMS cover of the acoustophoresis channel, the boundary driven acoustic streaming is suppressed in the bulk. The developed model can thus predict the streaming patterns in such devices, and we subsequently used it to show three aspects: (1) The incompressible nature of the soft PDMS cover introduces strong streaming rolls confined near the corners where the PDMS cover joins the aluminum base, while maintaining the conventional large Rayleigh streaming rolls extending from the aluminum-water interface; (2) An optimal thickness of the PDMS cover can be determined by simulation; (3) In devices with a dual-PDMS cover, the model predicts that the conventional Rayleigh streaming flow rolls should be suppressed and changed into vortices confined near the corners of the channel. Experimental work is in progress to verify these predictions.

Conflicts of Interest: The authors declare no conflict of interest.

Appendix A. Material Parameters

The following three tables contain the parameter values used in the numerical modeling of the PDMS-cover aluminum-based devices.

Table A1. Parameters for PZT transducer Pz26 [27] with damping coefficient $\Gamma_{sl} = 0.02$ [28].

Parameter	Value	Parameter	Value	Parameter	Value
ρ_{sl}	7700 kg/m^3	ε_{11}	828 ε_0	ε_{33}	700 ε_0
C_{11}	168 GPa	C_{33}	123 GPa	e_{31}	-2.8 C/m^2
C_{12}	110 GPa	C_{44}	30.1 GPa	e_{33}	14.7 C/m^2
C_{13}	99.9 GPa	C_{66}	29.0 GPa	e_{15}	9.86 C/m^2

Table A2. Parameters used in the linear-elastics modeling of aluminum, silver, and PDMS.

Parameter	Symbol	Aluminum 6061 [29]	Silver [30]	PDMS (10:1) Cured at 65 °C [31]	Unit
Mass density	ρ_{sl}	2700	10,485	1029	kg/m^3
Elastic modulus	C_{11}	$102\,(1 - i\Gamma_{sl})$	$134\,(1 - i\Gamma_{sl})$	$1.08 - i0.016$	GPa
Elastic modulus	C_{44}	$25.9\,(1 - i\Gamma_{sl})$	$25.9\,(1 - i\Gamma_{sl})$	$0.0075 - i0.0079$	GPa
Damping coefficient	Γ_{sl}	0.0013	0.0004	–	–

Table A3. Parameters for water and polystyrene tracer particles at 25 °C. The scattering coefficients are calculated in terms of the mass densities and compressibilities as $f_0 = 1 - \frac{\kappa_{pa}}{\kappa_{fl}}$ and $f_1 = \frac{2\left(\frac{\rho_{pa}}{\rho_{fl}} - 1\right)}{2\frac{\rho_{pa}}{\rho_{fl}} + 1}$ which in turn gives the acoustic contrast factor $\Phi = \frac{1}{3}f_0 + \frac{1}{2}f_1$.

Parameter	Symbol	Value	Parameter	Symbol	Value
Water [32]			**Polystyrene Particles [33]**		
Mass density	ρ_{fl}	997.05 kg/m^3	Mass density	ρ_{pa}	1050 kg/m^3
Compressibility	κ_{fl}	447.7 TPa^{-1}	Compressibility	κ_{pa}	238 TPa^{-1}
Dynamic viscosity	η_{fl}	0.890 mPa·s	Monopole coefficient	f_0	0.468
Bulk viscosity	η_{fl}^b	2.485 mPa·s	Dipole coefficient	f_1	0.034
Speed of sound	c_{fl}	1496.7 m/s	Contrast factor	Φ	0.173

References

1. Lenshof, A.; Evander, M.; Laurell, T.; Nilsson, J. Acoustofluidics 5: Building microfluidic acoustic resonators. *Lab Chip* **2012**, *12*, 684–695. [CrossRef] [PubMed]
2. Lilliehorn, T.; Simu, U.; Nilsson, M.; Almqvist, M.; Stepinski, T.; Laurell, T.; Nilsson, J.; Johansson, S. Trapping of microparticles in the near field of an ultrasonic transducer. *Ultrasonics* **2005**, *43*, 293–303. [CrossRef]
3. Evander, M.; Johansson, L.; Lilliehorn, T.; Piskur, J.; Lindvall, M.; Johansson, S.; Almqvist, M.; Laurell, T.; Nilsson, J. Noninvasive acoustic cell trapping in a microfluidic perfusion system for online bioassays. *Anal. Chem.* **2007**, *79*, 2984–2991. [CrossRef]
4. Hammarström, B.; Evander, M.; Barbeau, H.; Bruzelius, M.; Larsson, J.; Laurell, T.; Nillsson, J. Non-contact acoustic cell trapping in disposable glass capillaries. *Lab Chip* **2010**, *10*, 2251–2257. [CrossRef] [PubMed]
5. Lei, J.; Glynne-Jones, P.; Hill, M. Acoustic streaming in the transducer plane in ultrasonic particle manipulation devices. *Lab Chip* **2013**, *13*, 2133–2143. [CrossRef] [PubMed]
6. Mishra, P.; Hill, M.; Glynne-Jones, P. Deformation of red blood cells using acoustic radiation forces. *Biomicrofluidics* **2014**, *8*, 034109. [CrossRef]
7. Gralinski, I.; Raymond, S.; Alan, T.; Neild, A. Continuous flow ultrasonic particle trapping in a glass capillary. *J. Appl. Phys.* **2014**, *115*, 054505. [CrossRef]
8. Hammarström, B.; Laurell, T.; Nilsson, J. Seed particle enabled acoustic trapping of bacteria and nanoparticles in continuous flow systems. *Lab Chip* **2012**, *12*, 4296–4304. [CrossRef]

9. Evander, M.; Gidlof, O.; Olde, B.; Erlinge, D.; Laurell, T. Non-contact acoustic capture of microparticles from small plasma volumes. *Lab Chip* **2015**, *15*, 2588–2596. [CrossRef]

10. Harris, N.; Hill, M.; Keating, A.; Baylac-Choulet, P. A Lateral Mode Flow-through PMMA Ultrasonic Separator. *Intl. J. Appl. Biomed. Eng.* **2012**, *5*, 20–27.

11. Mueller, A.; Lever, A.; Nguyen, T.V.; Comolli, J.; Fiering, J. Continuous acoustic separation in a thermoplastic microchannel. *J. Micromech. Microeng.* **2013**, *23*, 125006. [CrossRef]

12. Gonzalez, I.; Tijero, M.; Martin, A.; Acosta, V.; Berganzo, J.; Castillejo, A.; Bouali, M.M.; Luis Soto, J. Optimizing Polymer Lab-on-Chip Platforms for Ultrasonic Manipulation: Influence of the Substrate. *Micromachines* **2015**, *6*, 574–591. [CrossRef]

13. Yang, C.; Li, Z.; Li, P.; Shao, W.; Bai, P.; Cui, Y. Acoustic particle sorting by integrated micromachined ultrasound transducers on polymerbased microchips. In Proceedings of the IEEE International Ultrasonics Symposium (IUS), Washington, DC, USA, 6–9 September 2017; pp. 1–4.

14. Savage, W.J.; Burns, J.R.; Fiering, J. Safety of acoustic separation in plastic devices for extracorporeal blood processing. *Transfusion* **2017**, *57*, 1818–1826. [CrossRef] [PubMed]

15. Silva, R.; Dow, P.; Dubay, R.; Lissandrello, C.; Holder, J.; Densmore, D.; Fiering, J. Rapid prototyping and parametric optimization of plastic acoustofluidic devices for blood-bacteria separation. *Biomed. Microdevices* **2017**, *19*, 70. [CrossRef]

16. Lissandrello, C.; Dubay, R.; Kotz, K.T.; Fiering, J. Purification of Lymphocytes by Acoustic Separation in Plastic Microchannels. *SLAS Technol.* **2018**, *23*, 352–363. [CrossRef]

17. Moiseyenko, R.P.; Bruus, H. Whole-System Ultrasound Resonances as the Basis for Acoustophoresis in All-Polymer Microfluidic Devices. *Phys. Rev. Appl.* **2019**, *11*, 014014. [CrossRef]

18. Adams, J.D.; Ebbesen, C.L.; Barnkob, R.; Yang, A.H.J.; Soh, H.T.; Bruus, H. High-throughput, temperature-controlled microchannel acoustophoresis device made with rapid prototyping. *J. Micromech. Microeng.* **2012**, *22*, 075017. [CrossRef]

19. Xu, K.; Clark, C.P.; Poe, B.L.; Lounsbury, J.A.; Nilsson, J.; Lauren, T.; Landers, J.P. Isolation of a Low Number of Sperm Cells from Female DNA in a Glass-PDMS-Glass Microchip via Bead-Assisted Acoustic Differential Extraction. *Anal. Chem.* **2019**, *91*, 2186–2191. [CrossRef]

20. Gautam, G.P.; Burger, T.; Wilcox, A.; Cumbo, M.J.; Graves, S.W.; Piyasena, M.E. Simple and inexpensive micromachined aluminum microfluidic devices for acoustic focusing of particles and cells. *Anal. Bioanal. Cham.* **2018**, *410*, 3385–3394. [CrossRef]

21. Skov, N.R.; Bach, J.S.; Winckelmann, B.G.; Bruus, H. 3D modeling of acoustofluidics in a liquid-filled cavity including streaming, viscous boundary layers, surrounding solids, and a piezoelectric transducer. *AIMS Math.* **2019**, *4*, 99–111. [CrossRef]

22. Bach, J.S.; Bruus, H. Theory of pressure acoustics with viscous boundary layers and streaming in curved elastic cavities. *J. Acoust. Soc. Am.* **2018**, *144*, 766–784. [CrossRef] [PubMed]

23. Settnes, M.; Bruus, H. Forces acting on a small particle in an acoustical field in a viscous fluid. *Phys. Rev. E* **2012**, *85*, 016327. [CrossRef] [PubMed]

24. COMSOL Multiphysics 5.4. 2018. Available online: http://www.comsol.com (accessed on 3 February 2020).

25. Barnkob, R.; Kähler, C.J.; Rossi, M. General defocusing particle tracking. *Lab Chip* **2015**, *15*, 3556–3560. [CrossRef] [PubMed]

26. Institut für Strömungsmechanik und Aerodynamik, Univeristät der Bundeswher. GDTPlab—How to Get It. Available online: https://www.unibw.de/lrt7/gdpt-1/gdptlab-how_to_get_it (accessed on 17 February 2020).

27. Meggit A/S, Porthusvej 4, DK-3490 Kvistgaard, Denmark. Ferroperm Matdat 2017. Available online: https://www.meggittferroperm.com/materials/ (accessed on 17 February 2020).

28. Hahn, P.; Dual, J. A numerically efficient damping model for acoustic resonances in microfluidic cavities. *Phys. Fluids* **2015**, *27*, 062005. [CrossRef]

29. ASM Aerospace Specification Metals Inc., Pompano Beach (Fl) USA. ASM Aluminum 6061. Available online: http://asm.matweb.com/search/SpecificMaterial.asp?bassnum=MA6061T6, (accessed on 3 February 2020).

30. AZO Materials, Manchester, UK. AZO—Applications and Properties of Silver. Available online: https://www.azom.com/properties.aspx?ArticleID=600 (accessed on 3 February 2020).

31. Skov, N.R.; Sehgal, P.; Kirby, B.J.; Bruus, H. Three-Dimensional Numerical Modeling of Surface-Acoustic-Wave Devices: Acoustophoresis of Micro- and Nanoparticles Including Streaming. *Phys. Rev. Appl.* **2019**, *12*, 044028. [CrossRef]

32. Muller, P.B.; Bruus, H. Numerical study of thermoviscous effects in ultrasound-induced acoustic streaming in microchannels. *Phys. Rev. E* **2014**, *90*, 043016. [CrossRef]
33. Karlsen, J.T.; Bruus, H. Forces acting on a small particle in an acoustical field in a thermoviscous fluid. *Phys. Rev. E* **2015**, *92*, 043010. [CrossRef]

6.2   Paper II: J. Acoust. Soc. Am. 149(5), 3096-3105 (2021)

Numerical study of the coupling layer between transducer and chip in acoustofluidic devices

Authors: W. N. Bodé and H. Bruus.

Numerical study of the coupling layer between transducer and chip in acoustofluidic devices[a)]

William Naundrup Bodé[b)] and Henrik Bruus[c)]

Department of Physics, Technical University of Denmark, Danmarks Tekniske Universitet Physics Building 309, Kongens Lyngby, DK-2800, Denmark

ABSTRACT:

By numerical simulation in two and three dimensions, the coupling layer between the transducer and microfluidic chip in ultrasound acoustofluidic devices is studied. The model includes the transducer with electrodes, microfluidic chip with a liquid-filled microchannel, and coupling layer between the transducer and chip. Two commonly used coupling materials, solid epoxy glue and viscous glycerol, as well as two commonly used device types, glass capillary tubes and silicon-glass chips, are considered. It is studied how acoustic resonances in ideal devices without a coupling layer are either sustained or attenuated as a coupling layer of increasing thickness is inserted. A simple criterion based on the phase of the acoustic wave for whether a given zero-layer resonance is sustained or attenuated by the addition of a coupling layer is established. Finally, by controlling the thickness and the material, it is shown that the coupling layer can be used as a design component for optimal and robust acoustofluidic resonances.
© 2021 Acoustical Society of America. https://doi.org/10.1121/10.0004871

I. INTRODUCTION

The acoustic impedance matching techniques for piezoelectric (PZT) sensors and transducers is, in general, a well-studied field as exemplified by the recent review by Rathod.[1] However, specifically for ultrasound acoustofluidic devices, the role of the coupling layer (also known as the carrier or matching layer) between the transducer and microfluidic chip remains poorly understood beyond one-dimensional (1D) planar systems.[2,3] Whereas the function of a matching layer for 1D traveling waves through layered structures is simply to couple acoustic energy more efficiently into subsequent layers, its role in resonant 1D acoustofluidic systems is less straightforward. As analyzed by Glynne-Jones *et al.*,[3] the function of the coupling layer may be more structural to isolate the transducer from the fluid layer. In the present work, we study the more complex case of a fully three-dimensional (3D) acoustofluidic system.

Extending the numerical study by Hahn and Dual, given for one specific device with a 20-μm-thick epoxy glue coupling layer,[4] we present 3D numerical simulations of a PZT transducer coupled to an acoustofluidic chip through a thin coupling layer of varying thickness, consisting of either a solid glue or viscous liquid. We consider two commonly used types of acoustofluidic devices sketched in Fig. 1, glass capillary tubes and silicon-glass chips. Capillary-tube devices have been applied as acoustic particle traps, relying on a

small transducer that actuates a vertical resonant pressure mode locally in the capillary.[5–8] Silicon-glass devices have been applied for continuous-flow focusing and separation of particle suspensions, relying on the bulk actuation of horizontal resonance modes in embedded microchannels.[9–11]

The paper is organized as follows. In Sec. II, we present the basic theory, including governing equations and boundary conditions. In Sec. III, we model the capillary-tube particle traps and show their dependency on the coupling-layer thickness. In Sec. IV, a similar analysis is carried out for the conventional acoustophoresis silicon-glass devices. Finally, in Sec. V, we present a concluding discussion regarding the criterion established in Secs. III and IV for designing acoustofluidic devices with acoustic resonance modes that are relatively insensitive to the thickness of the coupling layer.

II. THEORY AND MODEL ASSUMPTIONS

In establishing the numerical model, we closely follow the theory presented by Skov *et al.*[12] Our model consists of a lead-zirconate-titanate PZT transducer coupled to an elastic solid, which contains the fluid-filled microchannel. Theoretically, the system is described by three continuous fields: the electric potential φ in the PZT transducer, the mechanical displacement field $\boldsymbol{u}$ in the elastic solid and the PZT transducer, and the acoustic pressure p_1 in the fluid. The coupling layer is described by p_1 if it is a liquid and $\boldsymbol{u}$ if it is a solid. Due to the linearity of the governing equations, all fields have a harmonic time dependence $\mathrm{e}^{-\mathrm{i}\omega t}$ with an angular frequency $\omega = 2\pi f$ and frequency f. Thus, a given field has the structure $\tilde{f}(\boldsymbol{r}, t) = f(\boldsymbol{r})\,\mathrm{e}^{-\mathrm{i}\omega t}$, and we need only

(a) Glass capillary tube

Transducer

(b) Silicon-glass chip

Transducer

1 cm
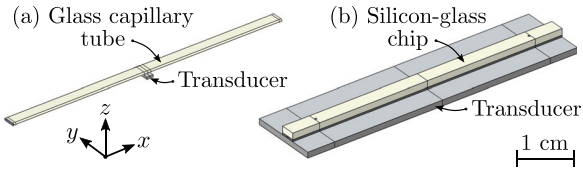
FIG. 1. (Color online) Sketch of the two types of acoustofluidic devices considered in this study. (a) A glass capillary tube (beige) mounted on a small PZT transducer (gray) and (b) a silicon-glass chip (black base, beige lid) mounted on a large PZT transducer (gray). The sketches are drawn to scale.

determine the complex-valued space-dependent amplitude $f(\boldsymbol{r})$.

The acoustic pressure field p_1 is modeled using the effective pressure acoustic theory by Bach and Bruus,[13] where the viscous boundary layers are included analytically in the effective boundary conditions. Using the effective theory, the acoustic pressure p_1 in a fluid with density ρ_0, sound speed c_0, dynamic viscosity η_0, and bulk viscosity η^b is governed by the Helmholtz equation, and the acoustic velocity $\boldsymbol{v}_1$ is proportional to ∇p_1,

$$\nabla^2 p_1 = -k_c^2 p_1, \quad \boldsymbol{v}_1 = -\mathrm{i}\frac{1-\mathrm{i}\Gamma}{\omega\rho_0}\nabla p_1, \qquad (1a)$$

with

$$k_0 = \frac{\omega}{c_0}, \quad k_c = \left(1 + \frac{\mathrm{i}}{2}\Gamma\right)k_0, \qquad (1b)$$

and

$$\Gamma = \left(\frac{\eta^b}{\eta_0} + \frac{4}{3}\right)\frac{\omega\eta_0}{\rho_0 c_0^2}. \qquad (1c)$$

In cases in which the fluid coupling-layer thickness Δ is comparable or smaller than the viscous boundary-layer

length scale $\delta_{\mathrm{visc}} = \sqrt{2\eta_0/(\rho_0\omega)}$, the effective theory fails, and the full perturbation model is used instead.[14,15]

The mechanical displacement field $\boldsymbol{u}$ is governed by the linear Cauchy equation, involving the stress tensor $\boldsymbol{\sigma}$,

$$-\rho_0\omega^2\boldsymbol{u} = \nabla\cdot\boldsymbol{\sigma}. \qquad (2)$$

The components σ_{ik} of $\boldsymbol{\sigma}$ are related to the strain components $\frac{1}{2}(\partial_i u_k + \partial_k u_i)$ by the stiffness tensor $\boldsymbol{C}$, which, for linear isotropic or cubic-symmetric elastic materials, are written in the Voigt notation as

$$\begin{pmatrix}\sigma_{xx}\\\sigma_{yy}\\\sigma_{zz}\\\sigma_{yz}\\\sigma_{xz}\\\sigma_{xy}\end{pmatrix} = \begin{pmatrix}C_{11} & C_{12} & C_{12} & 0 & 0 & 0\\C_{12} & C_{11} & C_{12} & 0 & 0 & 0\\C_{12} & C_{12} & C_{11} & 0 & 0 & 0\\0 & 0 & 0 & C_{44} & 0 & 0\\0 & 0 & 0 & 0 & C_{44} & 0\\0 & 0 & 0 & 0 & 0 & C_{44}\end{pmatrix}$$
$$\times \begin{pmatrix}\partial_x u_x\\\partial_y u_y\\\partial_z u_z\\\partial_y u_z + \partial_z u_y\\\partial_x u_z + \partial_z u_x\\\partial_x u_y + \partial_y u_x\end{pmatrix}. \qquad (3)$$

Mechanical damping is implemented as complex-valued elastic moduli, defined as $C_{ik} = (1 - \mathrm{i}\Gamma_{\mathrm{sl}})c_{ik}$. In the PZT transducer, the electric potential φ is governed by the quasi-static Gauss equation, involving the electric displacement $\boldsymbol{D}$,

$$\nabla\cdot\boldsymbol{D} = 0. \qquad (4)$$

Furthermore, in PZT, the complete linear electromechanical coupling relating the stress and electric displacement to the strain and electric field is given by the Voigt notation as

$$\begin{pmatrix}\sigma_{xx}\\\sigma_{yy}\\\sigma_{zz}\\\sigma_{yz}\\\sigma_{xz}\\\sigma_{xy}\\D_x\\D_y\\D_z\end{pmatrix} = \begin{pmatrix}C_{11} & C_{12} & C_{13} & 0 & 0 & 0 & 0 & 0 & -e_{31}\\C_{12} & C_{11} & C_{13} & 0 & 0 & 0 & 0 & 0 & -e_{31}\\C_{13} & C_{13} & C_{33} & 0 & 0 & 0 & 0 & 0 & -e_{33}\\0 & 0 & 0 & C_{44} & 0 & 0 & 0 & -e_{15} & 0\\0 & 0 & 0 & 0 & C_{44} & 0 & -e_{15} & 0 & 0\\0 & 0 & 0 & 0 & 0 & C_{66} & 0 & 0 & 0\\0 & 0 & 0 & 0 & e_{15} & 0 & \varepsilon_{11} & 0 & 0\\0 & 0 & 0 & e_{15} & 0 & 0 & 0 & \varepsilon_{11} & 0\\e_{31} & e_{31} & e_{33} & 0 & 0 & 0 & 0 & 0 & \varepsilon_{33}\end{pmatrix}\begin{pmatrix}\partial_x u_x\\\partial_y u_y\\\partial_z u_z\\\partial_y u_z + \partial_z u_y\\\partial_x u_z + \partial_z u_x\\\partial_x u_y + \partial_y u_x\\-\partial_x\varphi\\-\partial_y\varphi\\-\partial_z\varphi\end{pmatrix}. \qquad (5)$$

A. Acoustic energy density

Throughout this study, the time- and volume-averaged acoustic energy density E_{ac} in the water-filled channel is

used as a measure and indicator of how the acoustic resonances are affected by the coupling layer. In a fluid volume V, the averaged acoustic energy density is given as

$$E_{\text{ac}} = \frac{1}{V} \int \left(\frac{1}{4} \rho_0 |\boldsymbol{v}_1|^2 + \frac{1}{4} \kappa_0 |p_1|^2 \right) dV. \tag{6}$$

B. Boundary conditions

At the fluid–solid interface, the boundary conditions are no-slip and continuous stress, together with zero stress on the free surfaces. Introducing the mechanical displacement velocity $\boldsymbol{v}_{\text{sl}} = -\mathrm{i}\omega\boldsymbol{u}$ and a shear wave number $k_s = (1 + \mathrm{i})/\delta_{\text{visc}}$, the effective continuous velocity and stress boundary conditions become[13]

$$\boldsymbol{n} \cdot \boldsymbol{v}_1 = \boldsymbol{n} \cdot \boldsymbol{v}_{\text{sl}} + \frac{\mathrm{i}}{k_s} \boldsymbol{\nabla}_\parallel \cdot (\boldsymbol{v}_{\text{sl}} - \boldsymbol{v}_1), \tag{7a}$$

$$\boldsymbol{\sigma} \cdot \boldsymbol{n} = -p_1 \boldsymbol{n} + \mathrm{i}k_s\eta_0 \left(\boldsymbol{v}_{\text{sl}} + \frac{\mathrm{i}}{\omega\rho_0} \boldsymbol{\nabla}p_1 \right), \tag{7b}$$

where the unit vector $\boldsymbol{n}$ is the outward surface normal from the solid domain. In experiments, the electrical signal is driven by a sine-wave function generator coupled to the transducer electrodes. This setup is implemented as a constant-potential boundary condition on the electrode–transducer interface. Furthermore, we assume no free charges, which is implemented as a zero flux condition on the electric displacement field $\boldsymbol{D}$. In the 3D capillary-tube device, symmetries are exploited such that the full system can be reduced to one-quarter. The boundary conditions are listed in Table I. Except for the symmetry conditions, the same boundary condition applies for the silicon-glass device.

C. Unbounded perfectly matched layers

For long systems like the capillary tubes, a no-reflection boundary condition can be established closer to the origin of the domain by using the perfectly matched layer (PML) technique, thus, reducing the computational domain substantially. It involves a complex coordinate transformation of the form $x \to x + (\mathrm{i}/\omega)\int^x \theta(x')\,dx'$, such that outgoing waves are attenuated within a distance comparable to the wavelength. The PML technique requires a choice of damping function θ, and we adopt the one from Bermúdez *et al.*[16]

TABLE I. List of the boundary conditions used in the modeled acoustofluidic systems. The unit vector $\boldsymbol{n}$ is the surface outward normal with respect to the solid domain, and $\boldsymbol{t}$ is any of the two tangential unit vectors. $V_0 = 1$ V.

Domain ← boundary	Boundary condition
Solid domain ← air	$\boldsymbol{\sigma} \cdot \boldsymbol{n} = \boldsymbol{0}$
Fluid domain ← solid	Eq. (7a)
Solid domain ← fluid	Eq. (7b)
Fluid domain ← air	$p_1 = 0$
PZT domain ← bottom electrode	$\varphi = 0$
PZT domain ← top electrode	$\varphi = V_0$
Solid domain ← symmetry	$\boldsymbol{u} \cdot \boldsymbol{n} = 0,\ \boldsymbol{t} \cdot \boldsymbol{\sigma} \cdot \boldsymbol{n} = 0$
Fluid domain ← symmetry	$\boldsymbol{n} \cdot \boldsymbol{\nabla}p_1 = 0$

$$\theta(x) = \begin{cases} 0, & \text{for } x \leq L_{\text{cap}}, \\ \dfrac{\beta}{L_{\text{pml}} - (x - L_{\text{cap}})} - \dfrac{\beta}{L_{\text{pml}}}, & \text{for } x > L_{\text{cap}}. \end{cases} \tag{8}$$

The parameters defining $\theta(x)$ are chosen appropriately for a given system: L_{cap} is the position of the interface between the physical capillary tube and PML domain, L_{pml} is the length of the PML domain, and β is the damping strength. The axial coordinate x is complex valued for $x > L_{\text{cap}}$ inside the PML domain. The function θ is classified as a continuous unbounded damping function, and it is effective in terms of numerical error and reflections at the PML interface $x = L_{\text{cap}}$.[16]

D. Numerical implementation in COMSOL Multiphysics

The numerical model was implemented in the finite element software COMSOL Multiphysics[17] using "weak form PDE" in the mathematics module and closely following Ref. 12, where further implementation details can be found. The mesh settings are adopted from Ley and Bruus.[18] The scripts were computed on a workstation with a 12 core 3.5 GHz central processing unit (CPU) processor and 128 GB random access memory (RAM).

III. CAPILLARY-TUBE PARTICLE TRAPS

As the first example, we investigate the capillary-tube device that is widely used as a versatile acoustic trap in many experimental studies.[5–8] The corresponding model system is sketched in Fig. 2, indicating the different domains together with the PML layer and a zoom-in on the coupling layer. The dimensions and materials used in the numerical model are listed in Tables II and III, respectively. The model system is similar to the one studied by Ley and Bruus,[18] but now the model is extended to include a PZT transducer and coupling layer. Typically, the capillary-tube device is
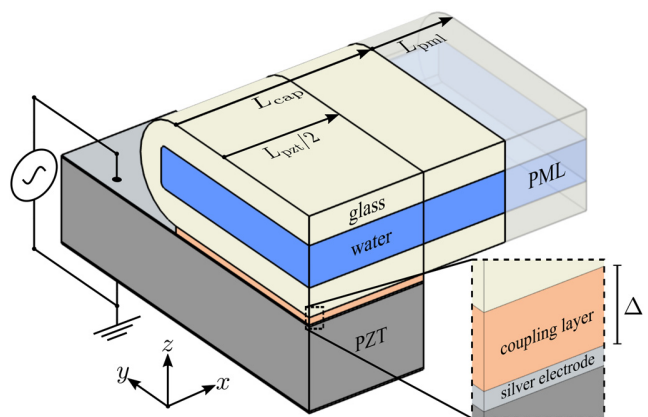
FIG. 2. (Color online) One-quarter of the capillary-tube-based model system with a zoom-in on the coupling layer of thickness Δ. The model system includes a water-filled glass capillary coupled to a PZT transducer with silver electrodes. The top electrode is coupled to a time-harmonic function generator and the bottom electrode is grounded.

TABLE II. The length (L), width (W), and height (H) of the glass capillary tube (cap), channel (ch), PZT transducer (pzt), and silver electrodes (el). The curvatures of the outer and inner rounded corners are $240\,\mu$m and $25\,\mu$m, respectively. The bottom ($H_{\mathrm{gl,bot}}$) and top ($H_{\mathrm{gl,top}}$) glass-wall thicknesses are both $140\,\mu$m.

Symbol	Value	Symbol	Value
L_{cap}	1573 μm	L_{ch}	1573 μm
W_{cap}	2280 μm	W_{ch}	2000 μm
H_{cap}	480 μm	H_{ch}	200 μm
L_{pzt}	1160 μm	L_{el}	1160 μm
W_{pzt}	3350 μm	W_{el}	3350 μm
H_{pzt}	400 μm	H_{el}	9 μm

characterized by having a standing half-wave-like resonance in the vertical direction. This is achieved with a PZT transducer having a predesigned mode at 5 MHz as used in preliminary experiments by the Laurell group at Lund University.

TABLE III. List of parameters used in the numerical simulations. Note that $C_{12} = C_{11} - 2C_{44}$ for the isotropic materials. Isotropy in the xy-plane implies $C_{66} = \frac{1}{2}(C_{11} - C_{12})$ for the PZT.

Parameter	Symbol	Value	Unit
Water at 25 °C (Ref. 19)			
Mass density	ρ_0	997.05	kg m^{-3}
Speed of sound	c_0	1496.7	m s^{-1}
Compressibility	κ_0	447.7	TPa^{-1}
Dynamic viscosity	η_0	0.890	mPa s
Bulk viscosity	η^{b}	2.485	mPa s
Isotropic Pyrex borosilicate glas (Ref. 20)			
Mass density	ρ_{sl}	2230	kg m^{-3}
Elastic modulus	c_{11}	69.7	GPa
Elastic modulus	c_{44}	26.2	GPa
Mechanical damping coeff.	Γ_{sl}	0.0004	—
Isotropic silver (Ref. 21)			
Mass density	ρ_{sl}	10 485	kg m^{-3}
Elastic modulus	c_{11}	133.9	GPa
Elastic modulus	c_{44}	25.9	GPa
Mechanical damping coefficient	Γ_{sl}	0.0004	—
Cubic-symmetric silicon (Ref. 22)			
Mass density	ρ_{sl}	2329	kg m^{-3}
Elastic modulus	c_{11}	165.7	GPa
Elastic modulus	c_{44}	79.6	GPa
Elastic modulus	c_{12}	63.9	GPa
Mechanical damping coefficient	Γ_{sl}	0.0001	—
Pz26 PZT ceramic (Refs. 4 and 23)			
Mass density	ρ_{sl}	7700	kg m^{-3}
Elastic modulus	c_{11}	168	GPa
Elastic modulus	c_{12}	110	GPa
Elastic modulus	c_{13}	99.9	GPa
Elastic modulus	c_{33}	123	GPa
Elastic modulus	c_{44}	30.1	GPa
Coupling constant	e_{15}	9.86	C/m^2
Coupling constant	e_{31}	−2.8	C/m^2
Coupling constant	e_{33}	14.7	C/m^2
Electric permittivity	ε_{11}	828	ε_0
Electric permittivity	ε_{33}	700	ε_0
Mechanical damping coefficient	Γ_{sl}	0.02	—

A. The specific PML

We implement no-reflection boundary conditions using a PML layer with parameter values $\beta = 2c_{\mathrm{lo}}^{(\mathrm{gl})} = 11.294$ m/s and $L_{\mathrm{pml}} = 413$ μm. The superscript refers to the material, in this case, glass (gl), and $c_{\mathrm{lo}}^{(\mathrm{gl})}$ and $\lambda_{\mathrm{lo}}^{(\mathrm{gl})}$ are the longitudinal sound speed and wavelength, respectively. The numerical error introduced by using the PML is shown in Fig. 3 in terms of the convergence parameter C, which for a given field solution g is defined by

$$C(g) = \sqrt{\frac{\int |g - g_{\mathrm{ref}}|^2 \mathrm{d}V}{\int |g_{\mathrm{ref}}|^2 \mathrm{d}V}}, \qquad (9)$$

where g_{ref} is a reference solution. The integration domain is taken as the transducer region for $x \leq L_{\mathrm{pzt}}/2$ as defined in Fig. 2. In Fig. 3, the error measure C is evaluated at six different geometries at a fixed frequency $f = 3.84$ MHz with $\lambda_{\mathrm{lo}}^{(\mathrm{gl})} = 1.47$ mm. The reference solution is taken as $L_{\mathrm{cap}} = 1.35\lambda_{\mathrm{lo}}^{(\mathrm{gl})}$. We choose the system length $L_{\mathrm{cap}} = 1.07\lambda_{\mathrm{lo}}^{(\mathrm{gl})}$ such that the maximal numerical error due to the unbounded PML is estimated to be $C = 3 \times 10^{-4}$.

B. Coupling-layer analysis in 3D and 1D models

Continuing with the physics studies, we consider two coupling materials: a viscous mixture of 99% volume-per-volume (v/v) glycerol and 1% v/v water, and a solid ED-20 epoxy resin, which from now on will be referred to as glycerol and epoxy for brevity. The coupling material parameters used in the simulations are listed in Table IV.

In practice, the glycerol coupling allows for reuseability of the acoustofluidic chip and/or transducer, whereas the epoxy is used to ensure a well-defined but permanent coupling.[9,24–27] These layers are reported to have a thickness in the range from 5 to 20 μm.[6,7,28–31] Here, we investigate the effect of the coupling layer by calculating the resonances as a function of coupling-layer material and thickness Δ using the 3D model. For each coupling-layer thickness Δ, the
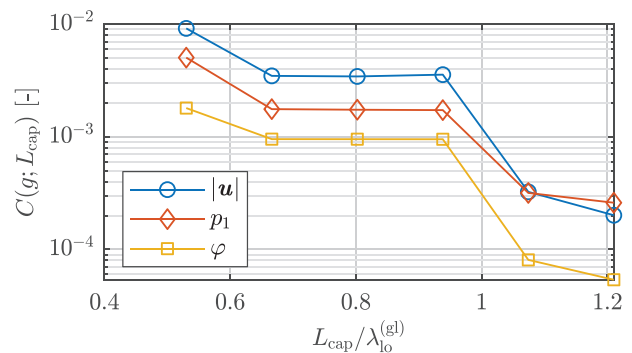
FIG. 3. (Color online) Numerical convergence C for $\boldsymbol{u}$, p_1, and φ in the PML of Fig. 2 at frequency $f_{\mathrm{res}} = 3.84$ MHz with wavelength $\lambda_{\mathrm{lo}}^{(\mathrm{gl})} = 1.47$ μm, PML length $L_{\mathrm{pml}} = 413$ μm, and the physical system length L_{cap} is varied as $L_{\mathrm{cap}}/\lambda_{\mathrm{lo}}^{(\mathrm{gl})} = 0.53$, 0.67, 0.80, 0.94, 1.07, and 1.21.

TABLE IV. List of the coupling layer parameters for glycerol (a 99% v/v glycerol and 1% v/v water mixture) and epoxy at 20 °C. The coefficient C_{12} of the epoxy is obtained through the relation $C_{12} = C_{11} - 2C_{44}$.

Parameter	Symbol	Value	Unit
Glycerol (Ref. 32–34)			
Mass density	ρ_{glc}	1260.4	kg m^{-3}
Speed of sound	c_{glc}	1922.8	m s^{-1}
Compressibility	κ_{glc}	214.6	TPa^{-1}
Dynamic viscosity	η_{glc}	1.137	Pa s
Bulk viscosity	η_{glc}^{b}	0.790	Pa s
Epoxy (Ref. 35)			
Mass density	ρ_{sl}	1205	kg m^{-3}
Elastic modulus	c_{11}	9.583	GPa
Elastic modulus	c_{44}	2.164	GPa
Mechanical damping coefficient	Γ_{sl}	0.01	—

average acoustic energy density E_{ac} in the water-filled channel is computed as a function of the frequency from 3.0 to 4.5 MHz. Resonances are then identified as peaks in the acoustic energy spectrum $E_{ac}(f)$. The resonances are illustrated in the scatterplot of Fig. 4, where the points represent resonances at a frequency f for a coupling-layer thickness Δ in the range from 0 to 100 μm with point areas proportional to E_{ac}/E_{ac}^{0}, where E_{ac}^{0} is the acoustic energy density without a coupling layer. The Δ-independent resonance frequencies of the unloaded PZT resonances are plotted to indicate where the transducer is most active.
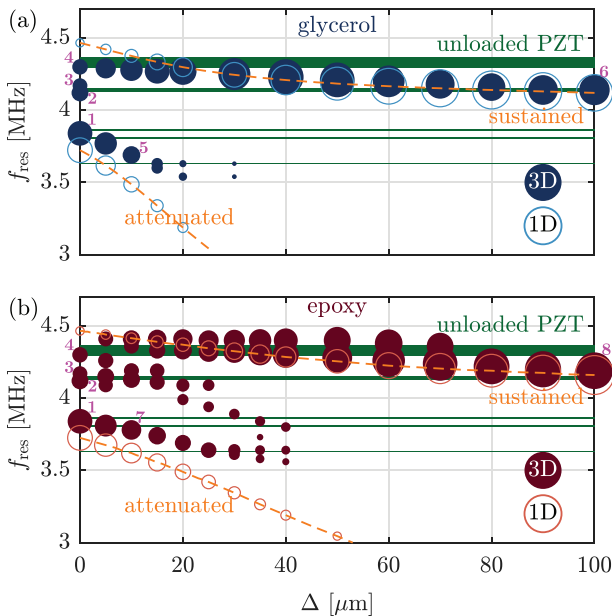
FIG. 4. (Color online) Resonance frequencies in the capillary-tube device as a function of increasing coupling-layer thickness Δ for (a) glycerol and (b) epoxy. The 3D and 1D model resonance frequencies are plotted as filled and empty circles, respectively, with an area proportional to E_{ac}/E_{ac}^{0}. The dashed lines represent the 1D resonance frequencies, indicating a sustained or attenuated behavior. The solid green lines indicate unloaded PZT resonances with a linewidth proportional to the logarithm of the acoustic energy density in the PZT. Animated gif-files of the eight modes enumerated 1–8 (magenta numbers) are given in the supplementary material (Ref. 36).

The 3D model reveals a distinct behavior for both glycerol and epoxy coupling layers: As the coupling layer Δ increases, one resonance is attenuated (E_{ac} decreases) and has a large downshift in frequency, whereas another is sustained (E_{ac} increases) and has a small downshift in frequency. This behavior is also observed in an idealized 1D layer model along the vertical z axis with seven domains: electrode, PZT, electrode, coupling layer, glass, water, glass of respective thicknesses H_{el}, H_{pzt}, H_{el}, Δ, $H_{gl,bot}$, H_{ch}, and $H_{gl,top}$. This 1D model takes into account only z-components, z-dependencies, densities, and longitudinal sound speeds in the governing equations. The 1D model resonances are plotted together with the 3D resonances in Fig. 4. Of course, Fig. 4 reveals that the 3D model exhibits more resonances than the 1D model due to the extended degrees of freedom in the transverse directions and shear waves.

In Fig. 4, we have selected eight 3D resonance modes enumerated 1–8 (magenta numbers). For each of these modes, we have computed an animated gif-file that shows the temporal behavior and is given in the supplementary material.[36] The five 3D resonance modes 1, 5, 6, 7, and 8, which are close to the 1D modes indicated by the orange-dashed lines in Fig. 4, indeed appear as 1D-like with a prominent standing wave in the vertical z-direction in the region above the transducer. This indicates that the attenuated and sustained resonance-mode effect represented by the 3D modes 1-5-7 and 6-8, respectively, can be explained by this 1D fluid-like model. The other three 3D resonance modes 2, 3, and 4, lying farther away from the 1D modes, have a more clear 3D nature with waves in all three spatial directions.

C. A design criterion for coupling layers

As the layer thickness Δ is changed from 0 to 100 μm, the sustaining and attenuating behaviors of the zero-layer resonances are elucidated by studying the pressure profiles for each of the resonances in the 1D model. For each profile, we choose a temporal phase factor $e^{-i\omega t}$ that gives the maximum *positive amplitude* in the PZT domain.

In Fig. 5(a), the 1D resonance pressure profiles are evaluated at three different epoxy coupling-layer thicknesses $\Delta = 0$, 20, and 50 μm for the sustained resonance. In Fig. 5(b), the same is shown for the attenuated resonance. Without the coupling layer, the fluid–solid interface is located at $z_0 = H_{pzt} + 2H_{el} + H_{gl,bot} = 558$ μm and has a coupling layer at $z_\Delta = z_0 + \Delta$. As a result, the value of the pressure $p_1(z_\Delta)$ is decreasing. In Fig. 5(a), labeled "sustained," we have $p_1(z_\Delta) < p_1(z_0) < 0$, yielding an *increased magnitude* of the pressure as Δ is increased. In contrast, in Fig. 5(b), labeled "attenuated," we have $0 < p_1(z_\Delta) < p_1(z_0)$, yielding a *decreasing magnitude* of the pressure for increasing Δ. Clearly, if a given zero-layer resonance has a negative (positive) value of $p_1(z_0)$ for the specified temporal phase factor, the resonance is sustained (attenuated). The sign of $p_1(z_0)$ is determined by the accumulated spatial phase factor $\Phi(z_0)$ of the fluid-solid value $p_1(z_0)$ relative to the surface value
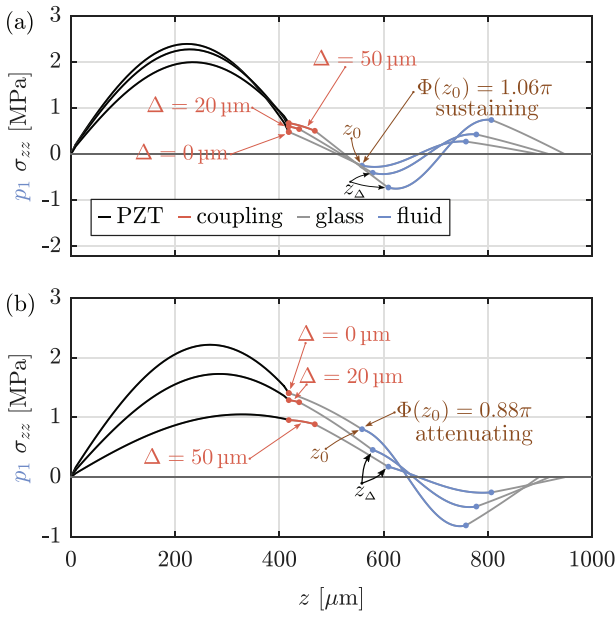
FIG. 5. (Color online) Plots of normal stress $\sigma_{zz}(z)$ and pressure $p_1(z)$ in the 1D model with an epoxy coupling layer for the three layer thicknesses $\Delta = 0$, 20, and 50 μm for (a) the sustained and (b) attenuated zero-layer resonance modes. The profiles are plotted at a phase where the amplitude is at a maximum. The accumulated phase Φ is calculated without a coupling layer at the fluid–solid interface at $z_0 = H_{pzt} + 2H_{el} + H_{gl,bot}$ (brown arrow).

$p_1(0)$. In the 1D model, $\Phi(z_0)$ is given by the wave number k_i and layer thickness H_i of each layer (i = PZT, electrodes, and glass placed at $z < z_0$). Consequently, we arrive at the criterion

$$\text{sustaining coupling if } \Phi(z_0) > \pi, \tag{10a}$$

$$\text{attenuating coupling if } \Phi(z_0) < \pi, \tag{10b}$$

with

$$\Phi(z_0) = \sum_i k_i H_i = \sum_i \frac{\omega}{c_{lo}^{(i)}} H_i. \tag{10c}$$

Note that this criterion is only valid for $|\Phi(z_0)| < \frac{3}{2}\pi$. For the given capillary-tube device, the values of $\Phi(z_0)$ for the sustained and attenuated zero-layer resonance are $3.32 = 1.06\pi$ and $2.77 = 0.88\pi$, respectively. The criterion [Eq. (10)] is an extension of previous 1D analyses[2,3] here shown to apply in a 3D analysis, and it is one of the main results of the paper. It can be used to design optimally coupled capillary devices with minimum attenuation caused by the coupling layer.

D. Characteristic coupling-layer attenuation thickness Δ_0

Based on the 1D model, we derive a semi-analytical estimate for the characteristic thickness Δ_0 at which the acoustic energy is attenuated for the abovementioned attenuated zero-layer resonance modes. The pressure solution $p_{1,i}$ to the Helmholtz equation in each domain i is written as

$$p_{1,i} = p_{a,i} \sin(k_i z + \phi_i) \quad \text{for } z \in \Omega_i. \tag{11}$$

At the interface between domain i and $i + 1$, the acoustic pressure and velocity must be continuous,

$$p_{1,i+1} = p_{1,i}, \quad \frac{1}{\rho_{i+1}} \partial_z p_{1,i+1} = \frac{1}{\rho_i} \partial_z p_{1,i}. \tag{12}$$

This results in an iterative formula for the amplitude $p_{a,i}$ and phase ϕ_i with coefficients $\beta_{i+1,i}$, $a_{i+1,i}$, and $b_{i+1,i}$,

$$p_{a,i+1} = \beta_{i+1,i} p_{a,i}, \tag{13a}$$

$$\phi_{i+1} = \phi_i - k_{i+1} \sum_j^i H_j + \arctan(a_{i+1,i}/b_{i+1,i}), \tag{13b}$$

$$\beta_{i+1,i} = \sqrt{1 + \cos^2\left(k_i \sum_j^i H_j + \phi_i\right)(Z_{i+1,i}^2 - 1)}, \tag{13c}$$

$$a_{i+1,i} = \beta_{i+1,i}^{-1} \sin\left(k_i \sum_j^i H_j + \phi_i\right), \tag{13d}$$

$$b_{i+1,i} = \beta_{i+1,i}^{-1} Z_{i+1,i} \cos\left(k_i \sum_j^i H_j + \phi_i\right), \tag{13e}$$

$$Z_{i+1,i} = \frac{\rho_{i+1} c_{lo}^{(i+1)}}{\rho_i c_{lo}^{(i)}}. \tag{13f}$$

For a coupling layer (cl) made of either epoxy or glycerol, we have a mismatch $Z_{cl,pzt} \ll 1$ in the acoustic impedance, and the pressure amplitude $p_1(z_0)$ at the interface z_0 can, therefore, be approximated as

$$p_1(z_0) \approx p_0 \sqrt{\alpha^2 + \beta^2} \sin(k_{cl} H_{pzt}) \\ \times \sin(\arctan(\alpha/\beta) + k_{gl} H_{gl}) + \mathcal{O}(Z_{cl,pzt}), \tag{14a}$$

with

$$\alpha = Z_{gl,cl} \sin(k_{cl}\Delta) \quad \text{and} \quad \beta = \cos(k_{cl}\Delta). \tag{14b}$$

By further assuming $E_{ac} \propto p_1^2(z_0)$ and $k_{cl}^2 \Delta^2 \ll 1$, the lowest order functional dependence in the layer thickness Δ becomes

$$E_{ac} \propto p_0^2 \sin^2(k_{cl} H_{pzt})\left[\cos^2(k_{gl} H_{gl}) - Z_{gl,cl} k_{cl}\Delta \sin(2k_{gl} H_{gl})\right]. \tag{15}$$

By setting $E_{ac} = 0$, we extract the characteristic thickness scale Δ_0 at which the resonance is attenuated

$$\Delta_0 = \frac{Z_{cl,gl} c_{lo}^{(cl)}}{2\omega} \cot\left(\frac{\omega H_{gl}}{c_{lo}^{(gl)}}\right). \tag{16}$$

In Fig. 6, the normalized acoustic energy density $E_{ac}(\Delta)/E_{ac}^0$ is plotted as a function of the normalized coupling-layer
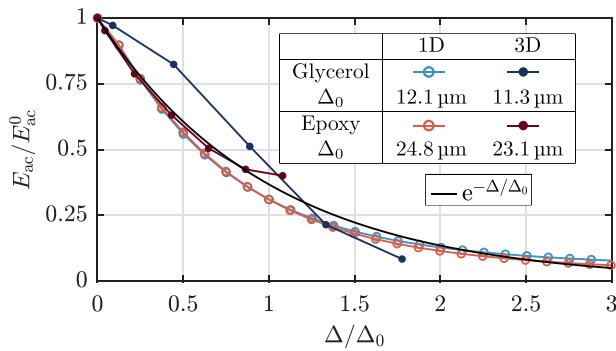
FIG. 6. (Color online) The normalized acoustic energy density E_{ac}/E_{ac}^0 for the attenuated capillary-tube resonance versus the normalized coupling-layer thickness Δ/Δ_0 for glycerol and epoxy, simulated in the 3D and 1D models. The exponential function $e^{-\Delta/\Delta_0}$ (black) is inserted as a guide to the eye.

thickness Δ/Δ_0. The acoustic energy is seen to be attenuated on the length scale Δ_0 as predicted by Eq. (16) with $\Delta_0 = 12.1\ \mu m$ and $24.8\ \mu m$ for glycerol and epoxy, respectively. For both coupling materials, we observe an approximate exponential decay, $E_{ac}(\Delta)/E_{ac}^0 = e^{-\Delta/\Delta_0}$. Figure 6 also shows that the attenuation computed in the 3D model is captured fairly well by the 1D model, including good quantitative agreement within 7% between the estimated characteristic length scale Δ_0 in the 1D and 3D models, respectively.

IV. ACOUSTOPHORETIC BULK DEVICES

We now move on to the second type of acoustofluidic devices, namely, the bulk silicon-glass devices used in many lab-on-a-chip applications as reviewed by Lenshof et al.[37] As sketched in Fig. 1(b), these devices consist of a silicon-glass-based acoustofluidic chip coupled to a bulk PZT transducer. In contrast to the capillary-tube devices, the manipulation of the particles in the silicon-glass chip relies on horizontal half-wave pressure resonances. Because the pressure half-wave is anti-symmetric around the vertical center plane of the channel, the symmetric motion actuated by a usual PZT transducer must be broken. This is normally done geometrically by placing the transducer off-center[9,15,38] or splitting the top electrode of the transducer and actuated it by an anti-symmetric voltage actuation.[27,39] The symmetry breaking could also be achieved by incorporating side walls with different angles or curvatures. In this work, we use the first method and displace the silicon-glass chip by $y_0 = 1$ mm with respect to the (xz)-mirror-plane of the PZT transducer; see Fig. 7.

A. Coupling layer analysis in 2D

It is well known that even with an ideal long straight channel in such devices, axial variations and acoustic hot spots appear along the channel.[40] However, when studying a region in the channel near a local maximum in the acoustic field where the axial gradients are vanishing small, 2D models describe the acoustic fields very well.[15,40] In this
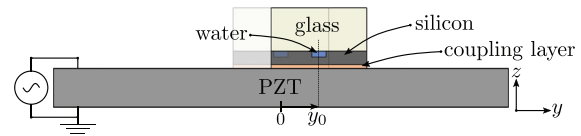
FIG. 7. (Color online) Cross section in the vertical yz-plane of the silicon-glass device in Fig. 1(b), showing the PZT transducer, coupling layer, and silicon-glass chip with the microchannel (blue). The chip is displaced from the PZT center plane by $y_0 = 1$ mm. The sketch defines the 2D model; see Table V.

analysis, we, therefore, study the silicon-glass device in a 2D model as shown in Fig. 7. As introduced in Sec. II, the PZT transducer is a z-polarized Meggitt-Pz26 transducer (Meggitt A/S, Kvistgaard, Denmark) but now with a thickness of $1000\ \mu m$ with a resonance mode near 2 MHz. The materials and dimensions used in the silicon-glass-device simulations are listed in Tables III and V, respectively.

The coupling layer analysis is analogous to the one in Sec. III. The acoustic resonances are located as peaks in the acoustic energy density spectrum $E_{ac}(f)$ in the frequency range 1.5–2.5 MHz as a function of the coupling material (glycerol or epoxy) and layer thickness Δ from 0 to $100\ \mu m$.

Similar to Fig. 4, in Fig. 8(a), we show a scatterplot in which the points represent resonances at the frequency f_{res} for a coupling layer of thickness Δ in the range from 0 to $100\ \mu m$ with point areas proportional to E_{ac}/E_{ac}^0. Multiple resonances are identified, however, the resonance at $f_{res} = 1.940$ MHz stands out with E_{ac}^0 being more than 60 times larger than any other zero-layer peak. The frequency of this resonance is nearly independent of the coupling material and layer thickness Δ. However, in Fig. 8(b), we see a fundamental difference between the two coupling materials: For glycerol, the normalized acoustic energy density E_{ac}/E_{ac}^0 decreases by one order of magnitude at a length scale ~ 100 nm, whereas for epoxy, E_{ac}/E_{ac}^0 stays nearly constant up to $\Delta \sim 1\ \mu m$, followed by a slow drop to 0.75 at $\Delta = 10\ \mu m$ and 0.2 at $\Delta \sim 50\ \mu m$. This behavior may be explained by the geometry of the acoustics and fundamental mechanical difference between elastic solids and viscous fluids. In the silicon-glass device, the direction of the standing pressure half-wave is orthogonal to the transducer polarization, and to excite this resonance mode, the transmission of shear waves from the transducer to the microchannel is required. However, only a solid coupling layer and not a viscous fluid can support such a transmission of shear waves.

TABLE V. The width (W) and height (H) of the silicon base (si), glass cover (gl), channel (ch), PZT transducer (pzt), and silver electrodes (el); see Fig. 7.

Symbol	Value	Symbol	Value
W_{si}	2520 μm	H_{si}	350 μm
W_{gl}	2520 μm	H_{gl}	1130 μm
W_{ch}	377 μm	H_{ch}	157 μm
W_{pzt}	12 000 μm	H_{pzt}	982 μm
W_{el}	12 000 μm	H_{el}	9 μm

William Naundrup Bodé and Henrik Bruus
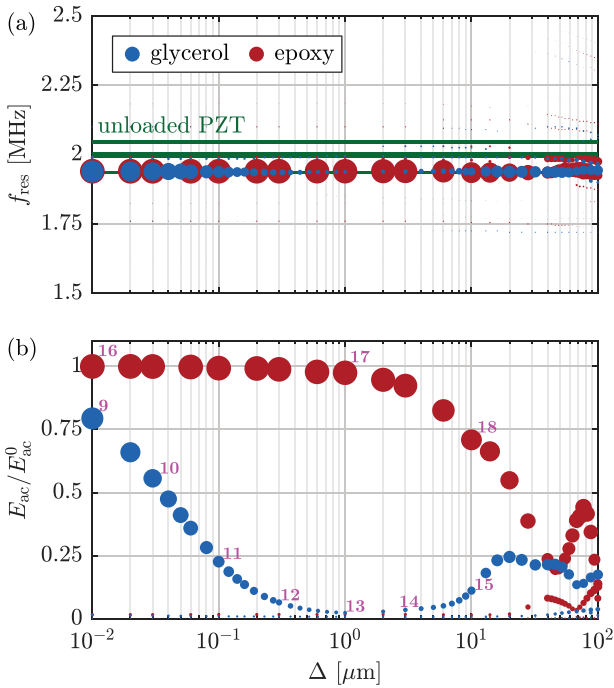
FIG. 8. (Color online) Scatter plots with point areas proportional to E_{ac}/E_{ac}^0 of responses to the increasing coupling-layer thickness Δ simulated in the 2D model of the silicon-glass device. (a) Resonance frequencies f_{res} and (b) normalized acoustic energy density E_{ac}/E_{ac}^0 are shown. Animated gif-files of the ten modes enumerated 9–18 (magenta numbers) are given in the supplementary material (Ref. 36).

In Fig. 8(b), we have selected ten 2D resonance modes enumerated 9–18 (magenta numbers). For each of these modes, we have computed an animated gif-file, given in the supplementary material,[36] that shows the temporal behavior. When studying the morphology of the modes through the animated gif-files, we find that the morphology of the sustained mode 16 without a coupling layer, $\Delta = 0$ μm, is maintained as a solid epoxy coupling layer of increasing thickness Δ is introduced, so mode 16 $\simeq$ mode 17 $\simeq$ mode 18. In contrast, the evolution of the attenuated mode 9 without a coupling layer, $\Delta = 0$ μm, is more complex. For mode 9, the vertical displacement u_z along the top of the microchannel is nearly anti-symmetric. As a fluid glycerol coupling layer of increasing thickness Δ is introduced, the symmetry of u_z evolves through modes 10, 11, and 12 to become nearly symmetric for mode 13 with $\Delta = 1$ μm. At the same time, the horizontal displacement u_y, which undergoes a nearly full wave oscillation along the vertical edges $y = \pm\frac{1}{2}W_{gl}$ of the chip, changes from having nodes at the top and bottom of the chip to having anti-nodes. This morphology is maintained for a further increase in Δ, so mode 13 $\simeq$ mode 14 $\simeq$ mode 15. In the following analysis, valid for very thin coupling layers, $\Delta \ll 0.1$ mm, we can explain the weakening of the resonance strength going from mode 9 to mode 13, but not the regaining of strength that sets in for the thicker coupling layer going from mode 13 to mode 15.

B. Dissipation in the glycerol coupling layer

The critical glycerol coupling-layer thickness $\Delta_{crit} = 100$ nm, observed in Fig. 8(b), requires a physical explanation as this length scales is far from any of the geometrical sizes or acoustic wavelengths in the system. The small thickness $\Delta < 0.1$ mm of the coupling layer implies large shear strain rates and a large amount of viscous dissipation. We assume that Δ_{crit} is the coupling-layer thickness, where the time-averaged viscous dissipation power $\langle P_{crit}^{visc} \rangle$ in the glycerol coupling layer equals the time-averaged acoustic power $\langle P_{ac} \rangle$ delivered to the half-wave pressure resonator. For an ideal resonator of length L_{ch}, width W_{ch}, height H_{ch}, average acoustic energy density E_{ac}, and quality factor Q, together with a coupling layer of thickness Δ_{crit}, width $W_{glc} = W_{gl}$, and dynamic viscosity η_{glc}, we obtain

$$\langle P_{ac} \rangle = \langle P_{crit}^{visc} \rangle, \tag{17a}$$

$$\langle P_{ac} \rangle = \int \langle p_1 \boldsymbol{v}_1 \cdot \boldsymbol{n} \rangle \, dA = \frac{16\pi}{Q} c_0 E_{ac} H_{ch} L_{ch}, \tag{17b}$$

$$\langle P_{crit}^{visc} \rangle = \int \langle \boldsymbol{\nabla} \boldsymbol{v}_1 : \boldsymbol{\tau} \rangle \, dV \approx \frac{4\pi^2 \eta_{glc} E_{ac}}{Q^2 \rho_0 \Delta_{crit}} W_{glc} L_{ch}. \tag{17c}$$

Solving for Δ_{crit}, we obtain

$$\Delta_{crit} = \frac{\pi \eta_{glc} W_{glc}}{4 Q \rho_0 c_0} H_{ch}. \tag{18}$$

The effect of the surrounding silicon-glass chip is included in the quality factor $Q = f_{res}/\Delta f$, found from the resulting full-width Δf at half maximum of the corresponding resonance peak $E_{ac}(f)$ at the resonance frequency f_{res}. The estimate for Δ_{crit} is validated numerically by varying the material and geometrical parameters in Eq. (18). The chosen material and geometric variations are listed in Table VI together with the resulting critical thickness Δ_{crit} and quality factor Q. Using the 2D model, the acoustic energy density E_{ac} is simulated, and the result is normalized by E_{ac}^0, which is the value without a coupling layer. In Fig. 9, the simulated

TABLE VI. 2D simulations of the critical coupling-layer thickness Δ_{crit} and quality factor Q for the standard configuration c0 defined in Fig. 7 and Tables III–V with a coupling layer of viscosity $\eta_{glc}^0 = 1.137$ Pa s and width $W_{gl}^0 = 2520$ μm, and a microchannel of height $H_{ch}^0 = 157$ μm, containing a fluid of density $\rho_0^0 = 997.05$ kg m^{-3}. Eight other configurations c1–c8 are obtained from c0 by changing one of the four parameter values as listed.

Configuration	$\frac{\eta_{glc}}{\eta_{glc}^0}$	$\frac{\rho_0}{\rho_0^0}$	$\frac{H_{ch}}{H_{ch}^0}$	$\frac{W_{gl}}{W_{gl}^0}$	Δ_{crit} (nm)	Q
c0	1.0	1.0	1.0	1.0	68.5	140
c1	0.05	1.0	1.0	1.0	3.4	140
c2	0.1	1.0	1.0	1.0	6.9	140
c3	0.2	1.0	1.0	1.0	13.7	140
c4	0.5	1.0	1.0	1.0	34.3	140
c5	2.0	1.0	1.0	1.0	137.0	140
c6	1.0	2.0	1.0	1.0	73.0	140
c7	1.0	1.0	0.5	1.0	202.2	95
c8	1.0	1.0	1.0	0.5	38.5	125
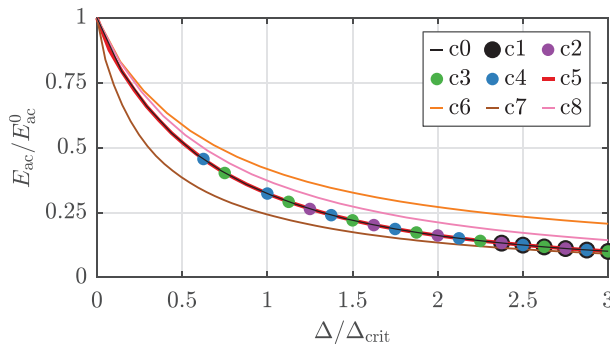
FIG. 9. (Color online) Simulated normalized acoustic energy density E_{ac}/E_{ac}^0 versus the normalized coupling-layer thickness Δ/Δ_{crit} for the nine different system configurations $c0$–$c8$ listed in Table VI.

ratio E_{ac}/E_{ac}^0 is plotted versus the normalized coupling-layer thickness Δ/Δ_{crit}, and for the wide range of parameters, it is seen that, indeed, E_{ac}/E_{ac}^0 decays on the critical coupling-layer thickness scale Δ_{crit}.

The obtained values for Q listed in Table VI range from 95 to 140, which is in line with values reported in the literature: For a acoustofluidic device with a thin glycerol layer with unspecified thickness, Barnkob *et al.* measured Q = 209 for one main resonance,[9] and in their thorough 3D analysis of the dissipation in the various parts of an acoustofluidic device with a 20-μm-thick epoxy coupling layer, Hahn and Dual computed $Q = 166$ and found that 40% of the loss per cycle was due to the epoxy layer.[4]

V. CONCLUSION

We have developed a numerical 3D model to study the role of coupling layers in acoustofluidic devices. The model includes the PZT transducer with electrodes, coupling layer, and acoustofluidic chip with the fluid-filled microchannel. The model is used to study two well-known types of acoustofluidic devices: a glass capillary tube and silicon-glass chip, classified as vertical and horizontal resonators, respectively, relative to the polarization axis of the transducer. For each device, a viscous glycerol and solid epoxy coupling layer was studied.

For vertical resonators, such as the capillary-tube device, we have found that for a given zero-layer resonance, the coupling layer can either result in a sustaining or attenuating resonance. We have established the criterion [Eq. (10)] to predict which of the two behaviors will occur, based on a relation involving the phase of the acoustic wave. For the attenuated waves, we have derived expression (27) to estimate the characteristic layer thickness Δ_0 at which the resonance is attenuated. The computed values for Δ_0, as shown in Fig. 6, are between 10 and 25 μm, which demonstrates the direct relevance of our analysis for glass-capillary-tube experiments, because the measured coupling-layer thickness Δ is reported in the literature to lie in the range from 5 to 20 μm.[6,7,28–31]

For horizontal resonators, such as the silicon-glass device, the acoustic resonances are partially powered by the shear-wave transmission through the coupling layer. For the device with an epoxy coupling layer, the slow weakening of the sustained resonance mode 16 of Fig. 8(b), which sets in at a layer thickness around 10 μm for mode 18, also happens at the experimentally relevant length scale given above. However, for the device with a glycerol coupling layer that cannot sustain shear waves, the coupling layer works as a strongly dissipative element that suppresses the resonance. For this case, a critical viscous dissipation thickness Δ_{crit} was presented in Eq. (18), based on scaling arguments in a 1D two-component model. All of the computed values for Δ_{crit} listed in Table VI are smaller than 0.2 μm, which is apparently much smaller than the experimentally relevant layer thickness. Nevertheless, the expression for Δ_{crit} and its numerical verification in Fig. 9 elucidate the physical mechanism from a theoretical point of view, although this regime may be difficult to access experimentally. How thin a glycerol layer can be in an acoustofluidic experiment is not known to us. In many research papers, where such layers are used, they are just stated to be thin without being assigned a measured value.

The simulation results presented have led to the formulation of design rules for choosing an optimal coupling layer between the PZT transducer and acoustofluidic device. The design rules involve material parameters, geometrical parameters, and information about the orientation of the given acoustic resonance mode relative to the polarization axis of the transducer. We hope that these rules will prove useful and their limitations will be understood better by experimental validation.

[1]V. T. Rathod, "A review of acoustic impedance matching techniques for piezoelectric sensors and transducers," Sens. **20**(14), 4051 (2020).

[2]M. Hill, Y. Shen, and J. J. Hawkes, "Modelling of layered resonators for ultrasonic separation," Ultrasonics **40**(1-8), 385–392 (2002).

[3]P. Glynne-Jones, R. J. Boltryk, and M. Hill, "Acoustofluidics 9: Modelling and applications of planar resonant devices for acoustic particle manipulation," Lab Chip **12**(8), 1417–1426 (2012).

[4]P. Hahn and J. Dual, "A numerically efficient damping model for acoustic resonances in microfluidic cavities," Phys. Fluids **27**, 062005 (2015).

[5]B. Hammarström, T. Laurell, and J. Nilsson, "Seed particle enabled acoustic trapping of bacteria and nanoparticles in continuous flow systems," Lab Chip **12**, 4296–4304 (2012).

[6]J. Lei, P. Glynne-Jones, and M. Hill, "Acoustic streaming in the transducer plane in ultrasonic particle manipulation devices," Lab Chip **13**(11), 2133–2143 (2013).

[7]P. Mishra, M. Hill, and P. Glynne-Jones, "Deformation of red blood cells using acoustic radiation forces," Biomicrofluidics **8**(3), 034109 (2014).

[8]I. Gralinski, S. Raymond, T. Alan, and A. Neild, "Continuous flow ultrasonic particle trapping in a glass capillary," J. Appl. Phys. **115**(5), 054505 (2014).

[9]R. Barnkob, P. Augustsson, T. Laurell, and H. Bruus, "Measuring the local pressure amplitude in microchannel acoustophoresis," Lab Chip **10**(5), 563–570 (2010).

[10]C. Magnusson, P. Augustsson, A. Lenshof, Y. Ceder, T. Laurell, and H. Lilja, "Clinical-scale cell-surface-marker independent acoustic

3104   J. Acoust. Soc. Am. **149** (5), May 2021

William Naundrup Bodé and Henrik Bruus

microfluidic enrichment of tumor cells from blood," Anal. Chem. **89**(22), 11954–11961 (2017).

[11] K. Petersson, O. Jakobsson, P. Ohlsson, P. Augustsson, S. Scheding, J. Malm, and T. Laurell, "Acoustofluidic hematocrit determination," Anal. Chim. Acta **1000**, 199–204 (2018).

[12] N. R. Skov, J. S. Bach, B. G. Winckelmann, and H. Bruus, "3D modeling of acoustofluidics in a liquid-filled cavity including streaming, viscous boundary layers, surrounding solids, and a piezoelectric transducer," AIMS Math. **4**, 99–111 (2019).

[13] J. S. Bach and H. Bruus, "Theory of pressure acoustics with viscous boundary layers and streaming in curved elastic cavities," J. Acoust. Soc. Am. **144**, 766–784 (2018).

[14] P. B. Muller, R. Barnkob, M. J. H. Jensen, and H. Bruus, "A numerical study of microparticle acoustophoresis driven by acoustic radiation forces and streaming-induced drag forces," Lab Chip **12**, 4617–4627 (2012).

[15] P. B. Muller, M. Rossi, A. G. Marin, R. Barnkob, P. Augustsson, T. Laurell, C. J. Kähler, and H. Bruus, "Ultrasound-induced acoustophoretic motion of microparticles in three dimensions," Phys. Rev. E **88**(2), 023006 (2013).

[16] A. Bermúdez, L. Hervella-Nieto, A. Prieto, and R. Rodríguez, "An optimal perfectly matched layer with unbounded absorbing function for time-harmonic acoustic scattering problems," J. Comput. Phys. **223**(2), 469–488 (2007).

[17] COMSOL Multiphysics 5.5 (2019), available at http://www.comsol.com (Last viewed 13 April 2021).

[18] M. W. H. Ley and H. Bruus, "Three-dimensional numerical modeling of acoustic trapping in glass capillaries," Phys. Rev. Appl. **8**, 024020 (2017).

[19] P. B. Muller and H. Bruus, "Numerical study of thermoviscous effects in ultrasound-induced acoustic streaming in microchannels," Phys. Rev. E **90**(4), 043016 (2014).

[20] CORNING, "Glass silicon constraint substrates" (Corning, Houghton Park C-8, Corning, NY), available at http://www.valleydesign.com/Datasheets/Corning%20Pyrex%207740.pdf (Last viewed 13 April 2021).

[21] AZoMaterials, "Silver—Applications and properties of silver" (AzoMaterials, Manchester, UK, available at https://www.azom.com/properties.aspx?ArticleID=600 (Last viewed 13 April 2021).

[22] M. A. Hopcroft, W. D. Nix, and T. W. Kenny, "What is the Young's modulus of silicon?," J. Microelectromech. Syst **19**, 229–238 (2010).

[23] Meggitt A/S, "Ferroperm matrix data" (Meggitt A/S, Kvistgaard, Denmark), available at https://www.meggittferroperm.com/materials/ (Last viewed 13 April 2021).

[24] J. J. Hawkes and W. T. Coakley, "Force field particle filter, combining ultrasound standing waves and laminar flow," Sens. Actuators, B **75**(3), 213–222 (2001).

[25] B. Hammarström, M. Evander, H. Barbeau, M. Bruzelius, J. Larsson, T. Laurell, and J. Nillsson, "Non-contact acoustic cell trapping in disposable glass capillaries," Lab Chip **10**(17), 2251–2257 (2010).

[26] P. Ohlsson, M. Evander, K. Petersson, L. Mellhammar, A. Lehmusvuori, U. Karhunen, M. Soikkeli, T. Seppa, E. Tuunainen, A. Spangar, P. von Lode, K. Rantakokko-Jalava, G. Otto, S. Scheding, T. Soukka, S. Wittfooth, and T. Laurell, "Integrated acoustic separation, enrichment, and microchip polymerase chain reaction detection of bacteria from blood for rapid sepsis diagnostics," Anal. Chem. **88**(19), 9403–9411 (2016).

[27] W. N. Bodé, L. Jiang, T. Laurell, and H. Bruus, "Microparticle acoustophoresis in aluminum-based acoustofluidic devices with PDMS covers," Micromachines **11**(3), 292 (2020).

[28] P. Hahn, O. Schwab, and J. Dual, "Modeling and optimization of acoustofluidic micro-devices," Lab Chip **14**, 3937–3948 (2014).

[29] R. J. Townsend, M. Hill, N. R. Harris, and M. B. McDonnell, "Performance of a quarter-wavelength particle concentrator," Ultrasonics **48**(6-7), 515–520 (2008).

[30] A. Lamprecht, S. Lakamper, T. Baasch, I. A. T. Schaap, and J. Dual, "Imaging the position-dependent 3D force on microbeads subjected to acoustic radiation forces and streaming," Lab Chip **16**, 2682–2693 (2016).

[31] V. Pereno, M. Aron, O. Vince, C. Mannaris, A. Seth, M. de Saint Victor, G. Lajoinie, M. Versluis, C. Coussios, D. Carugo, and E. Stride, "Layered acoustofluidic resonators for the simultaneous optical and acoustic characterisation of cavitation dynamics, microstreaming, and biological effects," Biomicrofluidics **12**(3), 034109 (2018).

[32] W. Slie, A. Donfor, Jr., and T. Litovitz, "Ultrasonic shear and longitudinal measurements in aqueous glycerol," J. Chem. Phys. **44**(10), 3712–3718 (1966).

[33] L. Negadi, B. Feddal-Benabed, I. Bahadur, J. Saab, M. Zaoui-Djelloul-Daouadji, D. Ramjugernath, and A. Negadi, "Effect of temperature on density, sound velocity, and their derived properties for the binary systems glycerol with water or alcohols," J. Chem. Thermodyn. **109**, 124–136 (2017).

[34] N.-S. Cheng, "Formula for the viscosity of a glycerol-water mixture," Ind. Eng. Chem. Res. **47**(9), 3285–3288 (2008).

[35] I. I. Perepechko, V. A. Danilov, and V. V. Nizhegorodov, "Ultrasonic velocity in epoxy resin at temperatures down to 4.2 K," Mech. Compos. Mater. **32**, 316–320 (1996).

[36] See supplementary material https://www.scitation.org/doi/suppl/10.1121/10.0004871 for details on the 18 resonance modes enumerated 1–18 in Figs. 4 and 8, as well as an animated gif-file of each of these modes.

[37] A. Lenshof, C. Magnusson, and T. Laurell, "Acoustofluidics 8: Applications in acoustophoresis in continuous flow microsystems," Lab Chip **12**, 1210–1223 (2012).

[38] A. Tahmasebipour, L. Friedrich, M. Begley, H. Bruus, and C. Meinhart, "Toward optimal acoustophoretic microparticle manipulation by exploiting asymmetry," J. Acoust. Soc. Am. **148**(1), 359–373 (2020).

[39] R. P. Moiseyenko and H. Bruus, "Whole-system ultrasound resonances as the basis for acoustophoresis in all-polymer microfluidic devices," Phys. Rev. Appl. **11**, 014014 (2019).

[40] P. Augustsson, R. Barnkob, S. T. Wereley, H. Bruus, and T. Laurell, "Automated and temperature-controlled micro-PIV measurements enabling long-term-stable microchannel acoustophoresis characterization," Lab Chip **11**(24), 4152–4164 (2011).

Supplementary material: Numerical study of the coupling layer between transducer and chip in acoustofluidic devices

William Naundrup Bodé[1, a)] and Henrik Bruus[1, b]

Department of Physics, Technical University of Denmark,
DTU Physics Building 309, DK-2800 Kongens Lyngby, Denmark

Supplementary material for details on the eighteen resonance modes enumerated in Figs. 4 and 8 as well as an animated gif-file of each mode.

S1. PARAMETERS OF THE RESONANCE MODES

In Table S1 are listed the parameters characterizing the eight 3D and ten 2D resonance modes enumerated in Figs. 4 and 8 of the paper, respectively: the device type, the coupling-layer material, the resonance frequency f_{res}, the coupling-layer thickness Δ, the peak-to-peak actuation voltage V_{pp}, the acoustic energy density E_{ac}, the maximum displacement amplitude $\max(|\boldsymbol{u}|)$, and the maximum pressure amplitude $\max(|p_1|)$. Animated movies in gif-format of each resonance mode are given in the Supplementary Material zip-file `SuppPub2.zip`. In these animations, the nm-sized displacement has been multiplied by a factor 10^5 to be visible in the mm-sized device simulations.

TABLE S1. Parameters characterizing the eighteen resonance modes 1-18 in Figs. 4 and 8 of the paper: the mode name, the device type, the coupling-layer material, the resonance frequency f_{res}, the coupling layer thickness Δ, the peak-to-peak actuation voltage V_{pp}, the acoustic energy density E_{ac}, the maximum displacement amplitude $\max(|\boldsymbol{u}|)$, and the maximum pressure amplitude $\max(|p_1|)$. Animations of each resonance are given in the Supplementary Material zip-file `SuppPub2.zip`.

Mode [.gif]	Simulation dimension and device type	Coupling material	f_{res} [MHz]	Δ [μm]	V_{pp} [V]	E_{ac} [J/m^3]	$\max(|\boldsymbol{u}|)$ [nm]	$\max(|p_1|)$ [MPa]
mode_01	3D glass capillary tube	–	3.83	0	2.0	1.8	0.83	0.14
mode_02	3D glass capillary tube	–	4.12	0	2.0	0.2	1.40	0.11
mode_03	3D glass capillary tube	–	4.17	0	2.0	0.1	1.50	0.10
mode_04	3D glass capillary tube	–	4.30	0	2.0	0.9	1.92	0.11
mode_05	3D glass capillary tube	Glycerol	3.69	10	2.0	1.5	1.07	0.23
mode_06	3D glass capillary tube	Glycerol	4.14	100	2.0	2.6	0.92	0.17
mode_07	3D glass capillary tube	Epoxy	3.78	10	2.0	1.1	0.92	0.11
mode_08	3D glass capillary tube	Epoxy	4.19	100	2.0	2.2	1.38	0.21
mode_09	2D silicon-glass chip	Glycerol	1.94	0.01	2.0	15.8	1.85	0.57
mode_10	2D silicon-glass chip	Glycerol	1.94	0.03	2.0	11.0	1.84	0.54
mode_11	2D silicon-glass chip	Glycerol	1.94	0.1	2.0	4.5	1.81	0.48
mode_12	2D silicon-glass chip	Glycerol	1.94	0.3	2.0	1.3	1.88	0.32
mode_13	2D silicon-glass chip	Glycerol	1.94	1	2.0	0.5	2.12	0.23
mode_14	2D silicon-glass chip	Glycerol	1.94	3	2.0	0.7	2.23	0.18
mode_15	2D silicon-glass chip	Glycerol	1.94	10	2.0	2.2	2.52	0.17
mode_16	2D silicon-glass chip	Epoxy	1.94	0.01	2.0	19.4	1.92	0.42
mode_17	2D silicon-glass chip	Epoxy	1.94	1	2.0	18.9	1.93	0.41
mode_18	2D silicon-glass chip	Epoxy	1.93	10	2.0	13.8	1.99	0.36

a) winabo@dtu.dk
b) bruus@fysik.dtu.dk

6.3 Paper III: Phys. Rev. Appl. resubmitted, 1-11 (2022)

Determination of the complex-valued elastic moduli of polymers by electrical impedance spectroscopy for ultrasound applications

ArXiv.org: 2204.06464

Authors: W. N. Bodé, F. Lickert, P. Augustsson, and H. Bruus.
Journal: Phys. Rev. Appl. **resubmitted**, 1-11 (2022)

Remarks: This paper is considered as the main contribution. In this publication, I have worked together with my PhD colleague Fabian Lickert. We have contributed equally and we share the first authorship. The paper has been submitted to Physical Review Applied. We have received a review. The paper has been improved and resubmitted and we are now waiting for the final verdict.

Determination of the complex-valued elastic moduli of polymers by electrical impedance spectroscopy for ultrasound applications

William N. Bodé,[1, *] Fabian Lickert,[1, †] Per Augustsson,[2, ‡] and Henrik Bruus[1, §]

[1]*Department of Physics, Technical University of Denmark,*
DTU Physics Building 309, DK-2800 Kongens Lyngby, Denmark
[2]*Department of Biomedical Engineering, Lund University, Ole Römers väg 3, 22363 Lund, Sweden*

(Dated: 30 September 2022)

A method is presented for the determination of complex-valued compression and shear elastic moduli of polymers for ultrasound applications. The resulting values, which are scarcely reported in the literature, are found with uncertainties typically around 1% (real part) and 6% (imaginary part). The method involves a setup consisting of a cm-radius, mm-thick polymer ring glued concentrically to a disk-shaped piezoelectric transducer. The ultrasound electrical impedance spectrum of the transducer is computed numerically and fitted to measured values as an inverse problem in a wide frequency range, typically from 500 Hz to 5 MHz, both on and off resonance. The method was validated experimentally by ultrasonic through-transmission around 1.9 MHz. The method is low cost, not limited to specific geometries and crystal symmetries, and, given the developed software, easy to execute. The method has no obvious frequency limitations before severe attenuation sets in above 100 MHz.

I. INTRODUCTION

Numerical simulations play an important role when optimizing and predicting piezoelectric device performance in applications including ultrasonic cleaning [1], energy harvesting [2], inkjet printing [3], and acoustofluidics [4, 5]. To perform precise, accurate, and predictive simulations, well-characterized material parameters such as the complex-valued elastic moduli are required. Whereas material databases exist [6], and manufactures may provide some of the required parameters, it is often not sufficient when attempting to perform reliable simulations and predictions. Polymers are in this regard a particularly challenging class of materials, since the elastic moduli of a given polymer may depend on unspecified parameters such as the distribution of polymer chain lengths and fabrication processes.

There exist a range of techniques to characterize an unknown material or substance mechanically. Dynamic techniques such as resonant ultrasound spectroscopy [7], transmission techniques [8, 9], impulse excitation [10], laser vibrometry and triangulation [11, 12], as well as static techniques, such as four-point bending, are widely used in various industries [13]. Those methods however often rely on a few mechanical eigenmodes or resonance frequencies of the material under study, a broad frequency spectrum due to a narrow pulse in the time domain, or even static or low-frequency measurements. Applications requiring actuation frequencies in the MHz-range however require material properties that were measured in similar frequency intervals for an accurate de-scription of the system.

In this work we aim to extend the field of ultrasound spectroscopy [12, 14] by utilizing an electrical impedance spectrum spanning a frequency range of several MHz to obtain a full set of complex-valued elastic moduli of polymers. With this technique, labeled ultrasound electrical impedance spectroscopy (UEIS), a piezoelectric disk, driving vibrations in an attached polymer ring, is used to characterize the complex-valued elastic compressional and shear moduli of the polymer ring. Similar techniques have been used in the past to fit piezoelectric material parameters by an inverse problem and numerical optimization procedures on a free oscillating piezoelectric transducer [8, 12, 14–18]. Here, the same principles are used to fit elastic material parameters. From the UEIS spectrum of a mass-loaded transducer, an inverse problem is constructed to deduce the elastic moduli of the mass load. The method is similar to those of Refs. [12, 19, 20], but by including an automated whole-spectrum fit and complex parameter values, it extends the previous method as suggested in the conclusion of Ref. [20]. Instead of a thin-film transducer and manual fitting of few selected resonance peaks in the impedance spectrum, the UEIS method makes use of several hundred impedance values measured on a mechanically-loaded bulk transducer in the frequency range from 500 Hz to 5 MHz, to extract both real and imaginary parts of the complex-valued elastic moduli, and not just the real parts obtained in Ref. [20]. The UEIS technique enables low-cost and in-situ measurements of elastic moduli over a wide frequency range from low kHz to several MHz. It is easy to execute, requiring only a disk-shaped piezoelectric transducer, a ring of the unknown polymer sample, an impedance analyzer, and the developed fitting software.

The paper is organized as follows. In Section II a brief overview of the relevant theory is given, before in Section III the experimental and numerical methodology of the UEIS technique is described in detail for polymer,

glue, and transducer. In Section IV we provide validation data based on ultrasonic-through-transmission (UTT) measurements, before we in Section V present the main results of the UEIS method in terms of the complex-valued electromechanical parameters of the unloaded piezoelectric transducer and the complex-valued elastic moduli of the UV-cured glue and the polymer ring. We conclude in Section VI.

II. THEORETICAL BACKGROUND

We follow Ref. [21] and describe isotropic polymers using the standard linear theory of elastic solids in the Voigt notation, in terms of the displacement vector $\boldsymbol{u}$ of a given material point away from its equilibrium position, and the 1×6 strain $\boldsymbol{s}$ and stress $\boldsymbol{\sigma}$ column vectors with the 6×1 transposed row vectors $\boldsymbol{s}^{\mathsf{T}} = (\partial_x u_x, \partial_y u_y, \partial_z u_z, \partial_y u_z + \partial_z u_y, \partial_x u_z + \partial_z u_x, \partial_x u_y + \partial_y u_x)$ and $\boldsymbol{\sigma}^{\mathsf{T}} = (\sigma_{xx}, \sigma_{yy}, \sigma_{zz}, \sigma_{yz}, \sigma_{xz}, \sigma_{xy})$, respectively. Representing the elastic moduli C_{ik} by the tensor $\boldsymbol{C}$, the constitutive equation for an elastic solid in the ∞mm-symmetry class is [22],

$$\boldsymbol{\sigma} = \boldsymbol{C} \cdot \boldsymbol{s}, \tag{1a}$$

$$\boldsymbol{C} = \begin{pmatrix} C_{11} & C_{12} & C_{13} & 0 & 0 & 0 \\ C_{12} & C_{11} & C_{13} & 0 & 0 & 0 \\ C_{13} & C_{13} & C_{33} & 0 & 0 & 0 \\ 0 & 0 & 0 & C_{44} & 0 & 0 \\ 0 & 0 & 0 & 0 & C_{44} & 0 \\ 0 & 0 & 0 & 0 & 0 & C_{66} \end{pmatrix}. \tag{1b}$$

For an isotropic polymer $C_{33} = C_{11}$, $C_{66} = C_{44}$, and $C_{13} = C_{12} = C_{11} - 2C_{44}$, so here, $\boldsymbol{C}$ is given only by the two complex-valued elastic moduli C_{11} and C_{44}, each with a real and imaginary part, $C_{ik} = C'_{ik} + \mathrm{i}C''_{ik}$, relating to the propagation and attenuation of sound waves, respectively. Many amorphous polymers, such as the injection-molded PMMA in this work, are isotropic, but if not, such as semi-crystalline polymers [23], a $\boldsymbol{C}$ tensor with the appropriate lower symmetry must be used. Since only positive power dissipation is allowed, the elastic moduli are restricted by the constraint that the matrix $\mathrm{Im}(-\boldsymbol{C})$ must be positive definite [24].

We also model the piezoelectric lead-zirconate-titanate (PZT) transducer in the ∞mm-symmetry class [22], again following the notation of Ref. [21]. Here, $\boldsymbol{u}$, $\boldsymbol{S}$, $\boldsymbol{\sigma}$, and $\boldsymbol{C}$ are supplemented by the electric potential φ, the electric field $\boldsymbol{E} = -\boldsymbol{\nabla}\varphi$, the dielectric tensor $\boldsymbol{\varepsilon}$, the electric displacement field $\boldsymbol{D} = \boldsymbol{\varepsilon} \cdot \boldsymbol{E}$, and the piezoelectric 3×6 coupling tensor $\boldsymbol{e}$. The constitutive equation becomes,

$$\begin{pmatrix} \boldsymbol{\sigma} \\ \boldsymbol{D} \end{pmatrix} = \begin{pmatrix} \boldsymbol{C} & -\boldsymbol{e}^{\mathsf{T}} \\ \boldsymbol{e} & \boldsymbol{\varepsilon} \end{pmatrix} \begin{pmatrix} \boldsymbol{S} \\ \boldsymbol{E} \end{pmatrix} = \boldsymbol{M} \cdot \begin{pmatrix} \boldsymbol{S} \\ \boldsymbol{E} \end{pmatrix} \tag{2a}$$

$$\boldsymbol{e} = \begin{pmatrix} 0 & 0 & 0 & 0 & e_{15} & 0 \\ 0 & 0 & 0 & e_{15} & 0 & 0 \\ e_{31} & e_{31} & e_{33} & 0 & 0 & 0 \end{pmatrix}, \ \boldsymbol{\varepsilon} = \begin{pmatrix} \varepsilon_{11} & 0 & 0 \\ 0 & \varepsilon_{11} & 0 \\ 0 & 0 & \varepsilon_{33} \end{pmatrix}. \tag{2b}$$

In the ∞mm-symmetry class, $C_{66} = \frac{1}{2}(C_{11} - C_{12})$, so the coupling tensor $\boldsymbol{M}$ is given by the five complex-valued elastic moduli C_{11}, C_{12}, C_{13}, C_{33}, and C_{44}, with $C_{ik} = C'_{ik} + \mathrm{i}C''_{ik}$, the two complex-valued dielectric constants ε_{11} and ε_{33} with $\varepsilon_{ik} = \varepsilon'_{ik} + \mathrm{i}\varepsilon''_{ik}$, and the three real-valued piezo-coupling constants e_{31}, e_{33}, and e_{15} with $e_{ik} = e'_{ik} + 0\mathrm{i}$. Since only positive power dissipation is allowed, the coupling constants are restricted by the following constraint on the matrix $\boldsymbol{K}$ [24],

$$\boldsymbol{K} = \mathrm{Im} \begin{pmatrix} -\boldsymbol{C} & \boldsymbol{e}^{\mathsf{T}} \\ \boldsymbol{e} & \boldsymbol{\varepsilon} \end{pmatrix} \text{ must be positive definite.} \tag{3}$$

We limit our analysis of the linear system to the time-harmonic response for a given angular frequency $\omega = 2\pi f$, where f is the excitation frequency of the system. Thus, any physical field $F_{\mathrm{phys}}(\boldsymbol{r}, t)$ is given by a complex-valued amplitude $F(\boldsymbol{r})$ as $F_{\mathrm{phys}}(\boldsymbol{r}, t) = \mathrm{Re}\left[F(\boldsymbol{r})\,\mathrm{e}^{-\mathrm{i}\omega t}\right]$, and we need only to compute $F(\boldsymbol{r})$. In our model of a polymer sample mounted on a PZT transducer having a bottom and top electrode, the system is excited by the excitation voltage $\varphi_{\mathrm{top}}^{\mathrm{phys}} = \mathrm{Re}\left[\varphi_{\mathrm{top}}\,\mathrm{e}^{-\mathrm{i}\omega t}\right]$ as follows,

$$\varphi_{\mathrm{bot}} = 0 \text{ V} \quad \text{and} \quad \varphi_{\mathrm{top}} = 1 \text{ V}. \tag{4}$$

By introducing the density ρ as an additional material parameter, the governing equations for the time-harmonic displacement field $\boldsymbol{u}$ in the polymer and in the PZT and for the quasi-electrostatic potential φ in the non-magnetic PZT without free charges, become

$$\boldsymbol{\nabla} \cdot \boldsymbol{\sigma} = -\rho\omega^2 \boldsymbol{u} \quad \text{and} \quad \boldsymbol{\nabla} \cdot \boldsymbol{D} = 0. \tag{5}$$

We neglect the effect of gravity in this formulation, as it only leads to a minor deformation of the geometry. The stress- and charge-free boundary conditions are imposed on free surfaces

$$\boldsymbol{\sigma} \cdot \boldsymbol{n} = \boldsymbol{0} \quad \text{and} \quad \boldsymbol{n} \cdot \boldsymbol{D} = 0. \tag{6}$$

The current density $\boldsymbol{J}$ in the PZT transducer is given by the polarization $\boldsymbol{P}$ as

$$\boldsymbol{J} = \partial_t \boldsymbol{P} = -\mathrm{i}\omega(\boldsymbol{D} - \varepsilon_0 \boldsymbol{E}). \tag{7}$$

Consequently, the electrical impedance Z central to the UEIS method can be computed via the flux integral of $\boldsymbol{J}$ through the surface $\partial\Omega_{\mathrm{top}}$ with surface normal $\boldsymbol{n}$ as,

$$Z = \frac{\varphi_{\mathrm{top}} - \varphi_{\mathrm{bot}}}{I}, \quad \text{with} \quad I = \int_{\partial\Omega_{\mathrm{top}}} \boldsymbol{n} \cdot \boldsymbol{J} \, \mathrm{d}A. \tag{8}$$

III. METHODOLOGY

The ultimate goal is to develop and test a method for determination of the complex-valued elastic moduli of polymers. However, to achieve an accuracy level of about 1-5%, we need also to determine the mechanical and electromechanical parameters of the piezoelectric transducer as well as the elastic moduli of the glue used to mount the polymer sample on the transducer.

A. Experimental procedure

Measurements of the electrical impedance spectrum $Z_{\exp}(f)$ were performed using a Vector Network Analyzer Bode 100 (OMICRON electronics GmbH, Klaus, Austria) in a linear interval with 10.000 steps between 500 Hz and 5 MHz, each frequency sweep taking less than 4 minutes. In a first step, the electrical impedance of an unloaded Pz27 disk (Meggitt A/S, Kvistgaard, Denmark) was characterized. The top and bottom electrode of the piezoelectric disk were contacted through spring-loaded pins in a custom-made sample holder, minimizing the contact force and area to a point in the center of the disk. In the following step, using a thin layer of the UV-curable glue NOA 86H (Norland Products, Jamesburg (NJ), USA), a polymer ring of known dimensions was glued on top of a Pz27 disk. This ring was made from either the NOA 86H glue itself or from polymethyl methacrylate (PMMA Diakon TD525, Lucite International, Rotterdam, Netherlands). We aimed at making the glue layer as thin (15-25 µm) and uniform as possible to reduce its influence on the combined system, as studied by Bodé *et al.* [25]. This was achieved by gently squeezing the system for a few seconds after assembly, just before curing the glue by UV illumination. The glue was cured at a UV-intensity of 15 mW/cm^2 at 365 nm for 167 s to achieve strong bonding between the transducer disk and the polymer ring. The glue NOA 86H was selected after performing experiments with several different adhesives, as it enables good adhesion between the PZT and the polymer and allows for good acoustic coupling due to acrylic-like properties in the cured state with an attenuation comparable to that found for the polymer ring. After curing, the electrical impedance of the polymer-loaded transducer was measured. The small hole of the polymer ring allows contacting the transducer

TABLE I. Measured thickness (TH) and outer diameter (OD) of the Pz27 disks (named Pz27-TH-OD). Measured TH, OD, and inner diameter (ID) of the rings made by the glue NOA 86H (named NOA86H-TH-OD) and of the polymer PMMA (named PMMA-TH-OD). Letters A, B, C are used as labels for samples with the same nominal dimensions. The precision is given as the standard deviation from six measurements.

Sample	TH (mm)	OD (mm)	ID (mm)
Pz27-0.5-6.35-A	0.510(1)	6.594(5)	–
Pz27-0.5-6.35-B	0.502(1)	6.587(2)	–
Pz27-0.5-10-A	0.500(1)	10.037(7)	–
Pz27-0.5-10-B	0.492(2)	10.039(3)	–
Pz27-0.5-10-C	0.505(2)	10.039(5)	–
NOA86H-1.4-20	1.5(2)	19.22(6)	1.90(2)
PMMA-1.4-20-A	1.428(2)	19.981(5)	1.98(1)
PMMA-1.4-20-B	1.440(4)	20.017(8)	1.94(1)
PMMA-1.4-25-A	1.427(5)	24.98(1)	1.92(1)
PMMA-1.4-25-B	1.437(5)	24.94(1)	1.94(2)

TABLE II. The measured glue-layer thickness of the five studied PMMA-ring-on-Pz27-disk configurations.

Pz27 disk	Polymer ring	Glue layer
Pz27-0.5-6.35-A	PMMA-1.4-20-A	15 µm
Pz27-0.5-6.35-B	PMMA-1.4-25-A	24 µm
Pz27-0.5-10-A	PMMA-1.4-25-B	21 µm
Pz27-0.5-10-B	PMMA-1.4-20-B	12 µm
Pz27-0.5-10-C	NOA86H-1.4-20	15 µm

disk using the above-mentioned spring-loaded pins. The average of three impedance measurements, taking less than 12 minutes to obtain, was used both for the unloaded and loaded case.

The diameter and thickness of the polymer ring and the Pz27 disk were measured before assembling the system using an electronic micrometer with an accuracy of ± 4 µm. The glue-layer thickness was obtained as the measured total thickness of the assembled system minus the sum of the individual thicknesses of the Pz27 disk and the polymer ring. The impedance measurements were performed at 24 °C using a combination of two different nominal transducer dimensions (diameter 6.35 mm and 10 mm, thickness 0.5 mm) and two different nominal polymer ring dimensions (diameter 20 mm and 25 mm, thickness 1.4 mm), yielding four transducer-polymer systems with the dimensions listed in Tables I and II.

B. Numerical model

The weak formulation of the finite element method (FEM) is used to implement the governing equations in the software COMSOL Multiphysics [26] to simulate the electrical impedance spectrum $Z_{\mathrm{sim}}(f)$ unloaded or loaded PZT transducer. In particular, we use the *weak form PDE* interface as described in our previous work [5, 21, 25]. The simulations are computed on a workstation with a 12-core, 3.5-GHz central processing unit and 128 GB random access memory. Third-order Lagrange polynomials are used as test functions for both $\boldsymbol{u}$ and φ. The model consists of three domains: a piezoelectric disk, a glue layer, and a polymer ring. Given the cylindrical geometry of the assembled stack and the axisymmetric structure of the coupling tensors $\boldsymbol{C}$ and $\boldsymbol{M}$ in Eqs. (1b) and (2a), the system can be reduced to an axisymmetric model as shown in Ref. [27] and illustrated in Fig. 1. This axisymmetrization reduces the computational time substantially. A suitable mesh element size is found by the mesh convergence study presented in Sec. S1 of the Supplemental Material [28], where in addition in Sec. S2, a COMSOL sample script is presented.

Using the "LiveLink for MATLAB"-interface provided by COMSOL, the MATLAB optimization procedures `fminsearchbnd` and `patternsearch` are used to fit the material parameters such that $Z_{\mathrm{sim}}(f)$ is as close to $Z_{\exp}(f)$ as possible. The `fminsearchbnd` algo-
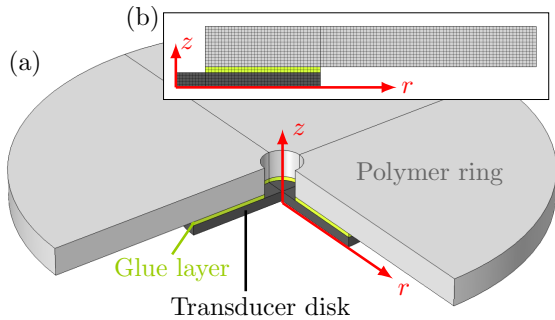
FIG. 1. (a) A 3D sketch of the system consisting of a polymer ring (light gray) glued (green) to a transducer disk (dark gray) whit a quarter cut away for visibility. (b) The inset shows the 2D axisymmetric domain in the r-z plane used for numerical simulations. The structured mesh is the one used at 5 MHz.

rithm [30] allows a bounded search in parameter space. The `patternsearch` algorithm (part of the `Global Optimization Toolbox`) makes twice as many function evaluations, but it covers a larger region in parameter space and is better to locate the global minimum for poor initial values. Both algorithms use a gradient-free direct search and are therefore well suited for non-smooth numerical optimization procedures. The algorithms require three inputs: (i) initial values, (ii) upper and lower bounds, and (iii) a cost function to minimize. Based on the measured and simulated electrical impedance values $Z_{\exp}(f_i)$ and $Z_{\sim}(f_i)$ obtained at ~ 500 frequencies f_i, we define the cost function $\mathcal{C}$ as

$$\mathcal{C} = \sqrt{\sum_i \left[\log_{10}\big(|Z_{\exp}(f_i)|\big) - \log_{10}\big(|Z_{\sim}(f_i)|\big) \right]^2}. \quad (9)$$

Here, we use the logarithm, because $Z(f_i)$, having many peaks, varies by orders of magnitude as a function of f_i.

C. Sensitivity analysis

To enhance the performance of our fitting procedure, we group the parameters into sets of similar sensitivity based on the following sensitivity analysis of the cost function $\mathcal{C}$ on each of the sixteen material parameters $(p_1, p_2, \ldots p_{16})^{\mathrm{pz27}} = (C'_{11}, C'_{12}, C'_{13}, C'_{33}, C'_{44}, \varepsilon'_{11}, \varepsilon'_{33}, e'_{31}, e'_{33}, e'_{15}, C''_{11}, C''_{12}, C''_{13}, C''_{33}, C''_{44}, \varepsilon''_{33})$ for the Pz27 disk and on the four polymer parameters $(p_1, \ldots p_4)^{\mathrm{polym}} = (C'_{11}, C'_{44}, C''_{11}, C''_{44})$. The sensitivity analysis is performed in the frequency range from 500 Hz to 5 MHz, with the initial value p_i^0 taken from literature for a given parameter p_i, and therefore the individual sensitivity values represent averages over the entire frequency range. A more detailed study of the frequency dependency of the sensitivity is shown in Sec. S2 of the Supplemental Material [28]. We use a discrete approximation of the relative sensitivity $\mathcal{S}(p_i) = p_i \partial_{p_i} \mathcal{C}(p_i)$ of $\mathcal{C}(p_i)$ based on a $\pm 10\%$ variation of p_i around p_i^0, while
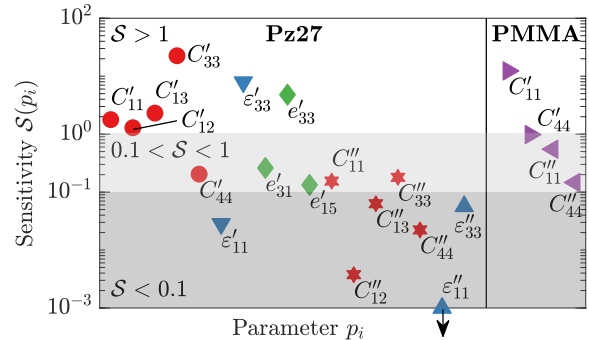
FIG. 2. The relative cost function sensitivity $\mathcal{S}(p_i)$ for the 17 piezoelectric material parameters p_i obtained as an average from four Pz27 disks in the frequency interval 500 Hz$-$5 MHz is shown in the left side of the figure. $\mathcal{S}(p_i)$ for the four PMMA parameters, calculated from the average of four Pz27–PMMA–systems, are shown on the right. Corresponding real and imaginary parts are visualized in the same color, and the regions of high ($\mathcal{S}(p_i) > 1$), medium ($0.1 < \mathcal{S}(p_i) < 1$) and low ($\mathcal{S}(p_i) < 0.1$) sensitivity are highlighted by gray shadows. The sensitivity of the parameter ε''_{11} is close to zero, as indicated by a black arrow.

keeping the remaining parameters fixed at p_j^0,

$$\mathcal{S}(p_i) = \frac{\mathcal{C}(1.1 p_i) - \mathcal{C}(0.9 p_i)}{1.1 - 0.9}, \quad p_j = p_j^0 \text{ for } j \neq i. \quad (10)$$

The obtained sensitivities $\mathcal{S}$ for the p_i^{pz27} and p_i^{pmma} parameters for Pz27 and PMMA, respectively, are shown in Fig. 2. The Pz27 parameters are classified in three groups of high $\mathcal{S}(p_i) > 1$, medium $0.1 < \mathcal{S}(p_i) < 1$, and low $\mathcal{S}(p_i) < 0.1$ sensitivity, respectively, and as described in the following section, a robust fitting is obtained by fitting the parameters group by group sequentially in descending order from high to low sensitivity. Since all four PMMA parameters have a medium-to-high sensitivity we fit them simultaneously in a single, undivided group.

D. The UEIS fitting procedure

The first step in the UEIS fitting procedure is to measure and simulate the electrical impedance $Z_{\exp}(f)$ and $Z_{\sim}(f)$, respectively, of an unloaded Pz27 transducer disk and then following Refs. [16–18] to fit the sixteen Pz27 parameters p_i^{pz27} in the form of an inverse problem by minimizing the cost function $\mathcal{C}$. In the second step, a characterized Pz27 disk is loaded by gluing on a given polymer ring using the UV-curable glue NOA 86H. To characterize the glue, the first studied polymer ring is made by the glue itself, and $Z(f)$ is used to similarly fit the four glue parameters p_i^{glue}. Subsequently, using the characterized glue, a PMMA ring is glued to a characterized Pz27 disk, and $Z(f)$ is used to similarly fit the four PMMA parameters p_i^{pmma}. See the flow chart in Fig. 3.
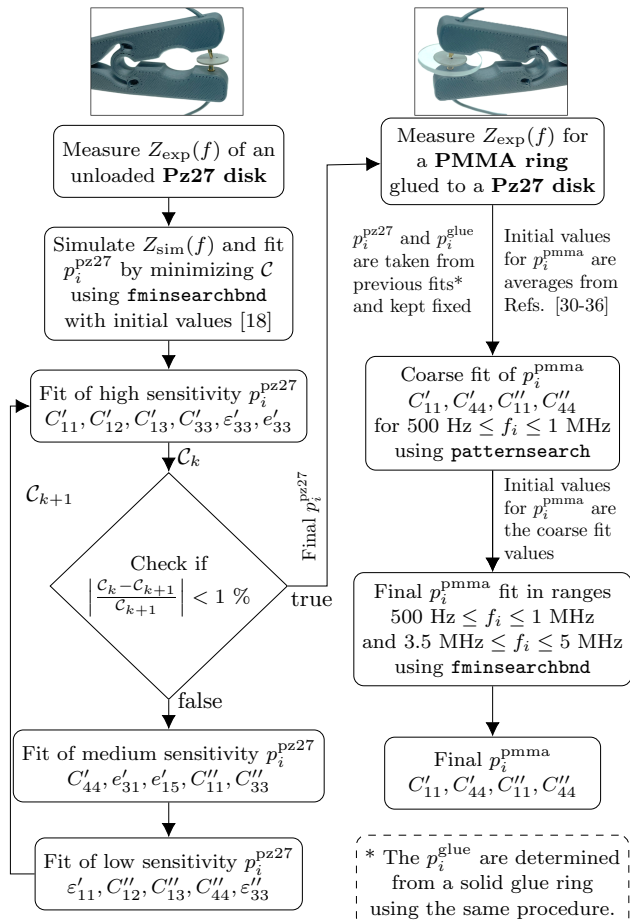
FIG. 3. A flow chart of the steps in the fitting procedure to obtain complex-valued elastic moduli for a polymer sample. First, the electrical impedance spectrum $Z_{\mathrm{exp}}(f)$ of a Pz27 transducer disk is measured in the range 500 Hz $< f_i <$ 5 MHz. Then, the Pz27 parameters p_i^{pz27} are fitted in the same frequency range with increments of $\Delta f = 10$ kHz based on their sensitivities in descending order, with initial values from Ref. [18]. Next step is the measurement of $Z_{\mathrm{exp}}(f)$ for the PMMA ring glued to the Pz27 disk in the range 500 Hz $< f_i <$ 5 MHz. Then, coarse fitting of the p_i^{pmma} is performed in the range 500 Hz $< f_i <$ 1 MHz with $\Delta f = 2$ kHz stepping, taking the initial values to be the average values of Refs. [31–37]. Lastly, a final fitting of p_i^{pmma} is done in the the range 3.5 MHz $< f_i <$ 5 MHz combined with previous range using steps of $\Delta f = 10$ kHz. A MATLAB-COMSOL sample script for the PMMA fitting procedure is presented in Sec. S2 of the Supplemental Material [28].

For the unloaded Pz27 disk, the initial values of p_i^{pz27} are taken from Ref. [18], and the kth iteration in the fit is divided into four sub-steps: (1) Fit the six parameters C_{11}', C_{12}', C_{13}', C_{33}', ε_{33}', and e_{33}' of highest sensitivity $\mathcal{S} > 1$ using the `fminsearchbnd` algorithm in the range 500 Hz $< f_i <$ 5 MHz in increments of 10 kHz with the bounds set to ± 30 %, while keeping the remaining eleven parameters fixed. (2) Check whether the cost function $\mathcal{C}_k$

of iteration k deviates less than 1 % relative to $\mathcal{C}_{k-1}$ (the fit is converged and p_i^{pz27} have been determined) or not (the fitting continues). (3) Similarly, fit the five parameters C_{44}', e_{31}', e_{15}', C_{11}'', and C_{33}'' of medium sensitivity $0.1 < \mathcal{S} < 1$. (4) Likewise, fit the last six parameters ε_{11}', C_{12}'', C_{13}'', C_{44}'', ε_{11}'', and ε_{33}'' of low sensitivity $\mathcal{S} < 1$ and move on to iteration $k + 1$. If during the fit a value of p_i^{pz27} is within 5 % of the pre-defined bound, the latter is changed by 50 %. Furthermore, for each evaluation of the cost function $\mathcal{C}$, it is checked if $\boldsymbol{K}$ in Eq. (3) is positive definite, and if not we set $\mathcal{C} = \infty$.

For the glue ring, the initial values of the four parameters p_i^{glue} are $C_{11}^{\mathrm{glue}} = (4.7 - 0.47\mathrm{i})$ GPa and $C_{44}^{\mathrm{glue}} = (0.9 - 0.09\mathrm{i})$ GPa inferred from Young's modulus of Ref. [38], the assumed value 0.38 of Poisson's ratio, and $C_{ik}'' = 0.1 C_{ik}'$. Moreover, the density of the glue ring is measured. The fitting is divided into two substeps to increase robustness and speed: (1) A coarse fit of the four parameters C_{11}', C_{44}', C_{11}'', and C_{44}'' using the `patternsearch` algorithm in the limited range 500 Hz $< f_i <$ 1 MHz in increments of 2 kHz with the bounds set to be ± 40 % covering the typically observed range for polymers [9, 35]. (2) A final fit of C_{11}', C_{44}', C_{11}'', and C_{44}'' using the `fminsearchbnd` algorithm in the combined ranges of 500 Hz $< f_i <$ 1 MHz and 3.5 MHz $< f_i <$ 5 MHz in increments of 2 kHz and 10 kHz, respectively, with the bounds set to ± 40 %, and with the coarse-fit values used as initial values. If during the fit a value of p_i^{glue} is within 5 % of the pre-defined bound, the bound is changed by 5 %, see the Supplemental Material [28]. Furthermore, for each evaluation of the cost function $\mathcal{C}$, it is checked if $\mathrm{Im}(-\boldsymbol{C})$ is positive definite, and if not we set $\mathcal{C} = \infty$.

For the PMMA ring, the initial values of p_i^{pmma} are taken to be the average of the values reported in Refs. [31–37]. This average is used due to the lack of parameter values provided by the manufacturer of our selected PMMA polymer. Since this PMMA consists of a toughened acrylic compound, we expect that it deviates from standard PMMA grades. Therefore we chose to use the average literature values only as initial values in our fitting routine, and we refrain from comparing them with the resulting UEIS values. Otherwise, the fitting procedure for the PMMA ring is the same as the one for the glue ring.

Note that for the selected materials in the studied frequency range from 500 Hz to 5 MHz, and measured with relative accuracies from 1% to 5%, the experimental results in Sections IV and V show that it is adequate to assume frequency-independent parameters p_i^{pz27}, p_i^{glue} and p_i^{pmma}. See further discussion in Section V C.

IV. ULTRASONIC-THROUGH-TRANSMISSION (UTT) VALIDATION DATA

For the polymer PMMA, we have carried out ultrasonic-through-transmission (UTT) measurements

[8, 37] to acquire data for experimental validation of the UEIS method. In UTT, a pulse, with center frequency f_c and width Δf in the frequency domain and width Δt in the time domain, is transmitted through a polymer slab of thickness d with its surface normal $\boldsymbol{n}$ tilted an angle θ_i relative to the incident pulse and emerged in water having the sound speed c_0. We have used $f_c = 1.90$ MHz, $\Delta f \approx 1$ MHz, and $\Delta t \approx 2$ µs. The UTT-method relies on the fact that at normal incidence only longitudinal waves are transmitted, whereas above a critical tilt angle $\theta_{\text{crit}} = \sin^{-1}(c_0/c_{\text{lo}})$ only transverse waves are transmitted in samples with $c_{\text{lo}} > c_0$. The longitudinal and transverse speed of sound, c_{lo} and c_{tr}, and the corresponding attenuation coefficients, α_{lo} and α_{tr}, of the slab can be determined based on the difference $\Delta\tau$ of arrival times, with and without the slab placed in the water,

$$c_{\text{lo}} = \left[1 + \frac{c_0}{d}\,\Delta\tau\right]^{-1} c_0, \tag{11a}$$

$$c_{\text{tr}} = \left[\sin^2\theta_i + \left(\frac{c_0}{d}\,\Delta\tau + \cos\theta_i\right)^2\right]^{-\frac{1}{2}} c_0, \tag{11b}$$

$$\alpha_{\text{lo}} = \alpha_0 + \frac{1}{d}\ln\left[\frac{T_{\text{lo}}A_0}{A_{\text{lo}}}\right], \tag{11c}$$

$$\alpha_{\text{tr}} = \alpha_0 \cos(\theta_s - \theta_i) + \frac{1}{d}\ln\left[\frac{T_{\text{tr}}A_0}{A_{\text{lo}}}\right]\cos\theta_s. \tag{11d}$$

Here, T_{lo} and T_{tr} are the longitudinal and transverse transmission coefficients, θ_s is the refractive angle of the shear wave, A_0 is the amplitude of the direct signal, and A_{lo} and A_{tr} are the longitudinal and transverse amplitudes of the transmitted signal after passing through the sample. Using the parameter values of water listed in Ref. [39], the attenuation coefficient α_0 of water is,

$$\alpha_0(T, f) = 2\pi^2\left[\frac{4}{3}\eta_0(T) + \eta^{\text{b}}(T)\right]\frac{f^2}{\rho_0 c_0^3}$$
$$\approx \left[1 - 0.0249\frac{T - 25\ ^\circ\text{C}}{1\ ^\circ\text{C}}\right]\frac{0.0217 f^2}{1\ \text{MHz}^2}\frac{\text{Np}}{\text{m}}. \tag{12}$$

As we do not control the room temperature in our UEIS measurements, but simply monitor it with a $1\ ^\circ\text{C}$ uncertainty, we have used the UTT experiments to determine the temperature dependence of the elastic moduli of our PMMA sample. To this end, the UTT tank was filled with warm water at temperature $T = 31\ ^\circ\text{C}$. Then over a period of 6 hours, as the water steadily cooled to $T = 23\ ^\circ\text{C}$, the elastic moduli were measured at regular intervals, corresponding to steps in temperature of about $-0.5\ ^\circ\text{C}$. As shown in Sec. S4 of the Supplementary Material [28], the resulting longitudinal and transverse speed of sound (c_{lo} and c_{tr}) and attenuation coefficients (α_{lo} and α_{tr}) of PMMA at the frequency $f_c = 1.90$ MHz are

found to depend linearly on temperature T (in $^\circ\text{C}$) as,

$$c_{\text{lo}}^{1.90\,\text{MHz}}(T) = \left[-11(2)\,\frac{T}{1\ ^\circ\text{C}} + 2743(46)\right]\frac{\text{m}}{\text{s}}, \tag{13a}$$

$$c_{\text{tr}}^{1.90\,\text{MHz}}(T) = \left[-4.5(4)\,\frac{T}{1\ ^\circ\text{C}} + 1267(9)\right]\frac{\text{m}}{\text{s}}, \tag{13b}$$

$$\alpha_{\text{lo}}^{1.90\,\text{MHz}}(T) = \left[1.7(4)\,\frac{T}{1\ ^\circ\text{C}} + 25(10)\right]\frac{\text{Np}}{\text{m}}, \tag{13c}$$

$$\alpha_{\text{tr}}^{1.90\,\text{MHz}}(T) = \left[7(2)\,\frac{T}{1\ ^\circ\text{C}} + 146(43)\right]\frac{\text{Np}}{\text{m}}. \tag{13d}$$

Here, the digits in the parentheses indicate 1σ uncertainties computed from on the sum-of-square differences between measured data and regression-line fits.

V. RESULTS OF THE UEIS METHOD

A. UEIS-fitted material parameters for Pz27

First, we determine the sixteen material parameters p_i^{pz27} for the four unloaded Pz27 disks with nominal outer diameters 6.35 mm and 10.0 mm and the measured dimensions listed in Table I. Using the UEIS method described in Section III involving the measured and fitted impedance spectra $Z_{\text{exp}}(f)$ and $Z_{\text{sim}}(f)$, we obtain the resulting parameters listed in Tables III and IV. In Table III we compare the real part of the obtained UEIS parameters to those provided in the literature (lit, [18]) and by the manufacturer (manf, [40]). The relative difference $\Delta_{\text{UEIS}}^{\text{lit}}$ between UEIS and literature values is in the range $\sim$2-8 %, whereas $\Delta_{\text{UEIS}}^{\text{manf}}$ is higher, typically in the range $\sim$5-40 %. The deviations are overall significant compared to the relative standard deviation $\hat{\sigma}_{\text{UEIS}} \lesssim 2\ \%$ of the mean of the UEIS values.

Similarly, in Table IV we compare the imaginary parts of the obtained UEIS parameters to those provided in the literature (lit, [18]). Note that ε_{11}'' is set to zero due to its low value and sensitivity, and that $e_{mj}'' = 0$ by assumption. In general, the imaginary parts are more difficult to measure than the real parts, which is reflected in the high values of $\hat{\sigma}_{\text{UEIS}}$ ($\lesssim$10 %), $\Delta_{\text{UEIS}}^{\text{lit}}$ ($\sim$5-50 %), but still with significant deviation between UEIS values and the values provided in the literature and by the manufacturer. The errors on the imaginary parts are about one order of magnitude larger than the errors on the real parts. This is in line with the previously found lower sensitivities of the former compared to the higher sensitivities of the latter shown in Fig. 2. Relative deviations of the initial values from the fitted values range from as little as 1.4 % for C_{13}'' and up to 50 % for C_{12}'' and above 200 % for ε_{33}''. Despite those deviations from the initial values, we find good convergence on the cost function and an excellent agreement between the measured and fitted impedance spectrum for the Pz27 disk. The uniqueness of the sixteen material parameters p_i^{pz27} is not guaranteed, but the simulated impedance spectrum fits the measured one, and thus they provide an adequate
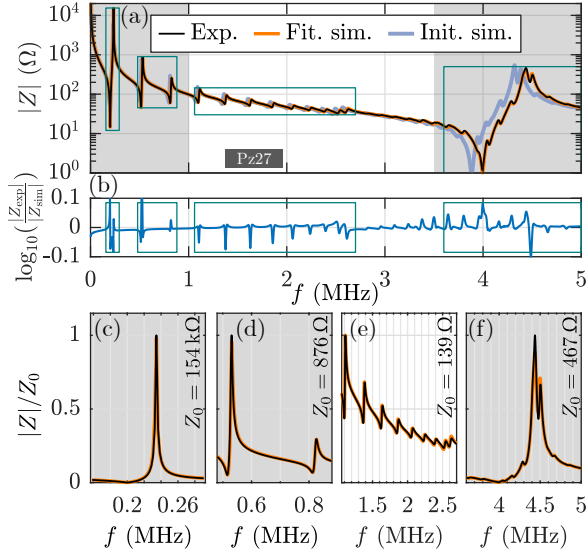
FIG. 4. (a) Semilog plot of the measured (black) and simulated UEIS $|Z(f)|$ of an unloaded Pz27-0.5-10 disk. In the simulations are used the UEIS-fitted (orange) and initial literature (blue) Pz27 parameters listed in Tables III and IV. The gray region indicates the frequency range used in the fitting. (b) The logarithmic difference $\Delta_{\mathrm{sim}}^{\mathrm{exp}} = \log_{10}(|Z_{\mathrm{exp}}|/|Z_{\mathrm{sim}}|)$ between measured and simulated impedance spectrum. (c)-(f) Zoom-in on different regions showing the measured and simulated spectrum on a linear and re-normalized scale. Each region is indicated by a frame in both (a) and (b).

FIG. 5. (a) Semilog plot of the measured (black) and simulated UEIS $|Z(f)|$ of a PMMA-1.4-25 ring glued to a Pz27-0.5-10 disk by a 21-µm-thick layer of NOA 86H glue. The UEIS-fitted simulation (orange) is computed using the UEIS parameter values listed in Tables III, IV, V, and VI. The initial-value simulation is shown in blue. The gray regions indicate the frequency ranges used in the fitting. (b) The logarithmic difference $\Delta_{\mathrm{sim}}^{\mathrm{exp}} = \log_{10}(|Z_{\mathrm{exp}}|/|Z_{\mathrm{sim}}|)$ between measured and simulated impedance spectrum. (c)-(f) Zoom-in on different regions showing the measured and simulated spectrum on a linear and re-normalized scale. Each region is indicated by a frame in both (a) and (b).

estimate for the subsequent determination of the polymer parameters p_i^{pmma}. In Fig. 4, an example is shown of the measured UEIS spectrum and the resulting simulated UEIS spectrum for a Pz27 disk of diameter 10 mm and thickness 0.5 mm.

B. UEIS-fitted material parameters for glue

The parameters p_i^{glue} of the used UV-cured NOA 86H glue were determined by the UEIS method as described in Section III D using a UV-cured glue ring glued to a Pz27 disk with the dimensions listed in Tables I and II. The resulting values for C_{11} and C_{44} are presented in Table V together with the corresponding values for the sound speeds c_{lo} and c_{tr}, the attenuation coefficients α_{lo} and α_{tr}, as well as Young's modulus E and Poisson's ratio ν. The expressions for these additional parameters, valid for any isotropic elastic material, are obtained by assuming frequency-independent moduli C_{11} and C_{44} in the limit of weak attenuation, $\left|C_{11}''\right| \ll C_{11}'$ and $\left|C_{44}''\right| \ll C_{44}'$, and by introducing the complex-valued wavenumbers $k_{\mathrm{lo}} = \omega/c_{\mathrm{lo}} + i\alpha_{\mathrm{lo}}$ and $k_{\mathrm{tr}} = \omega/c_{\mathrm{tr}} + i\alpha_{\mathrm{tr}}$,

$$c_{\mathrm{lo}} = \sqrt{\frac{C_{11}'}{\rho}}, \qquad \alpha_{\mathrm{lo}}(f) = \pi\sqrt{\frac{\rho}{\left(C_{11}'\right)^3}}\left|C_{11}''\right| f, \quad (14\mathrm{a})$$

$$c_{\mathrm{tr}} = \sqrt{\frac{C_{44}'}{\rho}}, \qquad \alpha_{\mathrm{tr}}(f) = \pi\sqrt{\frac{\rho}{\left(C_{44}'\right)^3}}\left|C_{44}''\right| f, \quad (14\mathrm{b})$$

$$\nu = \frac{\frac{1}{2}C_{11}' - C_{44}'}{C_{11}' - C_{44}'} \qquad E = \frac{3C_{11}' - 4C_{44}'}{C_{11}' - C_{44}'} C_{44}'. \quad (14\mathrm{c})$$

C. UEIS-fitted material parameters for PMMA

With the characterization of the Pz27 transducer disk and the glue completed, we move on to the determination of the complex-valued elastic moduli C_{11} and C_{44} for PMMA, which in principle could have been any other elastic polymer. We studied four PMMA polymer rings with the dimensions listed in Table I, all around 1.4 mm thick and with diameters of 20 or 25 mm, and glued to Pz27 disks with the dimensions listed in Table II.

The resulting UEIS-fitted parameters C_{11}', C_{44}', C_{11}'', and C_{44}'' at 24 °C for the PMMA are listed in Table VI together with the corresponding values obtained by the UTT technique. The relative standard deviation $\hat{\sigma}_{\mathrm{UEIS}}$ on the real parts is low ($\sim$0.5 %), and an order of magnitude higher on the imaginary parts (3-6 %). We find good agreement between the UEIS and the UTT values, in all cases with relative deviations $\Delta_{\mathrm{UEIS}}^{\mathrm{UTT}} < 3\hat{\sigma}_{\mathrm{UEIS}}$. In

TABLE III. The real part (single prime) of the material parameters p_i^{pz27} of the four Pz27 disks of Table I obtained by the UEIS method with initial values from the literature [18]. The digits in brackets denote one standard deviation, $\hat{\sigma}_{\mathrm{UEIS}}$ is the relative standard deviation of the UEIS mean, and $\Delta_{\mathrm{UEIS}}^{\mathrm{lit}}$ and $\Delta_{\mathrm{UEIS}}^{\mathrm{manf}}$ is the relative deviation from UEIS of the values given by Ref. [18] (lit) and by the manufacturer (manf) [40], respectively. The density of Pz27 was measured to be $\rho_{\mathrm{pz27}} = 7.7(1)$ g/cm^3.

Pz27 disk	C'_{11} (GPa)	C'_{12} (GPa)	C'_{13} (GPa)	C'_{33} (GPa)	C'_{44} (GPa)	ε'_{11} (ε_0)	ε'_{33} (ε_0)	e'_{31} (C/m^2)	e'_{33} (C/m^2)	e'_{15} (C/m^2)
Pz27-0.5-6.35 (A)	127	80.1	82.3	121	20.3	963	780	-5.3	16.4	11.8
Pz27-0.5-6.35 (B)	126	78.8	81.4	122	20.7	957	753	-5.2	15.9	11.0
Pz27-0.5-10 (A)	123	75.6	77.3	117	20.8	993	839	-5.0	16.4	10.8
Pz27-0.5-10 (B)	121	74.7	76.5	117	21.3	1015	842	-5.1	16.4	10.4
Mean of UEIS	124(3)	77(3)	80(3)	119(3)	20.8(4)	982(27)	804(44)	$-5.2(1)$	16.3(3)	11.0(6)
Literature [18]	117.64	73.66	73.46	110.17	20.41	959.10	816.61	-5.19	16.06	11.59
Manufacturer [40]	147(4)	105(3)	94(2)	113(3)	23.0(6)	1130(113)	914(91)	$-3.1(2)$	16.0(8)	11.6(6)
$\hat{\sigma}_{\mathrm{UEIS}}(\%)$	1.1	1.7	1.8	1.1	1.0	1.4	2.8	-1.5	0.8	2.6
$\Delta_{\mathrm{UEIS}}^{\mathrm{lit}}(\%)$	-5.2	-4.7	-7.5	-7.6	-1.8	-2.3	1.6	0.6	-1.3	5.5
$\Delta_{\mathrm{UEIS}}^{\mathrm{manf}}(\%)$	18	36	18	-5.2	11	15	14	-40	-1.7	5.5

TABLE IV. The imaginary part (double prime) of the material parameters p_i^{pz27} of the four Pz27 disks of Table I obtained by the UEIS method with initial values from the literature [18] and the parameters ε''_{11}, e''_{31}, e''_{33}, and e''_{15} set to zero by assumption. The digits in brackets denote one standard deviation, $\hat{\sigma}_{\mathrm{UEIS}}$ is the relative standard deviation of the UEIS mean, and $\Delta_{\mathrm{UEIS}}^{\mathrm{lit}}$ is the relative deviation from UEIS of the values of Ref. [18] (lit).

Pz27 disk	C''_{11} (MPa)	C''_{12} (MPa)	C''_{13} (MPa)	C''_{33} (MPa)	C''_{44} (MPa)	ε''_{11} (ε_0)	ε''_{33} (ε_0)	e''_{31} (C/m^2)	e''_{33} (C/m^2)	e''_{15} (C/m^2)
Pz27-0.5-6.35 (A)	-709	370	121	-280	-582	0	3.9	0	0	0
Pz27-0.5-6.35 (B)	-628	442	122	-377	-596	0	2.5	0	0	0
Pz27-0.5-10 (A)	-558	448	112	-518	-488	0	0.0	0	0	0
Pz27-0.5-10 (B)	-510	510	90.7	-538	-486	0	6.3	0	0	0
Mean of UEIS	$-601(87)$	442(57)	112(15)	$-428(122)$	$-538(59)$	0	3(3)	0	0	0
Literature [18]	-460	220	110	-400	-400	$-$	10.72	$-$	$-$	$-$
$\hat{\sigma}_{\mathrm{UEIS}}(\%)$	-7.2	6.4	6.6	-14	-5.5	$-$	41	$-$	$-$	$-$
$\Delta_{\mathrm{UEIS}}^{\mathrm{lit}}(\%)$	-23	-50	-1.4	-6.6	-26	$-$	235	$-$	$-$	$-$

terms of the derived sound speeds, c_{lo} and c_{tr}, and the derived Young's modulus E and Poisson's ratio ν, the relative deviation of UTT values from UEIS values is around 0.5 %. For the longitudinal and transverse attenuation α_{lo} and α_{tr} coefficients, the relative deviations of UTT values relative to UEIS values are higher, around 7-15 %.

Again, likely due to the lower sensitivity of the C''_{11} and C''_{44} coefficients, it proves more difficult to obtain the imaginary parts of the elastic moduli than the real

parts. Deviations of the UTT values from the UEIS values, may in part be explained by the fact that the

TABLE VI. The UEIS-fitted and UTT-measured elastic moduli for PMMA at 24 $^\circ$C with a measured density $\rho = 1162(4)$ kg/m^3, and α_{lo} and α_{tr} evaluated at 1.90 MHz. For UEIS, $\hat{\sigma}_{\mathrm{UEIS}}$ is the relative standard deviation of the UEIS mean. For UTT, the errors are based on 1σ-prediction intervals around linear regression fits. $\Delta_{\mathrm{UEIS}}^{\mathrm{UTT}}$ is the deviation of the UTT values relative to the UEIS values.

Param.	Unit	UEIS	$\hat{\sigma}_{\mathrm{UEIS}}$ (%)	UTT	$\Delta_{\mathrm{UEIS}}^{\mathrm{UTT}}$ (%)
C'_{11}	GPa	7.18(4)	0.6	7.1(1)	-1.1
C''_{11}	GPa	$-0.183(5)$	2.9	$-0.19(1)$	3.8
C'_{44}	GPa	1.553(8)	0.5	1.56(1)	0.5
C''_{44}	GPa	$-0.111(7)$	6.3	$-0.098(6)$	-11.7
c_{lo}	m/s	2486(8)	0.3	2469(19)	-0.7
c_{tr}	m/s	1156(4)	0.3	1160(4)	0.3
α_{lo}	Np/m	61(2)	3.2	66(4)	8.2
α_{tr}	Np/m	370(24)	6.4	322(18)	-13.0
E	GPa	4.23(2)	0.5	4.25(3)	0.5
ν	$-$	0.362(1)	0.4	0.358(3)	-1.1

TABLE V. The material parameters at 24 $^\circ$C of the UV-cured NOA 86H glue determined by the UEIS method. The density of the glue was measured to be $\rho = 1.3(2) \times 10^3$ kg m^{-3}, and the attenuation coefficients are for the center frequency $f_c = 1.90$ MHz of the UTT method described in Section IV.

Parameter	Parameter	Parameter
$C'_{11} = 4.65$ GPa	$c_{\mathrm{lo}} = 1891$ m/s	$E = 3.20$ GPa
$C'_{44} = 1.21$ GPa	$c_{\mathrm{tr}} = 965$ m/s	$\nu = 0.32$
$C''_{11} = -0.51$ GPa	$\alpha_{\mathrm{lo}}(f_c) = 346$ Np/m	
$C''_{44} = -0.12$ GPa	$\alpha_{\mathrm{tr}}(f_c) = 613$ Np/m	

UTT technique uses a frequency pulse with a width of 1 MHz around the center frequency 1.90 MHz, whereas UEIS is based on an entire frequency spectrum from 500 Hz to 5 MHz using a single frequency at a time. However, whereas different models exist, which assume a frequency-dependence of the elastic moduli of PMMA [12], similar to the frequency dependencies measured in PDMS [9], we do find it sufficient in the UEIS method to neglect the frequency-dependence of the complex-valued elastic moduli of PMMA.

In Fig. 5 is shown an example of the measured and the simulated UEIS spectra for a PMMA ring glued to a Pz27 disk. We find a good agreement between the measured and the fitted simulated UEIS spectrum, and it can also be seen, how even smaller features of the experimental impedance curve are captured in the simulated frequency spectrum. Relative deviations $\Delta_{\mathrm{sim}}^{\mathrm{exp}} = \log_{10} \frac{|Z_{\mathrm{exp}}|}{|Z_{\mathrm{sim}}|}$ up to 20 % are found in regions near resonance peaks. However, zoom-ins there show how a frequency-shift of a few percent can lead to high deviations $\Delta_{\mathrm{sim}}^{\mathrm{exp}}$, while still maintaining good agreement between measurement and simulation. For example, shifting a Lorentzian peak with a Q-value of $Q = 250$ by 1% of its resonance frequency, results in a relative deviation $\sim 10\%$.

We furthermore studied the impact of small deviations in the thickness and elastic moduli of the glue on the obtained coefficients for the polymer ring. A change of the Young's modulus E_{glue} by ± 1 % leads to changes in the real-valued coefficients C_{11}' and C_{44}' by less than 0.05 %, while the C_{11}'' and C_{44}'' coefficients change by 0.4 % and 0.6 % respectively. In a separate numerical study, when changing the thickness of the glue layer from 12 μm to 8 μm, a relative deviation of 33.3 %, we observe a decrease in the real-valued coefficients C_{11}' and C_{44}' by 0.8 % and 0.2 % respectively. The relative changes for the imaginary-valued coefficients C_{11}'' and C_{44}'' are slightly higher by $+2.4$ % and -1.3 %, respectively, but still much lower when compared to the relative change in thickness and well in line with the identified uncertainties of the parameters listed in Table VI.

As a further validation of the UEIS method, we use the UEIS-fitted values p_i^{pmma} to simulate selected resonance modes in the PMMA ring. Subsequently, as shown in Sec. S5 in the Supplemental Material [28], we have successfully compared these predicted modes with direct measurements of the corresponding modes obtained by using a single-point laser-Doppler vibrometer system VibroFlex Connect (Polytec, Waldbronn, Germany).

VI. CONCLUSION

We have developed a method based on measured and simulated ultrasound electrical impedance spectroscopy (UEIS) able to determine the frequency-independent complex-valued elastic moduli of polymers. The method is a two-step procedure: Firstly, the material parameters of the used, unloaded piezoelectric transducer disk are fitted by an inverse problem, matching the measured and simulated electrical impedance spectrum. Secondly, a polymer ring is glued onto the transducer, and the same technique is used to fit the complex-valued elastic moduli of the polymer. To evaluate its reproducibility, the method was applied on four different system geometries involving the polymer PMMA, achieving a relative error below 0.5 % for Young's modulus and Poisson's ratio, and below 7 % for the attenuation coefficients. The method was validated experimentally within the 3σ-level using ultrasonic through-transmission on PMMA samples.

It is noteworthy that the model assumption of frequency-independent elastic moduli C_{ik} leads to simulated UEIS spectra $Z_{\mathrm{sim}}(f)$ that predicts the measured UEIS spectra $Z_{\mathrm{exp}}(f)$ so well in the entire frequency range from 500 Hz to 5 MHz as shown in Figs. 4 and 5 for Pz27 and PMMA, as well as for the UV-curable glue NOA 86H (not shown). This frequency independence leads to the linear frequency dependence of the attenuation coefficients α_{lo} and α_{tr} exhibited in Eq. (14), a linearity which can be contrasted with the f^2-dependence of α_0 in Newtonian fluids, Eq. (12), and the non-integer powers observed in typically softer materials, such as the $f^{1.456}$-dependence of α_{lo} and the $f^{0.924}$-dependence of α_{tr} observed in the rubber PDMS [9]. It is straightforward to include such frequency-dependency of the elastic moduli in the UEIS model, should materials with that property be studied. One simply modify the respective moduli and coupling coefficients in the constitutive equations (1) and (2) at the cost of extending the list of parameters p_i with the necessary parameters needed to describe the frequency dependency. For the relatively stiff polymer PMMA, the elastic modulus tensor $\boldsymbol{C}$ can be taken as frequency independent, whereas modeling softer, rubber-like materials, the frequency dependency of $\boldsymbol{C}$ must be taken into account [41].

The UEIS technique extends the existing field of resonance ultrasound spectroscopy by making use of the electrical impedance spectrum over a wide frequency range of several MHz involving both on-resonance and off-resonance frequencies, it has no obvious frequency limitations before severe attenuation sets in above 100 MHz, and it contains information of all relevant parameters of the piezoelectric transducer disk, the glue layer, the polymer ring, and the geometry of the assembled stack. Experimentally, the technique is low-cost, easy-to-use, simple, and well-suited for materials used in ultrasound applications. The recording of a given impedance spectrum takes less than 4 minutes. Afterwards, within about 1 minute, the impedance spectrum can be loaded into our MATLAB script, and the automated UEIS fitting procedure is executed. After a run time of about 10 hours, the resulting UEIS-fitted impedance spectrum and the parameter values p_i^{pz27}, p_i^{glue}, or p_i^{pmma} are delivered by the software.

The UEIS technique is not limited to the chosen examples of Pz27, glue, and PMMA, but it can in principle be

used on other classes of elastic materials including rubbers, glasses, and metals. We believe that the presented UEIS technique will become a valuable and easy-to-use tool in the ultrasound application fields mentioned in the introduction, by providing well-determined parameter values for the materials used, namely the relevant complex-valued elastic moduli at the relevant ultrasound frequencies.

VII.   ACKNOWLEDGMENTS

[1] N. Bretz, J. Strobel, M. Kaltenbacher, and R. Lerch, Numerical simulation of ultrasonic waves in cavitating fluids with special consideration of ultrasonic cleaning, in *IEEE Int. Ultrason. Symp.* (2005) pp. 703–706.

[2] M. T. Todaro, F. Guido, V. Mastronardi, D. Desmaele, G. Epifani, L. Algieri, and M. De Vittorio, Piezoelectric MEMS vibrational energy harvesters: Advances and outlook, Microelectron. Eng. **183**, 23 (2017).

[3] M. Singh, H. M. Haverinen, P. Dhagat, and G. E. Jabbour, Inkjet printing-process and its applications, Adv. Mater. **22**, 673 (2010).

[4] W. N. Bodé, L. Jiang, T. Laurell, and H. Bruus, Microparticle acoustophoresis in aluminum-based acoustofluidic devices with PDMS covers, Micromachines **11**, 292 (2020).

[5] F. Lickert, M. Ohlin, H. Bruus, and P. Ohlsson, Acoustophoresis in polymer-based microfluidic devices: Modeling and experimental validation, J. Acoust. Soc. Am. **149**, 4281 (2021).

[6] MatWeb, LLC, http://www.matweb.com/ (2022).

[7] A. Migliori, J. Sarrao, W. M. Visscher, T. Bell, M. Lei, Z. Fisk, and R. Leisure, Resonant ultrasound spectroscopic techniques for measurement of the elastic moduli of solids, Physica B **183**, 1 (1993).

[8] H. Wang, W. Jiang, and W. Cao, Characterization of lead zirconate titanate piezoceramic using high frequency ultrasonic spectroscopy, J. Appl. Phys. **85**, 8083 (1999).

[9] G. Xu, Z. Ni, X. Chen, J. Tu, X. Guo, H. Bruus, and D. Zhang, Acoustic Characterization of Polydimethylsiloxane for Microscale Acoustofluidics, Phys. Rev. Applied **13**, 054069 (2020).

[10] G. Roebben, B. Bollen, A. Brebels, J. Van Humbeeck, and O. Van der Biest, Impulse excitation apparatus to measure resonant frequencies, elastic moduli, and internal friction at room and high temperature, Rev. Sci. Instrum. **68**, 4511 (1997).

[11] R. Willis, L. Wu, and Y. Berthelot, Determination of the complex young and shear dynamic moduli of viscoelastic materials, J. Acoust. Soc. Am. **109**, 611 (2001).

[12] J. Ilg, S. J. Rupitsch, A. Sutor, and R. Lerch, Determination of Dynamic Material Properties of Silicone Rubber Using One-Point Measurements and Finite Element Simulations, IEEE T. Instrum. Meas. **61**, 3031 (2012).

[13] M. Radovic, E. Lara-Curzio, and L. Riester, Comparison of different experimental techniques for determination of elastic properties of solids, Mat Sci Eng A-Struct **368**, 56 (2004).

[14] S. J. Rupitsch and R. Lerch, Inverse Method to estimate material parameters for piezoceramic disc actuators, Appl. Phys. A **97**, 735 (2009).

[15] J. Plesek, R. Kolman, and M. Landa, Using finite element method for the determination of elastic moduli by resonant ultrasound spectroscopy, J. Acoust. Soc. Am. **116**, 282 (2004).

[16] N. Pérez, M. A. B. Andrade, F. Buiochi, and J. C. Adamowski, Identification of elastic, dielectric, and piezoelectric constants in piezoceramic disks, IEEE Trans. Ultrason. Ferroelec. Freq. Contr. **57**, 2772 (2010).

[17] N. Pérez, R. Carbonari, M. Andrade, F. Buiochi, and J. Adamowski, A FEM-based method to determine the complex material properties of piezoelectric disks, Ultrasonics **54**, 1631 (2014).

[18] C. Y. Kiyono, N. Perez, and E. C. N. Silva, Determination of full piezoelectric complex parameters using gradient-based optimization algorithm, Smart Mater. Struct. **25**, 025019 (2016).

[19] J. Maynard, Resonant Ultrasound Spectroscopy, Physics Today **49**, 26 (1996).

[20] A. G. Steckel, H. Bruus, P. Muralt, and R. Matloub, Fabrication, characterization, and simulation of glass devices with AlN thin-film transducers for excitation of ultrasound resonances, Phys. Rev. Applied **16**, 014014, 1 (2021).

[21] N. R. Skov, J. S. Bach, B. G. Winckelmann, and H. Bruus, 3D modeling of acoustofluidics in a liquid-filled cavity including streaming, viscous boundary layers, surrounding solids, and a piezoelectric transducer, AIMS Mathematics **4**, 99 (2019).

[22] T. Ikeda, *Fundamentals of Piezoelectricity* (Oxford University Press, London, UK, 1996).

[23] G. H. Michler and W. Lebek, *Electron microscopy of polymers* (Wiley, Hoboken (NJ), 2016) pp. 277–293.

[24] R. Holland, Representation of Dielectric, Elastic, and Piezoelectric Losses by Complex Coefficients, IEEE T. Son. Ultrason **14**, 18 (1967).

[25] W. N. Bodé and H. Bruus, Numerical study of the coupling layer between transducer and chip in acoustofluidic

devices, J. Acoust. Soc. Am. **149**, 3096 (2021).

[26] COMSOL Multiphysics 5.5 (2019), http://www.comsol.com.

[27] A. G. Steckel and H. Bruus, Numerical study of acoustic cell trapping above elastic membrane disks driven in higher-harmonic modes by thin-film transducers with patterned electrodes, Phys. Rev. E **submitted**, 14 pages (2021), https://arxiv.org/abs/2112.12567.

[28] See Supplemental Material at [URL] for details on the mesh convergence analysis, a study on the sensitivity versus elastic moduli and frequency range, sample MAT-LAB and COMSOL scripts for the UEIS fitting procedure, the corresponding data for the impedance spectra, and the validation of the UEIS method by UTT and laser-Doppler vibrometry, which includes Refs. [16, 29].

[29] W. D. Callister Jr, *Materials Science and Engineering: An Introduction*, seventh ed. (John Wiley & Sons, York, PA, 2007) p. 975.

[30] John D'Errico, Matlab file exchange (2012), https://www.mathworks.com/matlabcentral/fileexchange/8277-fminsearchbnd-fminsearchcon, access 30 Sep 2022.

[31] B. Hartmann and J. Jarzynski, Polymer sound speeds and elastic constants, Naval Ordnance Laboratory **Report NOLTR 72-269**, 1 (1972).

[32] D. Christman, Dynamic properties of poly (methylmethacrylate) (PMMA) (plexiglas), General Motors Technical Center, Warren (MI), USA **Report No. DNA 2810F, MSL-71-24, 1**, 1 (1972).

[33] H. Sutherland and R. Lingle, Acoustic characterization of polymethyl methacrylate and 3 epoxy formulations, J. Appl. Phys. **43**, 4022 (1972).

[34] H. Sutherland, Acoustical determination of shear relaxation functions for polymethyl methacrylate and Epon 828-Z, J. Appl. Phys. **49**, 3941 (1978).

[35] J. E. Carlson, J. van Deventer, and A. S. C. Carlander, Frequency and temperature dependence of acoustic properties of polymers used in pulse-echo systems, IEEE Ultrasonics Symposium , 885 (2003).

[36] A. Simon, G. Lefebvre, T. Valier-Brasier, and R. Wunenburger, Viscoelastic shear modulus measurement of thin materials by interferometry at ultrasonic frequencies, J. Acoust. Soc. Am. **146**, 3131 (2019).

[37] H. T. Tran, T. Manh, T. F. Johansen, and L. Hoff, Temperature effects on ultrasonic phase velocity and attenuation in Eccosorb and PMMA, in *2016 IEEE International Ultrasonics Symposium (IUS)* (2016) pp. 1–4.

[38] *Norland Optical Adhesive 86H*, Norland Products Inc., Jamesburg, NJ 08831, USA, https://www.norlandprod.com/adhesives/NOA86H.html, accessed 30 Sep 2022.

[39] P. B. Muller and H. Bruus, Numerical study of thermoviscous effects in ultrasound-induced acoustic streaming in microchannels, Phys. Rev. E **90**, 043016 (2014).

[40] *Ferroperm matrix data*, Meggitt A/S, Porthusvej 4, DK-3490 Kvistgaard, Denmark, https://www.meggittferroperm.com/materials/, accessed 30 Sep 2022.

[41] T. Pritz, Frequency dependences of complex moduli and complex poisson's ratio of real solid materials, J. Sound Vib. **214**, 83 (1998).

Supplementary material: Determination of complex-valued elastic moduli of polymers by electrical impedance spectroscopy for ultrasound applications

William N. Bodé,[1, *] Fabian Lickert,[1, †] Per Augustsson,[2, ‡] and Henrik Bruus[1, §]

[1]*Department of Physics, Technical University of Denmark,*
DTU Physics Building 309, DK-2800 Kongens Lyngby, Denmark
[2]*Department of Biomedical Engineering, Lund University, Ole Römers väg 3, 22363 Lund, Sweden*
(Dated: 30 September 2022)

Supplementary material for details on the mesh convergence analysis, a study on the sensitivity versus elastic moduli and frequency range, sample MATLAB and COMSOL scripts for the UEIS fitting procedure, the corresponding data for the impedance spectra, and the validation of the UEIS method by UTT and laser-Doppler vibrometry.

S1. MESH CONVERGENCE

Third-order Lagrange polynomials are used as test functions for both $\boldsymbol{u}$ and φ. The model consists of three domains: a piezoelectric transducer disk, a glue layer, and a polymer ring. For each domain Ω_k, the maximum mesh element size is given as $h_{\max}^{(k)} = c_{\mathrm{tr}}^{(k)}/(sf)$, where s is a dimensionless mesh-size parameter, and f is the frequency. A mesh convergence is performed at $f = 5$ MHz by sweeping in s and computing the error $\mathrm{err}(g)$ defined by the L_2-norm for the solution $g(\boldsymbol{r})$,

$$\mathrm{err}(g) = \sqrt{\frac{\int_{\Omega_k} |g - g_0|^2 \, \mathrm{d}a}{\int_{\Omega_k} |g_0|^2 \, \mathrm{d}a}}, \qquad (1)$$

where g_0 refers to the solution with the best resolved mesh obtained by the given computational resources. Results of the mesh convergence are shown in Fig. S1, where the numerical error is seen to be below 1 % and exponentially decaying for $s > 2.2$.
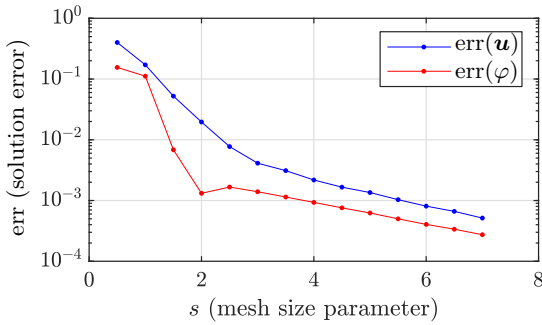
FIG. S1. Mesh convergence analysis presented as a semilog plot of the errors $\mathrm{err}(\boldsymbol{u})$ (blue) and $\mathrm{err}(\varphi)$ (red) versus the mesh size parameter s.

* winabo@dtu.dk; Equal share first-author
† fabianl@dtu.dk; Equal share first-author
‡ per.augustsson@bme.lth.se
§ bruus@fysik.dtu.dk

S2. SENSITIVITY OF $Z(f)$ VERSUS THE ELASTIC MODULI AND FREQUENCY RANGE

In Eqs. (9) and (10) of Sec. III-C in the main paper, we defined the sensitivity of the UEIS method as the logarithmic derivative $\mathcal{S}(p_i) = p_i \partial_{p_i} \mathcal{C}(p_i)$ of the cost function $\mathcal{C}$ with respect to the material parameters p_i, where $\mathcal{C}$ involves the difference between the measured and the simulated impedance spectrum $Z(f)$ averaged over the entire frequency range. Here, following the procedure in a similar study of the material parameters of a PZT transducer by Pérez *et al.* [1], we study the dependency on the elastic moduli of $Z(f)$ in two frequency ranges, the low-frequency range 0.5 - 1000 kHz and the high frequency range 3.5 - 5.0 MHz.

In Fig. S2, the changes of $Z(f)$ of a PMMA-loaded Pz27 transducer disk are observed, as the normalized elastic moduli $\tilde{C}_{ik} = C_{ik}/C_{ik}^{\mathrm{ueis}}$ of the PMMA ring are changed by from 0.80 to 1.20 in steps of 0.01, where C_{ik}^{ueis} are the values determined by the UEIS method, see Table VI. It is seen that the spectrum $Z(f)$ is nearly independent of $\tilde{C}_{11}'$ in the low frequency range (vertical ridges in the $\tilde{C}_{11}'$-f plane), and that it has a high sensitivity in the 3.5-5.0-MHz high frequency range (angled
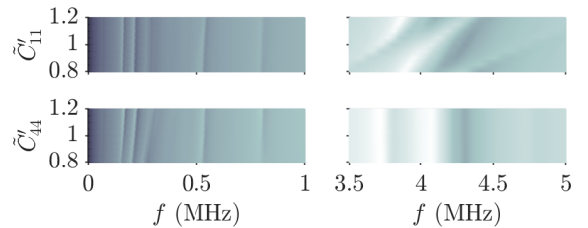
FIG. S2. Surface plot from 7 Ω (bright) to 128 kΩ (dark), using a logarithmic color scale, of the simulated electrical impedance spectrum $|Z(f)|$ of a Pz27-0.5-10 disk loaded by an on-glued PMMA-1.4-25 ring as a function of the frequency f and of the normalized real-part elastic moduli of PMMA, $\tilde{C}_{11}' = C_{11}'/C_{11}'^{\mathrm{ueis}}$ and $\tilde{C}_{44}' = C_{44}'/C_{44}'^{\mathrm{ueis}}$. Here $C_{11}'^{\mathrm{ueis}} = 7.18$ GPa and $C_{11}'^{\mathrm{ueis}} = 1.553$ GPa are the values determined by the UEIS method, see Table VI.

FIG. S3. Surface plot from 0.63 (bright) to 1.58 (dark), using a logarithmic color scale, of the simulated normalized electrical impedance spectrum $|Z(f)|/|Z_1(f)|$ of a Pz27-0.5-10 disk loaded by an on-glued PMMA-1.4-25 ring as a function of the frequency f and of the normalized imaginary-part elastic moduli of PMMA, $\tilde{C}_{11}'' = C_{11}''/C_{11}''^{\text{ueis}}$ and $\tilde{C}_{44}'' = C_{44}''/C_{44}''^{\text{ueis}}$. Here, $|Z_1(f)|$ is the reference spectrum calculated at $\tilde{C}_{11}'' = \tilde{C}_{44}'' = 1$, and $C_{11}''^{\text{ueis}} = -0.183$ GPa and $C_{44}''^{\text{ueis}} = -0.111$ GPa are the values determined by the UEIS method, see Table VI.

ridges in the $\tilde{C}_{11}'$-f plane). In contrast, $Z(f)$ has a small sensitivity to $\tilde{C}_{44}'$ in the low frequency range and is almost insensitive to $\tilde{C}_{44}'$ in the high frequency range. Similarly, Fig. S3 shows that $Z(f)$ is insensitive to $\tilde{C}_{11}''$ in the low frequency range, but sensitive in the high frequency range (large amplitude variations for fixed frequency). Conversely, $Z(f)$ is sensitive to $\tilde{C}_{44}''$ in the low frequency range and insensitive in the high frequency range.

S3. MATLAB AND COMSOL SCRIPTS FOR UEIS-FITTING OF PMMA PARAMETERS

In the Supplemental Material, we have included the sample files listed in Table S1. Using these files,

TABLE S1. List of the files provided in the Supplemental Material for redoing the UEIS fitting of the elastic moduli C_{11} and C_{44} of PMMA and for plotting $Z_{\text{exp}}(f)$ and $Z_{\text{sim}}(f)$ described in Section S3, as well as the animated gif files of the laser-Doppler vibrometer measurements presented in Section S6.

File name	File contents
UEIS_polymer_script.m	UEIS MATLAB script
UEIS_polymer_comsol_model.mph	UEIS COMSOL script
UEIS_fit_function.m	Support MATLAB script
Holland_check_elastic_iso.m	Support MATLAB script
Holland_check_pzt_infmm.m	Support MATLAB script
experiment_unloaded.txt	Data for $Z_{\text{exp}}(f)$, Fig. 4
simulated_fit_unloaded.txt	Data for $Z_{\text{sim}}(f)$, Fig. 4
experiment_loaded.txt	Data for $Z_{\text{exp}}(f)$, Fig. 5
simulated_fit_loaded.txt	Data for $Z_{\text{sim}}(f)$, Fig. 5
Animation_Fig_S7.gif	Animation of Fig. S7
Animation_Fig_S8a.gif	Animation of Fig. S8(a)
Animation_Fig_S8b.gif	Animation of Fig. S8(b)
Animation_Fig_S8c.gif	Animation of Fig. S8(c)
Animation_Fig_S8d.gif	Animation of Fig. S8(d)

the reader can redo the UEIS fitting procedure, described in Section V of the main paper, for the polymer PMMA based on the measured UEIS spectrum of a PMMA ring glued to a Pz27 transducer disk. The main MATLAB script UEIS_polymer_script.m is opened using the "LiveLink for MATLAB"-interface provided by COMSOL Multiphysics. It loads the COMSOL 6.0 script UEIS_polymer_comsol_model.mph together with the data points of the measured impedance spectrum experiment_loaded.txt of the PMMA-ring-glued-on-Pz27-disk system. It also calls the function UEIS_fit_function.m, which computes and minimizes the cost function $\mathcal{C}$ defined in Eq. (9) in the main paper, and which calls Holland_check_elastic_iso.m and Holland_check_pzt_infmm.m to check if $\text{Im}(-\boldsymbol{C})$ and $\boldsymbol{K}$ are positive definite. The main script requires the following user-input parameters: initial values and bounds for the polymer ring, the Pz27 parameters p_i^{pz27}, the glue-layer parameters p_i^{glue}, and the dimensions of the disk, the ring, and the glue layer.

Regarding the UEIS fitting, the path in parameter space during the fitting procedure of the complex-valued elastic moduli of PMMA is illustrated in Fig. S4. The path consists of (1) the initial values, (2) the results from the coarse fit using patternsearch, and (3) the final set of fitted PMMA parameters using fminsearchbnd, as illustrated in the flowchart of Fig. 3 in the main paper. The initial values are indicated by a single circle with a dot in the center, whereas the final fitted parameters are represented by a colored, star-shaped marker.
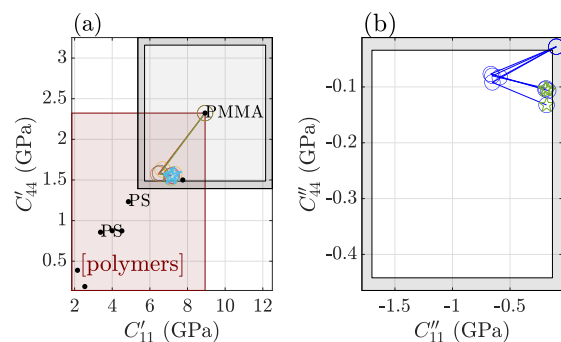
FIG. S4. The path in parameter space during the fitting procedure of the complex-valued elastic moduli $C_{11} = C_{11}' + iC_{11}''$ and $C_{44} = C_{44}' + iC_{44}''$, for four different Pz27-PMMA systems. (a) The path for the real parts C_{44}' and C_{11}'. The light-red shaded region indicates typical polymer values [2], PMMA and polystyrene (PS) are annotated. (b) The path of the imaginary parts C_{44}'' and C_{11}''. The gray frame indicates the region in parameter space, where the fitting procedure will expand the upper and lower bounds used in the last step.
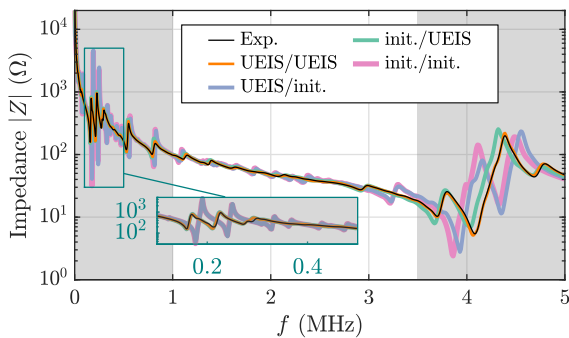
FIG. S5. The measured (Exp) and four simulated electrical impedance spectra $|Z(f)|$ for a PMMA-1.4-25 ring glued onto a Pz27-0.5-10 transducer disk. The four simulations labeled '(Pz27 parameters)/(PMMA parameters)' uses either the initial or the UEIS values as parameter values, for the Pz27 and the PMMA, respectively.

S4. SIMULATED ELECTRICAL IMPEDANCE FOR DIFFERENT MATERIAL PARAMETERS

In Fig. S5 is shown a comparison between a measured impedance spectrum and four simulated electrical impedance spectra using the four cases of material parameters obtained by combining either the initial values (init) or the final UEIS values (UEIS) of the Pz27 transducer disk with either the initial values (init) or the final UEIS values (UEIS) of the PMMA ring. Referring to Pz27 first and PMMA second, the four simulated spectra are labeled 'UEIS/UEIS', 'init/UEIS', 'UEIS/init', and 'init/init'. Clearly, 'UEIS/UEIS' fits the experimental curve best, and 'init/UEIS' comes close. Thus the final PMMA values are not so sensitive to the Pz27 values.

S5. VALIDATION DATA BY ULTRASOUND-TROUGH-TRANSMISSION

An ultrasonic-through-transmission (UTT) technique was used to validate the material parameters determined by the UEIS method. The UTT data is presented in Fig. S6, showing the temperature dependency of the longitudinal and transverse speed of sound (c_{lo} and c_{tr}) and the attenuation coefficients (α_{lo} and α_{tr}) for PMMA. The material parameters were measured at regular time intervals while the water cooled down from 31 ℃ to 23 ℃. Linear regression (LR) was performed based on the measured data points and a 1σ prediction interval (PI) as well as $\pm 1\sigma$ error bars were calculated based on the sum-of-square difference between regression line fit and the measured data points. The final UTT values of the elastic moduli C_{11} and C_{44} of PMMA are obtained by inserting the obtained UTT values for c_{lo}, c_{tr}, α_{lo}, and α_{tr} into expression (14), and they are listed in Table VI.
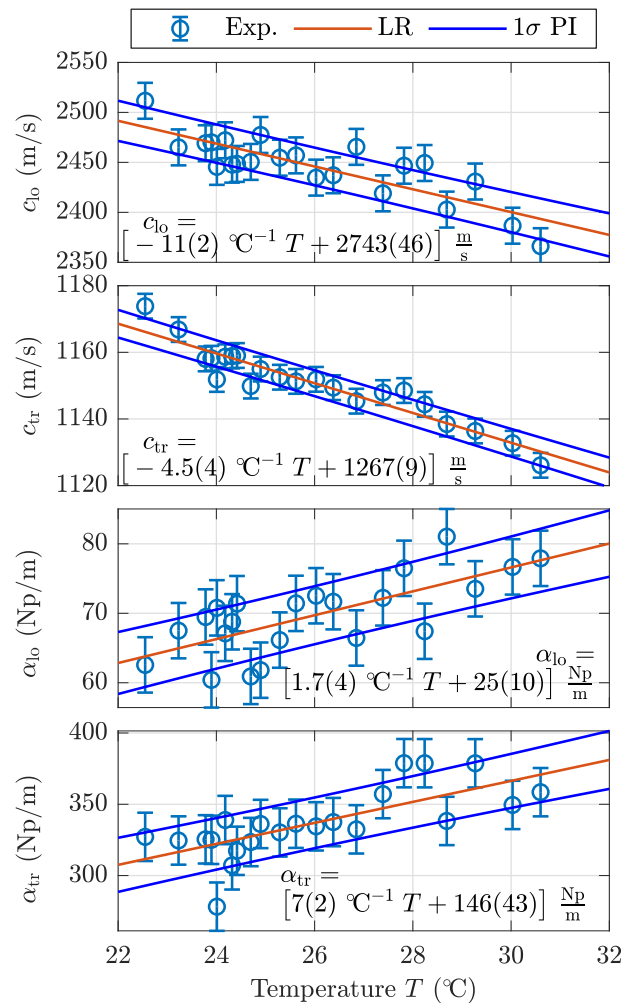
FIG. S6. Validation data obtained for a PMMA slab in water cooling steadily from 31 ℃ to 23 ℃ over a period of 6 hours using UTT measurements with a pulse of center frequency $f_c = 1.90$ MHz and width $\Delta f \approx 1$ MHz. The longitudinal and transverse sound speed (c_{lo} and c_{tr}) and the attenuation coefficients (α_{lo} and α_{tr}) of the PMMA are plotted versus temperature T. Linear regression (LR) and 1σ-prediction intervals (PI) are represented by red and blue lines, respectively. Error bars indicate the $\pm 1\sigma$ uncertainty based on the sum-of-square differences between measured data and the LR.

S6. VALIDATION DATA BY LASER-DOPPLER VIBROMETRY

Using a single-point laser-Doppler vibrometer system VibroFlex Connect (Polytec, Waldbronn, Germany), the normal displacement u_z was measured on the top-surface of an unloaded Pz27 transducer disk or of a PMMA ring glued to a Pz27 disk held in the point-contact sample holder shown in Fig. 2 of the main paper and brought into a resonance mode by applying a peak-to-peak voltage of $V_{pp} = 2$ V. The PMMA surface was sputtered with a thin gold layer (approximately 14 nm thick) to increase the signal strength of the reflected signal.
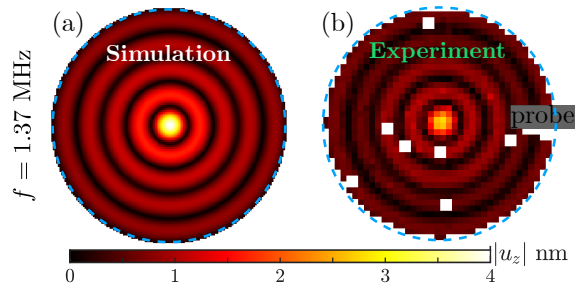
FIG. S7. (a) Simulated and (b) measured normal displacement amplitude $|u_z|$ of an unloaded Pz27-0.5-10 transducer disk (blue dashed line) driven by a 2-V peak-to-peak AC voltage at the resonance frequency $f_{\mathrm{res}} = 1.37$ MHz.

TABLE S2. Details of the vibrometer measurements including resonance frequency f_{res}, stepping size, and data acquisition time t_{acq} for each measured resonance mode.

System	Pz27	Pz27+PMMA	Pz27+PMMA
f_{res} (MHz)	0.058	0.164	1.370
x-y step size (mm)	1	0.5	0.25
t_{acq} (min)	23	81	110

The vibrometer measurements were limited by the stepping-motor range (x from 0 to 100 mm and y from 0 to 12 mm). The step-size and the data acquisition time can be found in Table S2 for each experiment. Note that there are no free parameters in the simulation, since the geometry, the material parameters, and the amplitude and frequency of the excitation voltage are all known.

Figs. S7 and S8, and the corresponding animations of the time-dependent displacement field listed in Table S1, show a comparison between the measured and the no-free-parameter-simulated normal displacement amplitude at the selected resonances. The good qualitative and quantitative agreement in the three cases Figs. S7, S8(b), and S8(d) provide an experimental validation of the UEIS method supplementing the UTT validation. Note in Fig. S8 the improved agreement between simulation and experiment, when the actual off-center position $\Delta = 0.4$ mm of the Pz27 disk relative to the PMMA ring is taken into account in the simulation.
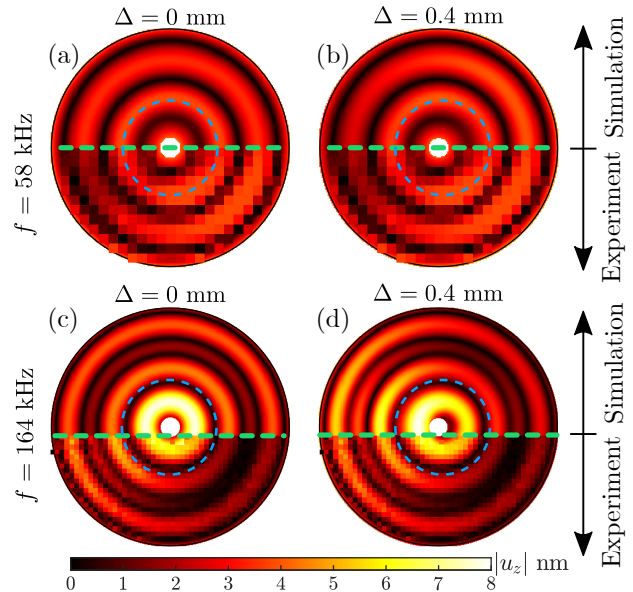
FIG. S8. Simulated and measured normal displacement amplitude $|u_z|$ of a PMMA-1.4-25 ring glued to a Pz27-0.5-10 disk (blue dashed line) driven by a 2-V peak-to-peak AC voltage at the two resonance frequencies $f_{\mathrm{res}} = 58$ and 164 kHz, respectively. The Pz27 disk was measured to be off-centered relative to the PMMA ring by $\Delta = 0.4$ mm. In each panel, the simulation (smooth) is above the green dashed line and the experiment (pixelated) is below. (a) $f_{\mathrm{res}} = 58$ kHz and an axisymmetric simulation with $\Delta = 0$ mm. (b) as (a) but $\Delta = 0.4$ mm in a nonsymmetric simulation. (c) $f_{\mathrm{res}} = 164$ kHz and an axisymmetric simulation with $\Delta = 0$ mm. (d) as (c) but $\Delta = 0.4$ mm in a nonsymmetric simulation.

REFERENCES

[1] N. Pérez, M. A. B. Andrade, F. Buiochi, and J. C. Adamowski, Identification of elastic, dielectric, and piezoelectric constants in piezoceramic disks, IEEE Trans. Ultrason. Ferroelec. Freq. Contr. **57**, 2772 (2010).

[2] W. D. Callister Jr, *Materials Science and Engineering: An Introduction*, seventh ed. (John Wiley & Sons, York, PA, 2007) p. 975.

Chapter 7

A 3D-printed polymer-based acoustofluidic device

Until this chapter, the UEIS method has been used to determine complex-valued material parameters for piezoelectric transducers, a UV-curable adhesive, and a polymer. In addition to those, the UEIS method will be used to determine the complex-valued elastic moduli of a 3D-print resin. Having a well-characterized 3D-print resin with known material parameters allows us to perform accurate computer-aided engineering of acoustofluidic devices, in which the design is only limited by the 3D printer's accuracy and capacity. Furthermore, using a 3D printer to fabricate acoustofluidic devices provides cheap and fast prototyping.

In addition to the acoustic fields, the model is extended to include a steady flow solution to the stationary velocity $\boldsymbol{v}_0(\boldsymbol{r})$ and pressure field $p_0(\boldsymbol{r})$. With this model, we are able to simulate acoustophoresis. The device will be evaluated in terms of acoustic energy density, throughput capacity, and separation efficiency by numerical simulations. This is an ongoing study, and the preliminary results will be presented here. The printer is currently under maintenance, so the chapter will only include numerical results for the stationary flow and the acoustophoresis response. Finally, by linking the COMSOL model to MATLAB, the design is optimized in terms of the acoustophoresis performance, using built-in MATLAB-optimization algorithms.

7.1   3D-print material characterization and device design

At the DTU workshop, we have access to a *Stratasys J35 Pro* 3D printer, with an accuracy of 150 μm, a print capacity of 1,174 cm$^2 \times$ 15.5 cm, and a minimal print layer thickness of 18.75 μm. Furthermore, the printer is compatible with different types of resin materials with different optical and mechanical properties. In this study, a transparent acrylic-like resin named VeroClear (VC) will be used, allowing optical measurements and visual inspection. Before designing the device geometry, the VC material was characterized, enabling the use of the 1D-layered design principle relying on the longitudinal sound speed in each layer.

Again, the UEIS method was used to determine the complex-valued elastic moduli of the VC resin: a 3D-printed VC ring with dimensions VC-TH1.4-OD25-ID2.0 was glued onto a Pz27-TH0.5-OD10 transducer using the already-characterized NOA86H adhesive. The loaded electrical impedance spectrum was loaded into the UEIS fitting software, and after ten hours, the complex-valued elastic moduli of the VC were determined. The parameters are provided in Table B.3. The resulting UEIS-fitted electrical impedance spectrum is plotted in Fig. 7.1 together with the measured spectrum. In Fig. 7.1(b)-(c), the electrical impedance spectrum is plotted on a linear scale in specific frequency intervals. All the features are captured in the UEIS-fitted spectrum but up to 20% deviations in amplitude. However, minor deviations in the resonance frequencies can result in large relative deviations due to the electrical impedance spectrum being peaked at resonances. Consider, for example, a Lorentzian-shaped peak with a quality factor of 20; in this case, a 1% shift in resonance frequency causes a 16% relative deviation in amplitude.
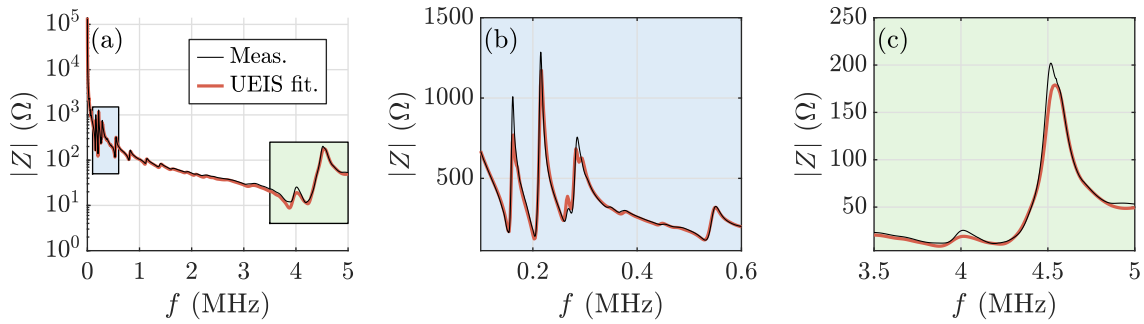
Figure 7.1: (a) Measured and UEIS-fitted electrical impedance spectrum $|Z(f)|$ for a VC-TH1.4-OD25-ID2.0 ring glued onto a Pz27-TH0.5-OD10 transducer using the NOA86H adhesive. (b) Zoom-in from 0.1-0.6 MHz on a linear scale. (c) Similar to (b) but in the frequency range 3.5-5 MHz. The zoom-in regions are indicated in (a) with corresponding colors.

In Section 5.3, the acoustofluidic chip design was limited by the PMMA-slide thickness. In this case, the design is only limited by the print capacity, accuracy, and print-layer thickness. The acoustofluidic device design is shown in Fig. 7.2. The microfluidic chip design consists of a VC cover, with an in- and outlet, glued onto a VC base containing an elliptical cavity and a bottom outlet. The final device is assembled by gluing the VC-based microfluidic cavity onto a Pz27 transducer. The elliptic cavity channel geometry is designed to cover the active region above the transducer. The two outlets are necessary for the separation of particles. The design is inspired by the acoustophoresis devices in Refs. [27, 29, 64] and relies on a so-called quarter-wave resonator principle as sketched in Fig. 7.3(a). The design builds on the 1D-layered-resonator principle, as was discussed in Section 5.2.1 and outlined here; the base and cover motion is matched to the quarter-wave in the fluid and the half-wave in the transducer, corresponding to a quarter-wave in the base and a half-wave in the cover. The quarter-wave resonator can be used to separate

particles from a fluid, e.g., separating plasma from whole blood. The working principle is simple: the acoustic radiation force moves the particle toward the top outlet while transported by the flow. If the particle has crossed the mid-height before reaching the outlets, the particle will be separated into the top outlet, as illustrated in Fig. 7.3(b).
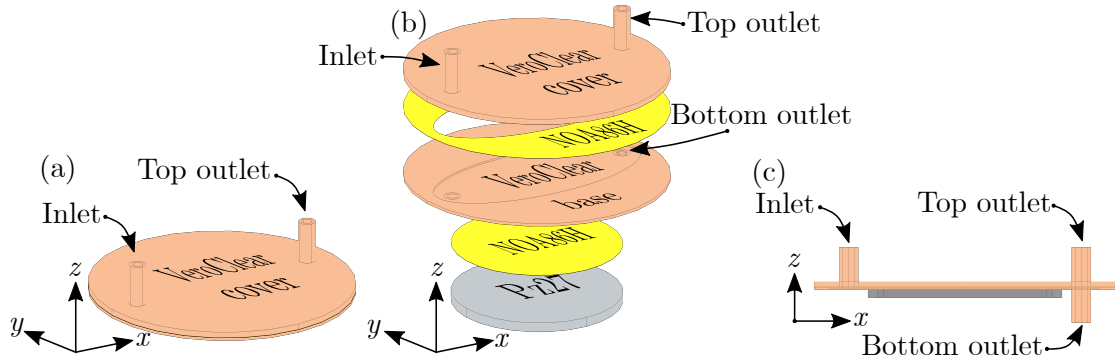
Figure 7.2: (a) Sketch of the 3D-printed quarter-wave design for acoustophoresis particle separation. (b) Exploded view, showing each device component: a VC cover with in- and outlet (beige), a VC base (beige) with an elliptic channel geometry and a single outlet, a Pz27 transducer (gray), and in-between NOA86H glue layers (yellow). (c) A cross-section view of the design in the xz mirror plane.
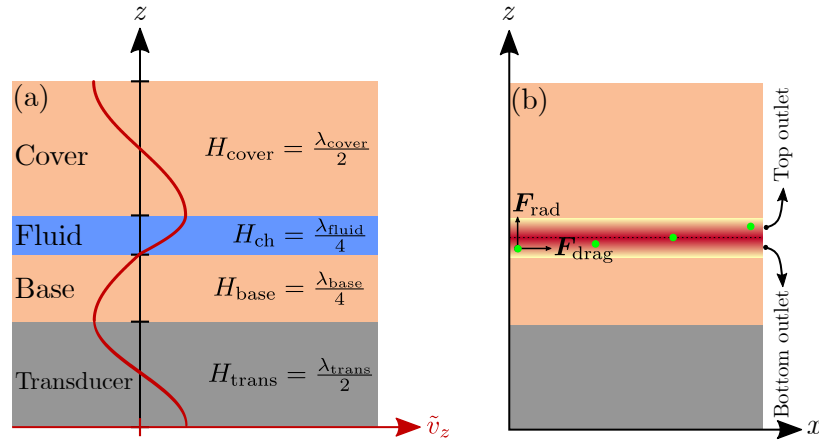
Figure 7.3: (a) Sketch of the 1D-layered principle used to design the VC-based quarter-wave acoustophoresis device. The idealized velocity/displacement profile (red line) is sketched as a function of the vertical coordinate z. (b) Sketch of the basic acoustophoresis principle in a quarter-wave resonator: a particle (green dot) gets transported by the drag. At the same time, the acoustic radiation force forces the particle toward the cover and the top outlet. The idealized positive-valued vertical radiation force amplitude is illustrated by a surface plot from minimum value (yellow) to maximum value (red).

Usually, an acoustofluidic device design is constrained by the accessibility to the transducer's top and bottom surface electrode for electrical actuation. However, using a wraparound transducer-electrode configuration, as shown in Fig. 7.4(b), both the electrodes can be accessed from a single surface. The Pz27-TH1.0-OD25 transducer with wraparound electrodes was characterized by the UEIS method. The fitted spectrum is shown in Fig. 7.4(a) together with the measured. Notice how the planar harmonics are "killed" by the electrode configuration. The primary thickness mode remains at $f_{\mathrm{t}} = 1.913\,\mathrm{MHz}$, and the quarter-wave resonator principle can be used to determine the thicknesses of each component: $H_{\mathrm{ch}} = c_0/(4f_{\mathrm{t}})$, $H_{\mathrm{base}} = c_{\mathrm{lo}}^{(\mathrm{base})}/(4f_{\mathrm{t}})$, and $H_{\mathrm{cover}} = c_{\mathrm{lo}}^{(\mathrm{cover})}/(2f_{\mathrm{t}})$, the values are provided in Table 7.1.
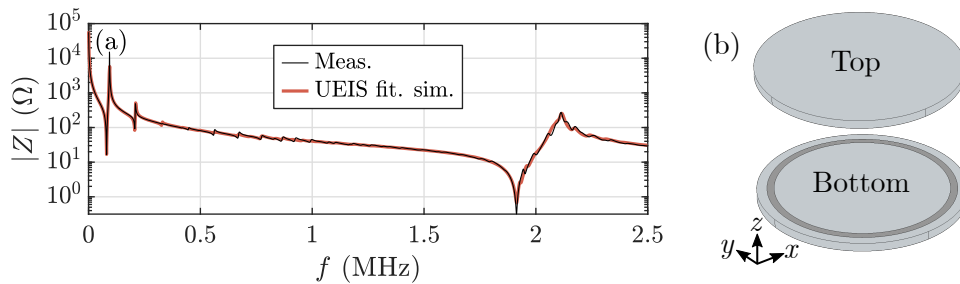
Figure 7.4: (a) Measured and UEIS-fitted electrical impedance spectra $|Z(f)|$ for a Pz27-TH1.0-OD25 transducer with wrap-around electrode configuration. (b) Sketch of a Pz27-TH1.0-OD25 transducer (dark gray) with wrap-around electrode (light gray) configuration for single-side actuation.

Table 7.1: 3D-printed quarter-wave design dimensions used in the simulation. The inner and outer diameters of the in- and outlet fittings are 1.5 and 2.5 mm, respectively, and positioned $\pm 15\,\mathrm{mm}$ from the center axis. The tube fittings extend $H_{\mathrm{in}} = 4.3\,\mathrm{mm}$ from the cover. Both NOA86H glue-layers are 17 μm thick.

	Thickness (μm)	Diameter (mm)	Semi-major (mm)	Semi-minor (mm)
VC cover	665	39.2	-	-
Cavity	196	-	17.6	8
VC base	332	39.2	-	-
Pz27	1,045	25.27	-	-

7.2   Acoustic response

As shown in Fig. 7.2, the model consists of a VeroClear cover with in- and outlet tube fittings. The VeroClear cover is glued onto a VeroClear base with an outlet tube fitting, comprising the microfluidic chip, which is glued onto a Pz27-TH1.0-OD25 transducer with a wrap-around electrode configuration. By gluing together the components co-axially, the model geometry can be reduced to one-half given by the xz-mirror-plane, using the symmetry boundary conditions in Table 3.2. However, even though the model geometry can be reduced to one-half by the mirror symmetry, the system is too large for calculating wide-ranged frequency spectra.

In Fig. 5.13, it was evident how the PMMA-based cavity with a nearly axisymmetric device geometry was well-approximated by a 2D axisymmetric model, which in turn allows calculations of wide-ranged frequency spectra due to the substantial reduction in degrees of freedom. The same approach will be applied here: the energy density spectrum $E_{ac}(f)$ will be calculated using a 2D axisymmetric model to locate the main resonance. Afterward, a narrow-range spectrum is calculated using the mirror-symmetry-reduced 3D model. The results are shown in Fig. 7.5(a). Again, the 2D axisymmetric model turns out to be a good approximation to the nearly axisymmetric geometry, and by looking at Fig. 7.5(b)-(c), the response is almost identical and invariant in the radial direction, resembling a 1D layered quarter-wave resonator. In both cases, the acoustic resonance is located at $f = 1.91$ identical to the transducer thickness mode f_t, and the acoustic energy density agrees within 5% with a value of $E_{ac} = 0.55\,\text{Pa}$ for the full 3D model.
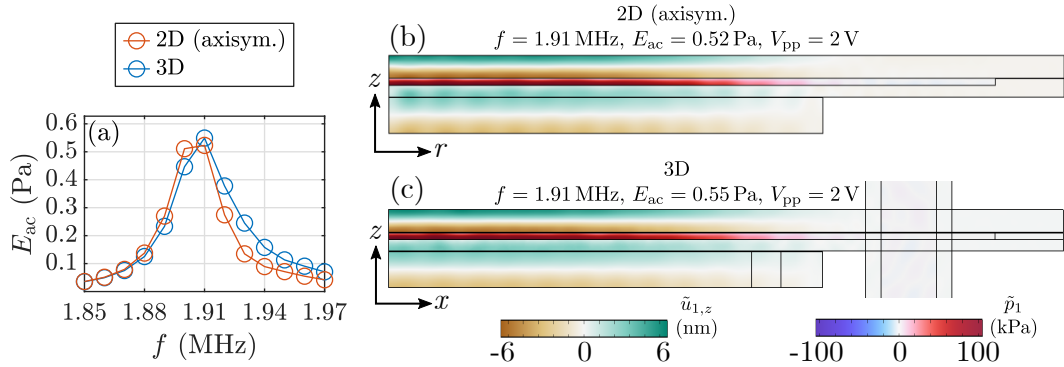
Figure 7.5: (a) Acoustic energy density spectrum $E_{ac}(f)$ for the 2D axisymmetric and the full 3D model near the main resonance frequency located at $f = 1.91\,\text{MHz}$. (b) Simulated response at resonance frequency $f = 1.91\,\text{MHz}$, for the 2D axisymmetric model. The response is illustrated with surface plots of the acoustic pressure field $\tilde{p}_1$ and the vertical displacement field $\tilde{u}_{1,z}$, at a phase with maximum pressure amplitude. (c) Similar to (b), but for the full 3D model. The surface plots are evaluated on the xz mirror plane.

The acoustic response, combined with the flow, determines the acoustophoresis performance. In the following sections, the stationary flow field will be solved numerically, and in combination with the simulated acoustofluidic response, we will be able to simulate the acoustophoresis performance.

7.3   Stationary flow solution

The stationary flow variables are solved numerically to evaluate the throughput efficiency in continuous-flow conditions. Since the steady flow field $\boldsymbol{v}_0$ is much slower than the sound speed $|\boldsymbol{v}_0|/c_0 \sim 10^{-6}$, the acoustic and the steady flow fields are decoupled and solved separately. Furthermore, this condition implies that the steady flow field can be considered as an incompressible flow, so the conservation of mass simplifies to

$$\boldsymbol{\nabla} \cdot \boldsymbol{v}_0 = 0, \tag{7.1}$$

and the conservation of momentum simplifies to the steady-state incompressible Navier–Stokes equation

$$\rho_0 \left(\boldsymbol{v}_0 \cdot \boldsymbol{\nabla}\right) \boldsymbol{v}_0 = \boldsymbol{\nabla} \cdot \boldsymbol{\sigma}_0 = \boldsymbol{\nabla} \cdot \left\{ -p_0 \boldsymbol{I} + \eta_0 \left[\boldsymbol{\nabla} \boldsymbol{v}_0 + (\boldsymbol{\nabla} \boldsymbol{v}_0)^{\mathsf{T}} \right] \right\}. \tag{7.2a}$$

The gravitational body force term $\rho_0 \boldsymbol{g}$ is canceled by the hydrostatic pressure included in p_0. These equations can be re-written as a strong form $\boldsymbol{\nabla} \cdot \boldsymbol{J} - \boldsymbol{F} = \boldsymbol{0}$ used for the implementation in COMSOL MULTIPHYSICS. For the pressure field p_0, the strong form reads

$$\boldsymbol{J}^{(p_0)} = \boldsymbol{0}, \quad \text{and} \quad F^{(p_0)} = \boldsymbol{\nabla} \cdot \boldsymbol{v}_0, \tag{7.3}$$

and

$$\boldsymbol{J}^{(\boldsymbol{v}_0)} = \boldsymbol{\sigma}_0, \quad \text{and} \quad \boldsymbol{F}^{(\boldsymbol{v}_0)} = \rho_0 \left(\boldsymbol{v}_0 \cdot \boldsymbol{\nabla}\right) \boldsymbol{v}_0, \tag{7.4}$$

for the velocity field $\boldsymbol{v}_0$. The flow is driven by a pressure difference Δp_0 between the in- and outlet. Numerically, this is implemented as a Dirichlet boundary condition. The no-slip condition for the flow field $\boldsymbol{v}_0$ is also implemented as a Dirichlet boundary condition on the fluid-solid interface. Furthermore, the in-plane velocity components at the in- and outlet are set to zero to enforce an axisymmetric velocity profile at the in- and outlets. This condition is also implemented as a Dirichlet boundary condition.

In a laminar flow, the flow profile is fully developed inside the inlet before reaching the microfluidic cavity. Numerically, this is ensured by an inlet longer than the entrance length $\mathcal{L} = \max\left(a_{\text{in}}, \frac{Re}{12} a_{\text{in}}\right)$, given by the inlet radius a_{in} and the Reynolds number Re, as shown in Ref. [81]. To estimate the Reynolds number, the flow rate Q_0, given the pressure difference Δp_0, is estimated by a series of hydraulic resistors

$$Q_0 \approx \frac{1}{2R_{\text{circ}} + R_{\text{plate}}} \Delta p_0 \approx \frac{1}{R_0} \Delta p_0, \text{ where} \tag{7.5a}$$

$$R_{\text{circ}} = \frac{8\eta_0 H_{\text{in}}}{\pi a_{\text{in}}^4}, \quad \text{and} \quad R_{\text{plate}} = \frac{12\eta_0 L}{H_{\text{ch}}^3 W_{\text{ch}}}. \tag{7.5b}$$

Inserting the inlet height $H_{in} = 4.3\,\text{mm}$, the channel height $H_{ch} = 196\,\mu\text{m}$, the channel width $W_{ch} = 8\,\text{mm}$, the inlet radius $a_{in} = 0.75\,\text{mm}$, and the length between in- and outlet $L = 30\,\text{mm}$ yields $R_0 = 5.4\,\text{GPa}\,\text{s/m}^3$. With this estimate, a pressure difference of $\Delta p_0 = 10\,\text{Pa}$ yields $Q_0 = 112\,\mu\text{L/min}$ and $Re = \frac{\rho_0 Q_0}{\pi a_{in} \eta_0} = 0.9$, so the laminar flow profile is well-established before reaching the entrance since $\mathcal{L} = a_{in} < H_{in}$. The steady flow solution for $\Delta p_0 = 10\,\text{Pa}$ is shown in Fig. 7.6. Instead of the estimated flow rate of $112\,\mu\text{L/min}$ we find $Q_0 = 93\,\mu\text{L/min}$ and $Re = 0.8$.
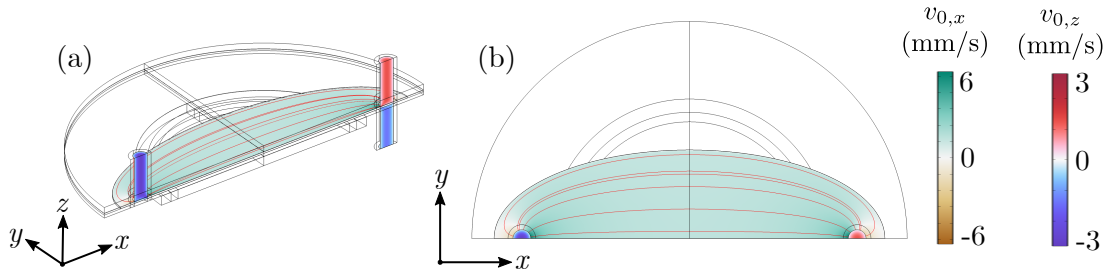
Figure 7.6: Pressure-driven steady-flow solution $\boldsymbol{v}_0$ for the 3D-printed quarter-wave microfluidic design driven at $\Delta p_0 = 10\,\text{Pa}$ between in- and outlet. (a) 3D-view showing the streamlines (red lines) together with the flow's z-component $v_{0,z}$ evaluated on the xz-mirror-plane and the x-component $v_{0,x}$ at the channel mid-height. (b) Top-view of (a).

7.4 Simulated acoustophoresis performance

In this section, the numerical solution to the steady flow will be combined with the acoustic response, enabling the simulation of acoustophoresis behavior, i.e., particle trajectories influenced by acoustic forces in a continuous flow.

As illustrated in Fig. 7.3(b), the resulting acoustic radiation force in a quarter-wave device forces the particles toward the cover and the top outlet due to the quarter-wave-shaped acoustic pressure field, with maximum pressure near the bottom and vanishing pressure near the top. The time t_{foc} it takes to move a particle at start-position $z_0 = H_{ch}/8$ to end-position $z_{end} = 5H_{ch}/8$ in an idealized quarter-wave resonator with acoustic pressure field $p_1 = p_a \cos(k_0 z)$ and wavenumber $k_0 = \frac{\pi}{2H_{ch}}$ is identical to Eq. (5.13). In this case the simulated resonance was located at $f = 1.91\,\text{MHz}$ with $E_{ac} = 0.55\,\text{Pa}$, and from the 10-µm-diameter polystyrene particle parameters provided in Table 5.3 the focusing time is $t_{foc} = 10\,\text{s}$. The time t_{foc} is also the minimum period of time the particles are allowed inside the cavity, above the actuation region, before being successfully separated into the top outlet. This period of time can be used to estimate an average critical velocity $v_{crit} = \frac{d_{trans}}{t_{foc}} = 2.45\,\text{mm/s}$ at which speed the particles can travel and still be separated after traveling a distance $d_{trans} = 25\,\text{mm}$ corresponding to the transducer diameter. The average critical velocity corresponds to a critical flow rate of $Q_{crit} = \pi a_{in}^2 v_{crit} = 260\,\mu\text{L/min}$.

In Section 5.3.1, the particle equation of motion for a quiescent fluid was solved numerically by using the COMSOL module *"particle tracing for fluid flow"*, in this case, the force balance is extended by including the drag induced by the steady-flow $\boldsymbol{v}_0$. As in Eq. (5.10), the equation of motion was simplified, inferring the low particle Reynolds number. Here, the particle Reynolds number $Re_\mathrm{p} = \frac{2\rho_0 a(v_\mathrm{t} + v_\mathrm{crit})}{\eta_0}$ acquires an extra contribution due to the flow yielding $Re_\mathrm{p} = 0.03$ and the "massless" equation of motion

$$\frac{\mathrm{d}\boldsymbol{r}_\mathrm{p}(t)}{\mathrm{d}t} = \boldsymbol{v}_\mathrm{p} = \frac{\boldsymbol{F}_\mathrm{rad}}{6\pi\eta_0 a} + \boldsymbol{v}_0, \tag{7.6}$$

is still a good approximation. The particle trajectories $\boldsymbol{r}_\mathrm{p}(t)$ are simulated by numerical integration of $\boldsymbol{r}_\mathrm{p}(t) = \int_0^t \boldsymbol{v}_\mathrm{p}(\boldsymbol{r}(t'))\mathrm{d}t'$ according to Eq. (7.6).

All the constituents required to simulate and evaluate the acoustophoresis performance of the suggested 3D-printed polymer-based acoustofluidic device are in place. To evaluate the acoustophoresis performance and the separation efficiency, we define the transfer ratio

$$\mathcal{T} = \frac{N_\mathrm{top}}{N_\mathrm{top} + N_\mathrm{bot}}, \tag{7.7}$$

to be the ratio between the number of particles reaching the top outlet N_top to the sum of particles in the top and bottom outlet $N_\mathrm{top} + N_\mathrm{bot}$. The particle trajectories are calculated during a period of $T = 3T_\mathrm{emp} = 3V_\mathrm{ch}/Q_0$, i.e., the time it takes to empty the channel volume three times, determined by the channel volume $V_\mathrm{ch} = 62\,\mu\mathrm{L}$ and the flow rate Q_0. The particles are released at the inlet at random positions in steps of $T/1000$, and the total number of particles released N_tot matches the particle concentration $c_\mathrm{N} = 450\,\mu\mathrm{L}^{-1}$ used in Section 5.3 that is $N_\mathrm{tot} = 3c_\mathrm{N}V_\mathrm{ch} = 83{,}700$. The acoustophoresis performance is evaluated by simulating 10-µm-diameter polystyrene particle trajectories and calculating the transfer ratio $\mathcal{T}$ at different flow rates at a constant voltage amplitude of $V_\mathrm{pp} = 2\,\mathrm{V}$. The results are tabulated in Table 7.2 together with the flow Reynolds number and the laminar entrance length.

Assuming following proportionality

$$Q_\mathrm{crit} \propto v_\mathrm{crit} \propto \frac{1}{t_\mathrm{foc}} \propto E_\mathrm{ac} \propto V_\mathrm{pp}^2, \tag{7.8}$$

we can provide a peak-to-peak voltage amplitude $\hat{V}_\mathrm{pp}$ required to achieve a throughput of 1 L/hour, the values are provided in Table 7.2 and ranges from 8 to 19 V. In Ref. [27] Adams et al. achieved a flow rate of 1 L/hour at $V_\mathrm{pp} = 55\,\mathrm{V}$ with a transfer ratio of 0.8, for a glass-based device. However, possible heating and non-linear effects set in at these voltage amplitudes, so the proportionality might not hold. These results are still to be verified by experiments when the 3D printer is up and running.

Table 7.2: Tabulated values for numerically evaluated separation efficiency including the flow rate Q_0 in units of $Q_{crit} = 260\,\mu L/min$, the particle counts N_{top} and N_{bot}, the transfer ratio $\mathcal{T}$, the Reynolds number Re, and the laminar entrance length condition $\mathcal{L}/a_{in}$. The values are obtained at a peak-to-peak voltage amplitude of $V_{pp} = 2\,V$. The amplitude $\hat{V}_{pp}$ corresponds to the required peak-to-peak voltage amplitude to achieve $Q_0 = 1\,L/hour$.

| Q_0 | N_{top} | N_{bot} | $\mathcal{T}$ | Re | $\mathcal{L}/a_{in}$ | $\hat{V}_{pp}$ |
(Q_{crit})	(-)	(-)	(-)	(-)	(-)	(V)
0.69	4,465	33	0.99	3	0.17	19.3
1.38	10,556	700	0.94	5	0.17	13.6
2.07	10,395	951	0.92	8	0.17	11.1
4.14	32,501	6,523	0.83	17	0.25	7.9

7.5 Numerical design optimization

By using the COMSOL built-in *"LiveLink for MATLAB"* module, our model can be linked with MATLAB and the built-in optimization algorithms in MATLAB can be used in model-optimization routines. In this case, the `fminsearchbnd` algorithm (described in Chapter C) is used to optimize the acoustofluidic device design. The same algorithm was also used in Paper III [3] to fit the electrical impedance spectrum, and it is a gradient-free method based on a direct and bounded simplex search.

The optimization routine is time-consuming and requires many iterations, which is infeasible for a full 3D model. Instead, a 2D axisymmetric model corresponding to the yz cross-section is used, resembling the nearly axisymmetric device. As was shown in Fig. 5.13 and Fig. 7.5 the 2D axisymmetric model turned out to be a good approximation to the full 3D model.

Using a 3D printer to fabricate the device, the geometry and device dimensions are only limited by the resolution and the print capacity. In this case, the device design is optimized in terms of the cover thickness H_{cover}, the base thickness H_{base}, the channel height H_{ch}, and the semi-minor cavity radius b_{ch}, constituting the set of optimization variables

$$\mathcal{P} = \{H_{cover}, H_{base}, H_{ch}, b_{ch}\}. \tag{7.9}$$

The semi-major cavity radius a_{ch} is fixed since the in- and outlet require space. The `fminsearchbnd` requires initial-values $\mathcal{P}_{init}$ for the optimization variables

$$\mathcal{P}_{init} = \left\{ \frac{\lambda_{cover}}{2}, \frac{\lambda_{base}}{4}, \frac{\lambda_0}{4}, 0.32 d_{trans} \right\}. \tag{7.10}$$

The initial values for the thicknesses are given in terms of the wavelengths according to the 1D principle illustrated in Fig. 7.3. The values are provided in Table 7.1. The initial-value for the semi-minor radius is 32% of the transducer diameter $b_{ch} = 0.32 d_{trans} = 8\,mm$. The upper and lower bounds were set to $\pm 50\%$ from the initial values.

For each geometry iteration, controlled by the `fminsearchbnd` algorithm, the figure of merit

$$\mathcal{F} = \frac{\int F_{\mathrm{rad},z}\,\mathrm{d}V}{\int |F_{\mathrm{rad},r}|\,\mathrm{d}V} A E_{\mathrm{ac}} = \mathcal{R} A E_{\mathrm{ac}}, \tag{7.11}$$

is calculated as a function of frequency f in the interval from 1.8 to 2.1 MHz in steps of 5 kHz, so each optimization-function evaluation includes 61 computations. Here, a modified version of the figure of merit Eq. (4.4) is used, suitable for vertical focusing toward the top outlet and minimal forces in the radial direction. Furthermore, it is weighted by the channel area $A = H_{\mathrm{ch}} b_{\mathrm{ch}}$ and the acoustic energy density E_{ac} for increased volume and throughput capacity. The cost function

$$\mathcal{C} = -\max\left[\mathcal{F}(f)\right], \tag{7.12}$$

is defined as the negative maximum value of $\mathcal{F}(f)$. The `fminsearchbnd` tries to minimize the cost function (maximizing $\max\left[\mathcal{F}(f)\right]$) by varying the optimization variables $\mathcal{P}$ according to algorithm presented in Chapter C. The initial-values yields $\mathcal{F} = 30\,\mu\mathrm{N}$ with $\mathcal{R} = 15$, $E_{\mathrm{ac}} = 1.2\,\mathrm{Pa}$, $A = 1.7\,\mathrm{mm}^2$. After 127 iterations, 237 function evaluations, and 14,457 computations, the optimization reaches a value of $\mathcal{F}_{\mathrm{fit}} = 99\,\mu\mathrm{N}$, with $\mathcal{R} = 36$, $E_{\mathrm{ac}} = 1.1\,\mathrm{Pa}$, $A = 2.5\,\mathrm{mm}^2$, given the following set of optimized parameters

$$\mathcal{P}_{\mathrm{opt}} = \{0.90, 0.62, 1.18, 1.24\}\,\mathcal{P}_{\mathrm{init}} = \{600\,\mu\mathrm{m}, 208\,\mu\mathrm{m}, 230\,\mu\mathrm{m}, 10.0\,\mathrm{mm}\}. \tag{7.13}$$

The cost function $\mathcal{C}$ is plotted as a function of iterations in Fig. 7.7(a), together with the acoustic response at resonance in Fig. 7.7(b)-(c) given the initial and optimized geometry. Even though the acoustic energy density in the optimized design is similar to the initial geometry, the focusability $\mathcal{R}$ has increased by a factor of 2.4, and the area A has increased by a factor of 1.5.
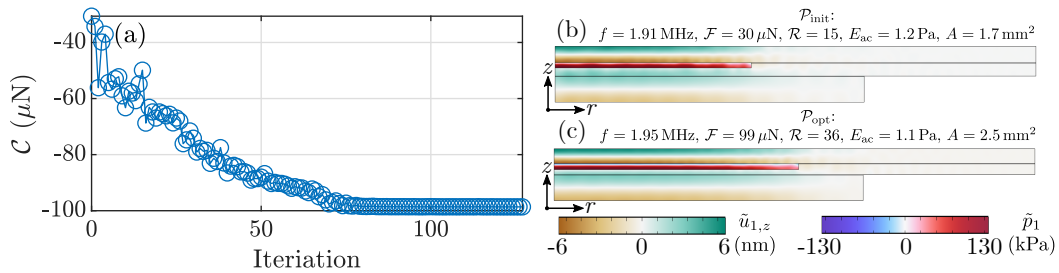
Figure 7.7: (a) Cost function $\mathcal{C}$ as a function of optimization iterations. (b) Simulated acoustic response at resonance for the initial 2D geometry, showing the vertical displacement $\tilde{u}_{1,z}$ and the acoustic pressure $\tilde{p}_1$ at the phase with maximum pressure amplitude. (c) Similar to (b) but for the optimized 2D design.

Following the same procedure as in Section 7.4, the transfer ratio was calculated using a full 3D model with the optimized 2D device geometry. The transfer ratio is plotted in Fig. 7.8 for the initial and optimized device designs as a function of flow rate. The optimized design achieves the same transfer ratios at flow rates approximately two times larger than the initial design. However, these results are purely numerical, but the corresponding experiments will be carried out when the 3D printer is up and running.
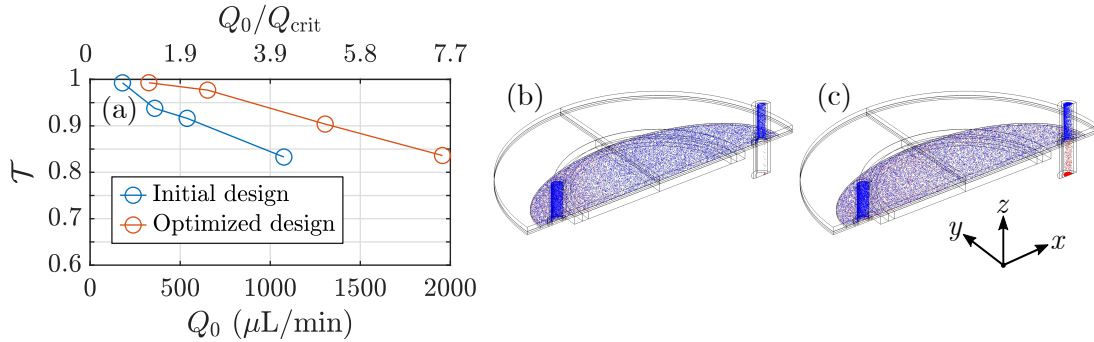
Figure 7.8: (a) Simulated transfer ratio $\mathcal{T}$ versus flow rate Q_0 for the initial and optimized designs. (b) Final particle positions at flow rate $Q_0 = 326\,\mu\text{L/min}$ after running the flow for $3T_\text{emp} = 91\,\text{s}$, for the optimized design. Particles above the channel mid-height are plotted as blue dots, whereas the red-colored particles are below the channel mid-height. (c) Similar to (b) but at $Q_0 = 1956\,\mu\text{L/min}$ after time $3T_\text{emp} = 15\,\text{s}$.

Chapter summary: The results presented in this chapter are an excellent example of how the UEIS method enables us to model acoustophoresis phenomena and assess performance in polymer-based acoustofluidic devices without free model parameters. Furthermore, the UEIS method provided the necessary material parameters to model a 3D-print resin, enabling accurate and fast prototyping of polymer-based acoustofluidic devices together with computer-assisted optimization routines. However, these results are still to be verified by experiments when the 3D printer is up and running.

Chapter 8

Conclusion and outlook

8.1 Conclusion

Polymer-based acoustofluidic devices suffer from complex system resonances and weak acoustofluidic response, and to compete with ideal glass/silicon-based acoustofluidic resonators requires optimization. Numerical models can be used to test, evaluate, and optimize device designs but require well-characterized material parameters. Otherwise, the model results can be inaccurate and misleading. Even though sometimes provided by the supplier, the parameters are often insufficient for a complete description lacking complex-valued elastic moduli. Surprisingly enough, in most cases, only the real-valued Young's modulus is provided, and we need to guess the Poisson ratio and the complex part. To overcome this, we have developed the UEIS method able to determine complex-valued piezoelectric and elastic material parameters for ultrasound applications.

The method is based on a fitting procedure matching measured and simulated electrical impedance spectra by varying the material parameters used in the model. Experimentally, the technique is low-cost, easy to run, and requires only simple equipment such as an impedance analyzer, a piezoelectric transducer, a sample holder, and a ring made out of the elastic material of interest. The recording of a given electrical impedance spectrum takes less than four minutes. Afterward, within about one minute, the impedance spectrum is loaded into the automated MATLAB script, and the fitting procedure is executed. Simulation-wise, a complete UEIS-fitting run-time is approximately ten hours for either the unloaded or the polymer-loaded transducer. After the fitting procedure has finished, the resulting UEIS-fitted impedance spectrum and the fitted elastic moduli are provided by the script. The method extends the field of resonance ultrasound spectroscopy for material characterization by including on- and off-resonance frequencies in a wide frequency range 500 Hz to 5 MHz and by providing complex-valued elastic moduli. The method is automatized and easy to execute.

In this thesis, the UEIS method was used to characterize device components for ultrasound acoustofluidic applications, including piezoelectric transducers, an adhesive, a polymer, and a 3D-print resin.

First, the UEIS method was used to determine the piezoelectric material parameters of two piezoceramic materials, a Pz26 and a Pz27. The Pz26 transducers showed in-batch variations, and the achieved UEIS-fitted electrical impedance spectrum was disappointing; both features and amplitudes were off. However, with the Pz27 transducers, we observed minor in-batch variations and achieved fitted spectra matching all features with minor deviations in amplitude. By these means, we decided to proceed with the Pz27 transducer despite having a smaller mechanical quality factor than Pz26. The modeled Pz27 transducer dynamics were further verified by laser-Doppler velocimetry measuring the displacement amplitude at different frequencies. The measured displacement amplitude was then compared to simulated results in which the UEIS-determined Pz27 parameters were used as input. Again, the features contained in the mechanical displacement were captured by the simulation, and the amplitudes agreed within 10% for five different frequencies corresponding to different mechanical modes.

Having a well-characterized and accurate model of the Pz27 transducer enabled the determination of loaded material parameters. A similar procedure, as for the determination of the unloaded Pz27 transducer, was used to determine the complex-valued elastic moduli of the UV-curable NOA86H adhesive. The procedure is simple: a NOA86H ring is glued onto a disk-shaped Pz27 transducer, and the electrical impedance spectrum is measured and loaded into the automated UEIS script. After approximately ten hours, the fitted spectrum is provided together with the NOA86H complex-valued elastic moduli. The stability of the adhesive was evaluated by measuring the impedance spectrum in ambient conditions for several hours.

The UEIS-determined adhesive and transducer material parameters further enabled the determination of a third material, in this case, the complex-valued elastic moduli of a polymer. This was achieved by gluing a PMMA ring onto a disk-shaped Pz27 transducer using the NOA86H adhesive. The UEIS method was applied to the polymer-glue-transducer-stacked system to determine the polymer parameters—this procedure constitutes the complete UEIS method. Ultrasound-through transmission and laser-Doppler velocimetry experiments verified the UEIS-determined elastic moduli of the PMMA.

The PMMA was then used to fabricate a cylindrical microfluidic cavity, which was glued onto a disk-shaped Pz26 transducer comprising an acoustofluidic device for which all the material parameters are determined by the UEIS method. The polymer-based acoustofluidic device was further analyzed by particle tracking in stop-flow conditions. The results were compared to simulated particle trajectories resulting from the acoustic radiation force, providing a frequency-resolved one-to-one comparison between experiment and simulation. These experiments were carried out while the Pz27 transducer was out-of-stock. We continued with a Pz26 transducer compromising the model accuracy.

However, we were still able to match the resonance frequency and the average particle velocity magnitude within 11%. These results showed that the complexity of the system resonances is reduced for layered acoustofluidic resonators with an axisymmetric geometry and large channel aspect ratio. Furthermore, the resonance mimics that of 1D layered resonators, almost invariant in the radial direction, different from WSUR observed in transverse resonators with a small channel aspect ratio. These findings can be used to design ideal, robust, and well-behaved polymer-based acoustofluidic devices.

Finally, the UEIS method was used to characterize a 3D-print material, enabling fast, cheap, and reliable prototyping of acoustofluidic device designs. The UEIS-determined 3D-print resin parameters were used as input parameters in our numerical model. The model included a full acoustophoresis simulation where the acoustic fields were combined with the stationary flow enabling the simulation of particle trajectories in a continuous and steady flow. The acoustophoresis performance was evaluated in terms of acoustic response and transfer ratio involving numerical particle tracking in realistic flow conditions. The device design was optimized by varying the channel and chip geometry while minimizing a cost function suitable for this type of acoustophoresis application. The optimization was achieved by linking our COMSOL model to MATLAB, enabling the use of built-in MATLAB optimization algorithms. The optimized design was evaluated in terms of acoustophoresis performance and compared to the initial design. The optimized design achieved the same transfer ratios at two times higher flow rates than the initial design. The optimized polymer-based design is competitive, providing transfer ratios comparable to glass-based devices.

We have developed a numerical model capable of modeling complex acoustofluidic systems, including an ultrasound transducer, a coupling layer, and a fluid-filled microfluidic chip. The model includes the electric potential, the mechanical displacement, the acoustic pressure, and the acoustic streaming. Furthermore, the model also includes a stationary flow solution. Combined with the acoustic fields, this provides the necessary variables to simulate acoustophoresis phenomena, i.e., particle trajectories affected by drag and acoustic forces. In combination with the UEIS method, the model provides an accurate and precise prediction of the acoustofluidic dynamics providing frequency-resolved one-to-one comparisons without free parameters—successfully bridging simulation and experiment.

8.2   Outlook and perspectives

The UEIS is a versatile technique. It is not limited to the chosen examples of Pz27, glue, and PMMA. In principle, the method can be used to characterize other classes of isotropic elastic materials, e.g., glass and metals. The method is easily extended to anisotropic materials by changing the stiffness tensor description accordingly. However, this might result in tensor symmetries for which the axisymmetric model is not applicable, and a 3D model is necessary, compromising numerical speed. In our case, the complex-valued elastic moduli were assumed independent of frequency. However, any frequency dependence can easily be included in the UEIS method, adding to the list of fitting parameters.

Similarly, adding and determining material parameters' temperature dependency is possible. A temperature-controlled two-step UEIS procedure can achieve this: first, the piezoceramic material parameters are determined at different temperatures. Afterward, the material of interest is glued onto the same transducer, and the UEIS procedure is executed at different temperatures. Furthermore, it is possible to include and characterize a fourth component, e.g., a fluid, again adding to the list of fitting parameters. I will repeat myself; the UEIS method is versatile, and it is easily expanded and evolved.

In this thesis, the UEIS method was used to characterize a 3D-print resin. This enables cheap and accurate prototyping by 3D-printed microfluidic chips for acoustofluidic applications assisted by numerical modeling. In combination with the fast-evolving 3D printer technology, this method supports and provides the necessary tool for the next generation of polymer-based acoustofluidics. Potentially, the UEIS method will lower the entry barrier for people aspiring to study acoustofluidics or ultrasound applications in general.

The UEIS method was used to characterize materials for ultrasound acoustofluidic application. Nevertheless, the method can be applied to other ultrasound applications where accurate and precise modeling is wanted, such as ultrasonic cleaning, energy harvesting, and inkjet printing, just to mention some.

The method also provides inside into fabrication and assembling procedures and can be used to assess material stability, e.g., UV exposure and curing time for curable adhesives and 3D-print resins. However, the UEIS method suffers from low sensitivity toward complex-valued material parameters, which remains a shortcoming and an obvious suggestion to improve upon. Suggestions for circumventing and studying this problem: alternative cost functions and different geometries. Both of which can be studied numerically. In our case, we have used a simple optimization algorithm; it will be interesting to see how alternative procedures and more evolved algorithms can improve the UEIS method.

I believe and hope that the UEIS method will be a valuable tool for computer-aided engineering when designing and optimizing devices for ultrasound applications. The development of the UEIS method was driven by our pursuit of accurate modeling of polymer-based acoustofluidic devices. As other people's work inspired us, I hope the UEIS method will also inspire and drive new research either as a tool or as inspiration for new techniques. I hope this thesis will provide insight and inspiration to people aspiring to work with polymer-based acoustofluidics or material science.

Appendix A

Dissipation in a piezoelectric material

In the following derivation the Voigt notation is used implicitly. Following Ref. [108], the generalized Poynting vector $\boldsymbol{S}$ for time harmonic fields ($\partial_t \to -\mathrm{i}\omega$) in a piezoelectric material can be written as

$$\boldsymbol{S} = \left[\boldsymbol{E} \times \boldsymbol{H} - \boldsymbol{\sigma} \cdot (-\mathrm{i}\omega\boldsymbol{u}_1)\right]. \tag{A.1}$$

The total dissipation density P_d can be calculated as the time-averaged divergence of $(-\boldsymbol{S})$

$$
\begin{aligned}
P_d = -\boldsymbol{\nabla} \cdot \langle \boldsymbol{S} \rangle &= -\boldsymbol{\nabla} \cdot \frac{1}{2} \operatorname{Re}\left(\boldsymbol{E} \times \boldsymbol{H}^* - \boldsymbol{\sigma} \cdot (-\mathrm{i}\omega\boldsymbol{u}_1)^*\right) \\
&= -\boldsymbol{\nabla} \cdot \frac{1}{2} \operatorname{Re}\left(\boldsymbol{E} \times \boldsymbol{H}^* - \mathrm{i}\omega\boldsymbol{\sigma} \cdot \boldsymbol{u}_1^*\right).
\end{aligned}
\tag{A.2}
$$

The divergence of $\boldsymbol{E} \times \boldsymbol{H}^*$ can be related to the electrical displacement field $\boldsymbol{D}$ using Maxwell's equations

$$
\begin{aligned}
\boldsymbol{\nabla} \cdot \left(\boldsymbol{E} \times \boldsymbol{H}^*\right) &= \left(\boldsymbol{\nabla} \times \boldsymbol{E}\right) \cdot \boldsymbol{H}^* - \left(\boldsymbol{\nabla} \times \boldsymbol{H}^*\right) \cdot \boldsymbol{E} \\
&= -\partial_t \boldsymbol{B} \cdot \boldsymbol{H}^* - \left(\partial_t \boldsymbol{D}\right)^* \cdot \boldsymbol{E} \\
&= \mathrm{i}\omega \boldsymbol{B} \cdot \frac{\boldsymbol{B}^*}{\mu_0} - \mathrm{i}\omega \boldsymbol{D}^* \cdot \boldsymbol{E}.
\end{aligned}
\tag{A.3}
$$

The divergence of the mechanical Poynting vector can also be re-written in terms of the strain $\boldsymbol{s}$

$$
\begin{aligned}
\boldsymbol{\nabla} \cdot \left(-\mathrm{i}\omega\boldsymbol{\sigma} \cdot \boldsymbol{u}_1^*\right) &= -\mathrm{i}\omega\left[\boldsymbol{\sigma} : \boldsymbol{\nabla}\boldsymbol{u}_1^* + \boldsymbol{u}_1^* \cdot (\boldsymbol{\nabla} \cdot \boldsymbol{\sigma})\right] \\
&= -\mathrm{i}\omega\left[\boldsymbol{\sigma} : \boldsymbol{s}^* + \boldsymbol{u}_1^* \cdot \left(\rho_{\mathrm{sl}}\partial_t^2\boldsymbol{u}_1\right)\right] \\
&= -\mathrm{i}\omega\left[\boldsymbol{\sigma} : \boldsymbol{s}^* - \boldsymbol{u}_1^* \cdot \left(\omega^2\rho_{\mathrm{sl}}\boldsymbol{u}_1\right)\right].
\end{aligned}
\tag{A.4}
$$

127

Returning to Eq. (A.2) the dissipation density now reads

$$
\begin{aligned}
P_d &= -\frac{1}{2}\operatorname{Re}\left\{ i\omega \boldsymbol{B}\cdot\frac{\boldsymbol{B}^*}{\mu_0} - i\omega\boldsymbol{D}^*\cdot\boldsymbol{E} - i\omega\left[\boldsymbol{\sigma}:\boldsymbol{s}^* - \boldsymbol{u}_1^*\cdot\left(\omega^2\rho_{\mathrm{sl}}\boldsymbol{u}_1\right)\right]\right\} \\
&= -\frac{1}{2}\operatorname{Re}\left(-i\omega\boldsymbol{D}^*\cdot\boldsymbol{E} - i\omega\boldsymbol{\sigma}:\boldsymbol{s}^*\right) = \frac{\omega}{2}\operatorname{Re}\left(i\boldsymbol{D}^*\cdot\boldsymbol{E} + i\boldsymbol{\sigma}:\boldsymbol{s}^*\right) \\
&= -\frac{\omega}{2}\operatorname{Im}\left(\boldsymbol{D}^*\cdot\boldsymbol{E} + \boldsymbol{\sigma}:\boldsymbol{s}^*\right) = -\frac{\omega}{2}\operatorname{Im}\left(\boldsymbol{D}^*\cdot\boldsymbol{E} - \boldsymbol{\sigma}^*:\boldsymbol{s}\right) \\
&= \frac{\omega}{2}\operatorname{Im}\left(-\boldsymbol{D}^*\cdot\boldsymbol{E} + \boldsymbol{\sigma}^*:\boldsymbol{s}\right).
\end{aligned}
\tag{A.5}
$$

Using the constitutive relation in Eq. (2.33) and the Voigt notation the dissipation can be written as a matrix product.

$$
P_d = \frac{\omega}{2}\operatorname{Im}\left[\begin{pmatrix}\boldsymbol{s}\\\boldsymbol{E}\end{pmatrix}\begin{pmatrix}\boldsymbol{C}^* & -\left(\boldsymbol{e}^{\mathsf{T}}\right)^*\\ -\boldsymbol{e}^* & -\boldsymbol{\epsilon}^*\end{pmatrix}\begin{pmatrix}\boldsymbol{s}^*\\\boldsymbol{E}^*\end{pmatrix}\right] = F_p M_{pq}^* F_q^*,
\tag{A.6}
$$

where $M_{pq} = M_{pq}' + iM_{pq}''$, so $\operatorname{Re}(M_{pq}) = M_{pq}'$ and $\operatorname{Im}(M_{pq}) = M_{pq}''$. Similar as Ref. [108] the phase between F_p and F_q is defined as θ_{pq}, expanding the sum in Eq. (A.6) yields

$$
\begin{aligned}
P_d &= \frac{\omega}{2}\operatorname{Im}\left(\sum_p\sum_q |F_p||F_q|(M_{pq}' - iM_{pq}'')(\cos\theta_{pq} - i\sin\theta_{pq})\right) \\
&= -\frac{\omega}{2}\sum_p\sum_q |F_p||F_q|M_{pq}''\cos\theta_{pq}.
\end{aligned}
\tag{A.7}
$$

Since the fields are independent, it is possible to define a basis where $\cos\theta_{pq} = 0$, so

$$
P_d = -\frac{\omega}{2}|F_p||F_q|M_{pq}''\cos\theta_{pq} = \frac{\omega}{2}|F_p||F_q|K_{pq}\cos\theta_{pq},
\tag{A.8}
$$

where we have defined the matrix

$$
\boldsymbol{K} = -\boldsymbol{M}'' = \operatorname{Im}\begin{pmatrix}-\boldsymbol{C} & \boldsymbol{e}^{\mathsf{T}}\\ \boldsymbol{e} & \boldsymbol{\epsilon}\end{pmatrix}.
\tag{A.9}
$$

Finally arriving to the constraint: in order for the dissipation density to be always positive, the matrix $\boldsymbol{K}$ has to be positive definite. A similar constraint can be imposed for an elastic solid by replacing $\boldsymbol{K}$ with $\boldsymbol{K}_{\mathrm{iso}} = \operatorname{Im}(-\boldsymbol{C})$.

Appendix B

Material parameters

B.1 UEIS material library

Table B.1: Real part of the UEIS-determined material parameters for disk-shaped Pz26 and Pz27 transducers. The standard error of the mean is given in parenthesis provided N samples.

	$\rho_{\rm sl}$ (kg/m^3)	C_{11}' (GPa)	C_{12}' (GPa)	C_{13}' (GPa)	C_{33}' (GPa)	C_{44}' (GPa)	ϵ_{11}' (ϵ_0)	ϵ_{33}' (ϵ_0)	e_{31}' (C/m^2)	e_{33}' (C/m^2)	e_{15}' (C/m^2)	N -
Pz26	7700	172(8)	115(5)	94(5)	122(3)	30.1(1)	780(48)	727(26)	$-2.92(5)$	14.8(3)	10.4(1)	2
Pz27	7700	122.3(6)	75.1(4)	76.1(6)	117.8(3)	21.4(1)	973(12)	812(5)	$-5.19(5)$	16.29(5)	11.6(3)	32

Table B.2: Imaginary part of the UEIS-determined material parameters for disk-shaped Pz26 and Pz27 transducers. The standard error of the mean is given in parenthesis provided N samples.

	C_{11}'' (GPa)	C_{12}'' (GPa)	C_{13}'' (GPa)	C_{33}'' (GPa)	C_{44}'' (GPa)	ϵ_{11}'' (ϵ_0)	ϵ_{33}'' (ϵ_0)	e_{31}'' (C/m^2)	e_{33}'' (C/m^2)	e_{15}'' (C/m^2)	N -
Pz26	$-0.056(7)$	$-0.028(5)$	$-0.028(2)$	$-0.046(7)$	$-0.009(1)$	0	2.3(2)	0	0	0	2
Pz27	$-0.58(5)$	0.1(3)	0.11(3)	$-0.48(4)$	$-0.66(7)$	0	2.88(8)	0	0	0	32

Table B.3: Complex-valued elastic moduli C_{11} and C_{44} obtained by the UEIS method for different elastic materials. Also including the sounds speeds $c_{\rm lo}$ and $c_{\rm tr}$, the Young's modulus E, the Poisson's ratio ν, and the Lamé parameters λ and μ.

	$\rho_{\rm sl}$ kg/m^3	C_{11} GPa	C_{44} GPa	$c_{\rm lo}$ m/s	$c_{\rm tr}$ m/s	E GPa	ν -	λ GPa	μ GPa
PMMA	1162(4)	$7.18(4) - i0.183(5)$	$1.553(8)(4) - i0.111(7)$	2486(8)	1156(4)	4.23(2)	0.362(1)	4.1	1.6
Noa86H	1300	$4.65 - i0.51$	$1.21 - i0.12$	1929	984	3.2	0.32	2.2	1.2
VeroClear	1120	$7.3 - i0.3$	$1.3 - i0.06$	2544	1072	3.6	0.39	4.7	1.3

Relation between real-valued elastic moduli

Formulas relating the real-valued elastic moduli are provided. The formulas relate the real-valued stiffness components C'_{11} and C'_{44}, to the sound speeds c_{lo} and c_{tr}, the Young's modulus E and Poisson's ratio ν, and the Lamé parameters λ and μ.

C'_{11} and C'_{44} to c_{lo} and c_{tr}

$$c_{\text{lo}} = \sqrt{\frac{C'_{11}}{\rho_{\text{sl}}}}, \quad \text{and} \quad c_{\text{tr}} = \sqrt{\frac{C'_{44}}{\rho_{\text{sl}}}}. \tag{B.1}$$

C'_{11} and C'_{44} to E and ν

$$E = C'_{44} \frac{3C'_{11} - 4C'_{44}}{C'_{11} - C'_{44}}, \quad \text{and} \quad \nu = \frac{C'_{11} - 2C'_{44}}{2\left(C'_{11} - C'_{44}\right)}. \tag{B.2}$$

C'_{11} and C'_{44} to λ and μ

$$\lambda = C'_{11} - 2C'_{44}, \quad \text{and} \quad \mu = C'_{44}. \tag{B.3}$$

Appendix C

Nelder–Mead simplex algorithm (fminsearch)

The Nelder–Mead algorithm uses the simplex search method of Lagarias et al. [119]. The algorithm requires initial values $\boldsymbol{\mathcal{P}}_0$ and iterates until certain stopping criteria are met.

The initial simplex is formed by adding 5% to the initial values. In the following the algorithm is outlined for a two-dimensional parameter space in which case the simplex forms a triangle with corresponding cost function values $\mathcal{C}_i$.

1. The current simplex is generated by the set of points $\boldsymbol{\mathcal{P}}_i$, where $i = 1, 2, 3$.

2. The points $\boldsymbol{\mathcal{P}}_i$ are ordered in ascending order according to the corresponding $\mathcal{C}_i$ i.e. $\mathcal{C}_1 < \mathcal{C}_2 < \mathcal{C}_3$

3. Generate a reflected point $\boldsymbol{\mathcal{P}}_r = 2m - \boldsymbol{\mathcal{P}}_3$ where $m = \frac{1}{3}\sum_i^3 \boldsymbol{\mathcal{P}}_i$ and calculate $\mathcal{C}_r$.

4. If $\mathcal{C}_1 \leq \mathcal{C}_r < \mathcal{C}_3$, accept $\boldsymbol{\mathcal{P}}_r$ to form the new simplex $\boldsymbol{\mathcal{P}}_i = \{\boldsymbol{\mathcal{P}}_1, \boldsymbol{\mathcal{P}}_2, \boldsymbol{\mathcal{P}}_r\}$ and iterate.

5. If $\mathcal{C}_r < \mathcal{C}_1$ expand the point $\boldsymbol{\mathcal{P}}_e = m + \boldsymbol{\mathcal{P}}_r$ and calculate $\mathcal{C}_e$

   (a) If $\mathcal{C}_e < \mathcal{C}_r$ accept $\boldsymbol{\mathcal{P}}_e$ as the new point, otherwise accept $\boldsymbol{\mathcal{P}}_r$ and iterate.

6. If $\mathcal{C} \geq \mathcal{C}_2$ perform a contraction either

   (a) If $\mathcal{C}_r < \mathcal{C}_3$ calculate the contracted point $\boldsymbol{\mathcal{P}}_c = m + \frac{\boldsymbol{\mathcal{P}}_r - m}{2}$, if $\mathcal{C}_c < \mathcal{C}_r$ accept $\boldsymbol{\mathcal{P}}_c$ to form the new simplex $\boldsymbol{\mathcal{P}} = \{\boldsymbol{\mathcal{P}}_1, \boldsymbol{\mathcal{P}}_2, \boldsymbol{\mathcal{P}}_c\}$ otherwise continue to step 7.

   (b) If $\mathcal{C}_r \geq \mathcal{C}_3$ calculate $\boldsymbol{\mathcal{P}}_{ci} = m + \frac{\boldsymbol{\mathcal{P}}_3 - m}{2}$, if $\mathcal{C}_{ci} < \mathcal{C}_3$ accept $\boldsymbol{\mathcal{P}}_{ci}$ to form the new simplex $\boldsymbol{\mathcal{P}} = \{\boldsymbol{\mathcal{P}}_1, \boldsymbol{\mathcal{P}}_2, \boldsymbol{\mathcal{P}}_{ci}\}$ and iterate. Otherwise continue to step 7.

7. Calculate three new points according to the iterative procedure $\boldsymbol{\mathcal{P}}_i = \boldsymbol{\mathcal{P}}_1 + \frac{\boldsymbol{\mathcal{P}}_i - \boldsymbol{\mathcal{P}}_3}{2}$ to from the new simplex and iterate.

Let $\mathcal{C}_n$ correspond to the cost function for the current iteration with corresponding simplex $\boldsymbol{\mathcal{P}}_n$, if $\frac{|\mathcal{C}_{n-1}-\mathcal{C}_n|}{1+|\mathcal{C}_{n-1}|} < \Delta_{\mathcal{C}}$ and $\frac{|\boldsymbol{\mathcal{P}}_{n-1}-\boldsymbol{\mathcal{P}}_n|}{1+|\boldsymbol{\mathcal{P}}_{n-1}|} < \Delta_p$ terminate the algorithm. Here, $\Delta_{\mathcal{C}}$ and Δ_p are set to 1×10^{-4}. The bounded version `fminsearchbnd` with upper and lower bounds $\boldsymbol{\mathcal{P}}^+$ and $\boldsymbol{\mathcal{P}}^-$ respectively, utilizes a transformation $\mathcal{C}(\boldsymbol{\mathcal{P}}) \to \mathcal{C}(f(\boldsymbol{\mathcal{P}}))$ where $f(\boldsymbol{\mathcal{P}})$ takes any $\boldsymbol{\mathcal{P}}$ and maps it onto $[\boldsymbol{\mathcal{P}}^-, \boldsymbol{\mathcal{P}}^+]$. In this case the transformation uses a sinusoidal transformation defined as

$$f(\boldsymbol{\mathcal{P}}) = \frac{\sin(\boldsymbol{\mathcal{P}}) + 1}{2} \left(\boldsymbol{\mathcal{P}}^+ - \boldsymbol{\mathcal{P}}^- \right) + \boldsymbol{\mathcal{P}}^-. \tag{C.1}$$

Bibliography

[1] W. N. Bodé, L. Jiang, T. Laurell, and H. Bruus, *Microparticle acoustophoresis in aluminum-based acoustofluidic devices with PDMS covers.* Micromachines **11**(3), 292 (2020).

[2] W. N. Bodé and H. Bruus, *Numerical study of the coupling layer between transducer and chip in acoustofluidic devices.* J. Acoust. Soc. Am. **149**(5), 3096–3105 (2021).

[3] W. N. Bodé, F. Lickert, P. Augustsson, and H. Bruus, *Determination of the complex-valued elastic moduli of polymers by electrical impedance spectroscopy for ultrasound applications.* Phys. Rev. Appl. **submitted**, 11 pages (2022), https://arxiv.org/abs/2204.06464.

[4] F. Petersson, A. Nilsson, C. Holm, H. Jönsson, and T. Laurell, *Separation of lipids from blood utilizing ultrasonic standing waves in microfluidic channels.* Analyst **129**(10), 938–43 (2004).

[5] J. Rufo, F. Cai, J. Friend, M. Wiklund, and T. J. Huang, *Acoustofluidics for biomedical applications.* Nature Reviews Methods Primers **2**(1), 30 (2022).

[6] M. Evander, L. Johansson, T. Lilliehorn, J. Piskur, M. Lindvall, S. Johansson, M. Almqvist, T. Laurell, and J. Nilsson, *Noninvasive acoustic cell trapping in a microfluidic perfusion system for online bioassays.* Anal. Chem. **79**(7), 2984–2991 (2007).

[7] B. Hammarström, T. Laurell, and J. Nilsson, *Seed particle enabled acoustic trapping of bacteria and nanoparticles in continuous flow systems.* Lab Chip **12**, 4296–4304 (2012).

[8] C. Magnusson, P. Augustsson, A. Lenshof, Y. Ceder, T. Laurell, and H. Lilja, *Clinical-scale cell-surface-marker independent acoustic microfluidic enrichment of tumor cells from blood.* Anal. Chem. **89**(22), 11954–11961 (2017).

[9] K. Petersson, O. Jakobsson, P. Ohlsson, P. Augustsson, S. Scheding, J. Malm, and T. Laurell, *Acoustofluidic hematocrit determination.* Anal. Chim. Acta **1000**, 199–204 (2018).

[10] P. Ohlsson, M. Evander, K. Petersson, L. Mellhammar, A. Lehmusvuori, U. Karhunen, M. Soikkeli, T. Seppa, E. Tuunainen, A. Spangar, P. von Lode, K. Rantakokko-Jalava, G. Otto, S. Scheding, T. Soukka, S. Wittfooth, and T. Laurell, *Integrated acoustic separation, enrichment, and microchip polymerase chain reaction detection of bacteria from blood for rapid sepsis diagnostics.* Anal. Chem. **88**(19), 9403–9411 (2016).

[11] K. Olofsson, B. Hammarstrom, and M. Wiklund, *Acoustic separation of living and dead cells using high density medium.* Lab Chip **20**(11), 1981–1990 (2020).

[12] C. Lissandrello, R. Dubay, K. T. Kotz, and J. Fiering, *Purification of lymphocytes by acoustic separation in plastic microchannels.* SLAS Technology **23**(4), 352–363 (2018).

[13] P. Ohlsson, K. Petersson, P. Augustsson, and T. Laurell, *Acoustic impedance matched buffers enable separation of bacteria from blood cells at high cell concentrations.* Sci. Rep. **8**, 9156 (2018).

[14] B. Kang, J. Shin, H.-J. Park, C. Rhyou, D. Kang, S.-J. Lee, Y.-s. Yoon, S.-W. Cho, and H. Lee, *High-resolution acoustophoretic 3D cell patterning to construct functional collateral cylindroids for ischemia therapy.* Nat. Commun. **9**(1), 5402 (2018).

[15] A. Tait, P. Glynne-Jones, A. R. Hill, D. E. Smart, C. Blume, B. Hammarstrom, A. L. Fisher, M. C. Grossel, E. J. Swindle, M. Hill, and D. E. Davies, *Engineering multi-layered tissue constructs using acoustic levitation.* Sci. Rep. **9**(1), 9789 (2019).

[16] K. Koo, A. Lenshof, L. T. Huong, and T. Laurell, *Acoustic Cell Patterning in Hydrogel for Three-Dimensional Cell Network Formation.* Micromachines **12**(1), 3 (2020).

[17] P. B. Muller, R. Barnkob, M. J. H. Jensen, and H. Bruus, *A numerical study of microparticle acoustophoresis driven by acoustic radiation forces and streaming-induced drag forces.* Lab Chip **12**, 4617–4627 (2012).

[18] P. B. Muller and H. Bruus, *Numerical study of thermoviscous effects in ultrasound-induced acoustic streaming in microchannels.* Phys. Rev. E **90**(4), 043016 (2014).

[19] P. B. Muller and H. Bruus, *Theoretical study of time-dependent, ultrasound-induced acoustic streaming in microchannels.* Phys. Rev. E **92**, 063018 (2015).

[20] R. P. Moiseyenko and H. Bruus, *Whole-system ultrasound resonances as the basis for acoustophoresis in all-polymer microfluidic devices.* Phys. Rev. Applied **11**, 014014 (2019).

[21] N. Harris, M. Hill, A. Keating, and P. Baylac-Choulet, *A lateral mode flow-through PMMA ultrasonic separator.* Intl. J. Appl. Biomed. Eng. **5**(1), 20–27 (2012).

[22] A. Mueller, A. Lever, T. V. Nguyen, J. Comolli, and J. Fiering, *Continuous acoustic separation in a thermoplastic microchannel.* J. Micromech. Microeng. **23**(12), 125006 (2013).

[23] I. Gonzalez, M. Tijero, A. Martin, V. Acosta, J. Berganzo, A. Castillejo, M. M. Bouali, and J. Luis Soto, *Optimizing polymer lab-on-chip platforms for ultrasonic manipulation: Influence of the substrate.* Micromachines **6**(5), 574–591 (2015).

[24] C. Yang, Z. Li, P. Li, W. Shao, P. Bai, and Y. Cui, *Acoustic particle sorting by integrated micromachined ultrasound transducers on polymerbased microchips.* IEEE International Ultrasonics Symposium (IUS) 1–4 (2017).

[25] W. J. Savage, J. R. Burns, and J. Fiering, *Safety of acoustic separation in plastic devices for extracorporeal blood processing.* Transfusion **57**(7), 1818–1826 (2017).

[26] R. Silva, P. Dow, R. Dubay, C. Lissandrello, J. Holder, D. Densmore, and J. Fiering, *Rapid prototyping and parametric optimization of plastic acoustofluidic devices for blood-bacteria separation.* Biomedical Microdevices **19**(3), 70 (2017).

[27] J. D. Adams, C. L. Ebbesen, R. Barnkob, A. H. J. Yang, H. T. Soh, and H. Bruus, *High-throughput, temperature-controlled microchannel acoustophoresis device made with rapid prototyping.* J. Micromech. Microeng. **22**(7), 075017 (2012).

[28] G. P. Gautam, T. Burger, A. Wilcox, M. J. Cumbo, S. W. Graves, and M. E. Piyasena, *Simple and inexpensive micromachined aluminum microfluidic devices for acoustic focusing of particles and cells.* Anal. Bioanal. Chem. **410**(14), 3385–3394 (2018).

[29] Y. Gu, C. Chen, Z. Wang, P.-H. Huang, H. Fu, L. Wang, M. Wu, Y. Chen, T. Gao, J. Gong, J. Kwun, G. M. Arepally, and T. J. Huang, *Plastic-based acoustofluidic devices for high-throughput, biocompatible platelet separation.* Lab Chip **19**, 394–402 (2019).

[30] R. Dubay, C. Lissandrello, P. Swierk, N. Moore, D. Doty, and J. Fiering, *Scalable high-throughput acoustophoresis in arrayed plastic microchannels.* Biomicrofluidics **13**(3), 034105 (2019).

[31] F. Lickert, M. Ohlin, H. Bruus, and P. Ohlsson, *Acoustophoresis in polymer-based microfluidic devices: Modeling and experimental validation.* J. Acoust. Soc. Am. **149**(6), 4281–4291 (2021).

[32] M. Hill, Y. Shen, and J. J. Hawkes, *Modelling of layered resonators for ultrasonic separation.* Ultrasonics **40**(1-8), 385–392 (2002).

[33] P. Glynne-Jones, R. J. Boltryk, and M. Hill, *Acoustofluidics 9: Modelling and applications of planar resonant devices for acoustic particle manipulation.* Lab Chip **12**(8), 1417–1426 (2012).

[34] A. G. Steckel, H. Bruus, P. Muralt, and R. Matloub, *Fabrication, characterization, and simulation of glass devices with* AlN *thin-film transducers for excitation of ultrasound resonances.* Phys. Rev. Applied **16**, 014014, 1–10 (2021).

[35] N. Pérez, M. A. B. Andrade, F. Buiochi, and J. C. Adamowski, *Identification of elastic, dielectric, and piezoelectric constants in piezoceramic disks.* IEEE Trans. Ultrason. Ferroelec. Freq. Contr. **57**(12), 2772–2783 (2010).

[36] J. Ilg, S. J. Rupitsch, A. Sutor, and R. Lerch, *Determination of Dynamic Material Properties of Silicone Rubber Using One-Point Measurements and Finite Element Simulations.* IEEE T. Instrum. Meas. **61**(11), 3031–3038 (2012).

[37] N. Pérez, R. Carbonari, M. Andrade, F. Buiochi, and J. Adamowski, *A FEM-based method to determine the complex material properties of piezoelectric disks.* Ultrasonics **54**(6), 1631–1641 (2014).

[38] C. Y. Kiyono, N. Perez, and E. C. N. Silva, *Determination of full piezoelectric complex parameters using gradient-based optimization algorithm.* Smart Mater. Struct. **25**(2), 025019 (2016).

[39] L. D. Landau and E. M. Lifshitz, *Theory of Elasticity. Course of Theoretical Physics*, vol. 7 (Pergamon Press, Oxford), 3rd edn. (1986).

[40] L. D. Landau and E. M. Lifshitz, *Fluid Mechanics*, vol. 6 (Pergamon Press, Oxford), 2nd edn. (1993).

[41] J. Lighthill, *Waves in Fluids* (Cambridge University Press) (2002).

[42] H. Bruus, *Theoretical Microfluidics* (Oxford University Press, Oxford) (2008).

[43] M. Settnes and H. Bruus, *Forces acting on a small particle in an acoustical field in a viscous fluid.* Phys. Rev. E **85**, 016327 (2012).

[44] N. R. Skov, J. S. Bach, B. G. Winckelmann, and H. Bruus, *3D modeling of acoustofluidics in a liquid-filled cavity including streaming, viscous boundary layers, surrounding solids, and a piezoelectric transducer.* AIMS Mathematics **4**, 99–111 (2019).

[45] J. S. Bach and H. Bruus, *Theory of pressure acoustics with viscous boundary layers and streaming in curved elastic cavities.* J. Acoust. Soc. Am. **144**, 766–784 (2018).

[46] W. Wagner and A. Pruss, *The IAPWS formulation 1995 for the thermodynamic properties of ordinary water substance for general and scientific use.* J. Phys. Chem. Ref. Data **31**(2), 387–535 (2002).

[47] M. L. Huber, R. A. Perkins, A. Laesecke, D. G. Friend, J. V. Sengers, M. J. Assael, I. N. Metaxa, E. Vogel, R. Mares, and K. Miyagawa, *New International Formulation for the Viscosity of H2O.* J. Phys. Chem. Ref. Data **38**(2), 101–125 (2009).

[48] M. J. Holmes, N. G. Parker, and M. J. W. Povey, *Temperature dependence of bulk viscosity in water using acoustic spectroscopy.* J. Phys. Conf. Ser. **269**(1), 012011 (2011).

[49] M. L. Huber, R. A. Perkins, D. G. Friend, J. V. Sengers, M. J. Assael, I. N. Metaxa, K. Miyagawa, R. Hellmann, and E. Vogel, *New International Formulation for the Thermal Conductivity of H2O.* J. Phys. Chem. Ref. Data **41**(3), 033102 (2012).

[50] R. Barnkob, P. Augustsson, T. Laurell, and H. Bruus, *Measuring the local pressure amplitude in microchannel acoustophoresis.* Lab Chip **10**(5), 563–570 (2010).

[51] R. Barnkob, P. Augustsson, T. Laurell, and H. Bruus, *Acoustic radiation- and streaming-induced microparticle velocities determined by microparticle image velocimetry in an ultrasound symmetry plane.* Phys. Rev. E **86**, 056307 (2012).

[52] P. B. Muller, M. Rossi, A. G. Marin, R. Barnkob, P. Augustsson, T. Laurell, C. J. Kähler, and H. Bruus, *Ultrasound-induced acoustophoretic motion of microparticles in three dimensions.* Phys. Rev. E **88**(2), 023006 (2013).

[53] T. Ikeda, *Fundamentals of Piezoelectricity* (Oxford University Press, London, UK) (1996).

[54] A. Bermúdez, L. Hervella-Nieto, A. Prieto, and R. Rodríguez, *An optimal perfectly matched layer with unbounded absorbing function for time-harmonic acoustic scattering problems.* Journal of Computational Physics **223**(2), 469–488 (2007).

[55] ERA-LEARN, *AcouPlast.* Project: Acoustofluidic blood plasma separation polymer chip for Point-of-Care diagnostics, accessed 18 October 2022.

[56] K. Xu, C. P. Clark, B. L. Poe, J. A. Lounsbury, J. Nilsson, T. Lauren, and J. P. Landers, *Isolation of a Low Number of Sperm Cells from Female DNA in a Glass-PDMS-Glass Microchip via Bead-Assisted Acoustic Differential Extraction.* Anal. Chem. **91**(3), 2186–2191 (2019).

[57] M. A. Hopcroft, W. D. Nix, and T. W. Kenny, *What is the Young's modulus of silicon.* J. Microelectromech. Syst **19**, 229–238 (2010).

[58] W. M. Haynes (ed.), *CRC Handbook of Chemistry and Physics* (CRC Press, Boca Raton, FL), 97th edn. (2016).

[59] G. Xu, Z. Ni, X. Chen, J. Tu, X. Guo, H. Bruus, and D. Zhang, *Acoustic Characterization of Polydimethylsiloxane for Microscale Acoustofluidics.* Phys. Rev. Applied **13**(5), 054069 (2020).

[60] J. Lei, P. Glynne-Jones, and M. Hill, *Acoustic streaming in the transducer plane in ultrasonic particle manipulation devices.* Lab Chip **13**(11), 2133–2143 (2013).

[61] P. Mishra, M. Hill, and P. Glynne-Jones, *Deformation of red blood cells using acoustic radiation forces.* Biomicrofluidics **8**(3), 034109 (2014).

[62] I. Gralinski, S. Raymond, T. Alan, and A. Neild, *Continuous flow ultrasonic particle trapping in a glass capillary.* J. Appl. Phys. **115**(5), 054505 (2014).

[63] J. S. Bach and H. Bruus, *Suppression of acoustic streaming in shape-optimized channels.* Phys. Rev. Lett. **124**, 214501 (2020).

[64] R. J. Townsend, M. Hill, N. R. Harris, and M. B. McDonnell, *Performance of a quarter-wavelength particle concentrator.* Ultrasonics **48**(6-7), 515–520 (2008).

[65] B. Hammarström, M. Evander, H. Barbeau, M. Bruzelius, J. Larsson, T. Laurell, and J. Nillsson, *Non-contact acoustic cell trapping in disposable glass capillaries.* Lab Chip **10**(17), 2251–2257 (2010).

[66] P. Augustsson, R. Barnkob, S. T. Wereley, H. Bruus, and T. Laurell, *Automated and temperature-controlled micro-PIV measurements enabling long-term-stable microchannel acoustophoresis characterization.* Lab Chip **11**(24), 4152–4164 (2011).

[67] A. Tahmasebipour, L. Friedrich, M. Begley, H. Bruus, and C. Meinhart, *Toward optimal acoustophoretic microparticle manipulation by exploiting asymmetry.* J. Acoust. Soc. Am. **148**(1), 359–373 (2020).

[68] Meggitt A/S, Porthusvej 4, DK-3490 Kvistgaard, Denmark, *Ferroperm matrix data.* https://www.meggittferroperm.com/materials/, accessed 7 October 2022.

[69] Institute of Electrical and Electronics Engineers (IEEE), *IEEE Standard on Piezoelectricity.* ANSI-IEEE Std. 176-1987 (1987).

[70] European Committe for Electrotechnical Standardization (CENELEC), *Piezoelectric properties of ceramic materials and components – Part 2: Methods of measurement – Low power.* EN 50324-2 (2002).

[71] S. J. Rupitsch, *Piezoelectric sensors and actuators: Fundamentals and applications* (Springer, Berlin, Germany) (2019).

[72] A. Migliori, J. Sarrao, W. M. Visscher, T. Bell, M. Lei, Z. Fisk, and R. Leisure, *Resonant ultrasound spectroscopic techniques for measurement of the elastic moduli of solids.* Physica B: Condensed Matter **183**(1), 1–24 (1993).

[73] H. Wang, W. Jiang, and W. Cao, *Characterization of lead zirconate titanate piezoceramic using high frequency ultrasonic spectroscopy.* J. Appl. Phys. **85**(12), 8083–8091 (1999).

[74] G. Roebben, B. Bollen, A. Brebels, J. Van Humbeeck, and O. Van der Biest, *Impulse excitation apparatus to measure resonant frequencies, elastic moduli, and internal friction at room and high temperature.* Rev. Sci. Instrum. **68**(12), 4511–4515 (1997).

[75] R. Willis, L. Wu, and Y. Berthelot, *Determination of the complex young and shear dynamic moduli of viscoelastic materials.* J. Acoust. Soc. Am. **109**(2), 611–621 (2001).

[76] M. W. H. Ley and H. Bruus, *Three-dimensional numerical modeling of acoustic trapping in glass capillaries.* Phys. Rev. Applied **8**, 024020 (2017).

[77] A. Lenshof, M. Evander, T. Laurell, and J. Nilsson, *Acoustofluidics 5: Building microfluidic acoustic resonators.* Lab Chip **12**, 684–695 (2012).

[78] S. J. Rupitsch and R. Lerch, *Inverse Method to estimate material parameters for piezoceramic disc actuators.* Appl. Phys. A **97**(4), 735–740 (2009).

[79] H. T. Tran, T. Manh, T. F. Johansen, and L. Hoff, *Temperature effects on ultrasonic phase velocity and attenuation in Eccosorb and PMMA.* In *2016 IEEE International Ultrasonics Symposium (IUS)*, 1–4 (2016).

[80] R. Barnkob and M. Rossi, *DefocusTracker: A Modular Toolbox for Defocusing-based, Single-Camera, 3D Particle Tracking.* J. of Open Research Software **9**(1), 22 (2021).

[81] H. Bruus, *Acoustofluidics 10: Scaling laws in acoustophoresis.* Lab Chip **12**(9), 1578 (2012).

[82] T. Lilliehorn, U. Simu, M. Nilsson, M. Almqvist, T. Stepinski, T. Laurell, J. Nilsson, and S. Johansson, *Trapping of microparticles in the near field of an ultrasonic transducer.* Ultrasonics **43**(5), 293–303 (2005).

[83] M. Evander, O. Gidlof, B. Olde, D. Erlinge, and T. Laurell, *Non-contact acoustic capture of microparticles from small plasma volumes.* Lab Chip **15**, 2588–2596 (2015).

[84] R. Barnkob, C. J. Kähler, and M. Rossi, *General defocusing particle tracking.* Lab Chip **15**, 3556–3560 (2015).

[85] Institut für Strömungsmechanik und Aerodynamik, Univeristät der Bundeswher, Werner Heisenberg Weg 39, 85577 Neubiberg, Germany, *GDTPlab - how to get it.* https://www.unibw.de/lrt7/gdpt-1/gdptlab-how_to_get_it, accessed 18 October 2022.

[86] P. Hahn and J. Dual, *A numerically efficient damping model for acoustic resonances in microfluidic cavities.* Physics of Fluids **27**, 062005 (2015).

[87] ASM Aerospace Specification Metals Inc., 2501 N.W. 34th Place #B28, Pompano Beach, Florida 33069, *ASM Aluminum 6061.* https://asm.matweb.com, accessed 3 February 2020.

[88] AZoMaterials, Charlotte Street, Manchester, UK, *Silver - Applications and Properties of Silver.* https://www.azom.com, accessed 27 November 2021.

[89] J. T. Karlsen and H. Bruus, *Forces acting on a small particle in an acoustical field in a thermoviscous fluid.* Phys. Rev. E **92**, 043010 (2015).

[90] V. T. Rathod, *A review of acoustic impedance matching techniques for piezoelectric sensors and transducers.* Sensors **20**(14), 4051 (2020).

[91] COMSOL Multiphysics 5.5, (2019), http://www.comsol.com.

[92] CORNING, Houghton Park C-8, Corning, NY 14831, USA, *Glass Silicon Constraint Substrates.* Corning_Pyrex_7740.pdf, accessed 2 Apr 2022.

[93] J. J. Hawkes and W. T. Coakley, *Force field particle filter, combining ultrasound standing waves and laminar flow.* Sensor Actuat B-Chem **75**(3), 213–222 (2001).

[94] P. Hahn, O. Schwab, and J. Dual, *Modeling and optimization of acoustofluidic microdevices.* Lab Chip **14**, 3937–3948 (2014).

[95] A. Lamprecht, S. Lakamper, T. Baasch, I. A. T. Schaap, and J. Dual, *Imaging the position-dependent 3D force on microbeads subjected to acoustic radiation forces and streaming.* Lab Chip **16**, 2682–2693 (2016).

[96] V. Pereno, M. Aron, O. Vince, C. Mannaris, A. Seth, M. de Saint Victor, G. Lajoinie, M. Versluis, C. Coussios, D. Carugo, and E. Stride, *Layered acoustofluidic resonators for the simultaneous optical and acoustic characterisation of cavitation dynamics, microstreaming, and biological effects.* Biomicrofluidics **12**(3), 034109 (2018).

[97] W. Slie, A. Donfor Jr, and T. Litovitz, *Ultrasonic shear and longitudinal measurements in aqueous glycerol.* Chem. Phys. **44**(10), 3712–3718 (1966).

[98] L. Negadi, B. Feddal-Benabed, I. Bahadur, J. Saab, M. Zaoui-Djelloul-Daouadji, D. Ramjugernath, and A. Negadi, *Effect of temperature on density, sound velocity, and their derived properties for the binary systems glycerol with water or alcohols.* The Journal of Chemical Thermodynamics **109**, 124–136 (2017).

[99] N.-S. Cheng, *Formula for the viscosity of a glycerol-water mixture.* Ind. Eng. Chem. Res. **47**(9), 3285–3288 (2008).

[100] I. I. Perepechko, V. A. Danilov, and V. V. Nizhegorodov, *Ultrasonic velocity in epoxy resin at temperatures down to 4.2 K.* Mech. Compos. Mater. **32**, 316–320 (1996).

[101] N. Bretz, J. Strobel, M. Kaltenbacher, and R. Lerch, *Numerical simulation of ultrasonic waves in cavitating fluids with special consideration of ultrasonic cleaning.* In *IEEE Int. Ultrason. Symp.*, 703–706 (2005).

[102] M. T. Todaro, F. Guido, V. Mastronardi, D. Desmaele, G. Epifani, L. Algieri, and M. De Vittorio, *Piezoelectric MEMS vibrational energy harvesters: Advances and outlook.* Microelectron. Eng. **183**, 23–36 (2017).

[103] M. Singh, H. M. Haverinen, P. Dhagat, and G. E. Jabbour, *Inkjet printing-process and its applications.* Adv. Mater. **22**(6), 673–685 (2010).

[104] MatWeb, LLC, *Online Materials Information.* http://www.matweb.com/ (2022).

[105] M. Radovic, E. Lara-Curzio, and L. Riester, *Comparison of different experimental techniques for determination of elastic properties of solids.* Mater. Sci. Eng. A **368**(1-2), 56–70 (2004).

[106] J. Plesek, R. Kolman, and M. Landa, *Using finite element method for the determination of elastic moduli by resonant ultrasound spectroscopy.* J. Acoust. Soc. Am. **116**(1), 282–287 (2004).

[107] J. Maynard, *Resonant Ultrasound Spectroscopy.* Physics Today **49**, 26–31 (1996).

[108] R. Holland, *Representation of Dielectric, Elastic, and Piezoelectric Losses by Complex Coefficients.* IEEE Transactions on Sonics and Ultrasonics **14**(1), 18–20 (1967).

[109] A. G. Steckel and H. Bruus, *Numerical study of acoustic cell trapping above elastic membrane disks driven in higher-harmonic modes by thin-film transducers with patterned electrodes.* Phys. Rev. E **submitted**, 14 pages (2021), ArXiv.org.

[110] W. D. Callister Jr, *Materials Science and Engineering: An Introduction* (John Wiley & Sons, York, PA), seventh edn. (2007).

[111] John D'Errico, *fminsearchbnd algorithm.* Matlab file exchange (2012), MATLAB Central File Exchange, Retrieved 28 Sep 2022.

[112] B. Hartmann and J. Jarzynski, *Polymer sound speeds and elastic constants.* Naval Ordnance Laboratory **Report NOLTR 72-269**, 1–10 (1972).

[113] D. Christman, *Dynamic properties of poly (methylmethacrylate) (PMMA) (plexiglas).* Report No. DNA 2810F, MSL-71-24 **1**(1) (1972), https://apps.dtic.mil/sti/pdfs/AD0743547.pdf, accessed 2 Apr 2022.

[114] H. Sutherland and R. Lingle, *Acoustic characterization of polymethyl methacrylate and 3 epoxy formulations.* J. Appl. Phys. **43**(10), 4022–4026 (1972).

[115] H. Sutherland, *Acoustical determination of shear relaxation functions for polymethyl methacrylate and Epon 828-Z.* J. Appl. Phys. **49**(7), 3941–3945 (1978).

[116] J. E. Carlson, J. van Deventer, and A. S. C. Carlander, *Frequency and temperature dependence of acoustic properties of polymers used in pulse-echo systems.* IEEE Ultrasonics Symposium 885–888 (2003).

[117] A. Simon, G. Lefebvre, T. Valier-Brasier, and R. Wunenburger, *Viscoelastic shear modulus measurement of thin materials by interferometry at ultrasonic frequencies.* J. Acoust. Soc. Am. **146**(5), 3131–3140 (2019).

[118] Norland Products Inc., Jamesburg, NJ 08831, USA, *Norland Optical Adhesive 86H.* https://www.norlandprod.com/adhesives/NOA86H.html, accessed 2 April 2022.

[119] J. C. Lagarias, J. A. Reeds, M. H. Wright, and P. E. Wright, *Convergence Properties of the Nelder–Mead Simplex Method in Low Dimensions.* SIAM Journal on Optimization **9**(1), 112–147 (1998).